



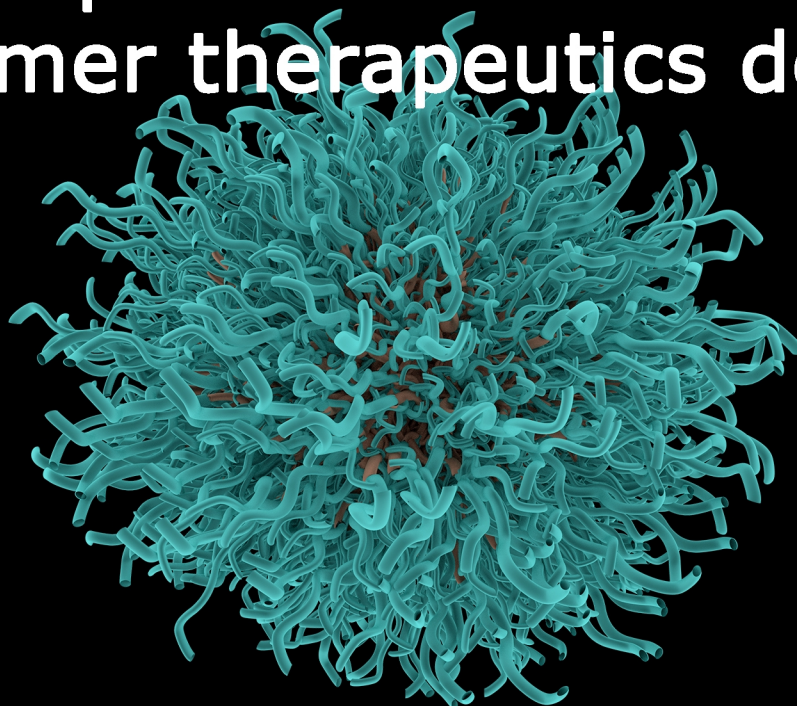
UNIVERSITAT
POLITÈCNICA
DE VALÈNCIA



PRÍNCIPE FELIPE
CENTRO DE INVESTIGACION

Oleksandr Zagorodko
Doctoral thesis

Conformationally switchable polyglutamates as a prospective material for polymer therapeutics design



Supervisors: Vicent J. Carda
Maria J. Vicent
Tutor: Ramon Martinez-Mañez

Valencia
December 2019

UNIVERSITAT POLITÈCNICA DE VALÈNCIA
CENTRO INVESTIGACION PRINCIPE FELIPE



UNIVERSITAT
POLITÈCNICA
DE VALÈNCIA



PRINCIPE FELIPE
CENTRO DE INVESTIGACION

CONFORMATIONALLY SWITCHABLE POLYGLUTAMATES AS A PROSPECTIVE MATERIAL FOR POLYMER THERAPEUTICS DESIGN

Doctoral Thesis
Oleksandr Zagorodko

Supervisors:
Dr. María J. Vicent
Dr. Vicent J. Nebot

Tutor:
Dr. Ramon Martínez-Mañez

December 2019
Valencia

ABSTRACT

Treatments based on polymer therapeutics offer numerous advantages when compared to conventional treatments and other nanomedicine approaches. These include passive tumor accumulation and the ability to cross specific biological barriers. Furthermore, polymer conjugation of drugs offers additional advantages such as improved pharmacokinetics, multivalency, co-delivery of drugs at the desired ratio, and specific release/activation at the required site of action via the application of polymer-drug linkers that respond to physiological stimuli. One of the most important types of polymers suitable for drug delivery belong to polypeptide polyelectrolytes, mainly due to their biocompatibility and synthetic plasticity of side chain modification.

The merging of polyelectrolyte science with other branches of chemistry seems very promising; however, it still remains in an embryonic state. While the control of polyelectrolyte self-assembly remains a complicated task, research in this area may provide more advanced biocompatible systems with unique profiles of action and new materials with yet unknown properties. The combination of polyelectrolytes with supramolecular moieties represents an especially interesting research topic, with the potential to derived more complicated architectures.

This thesis is focused on the development of supramolecular-polyelectrolyte-based drug delivery systems with high degree of control over physicochemical properties, focusing mainly on shape and size. Several families of star-polyglutamates with cores of different hydrophobicity have been studied in depth in order to determine how the core structure and polyelectrolyte chain length affect self-assembly mechanism.

Once these correlations were defined, the most promising candidates were selected for preparation of two drug delivery systems consisting of either spherical or rod-like particles. Finally, conjugation of several drugs (fasudil and dinaciclib) as single agents or in combination through different responsive linkers were also performed; physicochemical properties and *in vitro* activity of the conjugates were studied in depth and *in vivo* experiments with selected conjugates are currently ongoing in a preclinically relevant orthotopic Triple Negative Metastatic Breast Cancer Model.

RESUMEN

Los tratamientos en los que se utilizan Polímeros Terapéuticos ofrecen numerosas ventajas en comparación con los tratamientos convencionales y otros enfoques de nanomedicina. Entre estas ventajas se puede destacar la especificidad para cruzar ciertas barreras biológicas y su capacidad de acumulación pasiva en tumores. Además, la conjugación de fármacos a polímeros ofrece ventajas adicionales tales como una farmacocinética mejorada, multivalencia, co-entrega de fármacos en la proporción deseada y liberación/activación específica en el sitio de acción requerido a través de la aplicación de enlaces polímero-fármaco que responden a estímulos fisiológicos. Uno de los tipos más importantes de polímeros que se utiliza para la administración de fármacos pertenecen a los polielectrolitos polipeptídicos. Su uso se debe principalmente, a su biocompatibilidad, biodegradabilidad, multivalencia y versatilidad estructural, así como a la plasticidad sintética en la modificación de cadenas laterales.

La aplicación conjunta de ciencia de polielectrolitos con otras ramas de la química es muy prometedora; sin embargo, aún permanece en un estadio temprano en su desarrollo. Esto es debido a que, el control del autoensamblaje de polielectrolitos sigue siendo una tarea complicada y la investigación en esta área puede resultar muy laboriosa a la hora de encontrar sistemas biocompatibles más avanzados con un único perfil de acción y por supuesto, se abre un nuevo campo de estudio sobre las nuevas propiedades desconocidas de estos. Este tema es novedoso por la posibilidad de realizar diferentes estudios de combinación de polielectrolitos con residuos supramoleculares y representa el estudio de nuevas arquitecturas potencialmente mas complicadas.

En la presente tesis doctoral se estudiarán el desarrollo de sistemas de administración de fármacos basados en polielectrolitos supramoleculares con un alto grado de control sobre las propiedades fisicoquímicas, centrándose principalmente en el control de la forma y el tamaño. Se han estudiado en profundidad varias familias de poliglutamatos de forma estrella con núcleos de diferente hidrofobicidad para determinar cómo la estructura del núcleo y la longitud de la cadena de polielectrolitos afectan el mecanismo de autoensamblaje.

Una vez que se definieron estas correlaciones, se seleccionaron los candidatos más prometedores para la preparación de dos sistemas de transporte de fármacos que consisten en partículas esféricas o en forma de cilindro. Finalmente, también se realizó la conjugación de varios fármacos (fasudil y dinaciclib) como agentes únicos o en combinación a través de diferentes enlaces biodegradables. Las propiedades fisicoquímicas y la actividad *in vitro* de los conjugados se estudiaron en profundidad y actualmente se están llevando a cabo experimentos *in vivo* en un modelo de cáncer de mama metastásico triple negativo ortotópico preclínicamente relevante, con los conjugados previamente seleccionados.

RESUM

Els tractaments en els quals s'utilitzen Polímers Terapèutics ofereixen nombrosos avantatges en comparació amb els tractaments convencionals i altres enfocaments amb nanomedicina. Entre aquests avantatges es pot destacar l'especificitat per creuar certes barreres biològiques i la seva capacitat d'acumulació passiva en tumors. A més, la conjugació de fàrmacs a polímers ofereix avantatges addicionals com ara una farmacocinètica millorada, multivalència, co-lliurament de fàrmacs en la proporció desitjada i alliberament / activació específica en el lloc d'acció requerit a través de l'aplicació d'enllaços polímer-fàrmac que responen a estímuls fisiològics. Un dels tipus més importants de polímers que s'utilitza per a l'administració de fàrmacs pertanyen als polielelectròlits polipeptídics. El seu ús es deu principalment, a la seua biocompatibilitat, biodegradabilitat, multivalència i versatilitat estructural, així com a la plasticitat sintètica en la modificació de cadenes laterals.

L'aplicació conjunta de ciència de polielelectròlits amb altres branques de la química és molt prometedora; però, encara roman en un estadi primerenc en el seu desenvolupament. Això és degut al fet que, el control de l'autoensamblatge de polielelectròlits segueix sent una tasca complicada i la investigació en aquesta àrea pot resultar molt laboriosa a l'hora de trobar sistemes biocompatibles més avançats amb un únic perfil d'acció i per descomptat, s'obre un nou camp d'estudi sobre les noves propietats desconegudes d'aquests. Aquest tema és nou i que ofereix la possibilitat de realitzar diferents estudis de combinació de polielelectròlits amb residus supramoleculars i representa l'estudi de noves arquitectures potencialment més complicades.

En la present tesi doctoral s'estudiaran el desenvolupament de sistemes d'administració de fàrmacs basats en polielelectròlits supramoleculars amb un alt grau de control sobre les propietats fisicoquímiques, centrant-se principalment en el control de la forma i la mida. S'han estudiat en profunditat diverses famílies de poliglutamatos de forma estrella amb nuclis de diferent hidrofobicitat per determinar com l'estructura del nucli i la longitud de la cadena de polielelectròlits afecten el mecanisme de autoensamblatge.

Una vegada que es van definir aquestes correlacions, es van seleccionar els candidats més prometedors per a la preparació de dos sistemes de transport de fàrmacs que consisteixen en partícules esfèriques o en forma de cilindre. Finalment, també es va realitzar la conjugació de diversos fàrmacs (fasudil i dinaciclib) com a agents únics o en combinació a través de diferents enllaços biodegradables. Les propietats fisicoquímiques i l'activitat *in vitro* dels conjugats es van estudiar en profunditat i actualment s'estan duent a terme experiments *in vivo* en un model ortotòpic de càncer de mama metastàtic triple negatiu preclínicament rellevant, amb els conjugats prèviament seleccionats.

ACKNOWLEDGEMENT

I would like to express my immeasurable gratitude to Dra. Maria Jesus Vicent and Dr. Vicent J. Nebot for their instructive supervision, extensive help in experiment planning, their support and inexhaustible encouragement within the whole duration of the thesis.

Many thanks go to all the members of Polymer therapeutics laboratory for their help over the years and for perfect working environment they created in the laboratory. Special thanks go to the true chemists of our lab, known in narrow circles as Lunch Buddies, for our productive scientific discussions, national dinners and fun time we had together.

Another special thanks go to Stuart Atkinson, who went through the seven circles of chemical pandemonium while correcting this thesis and who unintentionally became a professional in advanced spectroscopic techniques. I should have thanked my master students, of course, who went through horrendous suffering while being under my supervision, but probably after the months of psychological recovery they will never read this thesis, so I'll skip this part.

I wish to thank to my family who gave me the freedom of choice and provided all possible support to achieve the life goals I have chosen.

Finally, special thanks to Tetiana Melnyk who always was a glimpse of light during the darkest moments of my life, who gave me an inestimable support whenever I needed it and who was there for me in spite of everything.

LIST OF ABBREVIATIONS

| | |
|---------------|--|
| ABA | p-aminobenzoic acid |
| AGM | Alanine:glyoxylate aminotransferase |
| AGM | Aminoglutethimide |
| AIP | 5-aminoisophthalic acid |
| BBB | Blood Brain Barrier |
| BTA | Benzene-1,3,5-tricarboxamide |
| CAC | Critical Aggregation Concentration |
| CD | Circular Dichroism Spectroscopy |
| CDI | 1,1-carbon diimidazole |
| CDK | Cyclin-Dependent Kinase |
| DIEA | N,N-diisopropylethylamine |
| Din | Dinaciclib |
| DLS | Dynamic Light Scattering |
| DMA | N,N-Dimethylacetamide |
| DMAP | 4-Dimethylaminopyridine |
| DMF | N,N-Dimethylformamide |
| DMSO | Dimethylsulfoxide |
| DMTMM | (4-(4,6-dimethoxy-1,3,5-triazin-2-yl)-4-methyl-morpholinium) |
| DNA | Deoxyribonucleic acid |
| DO3A | 1,4,7-Tris(carboxymethyl)-1,4,7,10-tetraazacyclododecane |
| DOSY | Diffusion Ordered Spectroscopy |
| Dox | Doxorubicin |
| DTAB | Dodecyltrimethylammonium bromide |
| DTT | Dithiothreitol |
| EPR | Enhanced Permeability and Retention |
| ER | Estrogen Receptor |
| ERK1/2 | The Extracellular Signal-Regulated Kinase 1/2 |
| FA | Folic Acid |
| Fas | Fasudil |
| FDA | Food and Drug Administration |
| Fmoc | Fluorenylmethyloxycarbonyl |
| GPC | Gel Permeation Chromatography |
| GSH | Glutathione |
| GTP | Guanosine Triphosphate |
| HBr | Hydrobromic Acid |
| HCl | Hydrogen Chloride |
| HER2 | Receptor Tyrosine-Protein Kinase erbB-2 |
| HMBC | Heteronuclear Multiple Bond Correlation |
| HPLC | High Performance Liquid Chromatography |
| HPMA | 2-(Hydroxypropyl) methacrylamide |
| HSQC | Heteronuclear Single Quantum Coherence Spectroscopy |
| MAPK | Mitogen-Activated Protein Kinase |
| MRI | Magnetic Resonance Imaging |

List of abbreviations

| | |
|-----------------|--|
| MS | Mass Spectrometry |
| MTT | 3-(4,5-dimethylthiazol-2-yl)-2,5-diphenyltetrazolium bromide |
| MTX | Methotrexate |
| NCA | N-Carboxyanhydrides of Amino Acids |
| NCE | New Chemical Entities |
| NHS | N-Hydroxysuccinimide |
| NMR | Nuclear Magnetic Resonance spectroscopy |
| NOESY | Nuclear Overhauser Spectroscopy |
| NR | Nile Red |
| PAA | Poly Amino Acid |
| pArg | Poly-L-arginine |
| pAsp | Poly-L-aspartic acid |
| PBLG | Poly-L-benzylglutamate |
| PBS | Phosphate Buffer Saline |
| PEG | Poly(ethylene glycol) |
| PEO | Poly(ethylene oxide) |
| PGA | Poly-L-glutamic acid |
| pHis | Poly-L-histidine |
| PI3K/Akt | Phosphatidylinositol 3-Kinase Pathway |
| PLL | Poly-L-lysine |
| PLO | Poly-L-ornithine |
| PR | Progesterone Receptor |
| PRZ | Phloridzin |
| PT | Polypeptide Therapeutics |
| PTX | Paclitaxel |
| PZLL | Poly(ϵ -carbobenzyloxy-L-lysine) |
| QC | Quality Control |
| ROCK | Rho-Associated Protein Kinase |
| ROP | Ring-Opening Polymerization |
| ROS | Reactive Oxygen Species |
| RSD | Relative Standard Deviation |
| SANS | Small Angle Neutron Scattering |
| SAXS | Small Angle X-ray Scattering |
| siRNA | Small interfering Ribonucleic Acid |
| stPGA | Star-Poly-L-glutamic acid |
| TDL | Total Drug Loading |
| TEM | Transmission Electron Microscopy |
| TFA | Trifluoroacetic Acid |
| TICT | Twister Intermolecular Charge Transfer |
| TNBC | Triple Negative Breast Cancer |
| UPy | 2-Ureido-4[1H]-Pyrimidone |
| UV | Ultraviolet |
| Wor | Wortmannine |
| XRD | X-ray Powder Diffraction |

TABLE OF CONTENTS

| | |
|--|-----------|
| Abstract..... | i |
| Resumen..... | iii |
| Resum..... | v |
| Acknowledgement..... | vii |
| List of abbreviations..... | ix |
| Table of content..... | xi |
| Objectives..... | xiv |
| Chapter 1. Introduction..... | 1 |
| 1.1. Historical Overview of Polymer Therapeutics..... | 1 |
| 1.2. Biomedical Applications of Polyamino Acids within Polymer Therapeutics Field..... | 3 |
| 1.3. Advanced Design of Polypeptide-based Conjugates..... | 7 |
| 1.3.1. Design of Structural Components..... | 7 |
| 1.3.1.1. The Polymeric Matrix..... | 7 |
| 1.3.1.2. Side-chains modifications: The Linking Moiety..... | 8 |
| 1.3.1.3. Crosslinking strategies to stabilize self-assembly polypeptide-based therapeutics..... | 9 |
| 1.3.1.4. Surface Decoration..... | 11 |
| 1.3.2. Design of Physicochemical Parameters..... | 13 |
| 1.3.2.1. Effect of Size..... | 13 |
| 1.3.2.2. Effect of Charge..... | 15 |
| 1.3.2.3. Effect of Conformation..... | 17 |
| 1.3.2.4. Effect of Geometry..... | 21 |
| 1.4. Merging Supramolecular and Polymer Chemistry as a Strategy to Control Polymer Morphology..... | 22 |
| 1.4.1. Supramolecular Polymers: Principles and Design..... | 23 |
| 1.5. References..... | 26 |
| Chapter 2. Towards Self-Assembling Polyglutamates..... | 31 |
| 2.1. Introduction..... | 31 |
| 2.2. Synthesis and Self-assembly of BTA-based Oligophenylalanines..... | 34 |
| 2.2.1. Synthesis of Oligophenylalanines Blocks..... | 34 |
| 2.3. Self-assembly Studies..... | 37 |
| 2.4. Study of BTA-oligophenylalanines with Mono and Diglutamate Termini..... | 40 |
| 2.5. Study of BTA-oligophenylalanine-based Polyglutamates..... | 44 |
| 2.6. Understanding the Mechanism of Assembly..... | 53 |
| 2.7. Self-assembly Studies of F3-based Star-polyelectrolytes including Different Amino Acid Sequences..... | 57 |
| 2.8. Effect of Counterions on Self-assembly of F3E10..... | 61 |

Table of contents

| | |
|---|----------------|
| 2.9. Conclusion..... | 65 |
| 2.10. Supplementary information..... | 66 |
| 2.11. References..... | 73 |
| Chapter 3. Role of aminoacid nature and order on the aqueous self-assembly of BTA-derivatives and corresponding polymers..... | 75 |
| 3.1. Introduction..... | 75 |
| 3.2. Synthesis and Self-assembly of Dipeptide Derivatives of BTA..... | 76 |
| 3.3. Synthesis and Self-assembly of star-PGAs with cores based on Dipeptide Derivatives of BTA..... | 82 |
| 3.4. Self-assembling of Tripeptide Derivatives of BTA..... | 84 |
| 3.5. Synthesis and Self-assembly of star-PGAs with cores based on tripeptide Derivatives of BTA..... | 92 |
| 3.6. Self-assembling of tetrapeptide derivatives of BTA..... | 93 |
| 3.7. Self-assembly of Tripeptide-derivatives of BTA with Different Chiralities.... | 97 |
| 3.8. Conclusion..... | 98 |
| 3.9. Supplementary information..... | 99 |
| 3.10. References..... | 113 |
| Chapter 4. Role of core and chain structure variations on star-PGA self-assembly..... | 114 |
| 4.1. Introduction..... | 114 |
| 4.2. Self-assembly of BTA Derivatives with Aromatic Insertions..... | 115 |
| 4.2.1. Self-assembly of BTA Derivatives with Aromatic Insertions as Hydrochloric Salts..... | 115 |
| 4.2.2. Self-assembly of stPGA based on ABA-F2 and AIP-F2..... | 125 |
| 4.3. Effect of Aliphatic Chain Hydrophobicity on Self-assembly of BTA-based Diphenylalanines..... | 128 |
| 4.3.1. Self-assembly of stPGA Based on F2C2 and F2C12..... | 133 |
| 4.4. Self-assembly of Complex BTA-based Derivatives..... | 135 |
| 4.5. Effect of Charge Density on Self-assembly of BTA-based PGAs..... | 138 |
| 4.6. Conclusion..... | 142 |
| 4.7. Supplementary Information..... | 143 |
| 4.8. References..... | 152 |
| Chapter 5. Development of poly-l-glutamate based combination conjugates designed as triple negative breast cancer therapy..... | 153 |
| 5.1. Introduction..... | 153 |
| 5.2. Optimization of PGA-Fasudil Conjugates as Anticancer Therapeutics..... | 155 |
| 5.2.1. Synthesis and Characterization of PGA-Fasudil Conjugates - Polymer-drug Linker Optimization..... | 155 |

| | |
|---|------------|
| 5.2.2. Drug Release Kinetics of PGA-Fasudil Conjugates..... | 159 |
| 5.2.3. <i>In vitro</i> Studies of PGA-Fasudil Conjugates..... | 160 |
| 5.2.4. Synthesis and Characterization of PGA-Fasudil Conjugates – Architectural Optimization..... | 163 |
| 5.2.5. Plasma Stability of Selected Conjugates..... | 164 |
| 5.2.5.1. Method Validation..... | 165 |
| 5.2.5.1.1. Linearity..... | 165 |
| 5.2.5.1.2. Stability..... | 165 |
| 5.2.5.1.3. Selectivity..... | 166 |
| 5.2.5.1.4. Precision and Accuracy..... | 166 |
| 5.2.5.1.5. Matrix Effect..... | 168 |
| 5.2.5.1.6. Recovery..... | 168 |
| 5.2.5.1.7. Process Efficiency..... | 168 |
| 5.2.5.2. Plasma Stability of the PGA-SS-FAS Conjugate..... | 169 |
| 5.2.6. <i>In vivo</i> Studies of the PGA-SS-FAS Conjugate..... | 170 |
| 5.3. Optimization of PGA-Dincaciclilb Conjugates..... | 172 |
| 5.3.1. Synthesis and Characterization of the Conjugates - Optimization of Polymer-drug Linkers..... | 172 |
| 5.3.2. Cell Viability studies with PGA-Dinaciclilb Conjugates..... | 176 |
| 5.3.3. Drug Release Kinetics of Selected PGA-Dinaciclilb Conjugates..... | 177 |
| 5.4. Optimization of a Polymer-Based Combination Conjugate..... | 178 |
| 5.5. Conclusion..... | 179 |
| 5.6. Supplementary information..... | 180 |
| 5.7. References..... | 187 |
| Chapter 6. Supramolecular Stabilization And Crosslinking..... | 189 |
| 6.1. Introduction..... | 189 |
| 6.2. Hydrophobic Stabilization of Supramolecular Polymers..... | 190 |
| 6.3. Polyelectrolyte Crosslinking in Water..... | 200 |
| 6.4. Conclusion..... | 208 |
| 6.5. Supplementary Information..... | 209 |
| 6.6. References..... | 211 |
| Chapter 7. General discussion..... | 213 |
| Annex. List of compounds..... | 224 |

OBJECTIVES

This thesis is included in a global project (ERC-Co-Grant-MyNano) with the objective of engineering tumour targeted polymer-based combination therapies specifically designed to treat metastatic breast cancer in a personalised manner. Accordingly, its **General Objective** is the development of self-assembling carriers and combination therapies suitable for treatment of cancer in general and triple-negative metastatic breast cancer (TNBC) in particular. Strategy to be always performed by using well-controlled synthetic approaches, validated by exhaustive characterization techniques and tested in relevant preclinical models in order to accelerate bench to bedside process.

This global aim frames the following **Specific Objectives**:

1. Synthesis and Characterization of star-shaped polyglutamates (stPGA)s based on BTA cores with capacity of self-assembling

1.1. A family of stPGAs with cores consisting of different number of BTA-derived oligophenylalanines and different polymerization degree will be designed and synthesized. All the compounds will be characterized in depth in order to find correlation between their structure and their self-assembly capacity.

1.2. In a second stage, in order to improve the self-assembly capacity, structural features such as the nature of aminoacids and their order, insertion of hydrophobic aromatic and aliphatic groups, variation of counterions and polymerization degree will be studied.

2. Development of Polypeptide-Based Combination Therapeutics for the treatment of triple-negative breast cancer (TNBC)

2.1. Two families of stPGA based conjugates with Rho-kinase inhibitor fasudil and CDK inhibitor Dinaciclib with different linkers will be synthesized and characterized. Polymer-drug bioresponsive linkers will be optimized to achieve adequate drug release kinetics. Fasudil and Dinaciclib were previously identified as a possible synergistic combination in TNBC models.

2.2. Successful candidates as single agents and as combinations will be selected for *in vitro* studies against breast cancer cell lines and *in vivo* in an orthotopic metastatic TNBC mouse model looking for anticancer synergism.

2.3. With those selected stPGA-drug conjugates from 2.2., two different crosslinking strategies will be developed in order to obtain stPGA combination conjugates with different shape and with the two drug in the same polymer main chain, important feature to achieve drug synergism. One approach will include non-covalent crosslinking through drug loading that will allow to obtain rod-like particles. The second approach will be a novel type of mild polyanion crosslinking with genipin in aqueous solution in order to obtain spherical particles.

Chapter 1

Introduction

1.1. Historical Overview of Polymer Therapeutics

In 1900, Paul R. Ehrlich proposed the idea of selective targeting in medicine with the concept of the “magic bullet” - a drug that targets only problematic/diseased cells without affecting healthy cells.¹ While this concept has yet to be fully realized, two strategies for precise targeting have emerged among others in medicine - the use of highly specific molecules and conjugates (e.g. antibodies) and the implementation of nanomedicine, in particular polymer-based drug delivery systems, known as Polymer Therapeutics. While they possess less selectivity when compared to antibodies, polymer therapeutics display greater versatility with an almost infinite variety of possible drug combinations, ample synthetic flexibility, and the ability to carefully and efficiently tune properties of the delivery system depending on the desired application.

The development of polymers possessing biological activity began in 1952 with the synthesis of polyvinylpyrrolidone and the application of an iodine complex as an antiseptic and a blood plasma extender.² The first attempts to prepare bioactive polymers by Overberger in 1954, tested (though unsuccessfully) the ability of polyvinyl pyrimidine derivatives to retard the growth of sarcoma-180 tumors (Lewis lung carcinoma),³ while a series of polyvinylpyrrolidone-mescaline conjugates with different linkers developed in 1955 by Von Horst Jatzkewitz represented the first known polymer-drug conjugate.⁴

The serious development of polymer therapeutics began in the 1970s, with the pioneering work of Ringsdorf, who developed homo- and copolymers of polyvinyl derivatives of cyclophosphamide and testosterone and demonstrated their anticancer activity *in vivo* on Yoshida ascites sarcomain mice.⁵ Recent years have seen the development of multiple polymer-based systems suitable for the delivery of drugs as a treatment for different diseases and pathological states. Five different families of Polymer Therapeutics exist, as depicted in **Fig. 1.1**.

Polymer therapeutics became a separate class of nanomedicines with a continual growth in the market with more than 25 products licenced for human use as polymeric drugs, sequestrants, conjugates, and as an imaging agent. Many exhibit both clinical and commercial success with new concepts already in clinical trials.⁶ Among Polymer Therapeutics, polymer conjugates have been the most successful examples; 1990 saw Food and Drug Administration (FDA) approval of the first polymer-protein conjugate, pegademase bovine or Adagen, used for the treatment of severe combined immunodeficiency disease associated with a deficiency of adenosine deaminase.⁷ Currently there are 18 polymer-protein conjugates and 1 polymer-drug conjugate in the market with many others in early and advanced clinical trials.^{8,9}

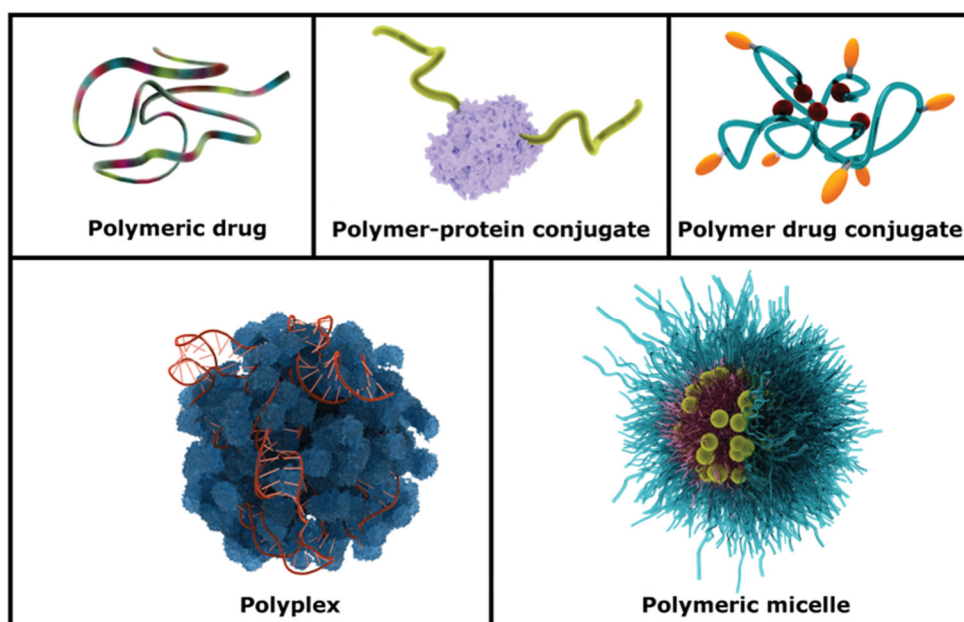


Figure 1.1. Schematic representation of existing Polymer Therapeutics families.

In each and any of these Polymer Therapeutics subtype are considered new chemical entities (NCE) rather than classical pharmaceutical formulations,¹⁰ the polymer in question can itself possess activity (mainly as a source of amino acids that affect

metabolic pathways) or play the role of a “carrier” (the conjugation of active agents or diagnostic agents), or a “shield” (the conjugation of biological macromolecules to induce stability). The other two families represented, polyplexes and polymeric micelles, self-assemble through ionic or hydrophobic interactions, respectively.¹¹

1.2. Biomedical Applications of Polyamino Acids within Polymer Therapeutics Field

Among many existing classes of polymers suitable for biomedical applications, polyaminoacids (PAA) or synthetic polypeptides are among the most promising due to substantial biocompatibility and low immunogenicity. This biocompatibility was recognized as early as 1959, when Kenny studied the application of sodium poly-L-glutamate (PGA) as a plasma expander.¹² Among the wide variety of synthetic polypeptides developed, those with the greatest promise bear functionalizable groups, such as the polyelectrolytes poly-L-aspartic acid (PAsp), PGA, and poly-L-lysine (PLL), as well as poly-L-ornithine (PLO), poly-L-arginine (pArg), poly-L-histidine (pHis). Many groups recognized the potential of PGA and PLL during the early development of the nanomedicine field, with PGA-melphalan, PLL-melphalan, PGA-doxorubicin, PGA-1-b-D-arabinofuranosylcytosine, and PGA-mitomycin C conjugates reported almost simultaneously in 1984.^{13–16}

The applicability of “simple” polypeptide therapeutics, where the polymer matrix acts exclusively as a carrier and does not provide any additional functionality, is determined by the properties of the conjugated or loaded drugs. Current developments in drug delivery systems of this type include the generation of new antimicrobial,^{17,18} anticancer,^{19–22} antidiabetic,²³ antiapoptotic,²⁴ antituberculosis,²⁵ antifungal,²⁶ MRI imaging,²⁷ and theranostic²⁸ agents. This is the most promising and rapidly growing area of polypeptide therapeutics and several compounds of this class are currently in early and advanced clinical trials as shown in the **Table 1.1**.

Polypeptides can also be applied in gene therapy approaches, as polycations can be used directly for polyplex preparation.^{37,38} The addition of supportive polymeric elements to polycations allows for the tuning of physicochemical properties, transfection efficiency, and silencing outcomes. Previous studies established that pArg and polyester amide polyplexes precisely regulated the immune response of oligonucleotides, providing a new nano-immunotherapeutic approach³⁹, while dendritic pLys decorated with polyglycerols were used for siRNA delivery.⁴⁰ The application of polyanions in gene delivery generally requires modification with cationic groups; as an example, grafting chitosan to pAsp provides polycationic characteristics suitable for the preparation of polyplexes with plasmid DNA.⁴¹

Another group of polymer therapeutics includes compounds with a two-step mode of action; the polymer acts as a carrier to concentrate an inactive prodrug to a desired site of action, and a secondary treatment activates the conjugated moiety, thereby

allowing for localized therapy. As an example, the conjugation of boron-containing agents allows the generation of conjugates suitable for neutron capture

Table 1.1. Polypeptide-based nanomedicine in clinical trials

| Name (Company) | Polymer carrier | Drug | Indications | Stage | Ref |
|-----------------------------------|-------------------------------------|-------------|---|--------------------------|---------------|
| NC-6004 (NanoCarrier) | PEG-b-PGA micelle | Cisplatin | Pancreatic cancer | Phase III (NCT02043288) | ²⁹ |
| Opaxio (CTI BioPharma) | PGA | Paclitaxel | Ovarian cancer, peritoneal cancer and fallopian tube cancer | Phase III (NCT00108745) | ³⁰ |
| NK012 (Nippon Kayaku) | PEG-b-PGA micelle | SN-38 | Breast cancer | Phase II (NCT00951054) | ³¹ |
| DEP docetaxel (Starpharma) | PEG-PLL dendrimer | Docetaxel | Solid tumours | Phase II (NA) | ³² |
| NC-6300 (NanoCarrier) | PEG-b-pAsp micelle | Epirubicin | Solid tumours and soft tissue sarcoma | Phase I/II (NCT03168061) | ³³ |
| DEP cabazitaxel (Starpharma) | PEG-PLL dendrimer | Cabazitaxel | Solid tumours | Phase I/II (NA) | ³⁴ |
| NC-4016 (NanoCarrier) | PEG-b-PGA micelle | Oxaliplatin | Solid tumours and lymphoma | Phase I (NCT03168035) | ³⁵ |
| RadProtect (Original BioMedicals) | PEG-b-PGA chelating complex micelle | Amifostine | Acute radiation syndrome | Phase I (NCT02587442) | ³⁶ |

therapy, such as block PEG-b-PGA-conjugated sodium borocaptate.⁴² Boron exists isotope capture gamma radiation leading to cell lysis and there many boron compounds in clinics and under studies;⁴³ however, PGA-containing polymers can increase borocaptate targeting and retention. Photosensitizing molecule-conjugates suitable for photodynamic therapy represent another example of therapeutics with a two-step mode of action. As an example, star-shaped PGAs with porphyrin cores or conjugated with phthalocyanines^{44,45} induce formation of reactive oxygen species (ROS) resulting in cell death (**Fig. 1.2**).

A third group of polymer therapeutics are those that display unique properties, such as responsiveness to external stimuli (pH, ROS, magnetic fields, GSH, etc.) or specific accumulation (e.g. targeting lymph nodes^{46,47} or specific intracellular organelles such as peroxisome.⁴⁸ The conjugation of Alanine:glyoxylate aminotransferase (AGT) to PEG-PGA derivatives through disulfide bonds to the enzyme showed intracellular trafficking modulation as AGT was clearly localized in the liver peroxisomal compartment and therefore was capable to show promising results in the rare disorder Primary Hyperoxaluria Type I.⁴⁸ pHis-based conjugates have been used to prepare pH-sensitive conjugates with enhanced endolysosomal escape properties,^{49–51} while hypoxia sensitive

micelles can be prepared by conjugating hypoxia-responsive agents such as nitroimidazole to PEG-PGA.⁵²

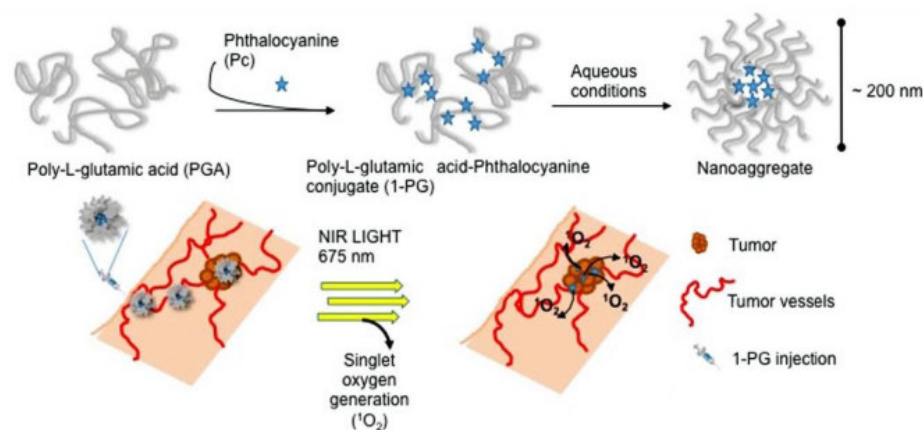


Figure 1.2. Example of PGA-based photodynamic therapy.³²

Many authors have proposed the use of polycations as polymer therapeutics suitable for intravenous injections, however bare polycations could trigger substantial *in vivo* toxicity due to a poor hematocompatibility.⁵³ One possible solution to this problem is to mask functional groups with labile anionic or neutral groups or polymers. DEP® technology in Phase II clinical trials (Table 1.1) from Starpharma is a clear example of this approach with a PLL dendrimer with stealth properties.^{54,55} PLL can be also modified with 2,3-dimethylmaleic anhydride to obtain charge reversible micelles. The β -carboxylic amides formed by this approach hydrolyze in the mildly acidic pH of the extracellular matrix, thereby switching PLL from anionic to cationic (**Fig. 1.3**).⁵⁶

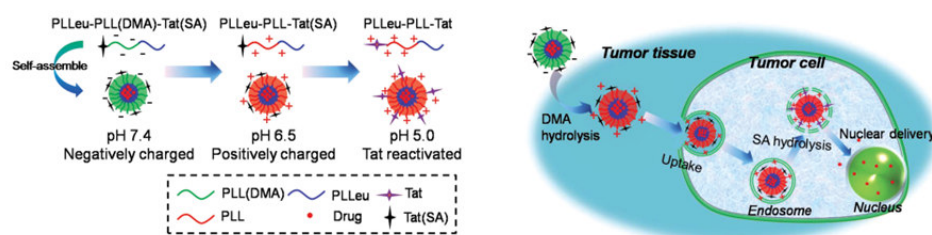


Figure 1.3. pH-triggered charge reversal micelles based on PLL and schematic representation of nuclear drug delivery with corresponding micelles.

Preparing polyplexes with polyanions represent an alternative means of changing the charge to neutral or weakly acidic; the application of PLL with polyacrylate represents an example of this approach.⁵⁷ A similar strategy can also be used for other polycations; oligoethyleneimine-graft PEG-pAsp displays significantly lower levels of

when compared to free oligoethyleneimine when studied as a contrast agent⁵⁸ and anticancer therapy.⁵⁹ Additionally, short pHis and pArg fragments can be used as cell-penetrating peptides, while pHis can also be employed for lysosome delivery.^{60,61}

The polypeptide-based materials discussed until this moment were developed for intravenous delivery; however, the last group of therapeutics contains those compounds suitable for alternative delivery strategies. All polypeptides can be tuned for mucosal delivery purposes; in general, polyamines have high mucoadhesivity. PArg and PLys are directly suitable for intranasal delivery and enhance nasal absorption,⁶² while polyplexes of a PGA conjugated with an antigen and trimethyl chitosan as a mucoadhesive molecule demonstrated their potential suitability for intranasal vaccine delivery.⁶³ Finally, polycations, as a part of formulations, are suitable for oral delivery as has been shown for pArg and pArg polyplexes with polyacrylate.⁶⁴

Although outside the scope of this thesis, just a short note to mention that PAAs can also be used for the surface modification of inorganic nanoparticles to increase biocompatibility. Surface modification of mesoporous silica loaded with doxorubicin with pHis allowed the preparation of gated nanoparticles with pH-controlled release (Fig. 1.4).⁶⁵ A similar approach was applied for pLys-modified mesoporous silica particles loaded with prednisolone for colon delivery.⁶⁶ PAsp has also been used as a “gatekeeper”, given its responsiveness to the acidic pH encountered in lysosomes and endosomes.⁶⁷

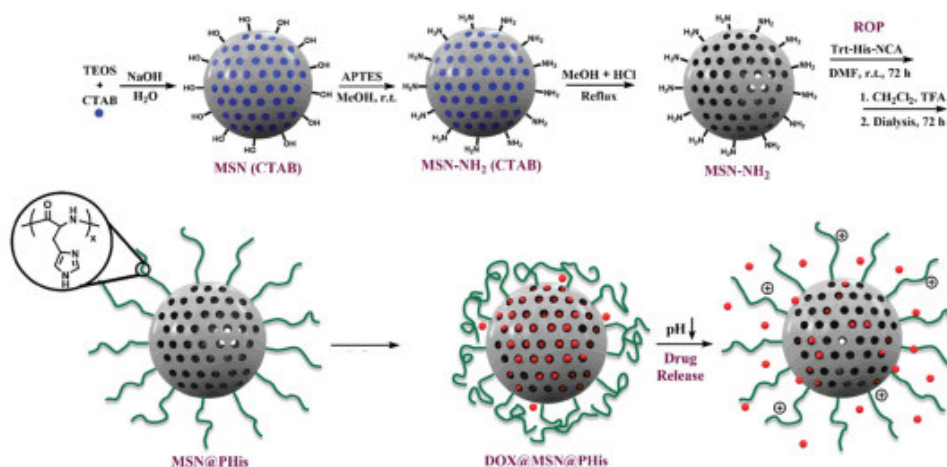


Figure 1.4. Schematic illustration of Dox-loaded pHis-functionalized mesoporous silica nanoparticles for pH-triggered release.⁶⁵

1.3. Advanced Design of Polypeptide-based Conjugates

Despite the significant advances made in the field of polypeptide therapeutics, as well as related scientific disciplines, the precise design of corresponding drug delivery systems remains a serious challenge. This is mainly due to the immense complexity of the biochemical network of interactive and regulative parameters that determine the fate of a given polymer therapeutic in the body. Nevertheless, extensive investigation in the area revealed some correlations between the physicochemical properties of the polypeptide-based conjugates and activity. Size, shape, conformation, surface charge, surface ligand pattern, and the intrinsic nature of the polypeptide material itself all represent critical physicochemical parameters to consider during the design of a conjugate.

1.3.1. Design of Structural Components.

The preparation of polypeptide-based nanomedicines mainly involves three stages, as shown in **Fig. 1.5**. The first and second stages involve the preparation of the macromolecular matrix and further conjugation of the functional moiety by post-polymerization modification approaches. The third stage involves the crosslinking of particles to reach a necessary size and stabilize the structure. Finally, post-synthetic modifications of particle surface can impart several varied advanced biological properties.

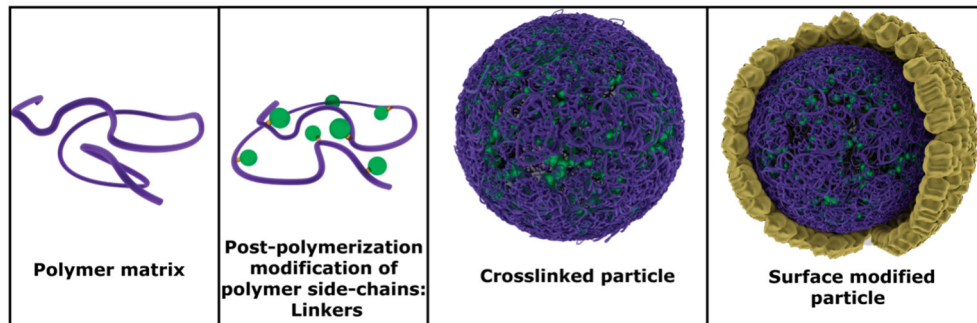


Figure 1.5. Stages of polypeptide-based nanomedicine preparation.

1.3.1.1. The Polymeric Matrix.

Recent advances in polymerization techniques, especially ring-opening polymerization (ROP) of N-carboxyanhydrides of amino acids (NCAs)⁶⁸ has allowed the synthesis of PAAs with narrow polydispersity, minimized levels of side products, and high reproducibility that, together with low price, represent some of the most important parameters determining success and applicability of a given material outside the research laboratory. The great advantage of polypeptide matrices is their possible implementation

linker. For example, beta-thiopropionate displays higher pH (acid) sensitivity due to the inductive effect of a sulfur atom and the formation of partial positive charge on the ester carbonyl carbon.⁸⁰ Orthoesters,⁸¹ beta-aminoesters,⁸² succinic esters or amides,⁸³ and beta-sulfonyl esters⁸⁴ all exhibit increased release rates in acidic medium. Other pH-sensitive linkers used include acetals, Schiff bases, cis-aconityl, carbonates, and carbamates.⁸⁵

Redox-sensitive linkers are represented almost exclusively by disulfide linker;⁴⁸ however, a few studies have reported the potential of diselenide linkers.⁸⁶ Meanwhile, ROS-sensitive linkers are represented by a few distinct families of compounds, including organochalcogens, boronic esters, thioethers, and thioketals.⁸⁷

Self-immolative linkers provide rapid and efficient release of a given active agent; these linkers usually consist of a stimuli-responsive component (e.g., a peptide sequence, disulfide linker, etc.), an immolative component, and the active agent. After cleavage of the bioresponsive part, active intermediate forms that usually rearranges and eliminates the active agent and any side products. Typical examples of self-immolative linkers contain fragments of aminobenzyl alcohol, carbamates, and carbonates with an N/S/O-containing group in the beta position or related compounds.⁸⁸

1.3.1.3. Crosslinking strategies to stabilize self-assembly polypeptide-based therapeutics.

While polypeptide conjugates can be employed without further modification, the relatively small size of polymers generally used for conjugation (below 50 kDa) could lead to short blood half-lives and even to non-specific biodistribution profiles. This fact could be overcome by increasing nanoconstruct size, for example, relying on self-assembly strategies among others. This is due to the fact that a given nanosystem can passively extravasate more selectively at inflamed or tumor tissues due to the increased permeability of the angiogenic tumor vasculature and defective lymphatic drainage. This selective effect, first described by Maeda and Matsumura, is known as the “Enhanced Permeability and Retention (EPR) effect”.^{89,90} EPR-mediated targeting is finally determined by circulating plasma concentration, stability, and plasma half-life of the polypeptide therapeutics.⁹¹ The EPR effect in human patients also presents with patient-to-patient variability, depending on a patient's pathological and physiological characteristics and clinical condition and has provoked diverse opinions regarding the real value of the EPR effect.^{92,93} Some studies support EPR-mediated accumulation of nanomedicines within tumors, while others show that the EPR effect depends on the tumor model, suggesting that the EPR effect alone may not provide the entire solution. Maeda himself recognizes this heterogeneity and has developed methods to enhance the EPR effect in order to overcome the heterogeneity and improve drug delivery to tumors.⁹⁴

In order to take the most of the (EPR) effect,^{91,94} in some cases, conjugates can be assembled into micelles that display susceptibility to disassembly upon dilution.²⁹ In

both instances, crosslinking strategies can stabilize the structure of the drug delivery system and enhance therapeutic outcomes.

Two main crosslinking strategies exist – crosslinking during or after synthesis (**Fig. 1.7**). In the first examples, the addition of bi- or trifunctional monomers to the polymerization reaction generates crosslinked particles. In this case, a high degree of control over size can be achieved by controlling synthetic parameters. Post-synthetic crosslinking employs chemical approaches used for linkers with previously synthesized polymers; however, crosslinkers are usually bi- or trifunctional. In general, post-synthetic crosslinking is preferred in drug delivery systems, because it allows to prepare particles with homogeneous distribution of the drug in the whole volume of the particle.

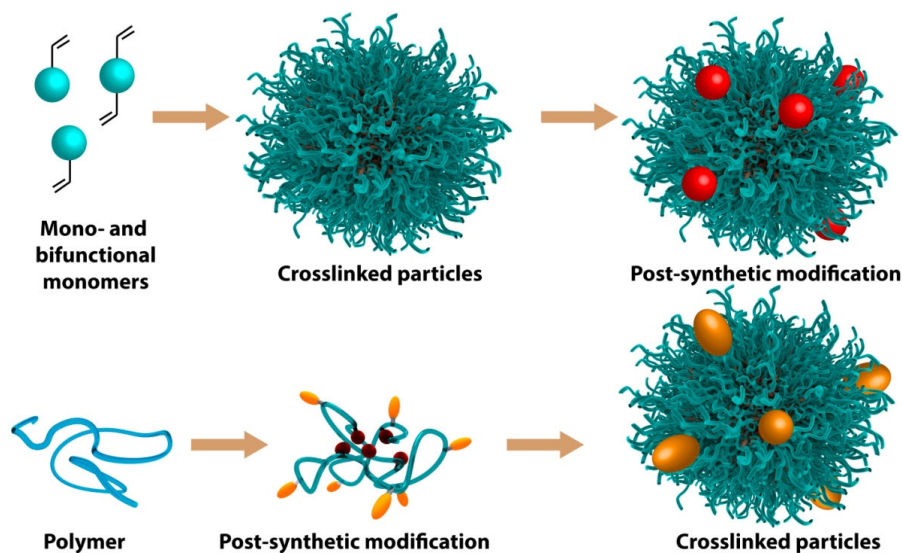


Figure 1.7. General scheme of crosslinking strategies.

Two different types of post-synthetic crosslinking exist depending on the nature of the chemical bonds – chemical (covalent) and physical (non-covalent). In both cases, crosslinkers can be designed to be responsive/non-responsive or degradable/non-degradable. Click-reaction azide-alkyne and Michael addition are among the widely used non-responsive non-degradable crosslinkers. On more rare occasions, photocrosslinkers able to form dimers under UV irradiation can be used (e.g. chalcon), however this approach requires complex synthetic modifications.⁹⁵ Site specific crosslinking strategies that depend on the nature of polymer side chain are also used; these include glutaraldehyde or genipin crosslinking (for amine-containing polymers), aziridines, diamines, carbodiimides (for carboxylate-containing polymers), and isocyanates (for hydroxyl-containing polymers).⁹⁶ Biodegradable/bioresponsive crosslinking strategies are practically identical to the approaches employed for the corresponding linkers and

include disulfides, boronic acid, vicinal diols, and acetal/ketal derivatives among others.⁹⁷

Although much less used in the drug delivery field, non-covalent crosslinking strategies could be also used.^{98,99} These include ionic interactions (e.g., the formation of polyplexes between oppositely charged polymers), metal complexation (e.g., the crosslinking of alginates with calcium or PGA with platinum, or PGA-catechols with iron¹⁰⁰), and a broad range of supramolecular interactions (e.g. host-guest interactions between cyclodextrin and hydrophobic molecules,¹⁰¹ crown ethers and secondary ammonium salts etc.).¹⁰² Of note, some self-assembled micelles can be non-covalently crosslinked by hydrophobic drugs.

1.3.1.4. Surface Decoration.

Crosslinked nanomedicines usually display non-specific accumulation in tissues through passive targeting by the EPR effect.¹⁰³ However, the EPR effect is for example influenced by tumor type, tumor region, presence of intratumoral necrotic or inflamed area, and tumor vascularization. Therefore, poorly-vascularized damaged tissues are less suitable for nanomedicine-based treatments,⁹¹ demonstrating for a requirement for new PT-based therapeutic approaches incorporating targeting moieties. The EPR effect also suffers from several additional limitations that promote the application of active targeting strategies.¹⁰⁴ These include (i) the inability of the nanomedicine to interact with blood components or blood vessels; (ii) the requirement for weakly negative to near neutral total surface charges; (iii) a requirement for systemic circulation times of several hours/days; and (iv) interactions of the nanomedicine with serum proteins and the subsequent alteration in size profiles.

Antibodies and specific proteins that serve both as a carrier and targeting moiety represent the exceptions allowing tissue tropism. Importantly, surface decoration of a given nanomedicine with molecules that specifically bind to a receptor allow for active targeting. Decoration with an antibody (or antibody subunits) provides the highest selectivity for selected receptor/tissue targeting,^{105,106} however, despite the benefits of this approach, it has been extremely difficult to develop a series of antibodies to target the whole range of heterogeneous malignant tissues. The overexpression of cell surface receptors can be used to target specific tissues; examples of small molecules used for surface decoration include folate (cancer),¹⁰⁷ biotin (cancer),¹⁰⁸ riboflavin (cancer)¹⁰⁹, saccharides (e.g. TriGalNAc¹¹⁰ and ribavirine¹¹¹ for liver and galactopyranose for cancer),^{112,113} and small peptides (e.g. Arginylglycylaspartic acid or des-octanoylghrelin¹¹⁴ to cross the blood-brain barrier).¹¹⁵

In addition to active targeting, surface modification can change the behavior of the drug delivery system in the systemic circulation and cellular uptake efficiency. Surface modification with hydrophilic moieties controls the recognition and opsonization of nanoparticles in the bloodstream.¹¹⁶ PEGylation of a nanomedicine forms “stealth” surface with significantly decreased opsonization; denser PEG-coating

and higher molecule length provide more efficient shielding against removal from the bloodstream by the reticuloendothelial system.¹¹⁷ PEGylation can also reduce uptake by tumor cells; however, this does not alter permeation across the endothelial cell monolayer maintaining transport across mucosa.^{118,116} Although PEGylation was an effective approach to improve pharmacokinetics, its use is limited by non-biodegradability and possible immune response and patient hypersensitivity. Recently, polysarcosine, non-ionic hydrophilic polypeptoid was proposed as an alternative to PEG.¹¹⁹ It is fully biodegradable (even though the mechanism of this is not fully understood) and does not cause acute immune response and toxicity.^{120,121}

Typical drug conjugate design includes the synthesis of nanoparticles with a random surface distribution of ligands that limits or completely restricts manipulations such as ligand grouping or control over cluster size and spacing. Some cell receptors exist as clusters on target cells/tissues, and targeting efficiency can be enhanced by designing the most efficient ligand pattern. This concept was never realized on polypeptide-based medicine, however was demonstrated on oligopeptide-based patchy micelles. Frison et al. demonstrated that fibroblasts display a differential uptake of (diglycoside clusters)_{n+1}-Lys_n depending on the cluster type.¹²² Poon et al. synthesized patchy micelles from linear dendritic polymer (PBLAsp)₁₂-PED (polyester Dendron)-PEG600-FA with 0-100 % folate functionalization, providing micelles with different cluster arrangements.¹²³ They determined that optimal cluster arrangement results in enhanced targeting properties due to the binding of more micelles to cells and a longer cell surface binding time, all of which increases the probability of endocytosis (**Fig. 1.8**). The binding energy increased with increasing folate modification from 10% to 40 % and then began to decrease due to steric binding interference caused by the excess of ligands clustered in a small binding area.¹²³

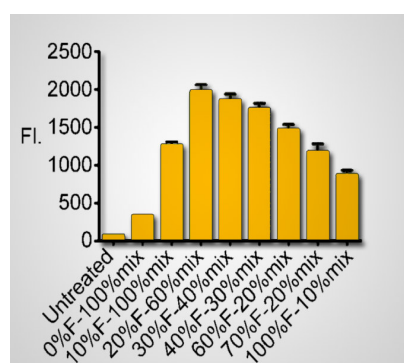


Figure 1.8. *In vitro* evaluation of patchy micelles on KB (folate receptor, FR+) cells. KB cell-associated fluorescence (Fl.) after 24 h of incubation with micelle formulations. Adapted from ¹²³.

1.3.2. Design of Physicochemical Parameters.

Fine tune of the physicochemical parameters of the polypeptide-based nanomedicine is the most essential and complicated part of its design. There are two types of physicochemical parameters - core (size, charge) and auxiliary (conformation, shape, architecture). Core parameters directly determine time of circulation and elimination from the bloodstream and biodistribution. Auxiliary parameters influence biodistribution, cell penetration and drug release kinetics and can be used for fine tuning of the nanomedicine properties.

1.3.2.1. Effect of Size.

The size of nanoparticles is a core physicochemical property that determines the immediate fate of particles in the bloodstream, as well as their biodistribution and subsequent cell uptake. In the bloodstream, particles with a size below 5 nm will rapidly diffuse through capillary fenestrae, equilibrate with the extracellular space, and become quickly cleared by the renal glomerular capillaries. Larger particles exhibit prolonged circulation times (except in cases when factors other than size guide clearance); however, the reticuloendothelial system will clear any particle whose size exceeds 200 nm. Thus, the size of nanoparticles for biomedical research should lie in a size range between 5 to 200 nm. Additionally, as shown in **Table 1.2**, different tissues in the body have different pore sizes and, therefore, the porosity of the desired targeting site should be considered to maximize the therapeutic efficiency of a conjugate. In some cases (blood-brain and blood-retinal barriers), the nature of the polymer, rather than size, exclusively determines the possibility of penetration due to specific polymer-cell interactions.¹²⁴

Table 1.2. Pore sizes in different tissues.

| Tissue | Pore size | Ref. |
|--|-----------|----------------|
| Normal intact endothelium | 4-11 nm | ¹²⁵ |
| Interstitial/lymphatic fenestration | > 20 nm | ¹²⁶ |
| Filtration-size threshold of the glomerular capillary wall | 6 nm | ¹²⁷ |
| Fenestrated capillaries | 70-90 nm | ¹²⁵ |
| Leaky tumor vasculature | < 200 nm | ¹²⁶ |
| Reticuloendothelial system threshold | > 200 nm | ¹²⁸ |
| Blood-bone barrier fenestrated capillaries | < 80 nm | ¹²⁹ |
| Blood-brain barrier | < 1 nm | ¹³⁰ |

As mentioned above, the enhanced permeability and retention effect (EPR) facilitates nanomedicine targeting in some cancers, due to the more permeable nature of the tumor-associated capillary endothelium. Macromolecules must remain in the

circulation for at least six hours to take full advantage of the EPR effect;¹³¹ thereby promoting preferential passive accumulation at the tumor site and decreasing non-specific accumulation in healthy tissues (which may entail off-target toxicity).¹³²

The size of polypeptide nanoparticles can be controlled by introducing hydrophobic moieties either by the synthesis of copolymers with one monomer bearing hydrophobic moieties or through conjugation with hydrophobic drugs.^{76,133} In both cases, phase separation results in the formation of micelles in aqueous solutions.

Key parameters that determine the self-assembly of polypeptides include the nature of the hydrophobic moiety, its content, the concentration in solution, and the ionic strength of the solvent. The conjugation of hydrophilic drugs does not usually stimulate self-assembly as was shown for a PGA-aminogluthathione conjugate, for example.¹³⁴ In the case of highly hydrophobic drugs that can form a non-covalent bond between its own molecules (such as doxorubicin, paclitaxel, camptothecin, etc.), aggregation behavior changes following an increase in loading. The conjugation of a low amount of drug (1-3 mol%) usually prompts the formation of large disordered aggregates due to point-to-point aggregation (**Fig. 1.9**), with PGA-doxorubicin (1.3 mol%, 390 nm) a notable example.¹³⁴

Smaller and more well-defined micelles tend to form upon an increase in drug content to ~5-15 molar percent (roughly 10-35 wt%). The size of the obtained particles generally varies between 25 to 150 nm, as shown for PGA-g-methoxyPEG-gemcitabine (15 mol% loading, 30-150 nm size),¹³⁵ PGA-g-methoxyPEG-patupilone (14.6 mol%, 80±20 nm),¹³⁶ PGA-combretastatin A4 (33.7 wt%, 28 nm),¹³⁷ PGA-mPEG-podophyllotoxin (21 wt%, 100±30nm),¹³⁸ PEG-pAsp-doxorubicin (17 wt%, 15-60 nm),¹³⁹ PLL-b-poly(methacryloyloxyethylphosphorylcholine)-doxorubicin (11.3 mol %, 88 nm),¹⁴⁰ and PGA-b-PEG-camptothecin (15.2 and 35.1 mol%, 30 and 60 nm, respectively).¹⁴¹

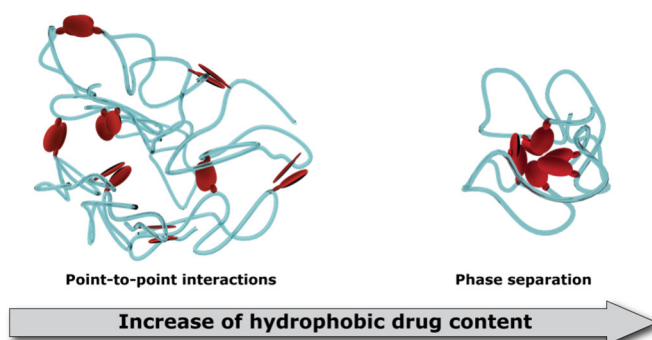


Figure 1.9. Schematic representations of the altered self-assembly of a conjugate upon an increase in hydrophobic drug content.

Micelles increase in size when the content of the conjugated drug increases further due to the formation of larger hydrophobic cores and smaller disordered polyelectrolyte coronae. Salmanpur et al. demonstrated the formation of conjugates assembled into spherical particles 100-500 nm in size following the modification of all residues in poly (2-ethyl 2-oxazoline)-b-PGA with irinotecan.¹⁴²

When drugs do not form non-covalent interactions, there may not exist any obvious dependence of size on drug loading. An investigation into a series of γ -PGA with different contents of the anti-diabetes drug phloridzin (PRZ) found that all conjugates formed spherical particles with an average size of 149 ± 23 , 187 ± 4.0 , and 170 ± 19 nm for PGA-PRZ-7%, PGA-PRZ-15%, and PGA-PRZ-25 wt%, respectively.¹⁴³ Another study found that PGA-doxycycline conjugates with 15 and 30 wt% loading possessed sizes of 6.2 ± 1.3 nm and 7.5 ± 0.7 nm, respectively.¹⁴⁴

Finally, while the effect of a combination of hydrophobic drugs on conjugate size is complicated to predict, the effect is normally additive. For example, [PEG-b-p(Asp-Hyd)] copolymer conjugates with a molar ratio of Dox and Wortmannin (Wor) varied from 0 to 100 % (with a total 100% modification of hydrazine groups), all particles measured less than 100 nm. There were some size variations between the samples with different Dox:Wor ratios, but the overall trend remained.¹⁴⁵ For a PGA-paclitaxel (PTX)-Dox, PTX and Dox affected the size of the conjugate in different ways;¹⁴⁶ while conjugation with PTX (13.5 %) did not affect the size significantly (4.6 nm against 4.5 nm for non-modified PGA), Dox conjugation (2.8 %) significantly increased particle size (17 nm), and the combination of both drugs (2 % PTX and 5 % Dox) increased particle size further to 37.5 nm.¹⁴⁶

Of note, the self-assembly of polyelectrolyte-based polypeptide copolymers is considerably more complex and resists a simple generalization. The principles described above are valid only for copolymers with a relatively low number of hydrophobic blocks, although, even in such “simple” cases, multiple morphologies exist.

1.3.2.2. Effect of Charge.

The surface charge of particles represents the second core physicochemical parameter, determining conjugate recognition in and clearance from the systemic circulation and regulating conjugate interaction with the cell membrane, cellular uptake, and toxicity.¹¹⁶ Additionally, surface charge determines the physical stability of the system and the tendency to aggregate (particles with a higher absolute ξ or zeta potential value have a lower tendency to aggregate due to increased electrostatic repulsion).¹⁴⁷

Directional synthesis of conjugates with preselected zeta-potential is a more straightforward task than controlling size, as zeta-potential is purely defined by the quantity of charged groups on the polymer and the pH of the solution. Polymers with larger number of negatively charged groups (carboxylic, sulfonic) will have a negative ξ -potential and vice versa. For example, all conjugates of PGA with neutral molecules

will have negative ξ -potential; however, the absolute value decreases upon an increase in the degree of conjugation or upon interaction with molecules displaying the opposite charge. For two samples of PGA-b-PEG with 10 and 20 wt% loading of cisplatin, the value of ξ -potential was found to be -17.7 ± 1.0 mV to -8.5 ± 1.3 mV due to the neutralization of the negative charge by a positively-charged platinum derivative.¹¹⁷ Charge neutralization of more than 50% by covalent modification or electrostatic interactions leads to charge reversal. Relatively high positive surface charge of cationic polypeptides, such as PGA(hydrazide)-b-PDMAPMA₃-g-PEG ($\xi = +46.3$ mV) can be balanced and reversed to -20.5 mV through complexation with small interfering (si)RNAs (**Fig. 1.10**).¹⁴⁸ Ma et al. demonstrated a charge reversal in PLL-b-polymethacryloyloxyethyl phosphorylcholine by covalent modification of amine groups with Dox and 4-carboxy benzaldehyde through hydrazone linkers, changing the zeta-potential from $+35$ mV to -10 mV. Of note, Zeta potential switched to the original value after hydrolysis of hydrazone linkers.¹⁴⁰

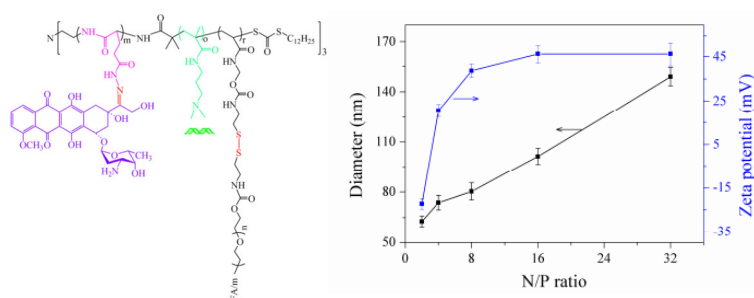


Figure 1.10. The general structure of polymer conjugates PGA(hydrazide)-b-PDMAPMA₃-g-PEG and zeta potential of micelles at different N/P ratio.¹⁴⁸

For the majority of polymer conjugates, mild tuning of zeta-potential can be achieved by modification of the nanoparticle surface with neutral molecules (e.g., PEG), forming so-called doubly-hydrophilic polymers.¹⁴⁹ One study discovered that the incorporation of 50 wt% of a PEO-PEG block into a PGA-based copolymer decreased the surface charge from -30 to -20 eV.¹⁵⁰ Of note, it is impractical to change ξ -potential significantly and impossible to prompt charge reversal with non-charged molecules because neutral chains do not modify the polyelectrolyte nature of the polymer.

In block-copolymers bearing opposite charges, ξ -potential can be controlled with a ratio of monomers of different nature or by pH change. One study of a series of random PGA-PLL polymers revealed that the molar ratio of Glu/Lys influenced surface charge of aggregates, which consequently affected the transition pH of surface charge reversion. When Lys/Glu content increased from 0.67/1 to 4.1/1, the zeta potential increased in a similar manner, from -30.3 to $+4.9$ mV.¹⁵¹

1.3.2.3. Effect of Conformation.

While the conformation of the polymer chain is a secondary physicochemical parameter determining the *in vivo* behavior of the conjugate, it remains an important characteristic to consider during drug delivery system design. In many cases, the careful control over conformation may expand the functionality and applicability of the conjugate (e.g. pH and thermal responsiveness). To a lesser extent than charge and size, conformation influences the interaction with the cellular membrane and therapeutic efficiency of the conjugate.¹⁵² For example, PEG-b-L-PGA-cisplatin and PEG-b-D-PGA-cisplatin, which adopt helical conformation with different handedness, display no differences with regards to biodistribution or anticancer activity. However, PEG-b-D,L-PGA-cisplatin micelles that failed to form helical conformation displayed lower activity and became cleared from the systemic circulation faster even though particle size for all the compounds remained similar (around 25 nm). Overall, the authors concluded that an α -helical structure further stabilizes micelles and extends bioavailability.¹⁵³

The conformation of the majority of polypeptides used in drug development is pH-dependent, due to the presence of charged groups. For example, ϵ -PLL in aqueous alkaline solution adopts a β -sheet conformation, but under acidic condition, the conformation undergoes further electrostatic expansion due to charge repulsions.¹⁵⁴ In general, both synthetic and natural polypeptides adopt α -helix, β -sheet, and random coil structures; however, and more often, several conformations coexist simultaneously.

Polypeptides containing amino acids that stimulate α -helical conformation (Ala, Phe, Leu) are generally much stronger membrane disrupting agents than amino acids that stimulating β -sheet conformation (Ile, Val).¹⁵⁵

For branched polypeptides, conformation can be changed by the insertion of stabilizing/destabilizing moieties at the terminal ends of the branches. Incorporation of a Ser and Leu moiety in the side chains of branched pLys led to a more ordered conformation in comparison with an Ala moiety (**Fig. 1.11**).¹⁵⁶ Polymers with terminal Ser have a higher tendency to form helical conformation, probably due to the presence or absence of hydrogen bonds between the hydroxyl group of Ser and the amide group of the side chain of neighboring amino acid.

Upon replacement of a Leu residue in poly[Lys(Leu_{1.0}-Ser_{0.9}-DL-Ala_{7.0})] to Glu, the tendency to form helical structure altered depending on the position of the amino acids in the sequence, as shown on the **Fig. 1.12**. Under acidic conditions, the stability of the helical structure of the Glu-containing polymer depended on the specific surroundings. Interestingly, under appropriate conditions, polymers with both Ser and Glu formed β -sheet structures. The authors concluded that terminal Ser favors the

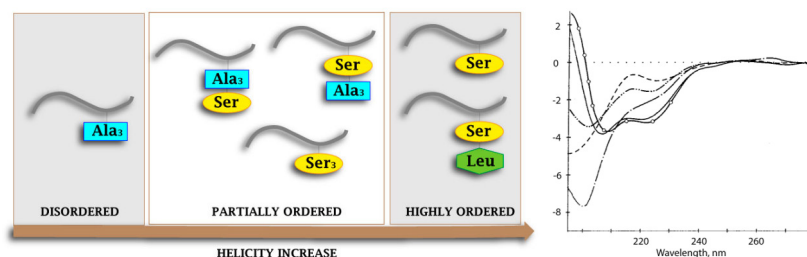


Figure 1.11. Control of polypeptide conformation by variation of amino acid order and corresponding CD spectra of the polypeptides.¹⁵⁶

formation of an ordered structure (either α -helix or β -sheet), while Ser insertion in the chain favored a less ordered structure.¹⁵⁷

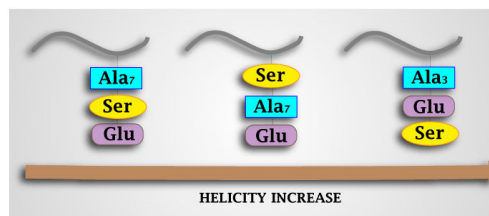


Figure 1.12. Control of polypeptide conformation by variation of amino acid order.

In some cases, chain conformation may be concentration-dependent. For example, PEG-PGA complexes with PLL at concentrations 0.02, 0.05, and higher than 0.1 mg/ml, micelles existed as a random coil, mixed, and pure β -sheet conformation, respectively. Side-chain charge neutralization (acidic or basic conditions) resulted in the formation of helical conformation, while the β -sheet is not typical for PGA or PLL and may be due to complexation. The authors supposed that the PEG chains mediated this behavior, suppressing the collapse of the particle into random coil due to increased surface area/volume ratio.¹⁵⁸

Conjugation of PEG-PGA copolymers with spiropyran allowed the synthesis of conformation-switchable (and reversible) photo-responsive flower-like micelles. After 180 min of exposure to ultraviolet (UV) light, micelles became disrupted and their size decreased from 70 to 10 nm; however, the ξ -potential value remained the same. The conformation of the block-copolymer changed during irradiation with a decrease in helicity (up to 14 %) after 5 min irradiation; however, micelles returned to their original size and conformation in response to normal light.¹⁵⁹

Modification to the PAA backbone with small molecules can affect the hydrophilic-hydrophobic ratio and, consequently, causes a change or stabilization to the overall conformation of the conjugate. Modification with neutral molecules, such as PEG, usually does not affect the helicity of the polymer.¹⁶⁰

Due to the high amount of reactive side chain groups, polypeptides can be modified post-polymerization to change their secondary structure by incorporating particular groups in a side chain. While PGA tends to form α -helix at pH lower than 4.5, conjugation with the hydrophilic anticancer agent D-penicillamine stabilized the helix conformation even in an entirely water-soluble state at pH 7.4.^{161,162} The secondary structure of PGA can also be preserved in the helical structure when functionalized with amine/guanidine as shown in **Fig.1.13**.

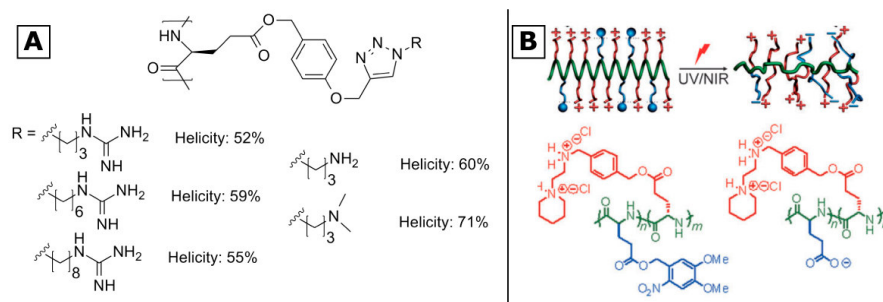


Figure 1.13. Helicity control by variation of functionalization. A) Effect of terminal functionalization on the helicity of the chain of PGA derivatives. B) Light-induced conformational switch of PGA functionalized with 4,5-dimethoxy-2-nitrobenzyl.

In another study, the authors revealed that the percent of helicity depended on the end-group and varied from 52 to 70%.¹⁶³ Furthermore, remarkably stable helicity up to 90-95 % can be achieved following γ -4-((2-(piperidin-1-yl)ethyl)aminomethyl)benzyl incorporation in the PGA structure. Interestingly, the helical structure remained even in the case of up to 40% addition of another group (light-sensitive 4,5-dimethoxy-2-nitrobenzyl) that allows the generation of a light-sensitive helical architecture suitable for DNA delivery (**Fig. 1.13B**).¹⁶⁴

Methotrexate has a tendency to destabilize the secondary structure of pLys, but pLys can be stabilized with helix-stabilizing amino acids (such as Leu) or destabilized with Glu. The poly[Lys-(MTX_j-L-Leu_{0.98}-DL-Ala_{3.1})] and poly[Lys-(MTX_j-D-Leu_{0.98}-DL-Ala_{3.1})] conjugates adopted a helical secondary structure, while a poly[Lys-(MTX_j-D-Glu_{0.95}-DL-Ala_{3.1})] conjugate displayed a partially ordered conformation. Under similar conditions, unmodified poly[Lys-L-Leu_{0.98}-DL-Ala_{3.1}], poly[Lys-(MTX_j-D-Leu_{0.98}-DL-Ala_{3.1}], and poly[Lys-D-Glu_{0.95}-DL-Ala_{3.1}] exhibited highly ordered, partially ordered, and non-ordered conformation, respectively.¹⁶⁵ Overall, the incorporation of D-amino acids into polymers with L-chirality seems to promote the destabilization of secondary structure.

Many polyaminoacids display tunable secondary conformation transformation from α -helix to β -sheet. Diethylene-glycol-monomethyl-ether-functionalized PGA (poly(L-EG₂Glu)) linked to a hexyl, dodecyl, and hexadecyl tails displayed a helicity of 65, 33, and 7 %, respectively, and a β -sheet content of 4, 21 and 39 %; this signifies an

increase in β -sheet conformation with an increase in alkyl chain length.^{166,167} The poly(L-EG₂Glu) segment adopted a mixed conformation (both α -helix and β -sheet) (**Fig. 1.14A**), and the alkyl tails were assumed to form the core and hydrophilic polyEG₂Glu arrange in a parallel manner.

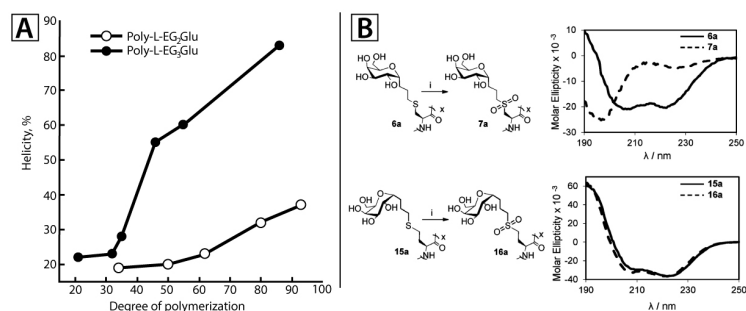


Figure 1.14. A) Helicity dependence of Poly(L-EG_nGlu) with various degree of polymerization in water (n=2,3) B) Example of α -helix destabilization through cysteine residue oxidation.

Even small changes in the backbone can destabilize the conformation of a given polypeptide conjugate. Galactose- or glucose-modified poly-cysteine (pCys) compounds exist predominantly in α -helical conformation in the solid-state and aqueous solution; however, the oxidation of a thiol to a sulfone group destabilized the α -helix and caused a transition to a disordered conformation (**Fig. 1.14B**). The mechanism of transition probably relies on the strong interaction of sulfone groups with water molecules that result in the disruption of peptide hydrophobic packing and an increase in steric crowding, consequently resulting in helix destabilization. Interestingly, following the separation of the thioester group by additional methylene group, the conjugate retained an α -helical conformation even after oxidation to a sulfone.¹⁶⁸

Chain topology also influences the number of secondary structure defects. For example, when comparing linear and 3-arm star poly(ϵ -carbobenzyloxy-L-lysine) (PZLL) and poly(γ -benzyl-L-glutamate) (PBLG), researchers discovered that both polypeptides formed α -helices; however, star-copolymers possessed shorter helix persistence length.¹⁶⁹ Due to increased steric effects and charge repulsion, the helicity of star copolypeptides usually remains lower than that observed for their linear analogs.¹⁶⁰

The conformation of polypeptide conjugates also relies on pH. For example, both unconjugated PGA and a PGA-Dox conjugate is negatively charged and has random coil conformation at pH 7.6; however, a decrease in pH neutralizes charges, and PGA/PGA-Dox adopt a α -helical conformation at pH below 5.7. The authors hypothesized that a hydrophobic Dox aggregate forms the core and PGA chains form a hydrophilic shell with mixed chain conformation (helical and random coil). Conjugates such as these dissolve slowly and may find future use in the synthesis of conjugates with sustained-release.¹⁷⁰

1.3.2.4. Effect of Geometry.

The overall 3D solution conformation of the design polypeptide therapeutics clearly affects drug release, biodistribution, and main chain degradation. Conjugate diameter affects particle velocity, diffusion, and adhesion to the blood vessels, airways, and intestine; however, shape influences these characteristics in a complex manner, as non-spherical particles can demonstrate flow-dependent alignment. Shape can also affect targeting, as local curvature affects ligand and opsonin adsorption and the degree to which particles fit the contours of cellular membrane. Shape may allow increased cell attachment and resistivity to detachment as well as cell internalization.^{171–173}

The synthesis of polypeptide nanosystems that exist in aqueous medium with a shape other than spherical remains a complicated and non-trivial task. While significant advances in shape-controlled synthesis have been made for metals and related compounds (e.g., oxides, chalcogenides, etc.),¹⁷⁴ the shape-controlled synthesis of polystyrene and PGA (soft matter) resulted in particle sizes in micrometer range through film stretching rather than self-assembly.¹⁷⁵ Pure polyelectrolytes and doubly hydrophilic block copolymers in solution do not show self-assembling behavior.¹⁷⁶ Different crosslinking and aggregation induction strategy applied to charged polymers nearly always result in the generation of spherical aggregates, and there exist no reports regarding non-spherical polyelectrolyte particles in water.

Block-copolymers provide more freedom for the synthesis of particles with varied shapes. Depending on the concentration and the content of hydrophobic monomer, block-copolymers can form a variety of different structures, including tubules, spheres, vesicles, and more complicated multidimensional superstructures.¹⁷⁷ An important parameter that determines the self-assembly pattern of amphiphilic polypeptides is the volume fraction of the hydrophilic block in polymer (f_{phi}). Copolymers with $f_{\text{phi}} > 50\%$ have tendency to form spherical micelles, while vesicles can be formed from diblock-copolymers with $f_{\text{phi}} < 33\%$, as shown for polypropyleneoxide-b-PLL.¹⁷⁸

Several groups have reported the synthesis of ellipsoidal particles from poly-benzyl-L-glutamate (PBLG)-cisplatin conjugates.^{179,180} The molecular weight of the initial polymer also influenced the morphology; a linear dependency of aspect ratio on the molecular weight of the polymer was found for a series of non-conjugated γ -PBLG. Nanoparticles had a tendency to be rounder for polymers of lower molecular weight.¹⁸¹

Particles with non-typical shapes for polypeptides morphologies have been synthesized from polyacrylic acid-graft-PBLG and PBLG homopolymers (**Fig. 1.15**), with rods, curved rods and toroidal micelles with a polyacrylate shell and PBGA core synthesized by varying the weight fraction of PBGA.¹⁸² Cylindrical particle synthesis occurred following mixing graft (PBLG-g-PEG) and block (PBLG-b-PEG) copolymers in different ratios while, interestingly, pure polymers formed spherical micelles.¹⁸³

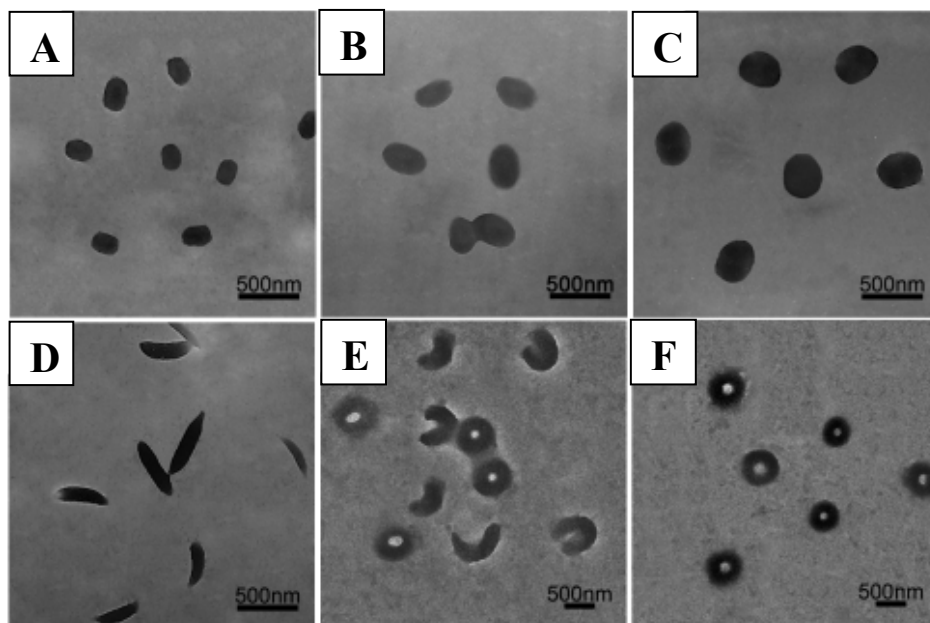


Figure 1.15. TEM images of aggregates with different shape obtained from PAsp-g-PBLG/PBLG mixtures with various weight fraction of PBLG: 0 (A), 0.01(B), 0.05 (C), 0.08 (D), 0.12 (E), and 0.22 (F).¹⁸²

Additional studies have constructed polypeptides with a fibrillar geometry; both ϵ -PLL and PGA form filaments upon heating at 60 °C and do not aggregate at room temperature.^{184,185} Of the more complicated approaches, one study mixed cationic surfactants (dodecyl trimethylammoniumbromide [DTAB]) with PGA-PEG to form ionic complexes. DTAB in solution behaves like a typical surfactant and can form spherical or wormlike micelles depending on the conditions, while PGA-PEG covers the surface of these particles due to electrostatic interactions.¹⁸⁶

1.4. Merging Supramolecular and Polymer Chemistry as a Strategy to Control Polymer Morphology

While polymer, and especially polyelectrolyte, chemistry has remained an isolated branch of material science and chemistry for some time, interdisciplinary research is now on the rise. The suitability of polymers for biomedical research has opened a new quickly developing field of biocompatible materials. The merging of polyelectrolyte science with other branches of chemistry seems very promising; however, it still remains in an embryonic state. While the control of polyelectrolyte self-assembly remains a complicated task, research in this area may provide more advanced biocompatible systems with unique profiles of action and new materials with yet unknown properties. The combination of polyelectrolytes with supramolecular moieties

represents an especially interesting research topic, with the potential to derive more complicated architectures. DNA, for example, is a polyelectrolyte (anionic polyphosphate) with supramolecular moieties (nucleotides) that not only functions as a means of genetic information storage and transmission, but can also assemble into astonishingly complicated structures.

1.4.1. Supramolecular Polymers: Principles and Design.

Supramolecular self-assembly depends greatly on the nature of the compound, with many different driving forces specific for each system involved in its regulation. The regulatory mechanisms influencing self-assembly include minimization of the interfacial energy directed by hydrophobic/hydrophilic balance, π - π stacking, dipole interactions, and hydrogen bonding among different domains.¹⁸⁷

The first water-soluble supramolecular polymers, PEG derivatives of 2-ureido-4-pyrimidone (UPy), associated through dimerization to form stable materials, assembling into long nanofibers in water.¹⁸⁸ The incorporation of different molecules into this building block allowed the synthesis of biocompatible water-soluble materials, and found use in the preparation of responsive self-healable hydrogels from polymethacrylate modified with ureidopyrimidone.^{189,190}

PEG-b-bisurea-b-PEG-b-bisurea-b-PEG pentablock copolymers self-assembled into rod-like particles linked with PEG spacers, while PEG with terminal guanosines assembled into supramolecular star polymers due to the formation of guanine quadruplexes. Upon an increase of PEG length, the study found a decrease in polymer stability.¹⁹¹

The incorporation of a ditopic hydrogen-bonding module (bis-DeAP) at the termini of polystyrene allowed the preparation of star-supramolecular polymers, due to the assembly of the bis-DeAP into C6 symmetric supramolecular structures.¹⁹² Other reports regarding supramolecular organization of macromolecules driven by complementary H-bonding associative units are based on polyvinylacetate.¹⁹³ However, while these advanced strategies are relatively exciting, the polymers self-assemble in organic solvents without the presence of water that interferes with hydrogen bonding.¹⁹⁴

Derivatives based on C- or N-centered benzyltricarboxamide (BTA) and cyclohexyltricarboxamide represent another group of supramolecular polymers that assemble into nanofibers due to directional C3-symmetric H-bond array (**Fig. 1.16**). One study employed the BTA-derivatization of polyacrylate to prepare single-chain polymeric nanoparticles in which BTA controlled the aggregation of the polymer chains.¹⁹⁶ In another, the conjugation of both chiral and achiral BTA moieties to methacrylate allowed the controlled formation of segregated BTA stacks within a single polymer molecule.¹⁹⁵ The combination of both BTA and o-nitrobenzyl-UPy

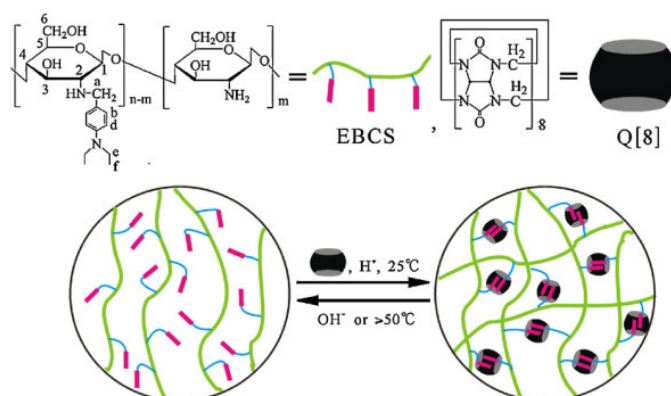


Figure 1.17. The schematic diagram for the formation of cucurbit[8]uril-N-(4-diethylaminobenzyl) chitosan supramolecular gel.¹⁷⁰

Short self-assembling peptides are yet another group of molecules that can self-assemble into a variety of morphologies in aqueous solutions. Besenius et al. synthesized PEG end-functionalized with short FMFMFM-sequences that self-assembled in water into nanorods that displayed ROS-responsiveness due to methionine oxidation (**Fig. 1.18**).²⁰⁵ Polysarcosine, functionalized with FHFHF sequences assembled into pH-sensitive nanorods in a similar manner.²⁰⁶ Peptide-polymer conjugates are mainly based on PEG because it is a neutral molecule with relatively low hydration shell.²⁰⁷ Other examples include polymethacrylates; however, in all cases, the functionalization of carboxylic groups employed electroneutral moieties.^{208,209} As in the previous case, we still lack studies considering polyelectrolytes (without neutral functionalized groups).

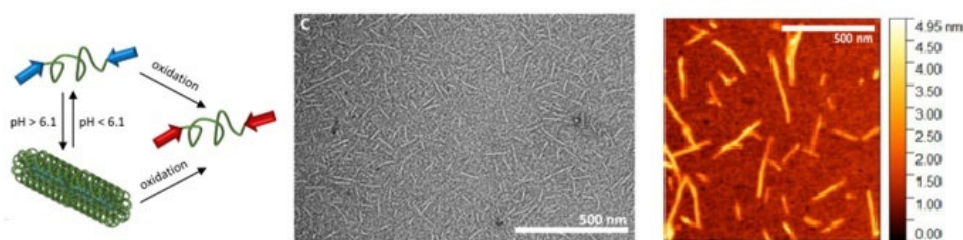


Figure 1.18. Schematic representation of pH-dependent β -sheet directed supramolecular nanorod assembly and oxidation-stimulated disassembly. TEM and AFM images of supramolecular nanorods.²⁰⁵

Taking into account all consideration above described, the research included in this PhD thesis focuses on the development of new classes of branched polypeptide constructs with capacity of self-assembly mainly based on PGA, and to lesser extent on PAsp and PLL, to be used as carriers in drug delivery. Therefore, their used in the

development of new single and combination PGA-drug conjugates is also included with previously selected drugs looking for efficient therapies in the treatment of metastatic triple negative breast cancer (TNBC).

1.5. References

1. Strebhardt, K. and Ullrich, A. *Nat. Rev. cancer*, **8**, 473–480 (2008).
2. Puetzer, B. *JACS*, **74**, 4959–4960 (1952).
3. Overberger C. *JACS*, **76**, 1953–1954 (1954).
4. Jatzkewitz, H. *Zeitschrift für Naturforsch. - Sect. B J. Chem. Sci.*, **10**, 27–31 (1955).
5. Batz, H. and Ringsdorf, H. *Die Makromol. Chemie*, **175**, 2229–2239 (1974).
6. Duncan, R. *J. Drug Target*, **25**, 759–780 (2017).
7. Kaitin, I. et al. *J Clin Pharmacol*, **34**, 120–127 (1994).
8. Ekladios, I., Colson, Y. L. and Grinstaff, M. W. *Nat. Rev. Drug Discov.*, **18**, 273–294 (2019).
9. Maso, K., Grigoletto, A., Vicent, M. J. and Pasut, G. *International Review of Cell and Molecular Biology* (Elsevier Inc., 2019). doi:10.1016/bs.ircmb.2019.03.001
10. Duncan, R. *Nat. Rev.*, **2**, 347–360 (2003).
11. Duncan, R. and Vicent, M. J. *Adv. Drug Deliv. Rev.*, **65**, 60–70 (2013).
12. Kenny, A. D. *Proc. Soc. Exp. Biol. Med.*, **100**, 778–780 (1959).
13. Recent advances in drug delivery systems. (Plenum Press, 1984).
14. Morimoto, Y. et al. *J. Pharm. Dyn.*, **7**, 688–698 (1984).
15. Kato, Y., Saito, M., Fukushima, H., Takeda, Y. and Harā, T. *Cancer Res.*, **44**, 25–30 (1984).
16. Sezaki, H. *Int. J. Pharm.*, **22**, 75–87 (1984).
17. Engler, A. C. et al. *Biomacromolecules*, **12**, 1666–1674 (2011).
18. McGowan, I. et al. *AIDS*, **25**, 1057–1064 (2011).
19. Feng, Z. et al. *Cancer Sci.*, **101**, 2476–2482 (2010).
20. Fox, M. E. et al. *Mol. Pharm.*, **6**, 1562–1572 (2009).
21. Nemunaitis, J. et al. *Int. J. Gen. Med.*, **4**, 5–11 (2011).
22. Kiew, L. V., Cheong, S. K., Sidik, K. and Chung, L. Y. *Int. J. Pharm.*, **391**, 212–220 (2010).
23. Karmaker, et al. *J. Inorg. Biochem.*, **100**, 1535–1546 (2006).
24. Vicent, M. J. and Pérez-Payá, E. *J. Med. Chem.*, **49**, 3763–3765 (2006).
25. Silva, M. et al. *Arch. Pharm. (Weinheim)*, **339**, 283–290 (2006).
26. Zia, Q., Khan, A. A., Swaleha, Z. and Owais, M. *Int. J. Nanomedicine*, **10**, 1769–1790 (2015).
27. Ke, T., Jeong, E., Parker, D. L. and Lu, Z. *Int. J. Nanomedicine*, **2**, 191–199 (2007).
28. Dumoga, S. et al. *ACS Appl. Mater. Interfaces*, **9**, 22195–22211 (2017).
29. Plummer, R. et al. *Br. J. Cancer*, **104**, 593–598 (2011).
30. Harburg, K., Hemer, L. and Freiburg, U. *Br. J. Cancer*, **98**, 1608–1613 (2008).
31. Hamaguchi, T. et al. *Clin Cancer Res*, **16**, 5058–5067 (2010).
32. Starpharma Holdings Limited. DEP® docetaxel positive phase 1 results; phase 2 commences. Starpharma <https://www.starpharma.com/news/339> (2017).
33. Mukai, H., Kogawa, T., Matsubara, N. and Naito, Y. *Invest. New Drugs*, **35**, 307–314 (2017).
34. Starpharma Holdings Limited. Starpharma to commence DEP® cabazitaxel phase 1/2 trial. Starpharma <http://www.starpharma.com/news/356> . (2018).
35. Takayoshi, U. et al. *Int. J. Nanomedicine*, **9**, 3005–3012 (2014).
36. Anselmo, A. C. and Mitragotri, S. *Bioeng Transl Med*, **1**, 10–29 (2016).
37. Barrett, S. E. et al. *J. Control. Release*, **183**, 124–137 (2014).
38. Conejos-Sánchez, I. et al. *Nanoscale*, just accepted (2019).

-
39. You, X. *et al. Acta Biomater.*, **74**, 180–191 (2018).
 40. Zhou, X. *et al. ACS Appl. Mater. Interfaces*, **8**, 12609–12619 (2016).
 41. Song, H. *et al. Nanoscale*, **7**, 5803–5814 (2015).
 42. Mi, P. *et al. J. Control. Release*, **254**, 1–9 (2017).
 43. Barth, R. F., Mi, P. and Yang, W. *Cancer Commun.*, doi:10.1186/s40880-018-0299-7 (2018).
 44. Dai, X. *et al. J. Photopolym. Sci. Technol.*, **29**, 823–832 (2016).
 45. Kiew, L. V. *et al. Nanomedicine Nanotechnology, Biol. Med.*, **13**, 1447–1458 (2017).
 46. Abellan-Pose, R. *et al. Eur. J. Pharm. Biopharm.*, **112**, 155–163 (2017).
 47. Duro-Castaño, A. *et al. Adv. Mater.*, **29**, 1702888 (2017).
 48. Roncador, A. *et al. Nanomedicine Nanotechnology, Biol. Med.*, **3**, 897–907 (2016).
 49. Li, Z. *et al. Acta Biomater.*, **11**, 137–150 (2015).
 50. Jia, N. *et al. Asian J. Pharm. Sci.*, **12**, 433–441 (2017).
 51. John, J. V *et al. J. Polym. Sci. part A Polym. Chem.*, **55**, 2061–2070 (2017).
 52. Ahmad, Z. *et al. J. Biomater. Sci. Polym. Ed.*, **27**, 40–54 (2016).
 53. Duncan, R. and Izzo, L. *Adv. Drug Deliv. Rev.*, **57**, 2215–2237 (2005).
 54. Mehta, D. *et al. Mol. Pharm.*, **15**, 4568–4576 (2018).
 55. Dendrimer Drug Delivery (DEP®). Available at: https://www.starpharma.com/drug_delivery.
 56. Han, S. *et al. Small*, **11**, 2543–2554 (2015).
 57. How, S. *et al. Colloids Surfaces B Biointerfaces*, **153**, 244–252 (2017).
 58. Jiang, B. *et al. J. Mater. Chem. B*, **4**, 3324–3330 (2016).
 59. Wang, Y., Wang, L., Chen, G. *Macromol Biosci.*, **17**, 1600292 (2017).
 60. Hayashi, T., Shinagawa, M., Kawano, T. and Iwasaki, T. *Biochem. Biophys. Res. Commun.*, **501**, 648–653 (2018).
 61. Sun, P. *et al. Int. J. Nanomedicine*, **12**, 3221–3234 (2017).
 62. Kawashima, R. *et al. Biol. Pharm. Bull.*, **39**, 329–335 (2016).
 63. Nevagi, R. J. *et al. Acta Biomater.*, **80**, 278–287 (2018).
 64. Gonzalez-Paredes, A., Torres, D. and José, M. *Int. J. Pharm.*, **529**, 474–485 (2017).
 65. Bilalis, P., Tziveleka, L., Varlas, S. and Iatrou, H. *Polym. Chem.*, **7**, 1475–1485 (2016).
 66. Nguyen, C. *et al. ACS Appl. Mater. Interfaces*, **9**, 9470–9483 (2017).
 67. Hakeem, A. *et al. Intern. J. Nanomed.*, **13**, 1029–1040 (2018).
 68. Deming, T. J. *Chem. Rev.*, **116**, 786–808 (2016).
 69. Zou, C. *et al. Gynecol. Oncol.*, **107**, 441–449 (2007).
 70. Singer, J. W. *et al. Annual N. Y. Acad. Sci.*, **922**, 136–150 (2007).
 71. Ghosh, S. C. *et al. J. Bioorganic Med. Chem. Lett.*, **19**, 1012–1017 (2009).
 72. Fante, C. *et al. J. Med. Chem.*, **54**, 5255–5259 (2011).
 73. Vicent, M. J. *AAPS J.*, **9**, E200–E207 (2007).
 74. Vaidya, A. *et al. Pharm. Res.*, **25**, 2002–2011 (2008).
 75. Cui, J. *et al. Adv. Mater.*, **25**, 3468–3472 (2013).
 76. Zagorodko, O., Arroyo-Crespo, J. J., Nebot, V. J. and Vicent, M. J. *Macromol. Biosci.*, **17**, 1600316 (2016).
 77. Zhong, Y., Shao, L. and Li, Y. *Int. J. Oncol.*, **42**, 373–383 (2013).
 78. Anami, Y. *et al. Nat. Commun.*, **9**, 2512 (2018).
 79. Xin, D., Wang, Y. and Xiang, J. *Pharm. Res.*, **27**, 380–389 (2010).
 80. Dan, K., Pan, R. and Ghosh, S. *Langmuir*, **27**, 612–617 (2011).
 81. Heller, J. J. *Control. Release*, **2**, 167–177 (1985).
 82. Shenoy, D., Little, S. and Langer R. *Mol Pharm.*, **2**, 357–366 (2005).
 83. Ndungu, J. *et al. J Med Chem.*, **53**, 3127–3132 (2010).
 84. Pon, R. T. and Yu, S. *Nucleic Acids Res.*, **25**, 3629–3635 (1997).
 85. Dendrimer-Based Drug Delivery Systems. (Wiley, 2012).
 86. Tian, Y. *et al. Part. Part. Syst. Charact.*, **32**, 547–551 (2015).

87. Saravanakumar, G., Kim, J. and Kim, W. J. *Adv. Sci.*, **4**, 19 (2017).
88. Blencowe, C. A., Russell, A. T., Greco, F. and Thornthwaite, D. W. *Polym. Chem.*, **2**, 773–790 (2011).
89. Matsumura, Y. and Maeda, H. *Cancer Res.*, **46**, 6387–6392 (1986).
90. Greish, K. *et al. Clin Pharmacokinet.*, **42**, 1089–1105 (2003).
91. Danquah, M. K., Zhang, X. A. and Mahato, R. I. *Adv. Drug Deliv. Rev.*, **63**, 623–639 (2011).
92. Nichols, J. W. and Han, Y. *J. Control. Release*, **190**, 451–464 (2014).
93. Tang, Y. *et al. Sci. Rep.*, **7**, 9359 (2017).
94. Maeda, H. *Adv. Drug Deliv. Rev.*, **91**, 3–6 (2015).
95. Shiraishi, K. *et al. Polymers*, **9**, 710 (2017).
96. Lee, H. J. and Bae, Y. *Biomacromolecules*, **12**, 2686–2696 (2011).
97. Horvát, G. *et al. Eur. J. Pharm. Sci.*, **67**, 1–11 (2015).
98. Penczek, P. and Jan, C. *Crosslinking in Materials Science*. (Springer-Verlag Berlin Heidelberg, 2005).
99. Hu, W., Wang, Z. and Xiao, Y. *Biomater. Sci.*, **7**, 843–855 (2019).
100. Sung, J. S., Park, J., Ho, S. and Kim, J. *J Polym Env.*, **23**, 90–96 (2014).
101. Schmitz, D. and Pich, A. *Polym. Chem.*, **7**, 5687–5697 (2016).
102. Arunachalam, M. and Gibson, H. W. *Prog. Polym. Sci.*, **39**, 1043–1073 (2014).
103. Maeda, H. *Bioconjugate Chem.*, **21**, 797–802 (2010).
104. Maeda, H., Nakamura, H. and Fang, J. *Adv. Drug Deliv. Rev.*, **65**, 71–79 (2013).
105. Davis, R. M. *et al. Nanomaterials* **8**, 953 (2018).
106. Richards, D. A., Maruani, A. and Chudasama, V. *Chem. Sci.*, **8**, 63–77 (2016).
107. Yang, X. *et al. J. Biomed. Mater. Res. Part A*, **86A**, 48–60 (2007).
108. Lee, E. S., Na, K. and Bae, Y. H. *Nano Lett.*, **5**, 325–329 (2005).
109. Wu, C. and Chen, Y. *Artif. Cells, Nanomedicine, Biotechnol.*, **47**, 210–220 (2019).
110. Tomiya, N. *et al. Bioorg. Med. Chem.*, **21**, 5275–5281 (2013).
111. Kaneko, K. and Ishihara, T. *Cogent Med.*, **21**, 1–11 (2018).
112. Onoke, S. S. *et al. Biol. Pharm. Bull.*, **34**, 1338–1342 (2011).
113. Wang, T. *et al. Macromol. Biosci.*, **16**, 774–783 (2016).
114. Chen, Y. C. *et al. Biomaterials*, **35**, 2051–2065 (2014).
115. Mignani, S. and Majoral, J.-P. *New J. Chem.*, **37**, 3337 (2013).
116. Honary, S. and Zahir, F. *Trop. J. Pharm. Res.*, **12**, 265–273 (2013).
117. Yu, H. *et al. J. Control. Release*, **205**, 89–97 (2015).
118. Li, S. D. and Huang, L. *J. Control. Release*, **145**, 178–181 (2010).
119. Barz, M., Luxenhofer, R., Zentel, R. and Vicent, M. J. *Polym. Chem.*, **2**, 1900 (2011).
120. Birke, A., Ling, J. and Barz, M. *Prog. Polym. Sci.*, **81**, 163–208 (2018).
121. Hu, Y., Hou, Y., Wang, H. and Lu, H. *Bioconjug. Chem.*, **29**, 2232–2238 (2018).
122. Frisont, N. *et al. J. Biol. Chem.*, **278**, 23922–23929 (2003).
123. Poon, Z. *et al. Angew. Chemie - Int. Ed.*, **49**, 7266–7270 (2010).
124. Rodríguez-Otormin, F., Duro-Castaño, A., Conejos-Sánchez, I. and Vicent, M. J. *WIREs Nanomed Nanobiotechnol.* **11**, e15322 (2019).
125. Liu, J., Yu, M., Zhou, C. and Zheng, J. *Mater. Today*, **16**, 477–486 (2013).
126. Tang, L. *et al. Proc. Natl. Acad. Sci.*, **111**, 15344–15349 (2014).
127. Longmire, M., Choyke, P. L. and Kobayashi, H. *Nanomedicine*, **3**, 703–717 (2008).
128. Li, S. and Huang, L. *Biochim Biophys Acta*, **1788**, 2259–2266 (2009).
129. De Miguel, L. *et al. Int. J. Pharm.* **460**, 73–82 (2014).
130. Blood–Brain Barrier in drug discovery. (Wiley, 2015).
131. Bonomi, P. *Expert Rev. Anticancer Ther.* **7**, 415–422 (2007).
132. Ye, H. *et al. Biomaterials*, **27**, 5958–5965 (2006).
133. Sang, M. *et al. Polymer*, **50**, 2252–2257 (2009).

-
134. Arroyo-Crespo, J. J. *et al. Biomaterials*, **186**, 8–21 (2018).
135. Yang, C. *et al. Int. J. Pharm.*, **550**, 79–88 (2018).
136. Yan, J. *et al. J. Biomater. Sci. Polym. Ed.*, **50**, 630–631 (2016).
137. Liu, T. *et al. Acta Biomater.*, **53**, 179–189 (2017).
138. Zhou, H. *et al. Acta Biomater.*, **73**, 388–399 (2018).
139. Nakanishi, T. *et al. J. Control. Release*, **74**, 295–302 (2001).
140. Ma, B. *et al. Acta Biomater.*, **70**, 186–196 (2018).
141. Tai, W. *et al. Biomaterials*, **35**, 7194–7203 (2014).
142. Salmanpour, M., Youse, G. and Mohammadi, S. *Eur. J. Pharm. Sci.*, **136**, 104941 (2019).
143. Ikumi, Y. *et al. J. Control. Release*, **125**, 42–49 (2008).
144. Conejos-Sanchez, I. *et al. J. Control. Release*, **198**, 80–90 (2015).
145. Bae, Y., Diezi, T. A., Zhao, A. and Kwon, G. S. *J. Control. Release*, **122**, 324–330 (2007).
146. Markovsky, E., Baabur-Cohen, H. and Satchi-Fainaro, R. *J. Control. Release*, **187**, 145–157 (2014).
147. He, C. *et al. Biomaterials*, **31**, 3657–3666 (2010).
148. Qian, J. *et al. Acta Biomater.*, **15**, 102–116 (2014).
149. Collfen, H. *Macromol. Rapid Commun.*, **22**, 219–252 (2001).
150. Lin, J. *et al. Biomaterials*, **30**, 108–117 (2009).
151. Huang, Y. *et al. Biomacromolecules*, **14**, 2023–2032 (2013).
152. Giménez, V. *et al. J. Control. Release*, **159**, 290–301 (2012).
153. Mochida, Y. *et al. ASC Nano*, **8**, 6724–6738 (2014).
154. Shukla, S. C., Singh, A., Pandey, A. K. and Mishra, A. *Biochem. Eng. J.*, **65**, 70–81 (2012).
155. Lu, H. *et al. Chem. Commun.*, **50**, 139–155 (2014).
156. Hudecz, F. *et al. C. Bioconjug. Chem.*, **10**, 781–790 (1999).
157. Mezo, G. *et al. J. Control. Release*, **63**, 81–95 (2000).
158. Mutaf, O. F. *et al. Macromol. Rapid Commun.*, **36**, 1958–1964 (2015).
159. Kotharangannagari, V. K., Sánchez-Ferrer, A., Ruokolainen, J. and Mezzenga, R. *Macromolecules*, **44**, 4569–4573 (2011).
160. Yin, L. *et al. Biomaterials*, **34**, 2340–2349 (2013).
161. Wadhwa, S. and Mumper, R. J. *J. Control. Release*, **158**, 215–223 (2012).
162. Wadhwa, S. and Mumper, R. J. *Mol. Pharm.*, **7**, 854–862 (2010).
163. Zhang, R. *et al. Biomaterials*, **35**, 3443–3454 (2014).
164. Yin, L. *et al. Angew. Chemie - Int. Ed.*, **52**, 9182–9186 (2013).
165. Hudecz, F. *et al. Bioconjug. Chem.*, **4**, 25–33 (1993).
166. Shen, Y., Fu, X. and Li, Z. *Chem. Soc. Rev.*, **44**, 612–622 (2015).
167. Chen, C., Wu, D., Fu, W. and Li, Z. *Biomacromolecules*, **14**, 2494–2498 (2013).
168. Kramer, J. R. and Deming, T. J. *JACS*, **134**, 4112–4115 (2012).
169. Gitsas, A. *et al. Biomacromolecules*, **9**, 1959–1966 (2008).
170. Lai, J. and Huang, Y. *RSC Adv.*, **5**, 48856–48860 (2015).
171. Champion, J. A., Katare, Y. K. and Mitragotri, S. *J. Control. Release*, **121**, 3–9 (2007).
172. Zhang, Y. *et al. ACS Appl. Mater. Interfaces*, **4**, 4099–4105 (2012).
173. Champion, J. a and Mitragotri, S. *PNAS*, **103**, 4930–4934 (2006).
174. Melillo, J. M. *et al. Science*, **298**, 2176–2180 (2002).
175. Yoo, J. and Mitragotri, S. *PNAS*, **107**, 11205–11210 (2010).
176. Nakashima, K. and Bahadur, P. *Adv. Colloid Interface Sci.*, **126**, 75–96 (2006).
177. Chen, C., Wylie, R. A. L., Klinger, D. and Connal, L. A. *Chem. Mater.*, **29**, 1918–1945 (2017).
178. Naik, S. S., Ray, J. G. and Savin, D. A. *Langmuir*, **27**, 7231–7240 (2011).
179. Martínez-Barbosa, M. E. *et al. Bioconjug. Chem.*, **20**, 1490–1496 (2009).
180. Martínez Barbosa, M. E. *et al. J. Mol. Recognit.*, **21**, 169–178 (2008).
181. Cauchois, O., Segura-Sanchez, F. and Ponchel, G. *Int. J. Pharm.*, **452**, 292–299 (2013).

182. Chen, L., Jiang, T., Lin, J. and Cai, C. *Langmuir*, **29**, 8417–8426 (2013).
183. Zhuang, Z. *et al. J. Phys. Chem. B*, **116**, 10125–10134 (2012).
184. Lai, J., Zheng, C., Liang, D. and Huang, Y. *Biomacromolecules*, **14**, 4515–4519 (2013).
185. Hernik-mago, A. *et al. Biomacromolecules*, **17**, 1376–1382 (2016).
186. Han, Y. *et al. Langmuir*, **28**, 15134–15140 (2012).
187. She, W. *et al. Biomaterials*, **34**, 1613–1623 (2013).
188. Dankers, P. Y. W. *et al. Adv. Mat.*, **24**, 2703–2709 (2012).
189. Cui, J., Wang, D. and Koynov, K. *ChemPhysChem*, **14**, 2932–2938 (2013).
190. Lin, Y. and Li, G. *J. Mater. Chem. B*, **2**, 6878–6885 (2014).
191. Gadwal, I. *et al. J. Polym. Sci. part A Polym. Chem.*, **50**, 2415–2420 (2012).
192. Todd, E. M. and Zimmerman, S. C. *JACS*, **129**, 14534–14535 (2007).
193. Fenet, B. and Bernard, J. *Macromol. Rapid Commun.*, **30**, 83–88 (2009).
194. Gibson, H. W. *et al. J. Polym. Sci. Part A Polym. Chem.*, **47**, 3518–3543 (2009).
195. Hosono, N., Palmans, A. R. A. and Meijer, E. W. *Chem. Commun.*, **50**, 7990–7993 (2014).
196. Gijs ter Huurne, M. *et al. Macromolecules*, **50**, 8562–8569 (2017).
197. Hosono, N. *et al. JACS*, **135**, 501–510 (2013).
198. Altintas, O., Lejeune, E. and Barner-Kowollik, C. *Polym. Chem.*, **3**, 640–651 (2012).
199. Houbenov, N. *et al. Angew. Chem. Int. Ed.*, **50**, 2516–2520 (2011).
200. Rinaudo, M. *Macromolecules*, **35**, 7955–7962 (2002).
201. Liu, Y. *et al. JACS*, 4138–4141 (2008).
202. Wang, J. *et al. RSC Adv.*, **5**, 46067–46073 (2015).
203. Lin, Y., Li, L. and Li, G. *Carbohydr. Polym.*, **92**, 429–434 (2013).
204. Guo, S. *et al. Polym. Chem.*, **8**, 5718–5725 (2017).
205. Otter, R., Marijan, C., Seiffert, S. and Besenius, P. *Eur. Polym. J.*, **110**, 90–96 (2019).
206. Otter, R. *et al. Chem. Commun.*, **54**, 401–404 (2018).
207. Otter, R. and Besenius, P. *Org. Biomol. Chem.*, **17**, 6719–6734 (2019).
208. Song, Y., Moore, E. G., Guo, Y. and Moore, S. *JACS*, **139**, 4298–4301 (2017).
209. Chin, S. M. *et al. Nat. Commun.*, **9**, 2395 (2018).

Chapter 2

Towards self-assembling polyglutamates

2.1. Introduction

Self-assembly, a unique yet ubiquitous phenomenon found in nature, is widely used in applied sciences.¹ Biological macromolecules can self-organize into a plethora of intricate structures with specific functionalities emerging from the supramolecular complexes rather than the individual components. The desire to mimic the complexity of biological systems has stimulated a focus on the study of synthetic polymers and their aqueous self-assembly.²⁻⁴ Synthetic polypeptides, or polyaminoacids, are the class of polymers most closely related to biomacromolecules, in that they consist of the same building blocks as natural proteins while keeping a high degree of structural versatility. These characteristics make polypeptides suitable for advanced drug delivery.⁵⁻⁸ Among the described biocompatible polypeptides, poly-L-glutamates (PGAs) display low immunogenicity, high biodegradability, and controlled biodistribution profiles, and these characteristics have made them a focus for research.^{9,10}

Many studies have demonstrated that physicochemical properties strongly influence the *in vivo* behavior of particles.⁸ The role of charge, size, and surface decoration have been previously described in detail; however, the role of shape has remained mostly unstudied. Recently, Zhao et al. demonstrated that mesoporous silica rods exhibit longer circulation times and higher bioavailability than spherical analogs.¹¹ Van Pomerén et al.

also established that the shape of gold nanoparticles determined biodistribution in zebrafish embryos.¹² Aqueous shaping of soft-matter nanoparticles and, in particular, polyelectrolytes remains a complicated issue due to multiple repulsive interactions; however, non-spherical polyelectrolyte particles have the potential to open new avenues in drug delivery studies.

In search of new morphologies, many studies have incorporated different structural elements, such as hydrophobic blocks, into the polymer to generate unique self-assembly properties.^{13–15} In this chapter, we will explore supramolecular polymers as our first source of such new polypeptidic morphologies.

Supramolecular polymers are a class of polymers in which monomer units connect through non-covalent interactions (hydrogen bonds, π - π hydrophobic effects, etc.).¹⁶ Said materials have been widely studied in organic solvents due to the absence of strong solvation by the solvent molecules.¹⁷ However, the use of organic solvents wholly eliminates the possibility of using supramolecular polymers for biological applications. Recent novel strategies to promote aqueous supramolecular self-assembly¹⁸ use a non-charged hydrophobic group shielded with a neutral hydrophilic group that increases the solubility of the system while not interfering with self-assembly.

Benzenetricarboxamide (BTA) represents one of the most well-studied motifs in aqueous supramolecular polymers.^{19,20} Following the covalent attachment of sufficient hydrophobic groups to provide shielding, BTA can assemble into one-dimensional (1D) fibers and rods with C₃-symmetry due to the formation of a system of directional non-covalent bonds (**Fig. 2.1**). Fibers or rods can consist of a single stack of BTA units or can form more complicated aggregates of several fibers.²¹

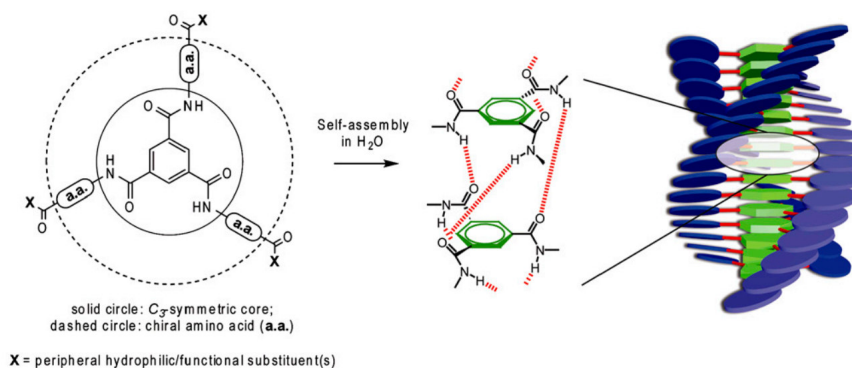


Figure 2.1. Schematic representation of molecules self-assembling into helical fibers. The BTA core (unbroken circle, image on the left) guiding the self-assembly is surrounded by amino acids (in dashed lines, image on the left), which determines the stability of the macromolecular structure (shown on the right) by the addition of non-covalent interactions.²²

BTA motifs have been widely studied, with a variety of systems with different self-assembly mechanisms already described; however, the nature of the substituents plays a

pivotal role in the property of the final material. Alkyl-derivatives of BTA form liquid crystalline materials and display highly-ordered structures,^{23,24} and such materials have found use in the field of advanced materials, including in diodes, memory appliances, and small porous membranes, and as nucleation and clarifying agents in polymer chemistry.^{25–28} Attachment of short polyethylene glycol (PEG) fragments at molecule termini provided for heightened water solubility, and the corresponding aggregates assembled into micrometer-long thin nanofibers.²⁹ These systems found use in the encapsulation of hydrophobic molecules (e.g., the Nile Red [NR] lipophilic dye) and the complexation of small interfering (si)RNA for intracellular delivery.³⁰

The incorporation of amino acid residues into BTA represents another strategy to obtain self-assembling compounds in water. Hydrophobic amino acids of natural (e.g., phenylalanine (F), leucine (L)), or synthetic (fluorinated phenylalanines) origin are generally employed due to their ability to form additional π - π or Van-der-Waals bonds.^{31,32} As an example, Besenius et al. designed a compound with pentafluoro-L-phenylalanine and an aminobenzoate spacer with a terminal Gd(III) complex as a promising agent for magnetic resonance imaging.³³

Even given the vast number of studies into different BTA-based molecules (including polypept(o)ids), the majority of self-assembling molecules are essentially uncharged.³⁴ A few studies attempted to combine BTA-cores with PGA derivatives; however, the protection of PGA with hydrophobic groups such as Boc completely prohibited the possibility of chain functionalization in all cases. The Besenius group pioneered a method of charge screening for small BTA-based molecules bearing ionizable groups with low molecular weight salts, reaching control for up to nine charges for Newkome dendron-decorated molecules.³⁵

Despite the wide versatility of BTA-based supramolecular polymers, all suffer from low stability upon dilution due to disassembly, which makes them unsuitable for direct *in vivo* applications. The minimal number of functional groups suitable for modification in comparison with classical drug delivery carriers represent an additional problem related to these materials.

During the first preparation of BTA-based polymers of star-shaped (st)PGAs by Duro-Castaño et al.,³⁶ which all behaved as classical star-polyelectrolytes, the presence of multiple charges completely disrupted supramolecular assembly. Now, we present the development of stPGAs that self-assemble into 1D supramolecular structures through the variation of core hydrophobicity and chain length. We also studied the self-assembly of BTA-based compounds bearing three and six charges to understand the mechanism of supramolecular polymer formation by stPGAs.

2.2. Synthesis and Self-assembly of BTA-based Oligophenylalanines

Special Note: For representational simplicity, the compounds studied in this thesis will be coded in a way to describe the sequence of one arm of a BTA-centered compound, for example, the F3E10 compound comprises a BTA core with triphenylalanine peptide (F3) and ten glutamic units (E10) attached to each arm. Intermediate compounds will be labeled as “ic” with the corresponding number.

There exist several studies devoted to the aqueous self-assembly of BTA-based compounds, including BTA-hexaphenylalanines and BTA-nonaphenylalanines.^{37,38} A characteristic property of the aforementioned compounds is their essentially uncharged status – they usually bear neutral hydrophobic components to enable water solubility. In this section, we studied a family of BTA-based compounds bearing from zero to three phenylalanines per arm; however, instead of attaching terminal hydrophilic domains, we prepared molecules bearing amines in the form of hydrochloride salt as an end-group (Fig. 2.2).

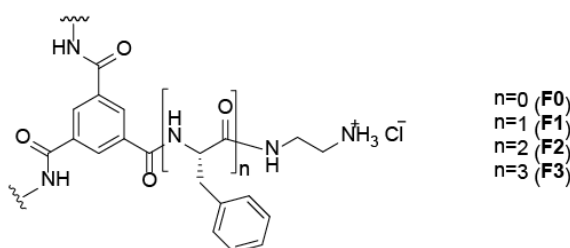


Figure 2.2. The general structure of BTA-based oligophenylalanines.

Hydrochlorides, while being much smaller than more common hydrophilizing groups, display high solvation strength, and we hypothesized that they could increase the solubility of BTA-based oligophenylalanines, thereby allowing us to study the role of charge on self-assembly in water. Alternatively, BTA-oligophenylalanines with terminal amine groups represent perfect initiators for stPGA synthesis.

2.2.1. Synthesis of Oligophenylalanines Blocks

As a first step, we prepared mono-, di-, and triphenylalanines with N'-Boc ethylenediamine groups (Fig. 2.3). We used classical liquid phase peptide synthesis, taking advantage of the interplay between orthogonal *tert*-butoxycarbonyl (Boc) and N-carboxybenzyl (Z) protecting groups. In this first step, we performed classical amide coupling with N-hydroxysuccinimide (NHS) or DMTMM (4-(4,6-dimethoxy-1,3,5-triazin-2-yl)-4-methyl-morpholinium) chloride as a coupling agent (Fig. 2.4). In both cases, we found a similar purity for the final products; however, we chose a DMTMM

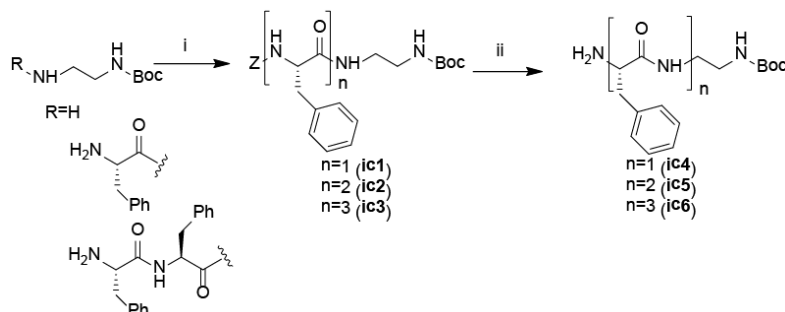


Figure 2.3. Synthesis scheme for compounds **ic4-ic6**. i) DMTMM Cl, MeOH, Z-L-Phe; ii) Pd/C, H₂, MeOH.

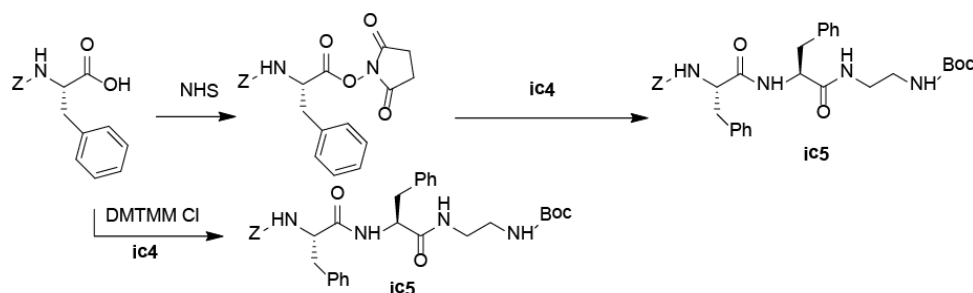


Figure 2.4. Scheme of synthetic routes employed to prepare compound **ic5**.

coupling strategy as coupling with NHS requires extra steps for isolation and purification of the activated intermediate. The main benefits of DMTMM in comparison with other amide activation agents (e.g., carbodiimides) are the broad pH activity range and perfect stability in aqueous medium and the lack of amine interference during carboxylic group activation.³⁹

The second step of synthesis is the orthogonal deprotection of the Z-group through catalytic hydrogenolysis, which can take advantage of several different catalysts containing palladium. We chose palladium hydroxide on carbon (Pearlman's catalyst) in methanol; the standard procedure for the reaction uses 10% catalyst (w/w), but we discovered that even 0.5-2% (w/w) suffices for deprotection after 3h. We performed the deprotection reaction for **ic3** at 40 °C, as, after 2-3 h, the performance of the catalyst decreased due to unspecific absorption of **ic6** on the surface or partial precipitation of the product.

We studied three different approaches of coupling of oligophenylalanines to the BTA core: acid chloroanhydride, DMTMM chloride, or DMTMM tetrafluoroborate amide coupling (**Fig. 2.5**). Coupling with chloroanhydrides represents the most straightforward approach; however, viscous colored products that are difficult to separate during purification form after the addition of amine or N,N-diisopropylethylamine (DIEA). Both DMTMM-based methods provided identical

results with no observed formation of colored impurities. Coupling with DMTMM chloride in methanol resulted in the gelation of the entire mixture due to the low solubility and strong aggregation of the product.

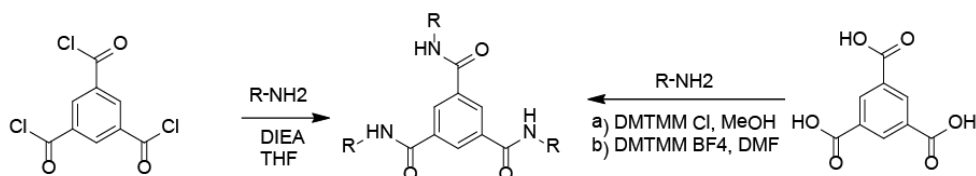


Figure 2.5. Synthetic approaches used for the synthesis of BTA-oligophenylalanines.

As a result, we observed an increased amount of doubly and single substituted BTA-derivatives due to the decreased diffusion of reagents in a gel. As the addition of dimethylformamide avoided this problem by promoting the complete solubility of the compounds, we prepared compounds **ic8-10** in this manner (**Fig.2.6**).

We synthesized compound **ic7** (which does not contain phenylalanine) to serve as a control using the trimesyl chloride approach developed by Duro-Castaño et al.³⁶ We also simplified the purification procedures; we found that precipitation in methanol sufficed to obtain pure compounds (as shown by NMR).

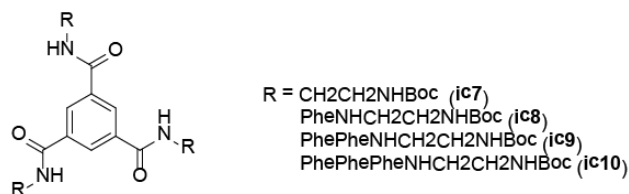


Figure 2.6. General scheme of compounds **ic7-ic10**.

In the last step, we deprotected the terminal amine; acidic treatment represented the most popular deprotection strategy applied for the Boc group.⁴⁰ We evaluated three different acidic deprotection approaches: treatment with trifluoroacetic acid (TFA), anhydrous hydrogen chloride (HCl) in dioxane, and tetrafluoroboric acid in ether. All three methods provided 100% deprotection and allowed the synthesis of three different amine salts. Additionally, tetrafluoroboric salts (BF₄) of amines can function as suitable initiators for stPGA synthesis, as will be described below.

Trifluoroacetates compounds displayed high viscosity, and we isolated them only at low yields (20-50%). Meanwhile, we isolated tetrafluoroborates at good to excellent yields; however, these compounds failed to dissolve in water, and we did not study them further. However, we isolated chlorides at excellent yields, and all displayed water-solubility. We selected deprotection with 4M HCl/dioxane as the method of choice for all the compounds of this type, synthesizing compounds **F0-F3** (**Fig. 2.7**).

We studied compound purity by $^1\text{H-NMR}$ (see SI) and thin-layer chromatography, and structure proof by 1D and 2D nuclear magnetic resonance (NMR) methods.

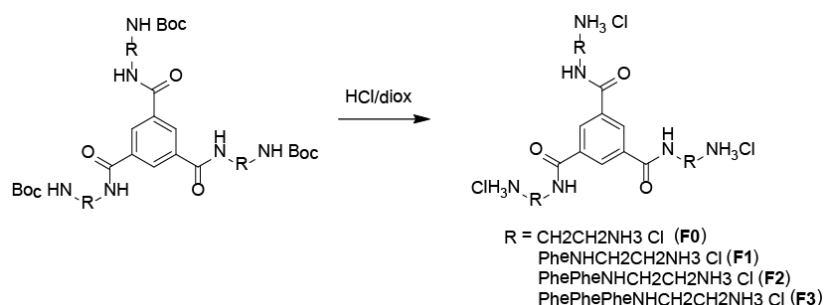


Figure 2.7. General scheme of compounds **F0-F3**.

2.3. Self-assembly Studies

Fluorimetry is a versatile technique used for the study of self-assembly in aqueous solutions. In this thesis, we used the hydrophobic dye NR (**Fig 2.8**) as a fluorescent probe.

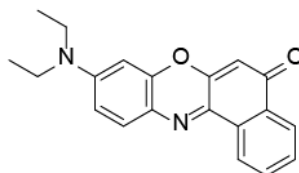


Figure 2.8. Molecular structure of the dye NR used as a fluorescence probe.

NR is a lipophilic solvatochromic dye extensively used to probe the presence of hydrophobic microdomains in supramolecular aggregates or phase-separated polymer solutions.⁴¹ Depending on the polarity of the environment, the maximum emission wavelength of NR changes due to the twisted intramolecular charge transfer (TICT) phenomenon. Excitation prompts the transfer of an electron from the diethylamino group to the quinoid section of the molecule, resulting in a hypsochromic shift. According to previous reports, NR in water has an emission ($\lambda_{\text{max,em}}$) at 654 nm, with very low fluorescence intensity irrespective of the salt concentration. In the presence of hydrophobic microdomains in solution, NR changes its conformation, which is accompanied by both an increase in intensity and a hypsochromic shift. The value of the hypsochromic shift directly correlates with the hydrophobicity of the environment. We determined that compound **F0** does not self-assemble in water even at concentrations as high as 100 mg/ml, at which the NR shift and intensity increase become unreliable because of the increased lipophilicity of the solution. We determined the critical

aggregation concentration (CAC) of compounds **F1-F3** using wavelength shift. Any determination can also be undertaken by plotting intensity vs. concentration; however, this strategy was not applicable for compounds **F0-F1** as the solubility of the NR increased at high concentrations, resulting in an intensity increase with no hypsochromic shift observed. Both CAC determination methodologies provided identical results for compounds **F2-F3**. In water, we obtained CACs for **F1-F3** as 91, 0.77, and 0.006 mM, respectively (Fig. 2.9).

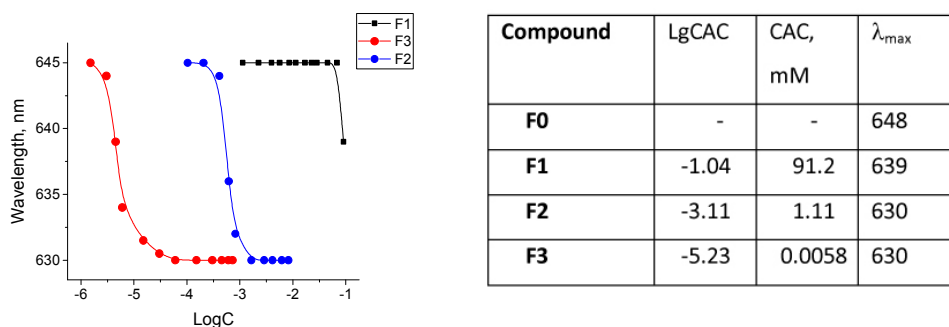


Figure 2.9. Dependence of NR peak maximum as a function of compound concentration and determined CAC values.

Next, we performed small-angle X-ray scattering (SAXS) studies for compounds **F0-F3** to determine the sizes, shapes, and conformations of single molecules or their aggregates. Compound **F2** in pure water at 1.2 mM solution (below CAC) failed to self-assemble, and we observed a slight negative trend at a low q -range due to interparticle repulsions (Fig. 2.10A). Interaction screening with 20 mM NaCl resulted in a clear SAXS profile with a power law dependence -1 typical for rod-like particles. For the more concentrated solution (5 mM, above CAC), the SAXS profile in pure water provides more apparent evidence of aggregation; however, the effect of repulsive structure factor is also more pronounced at higher concentrations (Fig. 2.10B).⁴² The presence of the peak at $q=0.25$ is due to the pseudo-crystalline ordering of the molecules in the solution typical for repulsive interactions. The final profile is a sum of two curves - one describing polydisperse rods in solution and another describing the structure factor for the solution of repulsive interactions. From the Guinier plot for rods,⁴³ we determined a radius of gyration of cross-section ($R_{g,c}$) as 0.806 nm. Considering that radius of cross-section $R_c = 1.4 \cdot R_{g,c}$, the R_c is equal to 1.13 nm. We did not perform similar studies for compounds **F0-F1** due to their low self-assembly. For compound **F3**, we already observed rod-like particles in solutions at a concentration of 0.113 mM; however, the power law dependence was slightly lower than -1, probably as a result of the structure factor influence. At higher concentrations, we observed an expected increase in the intensity of the curves as the concentration of fibers and rods in the solution increased sharply (Fig. 2.10).

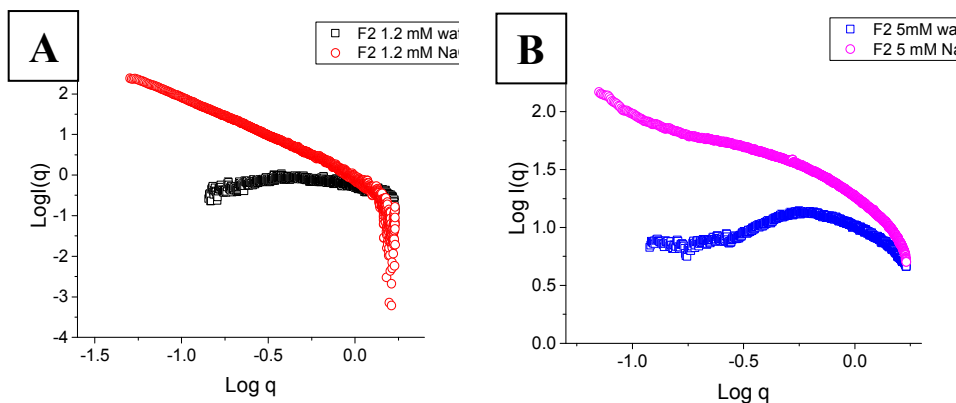


Figure 2.10. SAXS profiles of **F2** at 1.2 mM (**A**) and 5mM (**B**) in water and 20mM and 5mM NaCl, respectively.

Due to the strong aggregation of particles (an upturn of the curve at low q -range) and polydispersity, the Guinier approximation was not reliable. We estimated $R_{g,c}$ from a modified Guinier plot, and found an almost identical value of 2.6-2.7 nm for the three samples. By calculating the value into the real value, we obtained an R_c of 3.7 nm, which is surprisingly much higher than the theoretically calculated value. At 2.8 mM, the compound forms supramolecular gels with very long fibers, so the constancy of the R_c value proves that increases do not arise from gelation or concentration issues. The Kratky plot for compound **F3** possesses a pronounced maximum at $q=0.38 \text{ nm}^{-1}$, which is typical for the appearance of so-called frozen aggregates (rather large aggregates with low dynamic exchange between molecules) or highly ordered structures.

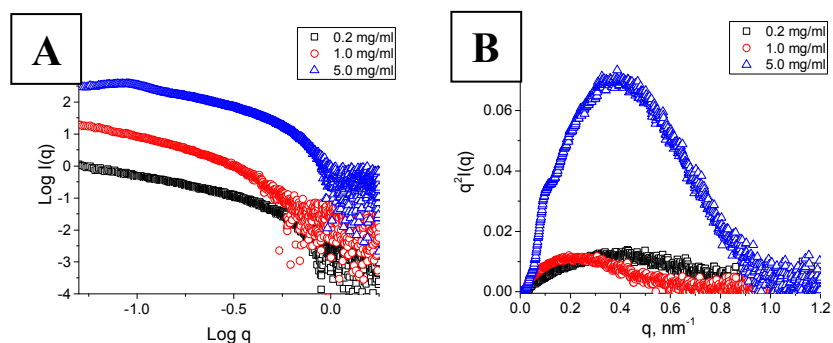


Figure 2.11. SAXS profiles (**A**) and corresponding Kratky plots (**B**) of **F3** at 0.113 mM, 0.565 mM, and 2.8 mM.

As a final proof of structure, we used standard transmission electron microscopy (TEM) with negative staining (phosphotungstic acid) and cryo-TEM. In both cases (**F2** and **F3**), we observed fiber formation (**Fig. 2.12**); indeed, **F3** formed very long fibers that reached several micrometers in length. For the cryo-TEM study, we chose a

concentration equal to 10-times the CAC to improve the visualization of the structures. In both cases, we observed the formation of fibers, although shorter than in the case of negative staining.

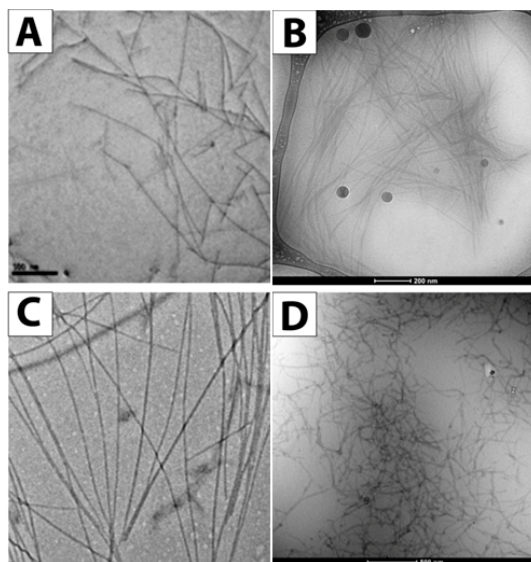


Figure 2.12. Normal and cryo-TEM of F2 (A, B) and F3 (C, D).

2.4. Study of BTA-oligophenylalanines with Mono and Diglutamate Termini

We prepared compounds **F₀₋₃G₁₋₂**, direct analogs of **F0-F3**, with terminally attached mono- and diglutamate residues to determine the role of repulsive interactions at different distances from the core (Fig. 2.13).

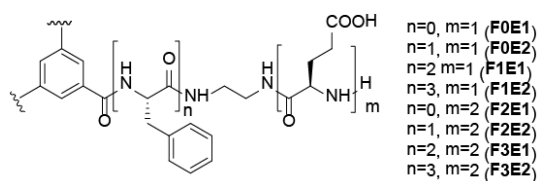


Figure 2.13. The general structure of compounds **F₀₋₃G₁₋₂**.

We synthesized compounds with one terminal glutamic unit in two steps, using **F0-F3** as starting materials. We used amine coupling with DMTMM chloride as an activating agent as a first step, followed by deprotection in acidic conditions. Initially, we used 4M HCl in dioxane, but the Z-group displayed partial resistance even after 24 h. We changed to a deprotection strategy with two eq. 48% hydrobromic acid in TFA,

which resulted in full deprotection after 4-14 h. We isolated the products as hydrobromide salts (**Fig. 2.14**).

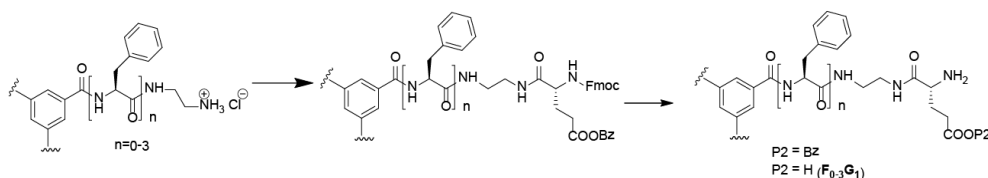


Figure 2.14. Synthesis scheme for compounds **ic17-ic19**.

We synthesized compounds **F₀₋₃E₁** in two forms - as sodium salts and as hydrobromic salts that will be designated with corresponding Na or Br in the following text (e.g., **F₃E₁Na**). We synthesized sodium forms by the basic treatment of compounds **F₀₋₃E₁**.

We synthesized compounds with two terminal glutamic units in four steps, using **F0-F3** as starting materials (**Fig. 2.15**). Initially, we attempted to simplify the procedure using compound **ic13** as a starting material and aimed to selectively deprotect the Z-group via hydrogenolysis. However, the reaction failed to proceed in THF and terminated at 50 % conversion in THF/MeOH (1:1) mixture after 48 h.

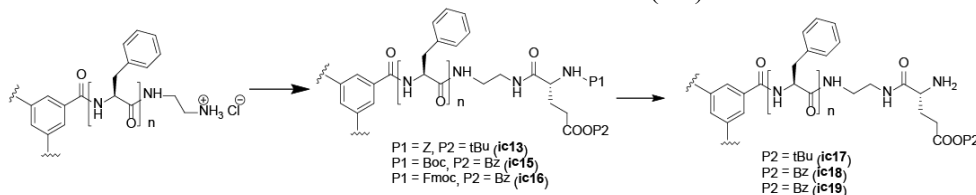


Figure 2.15. Synthesis scheme for compounds **ic17-ic19**.

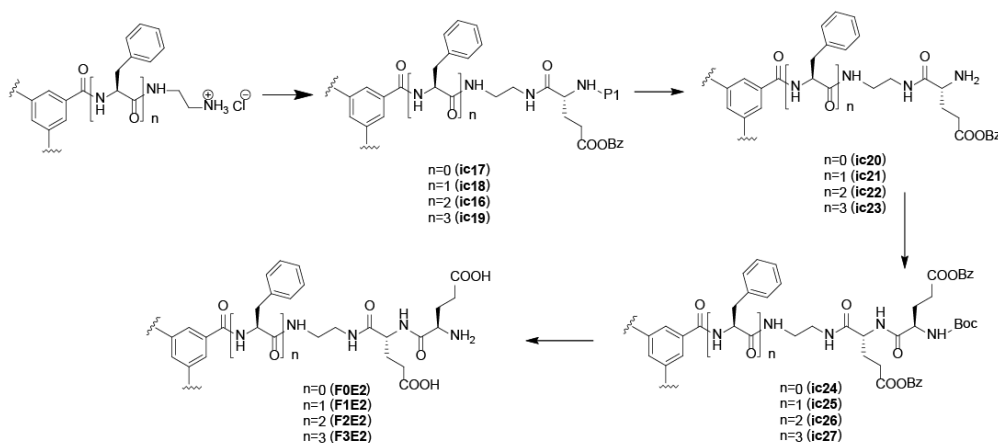
Deprotection in DMF resulted in full deprotection in 16 h but activated the carbon supporting palladium catalyst that dispersed to the level that we could not separate it via celite filtration.

Next, we evaluated additional deprotection groups: N-Boc and OBz. The Boc group displays lower susceptibility to acid hydrolysis, and studies have reported the selective deprotection of the Boc group in the presence of either Z- or benzyl ester-protecting groups.⁴⁴⁻⁴⁶ We studied several deprotection strategies and detailed the results in **Table 2.1**. As all our attempts to synthesize **ic-18** failed, we evaluated another derivative of glutamic acid with N-Fmoc and OBz protecting groups. The standard deprotection with 20% piperidine in DMF provided pure compound **ic19** with complete Fmoc deprotection and an intact Bz ester group.

Next, we applied direct amide coupling in the presence of DMTMM tetrafluoroborate in DMF and then acidic deprotection with hydrogen bromide (HBr) in TFA for 4-14 h (**Fig. 2.16**). We isolated pure **F₀₋₃E₂** as hydrobromide salts, and we obtained sodium salts of the compounds as described for **F₀₋₃E₁**.

Table 2.1. Efficiency of different agents in selective Boc deprotection of **ic15**

| N | Deprotection agent | Boc deprotection (%) | Bz deprotection (%) |
|---|--|----------------------|---------------------|
| 1 | 4M HCl/dioxane-methanol (1:1), 4h | 100 | 80 |
| 2 | Water, 100 °C, 3h | 0 | 0 |
| 3 | Water, 100 °C, pH3.0, 6h | 0 | 0 |
| 4 | 0.1M HCl/dioxane-methanol (1:1) | 0 | 0 |
| 5 | 4M HCl/dioxane-ethyl acetate (1:4), 0.5h | 85-90 | 5-7 |
| 6 | Phosphoric acid, 15eq. 24h | 30 | 0 |
| 7 | Phosphoric acid/THF (3:1), 50 °C, 4h | 100 | 50 |
| 8 | Phosphoric acid/THF (3:1), 40 °C, 1h | 70 | 10 |

**Figure 2.16.** Synthesis scheme for compounds **F0-3E2**.

We performed fluorimetry studies with NR at pH 3.0 and 8.0 to study both tri-charged compounds with terminal amine chloride and tri- and hexa-charged compounds with sodium carboxylates. We determined that compounds **F0E1**, **F0E2**, and **F1E2** failed to assemble in water or the presence of salts, independent of concentration. Compound **F1E1** assembled only in the presence of salt, with a CAC in 120 mM NaCl being equal to 6.1 mM. Other compounds assembled both in water and in the presence of salt, with the CAC values shown in **Table 2.2**. Compounds containing one terminal glutamic unit displayed almost identical CAC values at pH 3.0 and 8.0, while compounds with two glutamic units possessed significantly different CAC values in acidic and basic conditions. At acidic pH, compounds possessed a single terminal charge on each arm, and CAC values decreased significantly upon an increase in the distance from the center of the molecule to the charged group. Here, carboxylic groups remain non-charged, and the hydrogen bonds between peptide backbones provide additional stabilization. However, at basic pH, two carboxylic groups become protonated, and the CAC values are lower than for the corresponding compounds with one glutamic unit in all cases. In this case, in addition to a doubly strong Coulomb repulsive force, chain flexibility diminishes the possibility of hydrogen bond formation between the neighbor molecules.

Table 2.2. CAC values for compounds **F**₁₋₃**E**₁₋₂ at different pH levels

| Compound | pH 3.0 | | | pH 8.0 | | |
|-------------|--------|---------|-----------------------------|----------------|---------|-----------------------------|
| | LogCAC | CAC, mM | λ_{max} , nm | LogCAC (120mM) | CAC, mM | λ_{max} , nm |
| F2E1 | -3.86 | 0.138 | 630 | -3.89 | 0.135 | 630 |
| F2E2 | -6.04 | 0.0009 | 627 | -3.39 | 0.41 | 630 |
| F3E1 | -5.40 | 0.004 | 626 | -5.31 | 0.005 | 630 |
| F3E2 | -6.41 | 0.0003 | 622 | -4.49 | 0.032 | 630 |

Next, we performed negative-staining TEM and observed that, in all cases, the compounds formed long fibers of micrometer length; in some cases, fibers reached ten to a few tens of micrometers (**Fig. 2.17**). The only exception was **F3E1**, for which we observed short nanorods with lengths in a range of 20 to 300 nm. We failed to observe any significant morphological changes for any of the compounds, and fibers were well-separated from each other. For compounds with two glutamic units per arm, we observed lower staining contrast, which relates to decreased interactions between negatively charged chains and phosphotungstic acid. When we performed a similar study for **F3E2** at pH 3.0, we observed a change in morphology of the observed particles. Instead of long nanofibers, we observed relatively short nanorods that did not exceed 500 nm in length. This compound also displayed strong interfiber interactions, with the formation of bundles of fibers or long helical rods that comprised several fibers twisting around each other. Some particles formed ribbons with a low twisting angle.

SAXS profiles for compounds **F2E1-F3E2** at pH 8.0 provided evidence for rod-like particles, following the previously observed trends (**Fig. 2.18**). We obtained a power law dependence close to -1 for all the compounds except **F2E1**, which was slightly lower due to the lower concentration of the compound used. Both **F3E1** and **F3E2** possessed a well-defined peak on the Kratky plot with a peak maximum of 0.45 nm^{-1} . For **F3E1** and **F2E1**, the peak shifted to 0.14 nm^{-1} and around 0.9 nm^{-1} , respectively. The appearance of the defined peak, independent of position, unambiguously indicates the presence of organized systems. The analysis of modified Guinier plots allowed us to determine R_c values, as shown in **Table 2.3**.

The obtained values are in a range of 2.7-4.4 nm, which correlate well with TEM data. Nevertheless, in all the cases, we found R_c values higher than a radius of a completely stretched molecule.

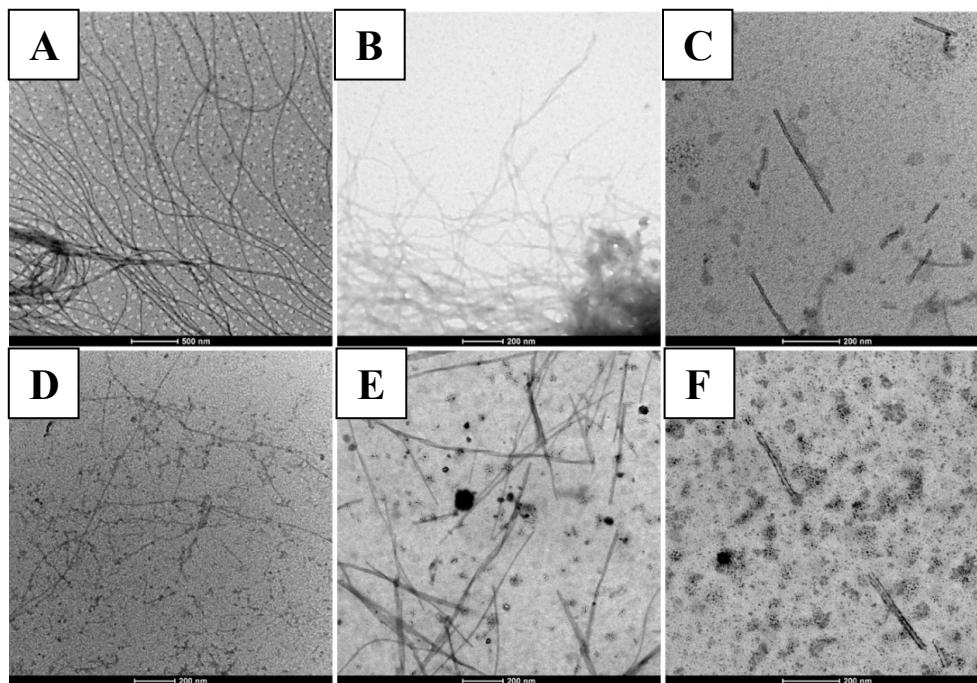


Figure 2.17. TEM images of compounds **F2E1** (A), **F2E2** (B), **F3E1** (C), **F3E2** (D) at pH 8.0 and of **F3E2** (E, F) at pH 3.0.

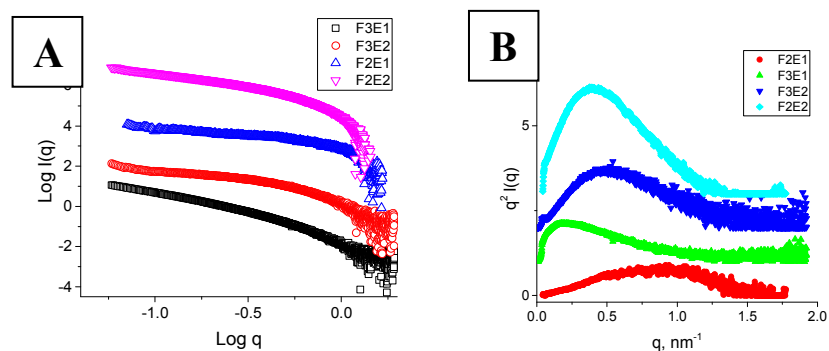


Figure 2.18. SAXS profiles (A) and corresponding Kratky plots (B) of compounds **F2E1-F3E2** at pH 8.0.

2.5. Study of BTA-oligophenylalanine-based Polyglutamates

We next extended the previously described synthetic procedure based on the use of terminal amine initiators in the form of tetrafluoroborate salts³⁶ to prepare stPGAs

with polymerization degrees ranging from 30 to 150 (10 to 50 units per arm). As initiators, we used **F0-F2 BF₄**, whose synthesis we described earlier in this chapter. We first purified and lyophilized all compounds and then conducted the polymerization reaction using NCA-Glu(OBz) as a monomer for two days under anhydrous conditions,

Table 2.3. Parameters obtained from SAXS data analysis

| Compounds | Power law | Power law (Porod) | Model | R _{g,c} , nm | R _c , nm |
|-------------|-----------|-------------------|-------|-----------------------|---------------------|
| F2E1 | -0.67 | -4 | rod | 2.67 | 3.74 |
| F2E2 | -1 | -4 | rod | 2.51 | 3.51 |
| F3E1 | -1 | -4 | rod | 3.15 | 4.41 |
| F3E2 | -1 | -4 | rod | 1.94 | 2.72 |

and lastly, characterized obtained polymers by GPC and NMR. We deprotected the benzyl group using 48% HBr in TFA for 10-14 h. We report the properties of the obtained polymers in **Table 2.4**.

Table 2.4. Physico-chemical properties of synthesized polymers

| Polymer | Initiator | Theor. DP | M _n ^a | M _w ^a | PDI ^a | DP ^b | DP/arm |
|---------------|-----------------|-----------|-----------------------------|-----------------------------|------------------|-----------------|--------|
| F0E10 | BF ₄ | 30 | 9908 | 11097 | 1.123 | 48 | 16 |
| F0E25 | BF ₄ | 75 | 16305 | 18755 | 1.151 | 72 | 24 |
| F0E50 | BF ₄ | 150 | 22922 | 35710 | 1.560 | 102 | 34 |
| F1E10 | BF ₄ | 30 | 7639 | 10535 | 1.385 | - | - |
| F1E25 | BF ₄ | 75 | 20984 | 31390 | 1.496 | - | - |
| F1E50 | BF ₄ | 150 | 27446 | 39552 | 1.440 | - | - |
| F1E10 | NH ₂ | 30 | 7713 | 8439 | 1.094 | 30 | 10 |
| F1E25 | NH ₂ | 75 | 18684 | 19501 | 1.044 | 81 | 27 |
| F1E50 | NH ₂ | 150 | 29534 | 32790 | 1.110 | 135 | 45 |
| F2E10 | NH ₂ | 30 | 7872 | 8591 | 1.091 | 30 | 10 |
| F2E25 | NH ₂ | 75 | 17478 | 18452 | 1.056 | 75 | 25 |
| F2E50 | NH ₂ | 150 | 32832 | 36539 | 1.113 | 144 | 48 |
| F2E200 | NH ₂ | 600 | 135416 | 171700 | 1.268 | 612 | 204 |
| F3E10 | NH ₂ | 30 | 7872 | 8591 | 1.091 | 28-32 | 10 |
| F3E15 | NH ₂ | 45 | 10825 | 11393 | 1.053 | 45 | 15 |

^a Determined by SEC, ^b Determined by NMR

While the **F0 BF₄** polymerization reaction proceeded well, as previously described by Duro-Castaño et al,³⁶ tetrafluoroboric salts of phenylalanine derivatives were less useful initiators, probably due to the lower basicity of the amines and lower overall reactivity, that resulted in the formation of products with high polydispersity. Non-protected amine initiators provided much better results with the observed polymer polydispersity lying in a range from 1.05-1.15. Consequently, we synthesized all the following polymers using amine initiators. At the concentrations used, in gram scale, we

also found that we could reach higher monomer conversion and polymers with higher molecular weights (up to 120 kDa) with a polydispersity of 1.27 using amine initiators. However, attempts to reach polymerization degrees above 1000 were not successful.

As a first step, we performed fluorimetry experiments using NR as a solvatochromic dye to determine the CAC values for **F2E10**, **F3E10**, and **F3E15** in pure water (**Fig. 2.19 A,B**). We observed that three compounds demonstrated a substantial increase in intensity and a hypsochromic shift of the peak maximum to 630-633 nm, signifying compound self-assembly with the formation of hydrophobic microdomains. The stronger shift for **F3E10** at a three-times lower concentration emphasizes the stronger tendency for aggregation. By plotting λ_{\max} against polymer concentration, we determined a CAC of **F2E10** and **F3E10** of 6.25 and 0.457 mM in pure water and 3.98 and 0.22 mM in 120 mM NaCl, respectively. For **F3E15**, we determined CAC values as 1.41 and 0.34 mM in water and 120 mM NaCl, respectively.

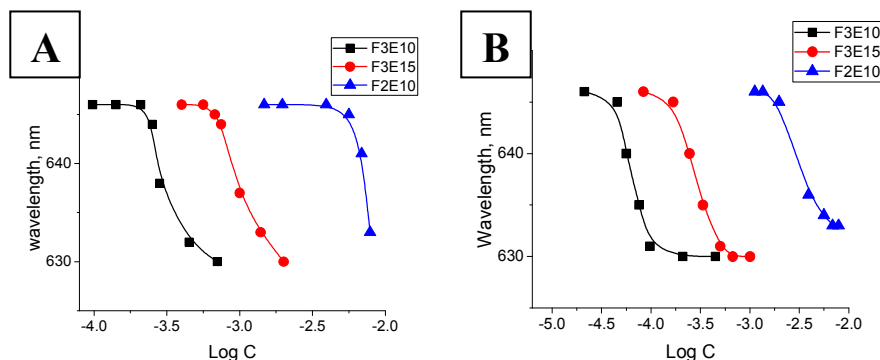


Figure 2.19. Dependence of peak maximum of NR on **F2E10**, **F3E10**, and **F3E15** concentration in water (A) and 120 mM NaCl (B).

We further demonstrated this effect with ionic strength variation experiments. By keeping the concentrations of **F2E10** and **F3E10** stable at 0.2 mM and varying salt concentration from 0 to 1.2 M, we determined the concentrations of salt necessary to induce self-assembly as 0.73 and 0.068 M, respectively (**Fig. 2.20**). **F3E10** reached an intensity plateau at much lower salt concentration and higher intensity value. Complete charge screening can be reached in solutions with high salt concentration, so forcing compounds to self-assemble even at lower concentrations. However, this is not practical due to the induced aggregation of polyelectrolyte chains.

To check that the NR signal does not arise from alternative mechanisms, we synthesized compounds **F1E10** and **F2E25**. We employed compound **F1E10**, a stPGA lacking a hydrophobic core, as a control compound to demonstrate that the specific properties of supramolecular polyglutamates do not arise due to topological or polyelectrolyte issues. Compound **F2E25**, with a hydrophobic core with two phenylalanines and 25 glutamate units per arm, allowed us to eliminate the possibility

of assembly due to core flexibility and the formation of hydrophobic domains within a single molecule. We discovered that, as expected, the NR fluorescence intensity quenched rapidly to zero for solutions of compounds **F1E10** and **F2E25**, irrespective of concentration (up to 70 mg/ml) and ionic strength (5 mM to 1.0 M). These data exclude these proposed mechanisms (**Fig. 2.21**).

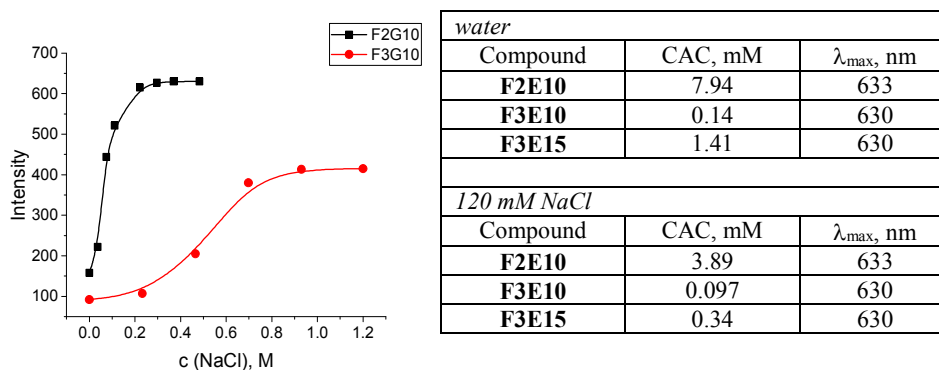


Figure 2.20. Fluorescent salt titration of **F2E10** and **F3E10** and determined CAC values for the polymers in water and 120 mM NaCl.

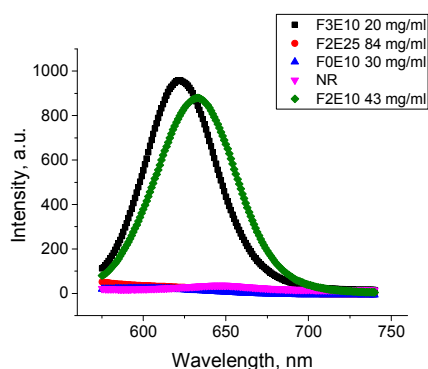


Figure 2.21. Fluorescence spectra of compounds **F3E10**, **F2E10**, **F2E25**, **F0E10** and NR.

Next, we performed TEM studies of compound **F3E10** at concentrations of 10 and 30 mg/ml. At concentrations below the CAC, fluorimetry (no NR peak shift) demonstrated, and TEM confirmed a lack of self-assembly. At a concentration around the CAC value (**Fig. 2.22A**), we found short flexible nanofilaments with a diameter of around 15 nm and length varying from 40 to 150 nm. At a concentration above the CAC, we observed very long fibers with a length of few microns (**Fig. 2.22B**). When we used phosphotungstic acid staining, we observed rods identical to those obtained by cryo-TEM; however, the contrast of these images was very low (**Fig. 2.22C**).

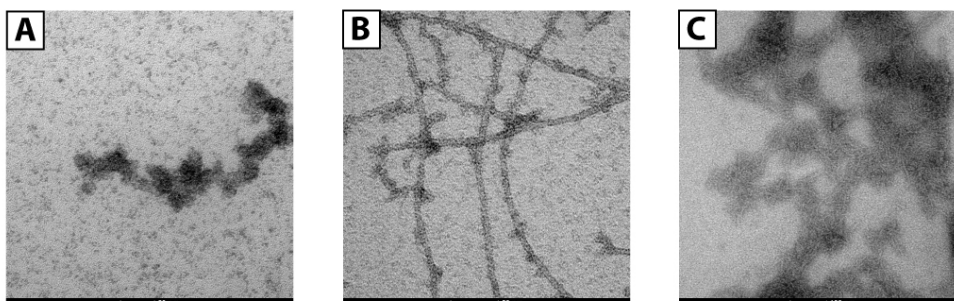


Figure 2.22. TEM images of **F3E10** in water at 0.45 mM stained with uranyl acetate (A), 3.5 mM (B) stained with uranyl acetate, and 3.5 mM stained with phosphotungstic acid (C).

We also performed cryo-TEM for solutions near the CAC to confirm the structures (**Fig. 2.23A**), observing nanorods with a length from 50 to 140 nm and a diameter of around 7 nm. In contrast with standard TEM images, where particles appeared as flexible filaments, cryo-TEM images demonstrated rod-like particles without apparent bending. The appearance of these artifacts may be explained by the fact that at concentrations around the CAC, only a portion of the molecules in solution becomes aggregated into rods, while the majority of the molecules exist as unimers. The uranyl acetate first interacts with nanorods and, in parallel, forms complexes with the unimers to form thick, flexible aggregates. A supporting argument for this assumption is the presence of more defined long fibers at concentrations above the CAC - the majority of the molecules now form aggregates, and the small fraction of unimeric molecules then form only a low number of artifacts around the fibers.

Image reconstruction of cryo-TEM images demonstrated a helical and periodic structure of the nanorods (**Fig. 2.23B**). Of note, the reconstructed images resembled a double helix - a challenging finding to explain in the framework of existing concepts regarding the self-assembly of BTA-based molecules. A periodic structure may arise from unusual self-assembly mechanisms of BTA-based molecules, involving the overlap of two nanofilaments; a more detailed discussion about the mechanism will be presented below. We measured the distance between the two maxima of the nanorods as 4.6-4.9 nm (**Fig. 2.23C**), while the diameter of nanorods was around 5 nm; these values fit well with the theoretically calculated diameter of the molecule of 5.2 ± 0.4 nm. Of note, we failed to observe any aggregated or assembled particles for **F2E10**, even in solutions with concentration far above the CAC. Considering the lower hypsochromic shift obtained for **F2E10**, we hypothesize that this compound forms tiny aggregates incorporating only a few molecules.

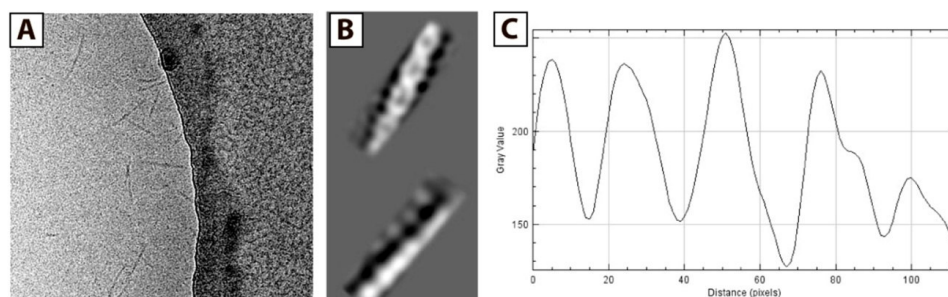


Figure 2.23. Cryo-TEM images of **F3E10** (A), image reconstructions (B), and corresponding distance distributions (C). Scale bar in (A) = 100 nm.

We next performed SAXS experiments to determine the nanorod structure. At low concentration, all the compounds behaved as typical polyelectrolyte solutions with identical scattering curves at a concentration of 0.1 mM in pure water (**Fig. 2.24A**). These curves fit well in terms of the isotropic model developed by de Gennes et al.^{47–49} These curve profiles are typical for stPGAs and polyelectrolyte solutions in general, with a dip at low q -values and curve bending in the medium q -range, which vary slightly with molecular weight.

For similar 0.1 mM solutions containing 120 mM NaCl, we observed almost identical curves for both **F0E10** and **F2E10**, giving scattering profiles typical for unimolecular solutions (**Fig. 2.24B**). Both compounds behave as dilute polyelectrolyte solutions with repulsive interactions screened by salt ions, resulting in the linear range in low q -values. However, we observed a completely different curve corresponding to **F3E10**, characterized by a power law -1 dependence typical for cylindrical objects. Guinier analysis allowed us to determine the $R_{g,c}$ of **F3E10** as 1.65 nm, which corresponds to an R_c value of 2.31 nm.

We also performed SAXS studies at higher concentrations to study the possible self-assembly of **F2E10** and confirm the formation of long fibers for **F3E10** (at a concentration of 3.5 mM, which is below the CAC for **F2E10** but far above the CAC for **F3E10** in water and 120 mM salt solution). At higher concentrations in solutions of varying concentrations of salt (from 0 to 640 mM), we discovered different SAXS curves for compounds **F3E10**, **F0E10**, and **F2E10**. The differences in curve appearances were already apparent in pure water (**Fig. 2.24C**); we found a less pronounced dip in the low q -region of the curve for **F0E10** than for the diluted compound, and this shifted to the higher q -value. This alteration occurs since charged particles at higher concentrations remain at smaller distances between each other in solution. The curves acquired for **F2E10** appeared similar to the curves for **F0E10** in water, with the uphill section in the low q -range shifted to $q = 1 \text{ nm}^{-1}$. In 120 mM NaCl solution, we observed similar profiles for **F0E10** and **F2E10** in the high and medium q -range with a power law dependence of 0, corresponding to a unimolecular solution. Small uphill sections at low q -values on the curve corresponding to **F2E10** may be related to a clustering effect. Curves obtained for

compound **F3E10** in the presence and the absence of salt, possess -1 power law dependence in low to medium q -range corresponding to cylindrical particles, and -4 at high q -range corresponding to the scattering of individual molecules. At 120 mM salt solution, the curve possesses a more defined S-shape that can be explained in terms of two overlapping curves - polyelectrolyte repulsive scattering and rod scattering (**Fig. 2.24D**). Of note, a Guinier approximation is not valid for these systems as the aggregation distorts low- q regions. Therefore, we employed a modified Guinier approximation for rod-like particles and determined a radius of the rod cross-section of around 2.3 nm.

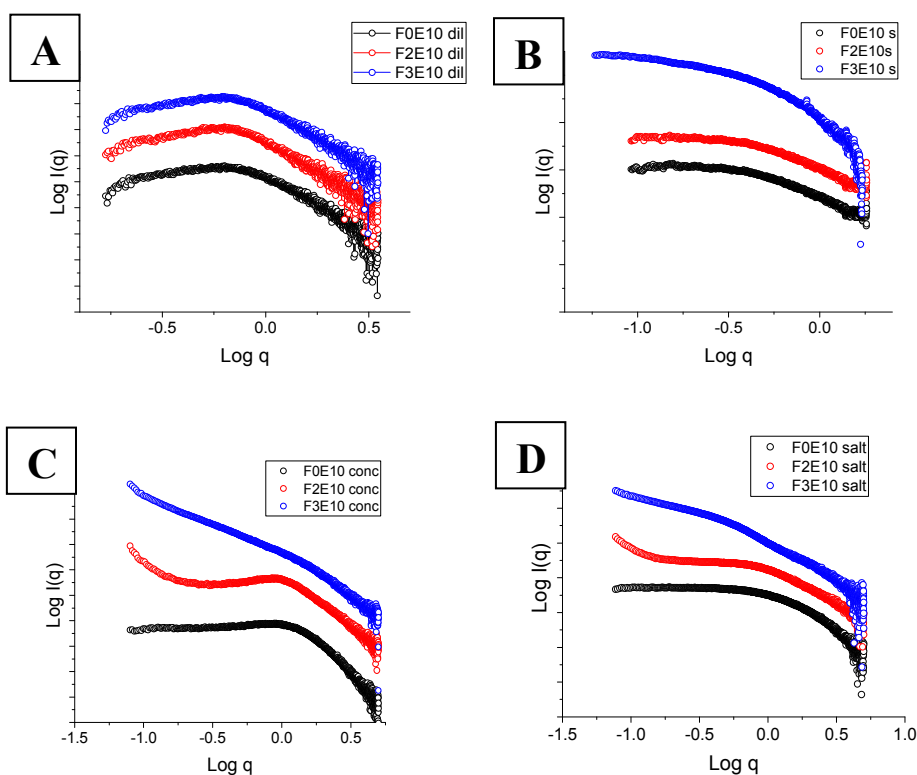


Figure 2.24. SAXS profiles of F2E10 in water (A) and 120mM NaCl (B), F3E10 in water (C) and 120mM NaCl (D), with concentration 5 and 40 mg/ml.

We performed a more detailed study of **F3E10** at a higher salt concentration (0-640 mM) and observed a smooth transition with an isosbestic point at $q=0.89 \text{ nm}^{-1}$ (**Fig. 2.25A**). We observed an increase in intensity at the low to middle q -range due to an increased fraction of aggregated fibers, and a slight decrease in the slope at the high q -range corresponding to a chain collapse. Kratky plots (**Fig. 2.25B**) demonstrated the appearance of a hyperbolic peak with a maximum at 0.48 nm^{-1} with increasing intensity typical for the formation of ordered or frozen structures in solution. There existed a

similar trend for compound **F2E10** at the same concentration but at a much lower scale, thereby suggesting the presence of a minuscule fraction of very short aggregates.

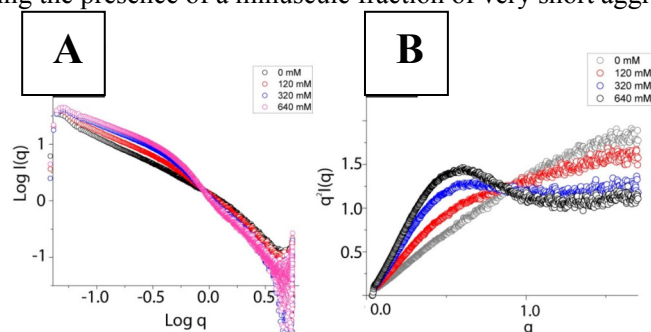


Figure 2.25. SAXS profiles (A) and corresponding Kratky plots (B) of **F3E10** (40 mg/ml) in 0-640 mM salt concentration.

For compounds **F0E10** and **F0E200**, we observed similar changes in the curve appearance (**Fig. 2.26 A,B**). The disappearance of the curve downhill at low q-range on the doubly logarithmic representation occurs due to charge screening and the change of chain conformation. Guinier analysis of the curves provided an R_g value corresponding to the radius of a single molecule.

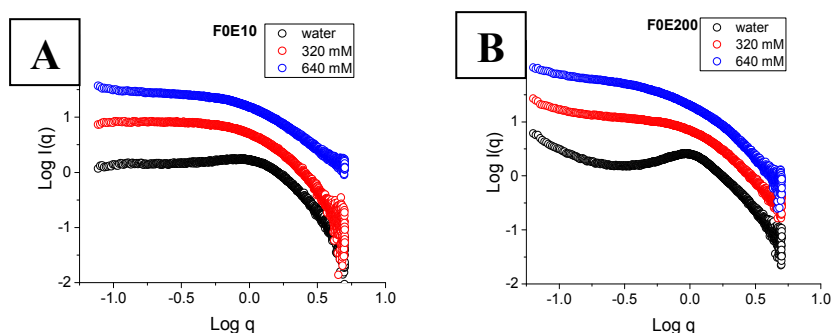


Figure 2.26. SAXS profiles for **F0E10** (A), and **F0E200** (B), in 0-640 mM salt concentration.

Next, we performed a more in-depth analysis of **F3E10** curves to extract structural information. To determine the radius of the fibers, we plotted R_c values obtained for the samples at different ionic strengths against salt concentrations (**Fig. 2.27**).

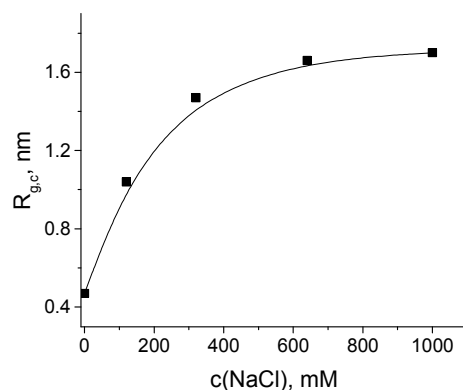


Figure 2.27. $R_{g,c'}$ values determined from Modified Guinier plot as a function of salt concentration.

The obtained graph reached an R_c plateau of around 1.7 nm, which corresponds to a radius of 2.4 nm, which agrees with cryo-TEM data. To obtain the length of the fibers, we calculated pair length distribution function, $P(r)$, because, in this case, Guinier approximations provide a less precise estimation (**Fig. 2.28**). For this system, we constructed $P(r)$ functions only for solutions with a high salt concentration to avoid the interference from chain interactions that strongly distort the results.

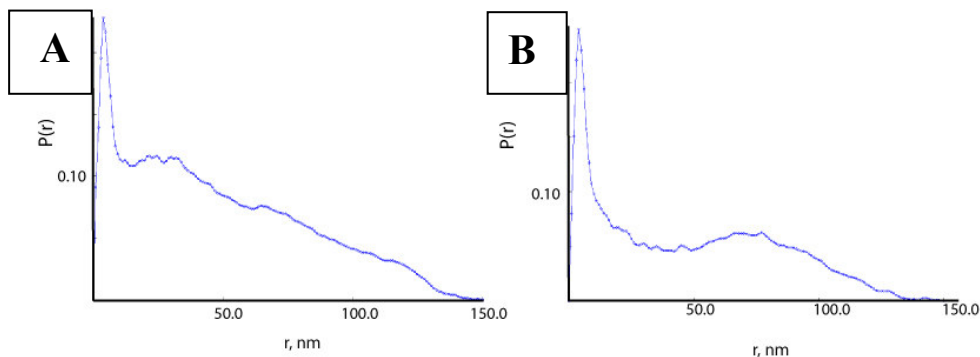


Figure 2.28. $P(r)$ distribution function of **F3E10** in 620 (A) and 1000 mM NaCl (B).

In both cases, the $P(r)$ distribution function has an appearance of a typical rod-like particle with one maximum at around 5 nm corresponding to the diameter of the fiber. In both cases, we found D_{\max} values estimated from $P(r)$ functions of around 120 nm; however, this number cannot be considered reliable as the length of the fibers (estimated from TEM data) exceeds the resolution of the SAXS instrument.

We additionally proved the presence of supramolecular fibers using a SANS study of **F3E10** in water and 120 mM NaCl (**Fig. 2.29**). While this system scatters

weakly, the results confirmed SAXS results; we observed a -1 power law dependence typical for rod-like particles and salt-induced aggregation. At this concentration, the length of the particles is higher than the resolution of the instrument, and Guinier approximation cannot be applied to determine the absolute length.

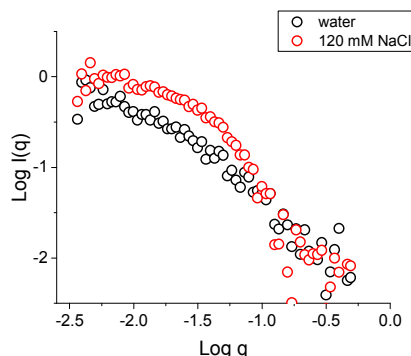


Figure 2.29. SANS profiles of **F3E10** in water and 120 mM NaCl.

2.6. Understanding the Mechanism of Assembly

The accepted mechanism of the self-assembly of BTA-based compounds is the formation of a C₃-symmetric system of hydrogen bonds leading to 1D assemblies. In this model, the centers of the molecules are situated one above the other. It is reasonable to assume that direct stacking, as shown in **Fig. 2.30A**, is energetically unfavorable due to the repulsions between corresponding donors and acceptors.

An alternative explanation for self-assembly includes a twist of the ring, as shown in **Fig. 2.30B**. In this case, repulsions between corresponding donors and acceptors are balanced by the formed hydrogen bonds. This model can explain the appearance of chirality in the systems and the self-assembly of the majority of BTA-based low molecular weight systems.

Despite a significant amount of studies published using the two models mentioned above, our data suggest that the **F3E10** system studied in this thesis assembles differently. We hypothesized that our systems assemble into helical structures according to a molecule twist mechanism, as shown in **Fig. 2.30B** but also accompanied by a shift of the molecule in the XY-plane, as shown in **Fig. 2.30C**. In this way, the system of directional hydrogen and aromatic stacking interactions will not be disrupted; however, BTA rings in the center of the molecule will be shifted one against the other in a way that interactions will occur through amide- π stacking or displaced π - π stacking.

Considering the distance between the groove maxima as 11.5 ± 1.5 nm (from cryo-TEM data), which corresponds to a full 360-degree twist, and the distance between

molecules in the assembly as 0.3 nm, we estimate the number of the molecules per full twist as 38 ± 5 units. These figures provide a twist angle of 9.47 ± 1.43 degrees. Considering that the maximum distance from the z-axis to the chain center is around 1.4 nm, we can easily determine that the shift of each molecule in the XY plane is equal to around 0.15 nm.

By applying these rough estimates, molecules in the stack should assemble, as shown in **Fig. 2.30C**. Central benzene rings shifted 1.5 \AA along both x and y axes result in a familiar parallel-displaced stacking that is energetically more favorable than parallel stacking. The system forms two arrays of directional hydrogen bonds similar to that which occurs in the classic BTA stacking model. However, one array does not form a directional system of bonds and might be stabilized by amide- π interactions because of a partial overlap with the benzene ring. The effect of a 10° twist on the stability of the system, as well as energy gain, remains relatively unclear. However, we do know that peptide sequences in β -sheets also tend to form into helices instead of parallel stacking. The typical angle in these structures can reach 25° . It is not completely clear why such twists are energetically favorable.

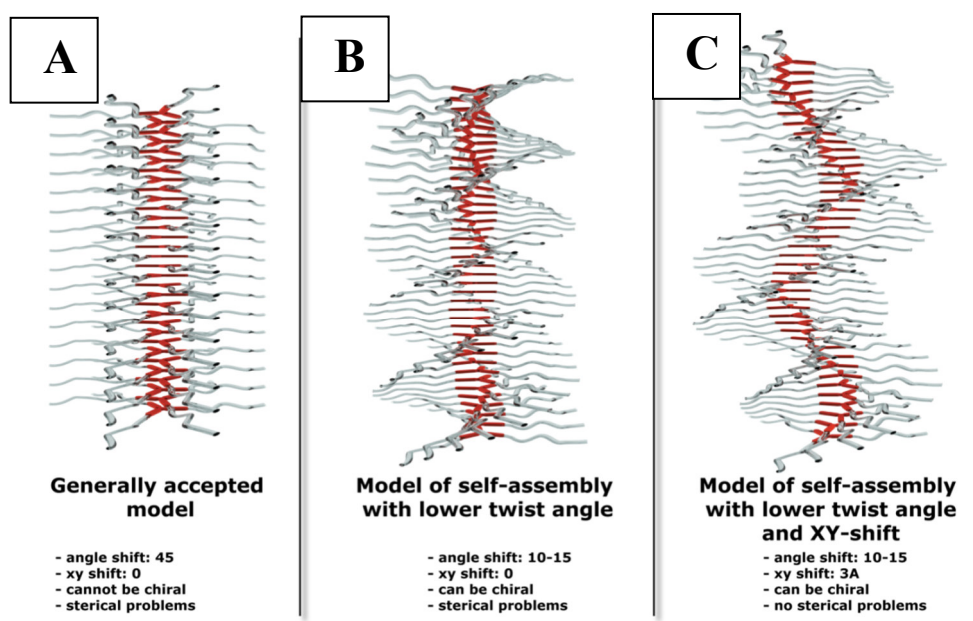


Figure 2.30. Existing (A,B) and hypothetical (C) model of self-assembly of BTA-based compounds.

Burian and Amenitsch performed dummy atom modeling for SAXS scattering for helical and twisted structures (**Fig. 2.31**).⁵⁰ They calculated that the $P(r)$ functions of helical assemblies should be represented as shown in **Fig. 2.32**. All helical assemblies possess a similar appearance, with the presence of a sharp peak corresponding to the diameter of the fiber, and decaying oscillations corresponding to the distance between

the two ridges of the 360-degree twist. We expect that the structure we obtained for **F3E10** to resemble either single or double helix based on cryo-TEM data.

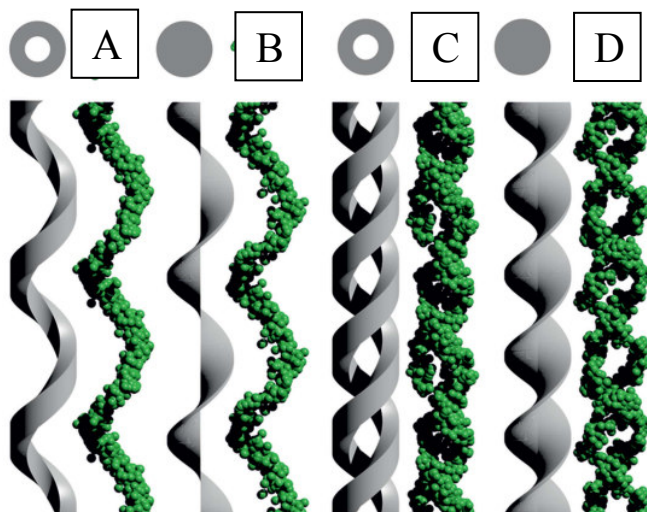


Figure 2.31. Helical structures A-D modeled using the dummy atom modeling.

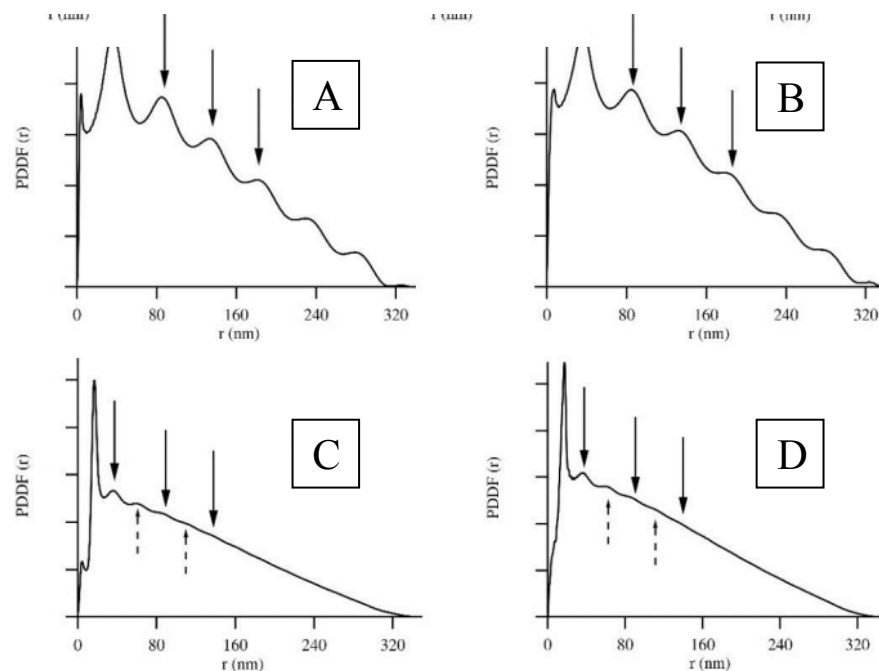


Figure 2.32. Modeled $P(r)$ functions obtained for different helices A-D.

To compare the modeled $P(r)$ functions with our systems, we considered three points:

1. The presence of PGA chain repulsions in our systems distorts the $P(r)$ function strongly, so we performed the study only for solutions containing high salt concentrations to screen electrostatic interactions and ensure that the distortions of the function do not expand further than the chain dimension.
2. Theoretical models have been calculated for infinitely long particles; therefore, we used a concentrated polymer solution because the length of the fibers should exceed the resolution of the detector, and the particles can be approximated as infinitely long.
3. The presence of very long particles provokes the appearance of oscillations in the $P(r)$ function; however, those oscillations increase in amplitude with increased distance. Therefore, we discarded all samples where the oscillation of the function increased or stayed steady in amplitude.

We compared the core **F3** compound and the corresponding polymer **F3E10** in 640 mM NaCl as we expect they self-assemble according to a similar mechanism (**Fig. 2.33**).

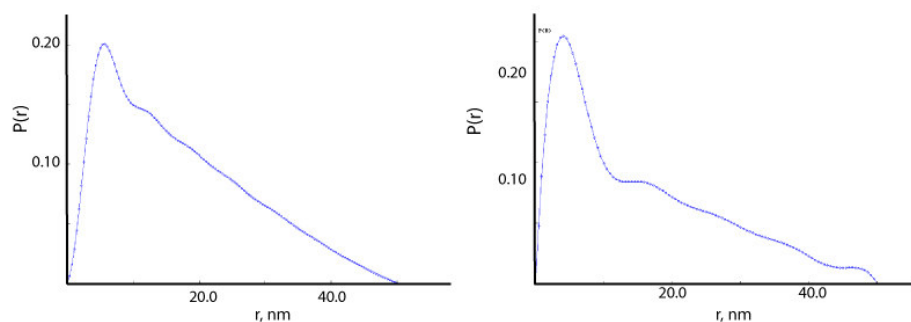


Figure 2.33. Obtained $P(r)$ functions for **F3** (left) and **F3E10** (right) in 640 mM NaCl.

To obtain these $P(r)$ functions, we performed another set of SAXS experiments with more scans to eliminate noise and function oscillations as much as possible. Both $P(r)$ functions have similar appearance typical for cylindrical particles, with a sharp peak corresponding to rod diameter and linear decaying line up to D_{\max} . On both curves, we also observed the presence of oscillations of low intensity, which decay with increasing distance. In the case of the **F3E10**, the $P(r)$ function does not smoothly decay at high r values because we chose a lower r -range than D_{\max} to avoid induced oscillation. We found that the distance between the peaks was equal to 10-11 nm, which corresponds to the distance between the grooves after a full 360-degree twist, which correlates well with our calculations. While these models do not allow us to differentiate between single and double helices, we believe that the helix formed for **F3E10** is a single helix because of steric complications from one side and because the distance between the fibers is equal

to approximately 1.4 nm, which exceeds core diameter, and is thus improbable. The origin of the double helix might be an artifact of the cryo-TEM mathematical treatment, as there will be an equal number of helices pointing in different directions, and their average may represent a double helix. This assumption is purely hypothetical and will require additional experiments with careful analysis of the data.

We expect that the molecules in our structure overlap, as shown in **Fig. 2.34**. Additionally, twisting should provide similar benefits as in the case of DNA – an increase in the total stability by increasing the density packing and decreasing the area exposed to solvent.

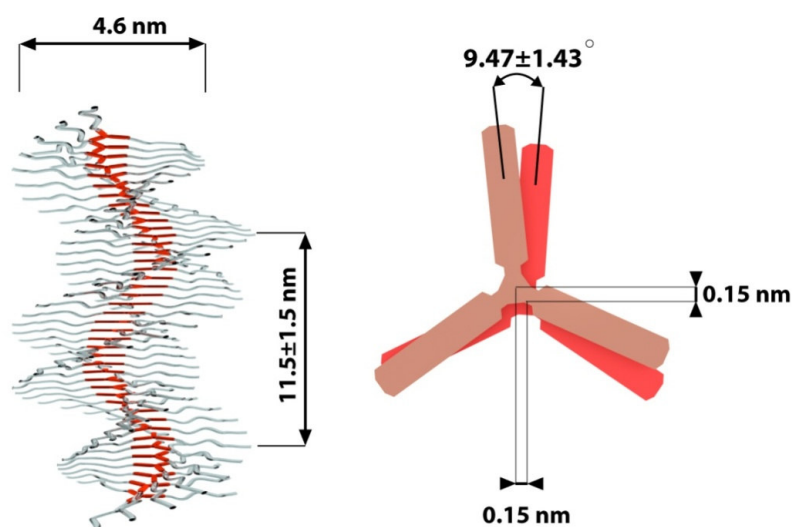


Figure 2.34. Graphical representation of the proposed stacking mechanism between BTA-based molecules.

2.7. Self-assembly Studies of F3-based Star-polyelectrolytes including Different Amino Acid Sequences

Polyelectrolyte nature plays an essential role in self-assembly, and to study how the length of methylene chains in the monomer affects self-assembly, we prepared a small family of star-polypeptides with **F3** cores, as shown in **Fig. 2.35**.

All the compounds assayed are charged polypeptides with an increasing number of methylene units, from one (in **F3D10**) to four (**F3K10**). Two of the polypeptides are anionic (Glu and Asp), and two are cationic (Lys and Orn).

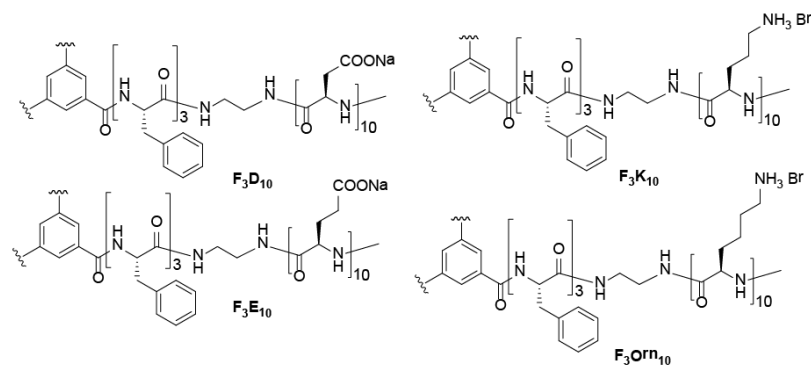


Figure 2.35. The general structure of different star-polyelectrolytes

We synthesized polymers via the ring-opening polymerization of α -amino acid N-carboxyanhydrides (NCA-ROP) of corresponding monomers in DMF. We observed that NCA-Asp-OBz failed to polymerize under NCA-ROP conditions; synthesis at 40 °C in DMF for two days resulted in partial polymerization (around 50%), while polymerization at 40 °C in DMF for four days with 1.5 times excess of the monomer resulted in the target polymer. We deprotected **F3D10** with TFA/HBr, a comparable manner to **F3E10**, and additionally dialyzed through a 3.5kDa-molecular weight cutoff membrane to remove the residual linear polymer and non-reacted monomer. We deprotected **F3K10** using potassium carbonate in a methanol/water mixture followed by treatment with hydrobromic acid. We deprotected **F3Orn10** with HBr in acetic acid and dialyzed through a 3.5 kDa-molecular weight cutoff membrane. We detail the properties of the prepared polymers in **Table 2.5**.

Table 2.5. Properties of prepared star-polyelectrolytes

| Polymer | Theor. DP | Obtained DP | Mn | PDI |
|----------------|-----------|-------------|-------|------|
| F3D10 | 30 | 28 | 7389 | 1.19 |
| F3E10 | 30 | 31 | 10825 | 1.05 |
| F3Orn10 | 30 | 34 | 10706 | 1.07 |
| F3K10 | 30 | 31 | 9550 | 1.07 |

We determined CAC values in water and 120 mM NaCl by fluorescence spectroscopy (**Fig. 2.36**). **F3Orn10** deviates strongly from the general tendency of decreasing CAC values with increased chain length. This deviation arises from the change of a hard-hard base pair in sodium-carboxylate to a hard-medium base pair in

ammonium-bromide, resulting in higher CAC (as will be described for **F3E10** with different counterions)

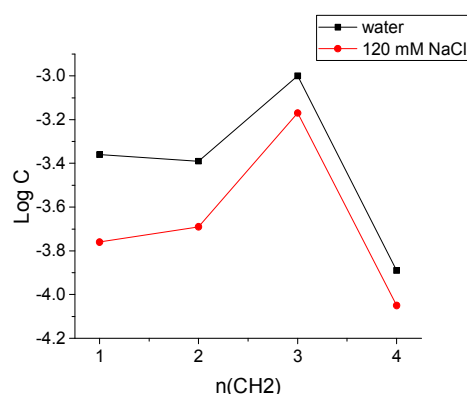


Figure 2.36. Dependence of Log CAC on the number of methylene units in the side chain.

Next, we performed SAXS studies of **F3D10** and **F3K10** in solutions with different ionic strengths (0-640 mM) and compared them to the data for **F3E10** obtained earlier. On the SAXS profiles and Kratky plots of **F3D10**, we observed a transition similar to **F3E10** with the appearance of a peak around 0.5 nm^{-1} at the Kratky plot, which corresponds to system ordering (**Fig. 2.37**).

However, even at a high concentration of salt, the power law dependence in low q -region remained close to zero, suggesting the absence of fiber-like particles. Profiles of **F3K10** at similar concentrations were almost identical, independent of ionic strength. When we studied power law dependence at a low q -range, we observed power law dependence close to -1, which is typical for rod-like particles (**Fig. 2.38**). However, we do note that the profiles lacked clearly defined linear regions, thereby suggesting the simultaneous presence of multiple species with different lengths.

The $P(r)$ distribution function of **F3D10** possessed a close to Gaussian shape with a maximum at 3.5 nm, slightly stretched in 6-11 nm range, with a D_{max} of 11 nm (**Fig. 2.38A**). From these data, we conclude that only a small portion of very short rods (not exceeding 11 nm in length) are presenting the solution. For **F3K10**, the $P(r)$ function is more typical for rod-like objects, with a D_{max} of 25 nm; however, most of the species are short rods (**Fig. 2.38B**). Negative TEM confirmed the presence of short rods not exceeding a length of 50 nm, with few longer rods on the field (**Fig. 2.39**).

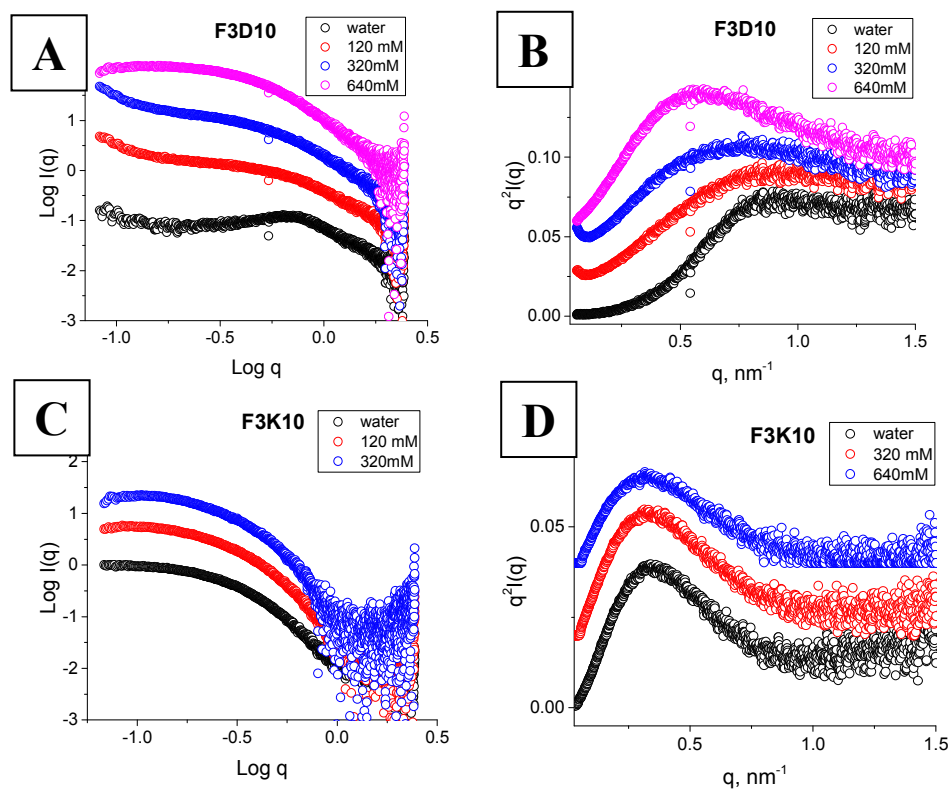


Figure 2.37. SAXS profiles and corresponding Kratky plots of **F3D10** (A,B) and **F3K10** (C,D).

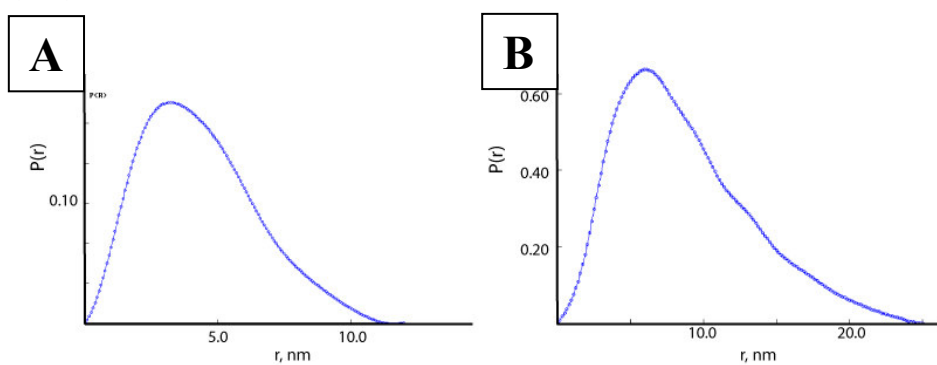


Figure 2.38. $P(r)$ functions of **F3D10** (A) and **F3K10** (B).

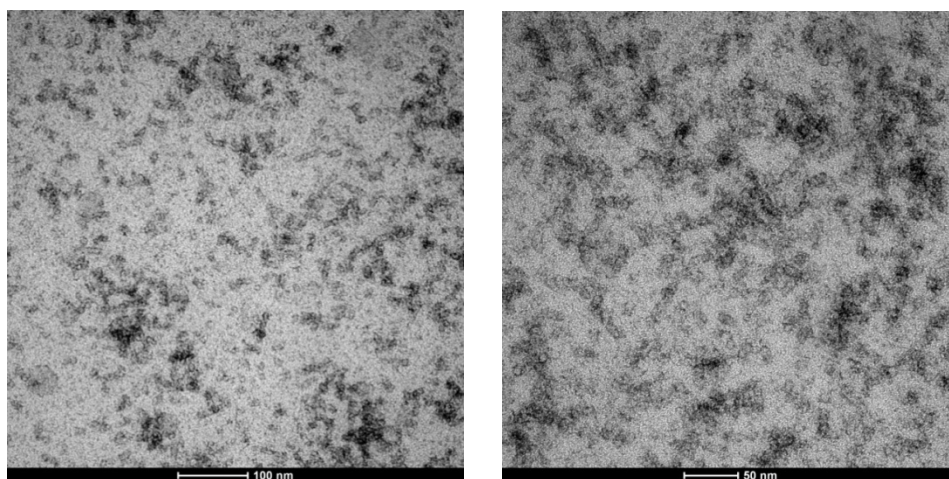


Figure 2.39. Representative TEM images of **F3K10** at 10 mg/ml in water.

It is not completely clear why **F3K10** forms only short rods that do not grow longer at high concentrations and ionic strength of the solution. We suggest that large and deformable bromine counterions destabilize supramolecular assembly. Harder counterions, such as chloride, may stabilize the assembly, similar to what we observed for **F3E10** with different counterions.

2.8. Effect of Counterions on Self-assembly of **F3E10**

Next, we evaluated how counterion variation affects the self-assembly of **F3E10**. We prepared samples with five different counterions (Li, Na, K, Cs, and NH_4). We selected ions in order of increasing charge density, ionic radius, and hardness according to “hard and soft (Lewis) acids and bases” or HSAB theory. We prepared compounds by treatment of **F3E10** in the acidic form with corresponding bases and purified by extensive dialysis.

We first determined the CAC values of the polymers in water and 120-640 mM solution of salt. For this experiment, we used salts with corresponding counterions to avoid ion exchange in the polymer, which would result in modified self-assembly behavior. We allowed samples to equilibrate for three days before making any measurements.

We observed that independent of the conditions, cesium promoted the largest destabilization of self-assembly (**Fig 2.40**). This occurrence can be explained in terms of the polyelectrolyte collapse model and, to a lesser extent, with the HSAB model. The cesium ion is a soft acid with low spatial charge density, and it screens the charges in a weaker manner than hard acids. This, in turn, results in chain swelling and stronger chain repulsions and lower CAC values. This effect is less pronounced in water, but counterion

condensation results in stronger chain swelling in the presence of a higher amount of cesium salt.

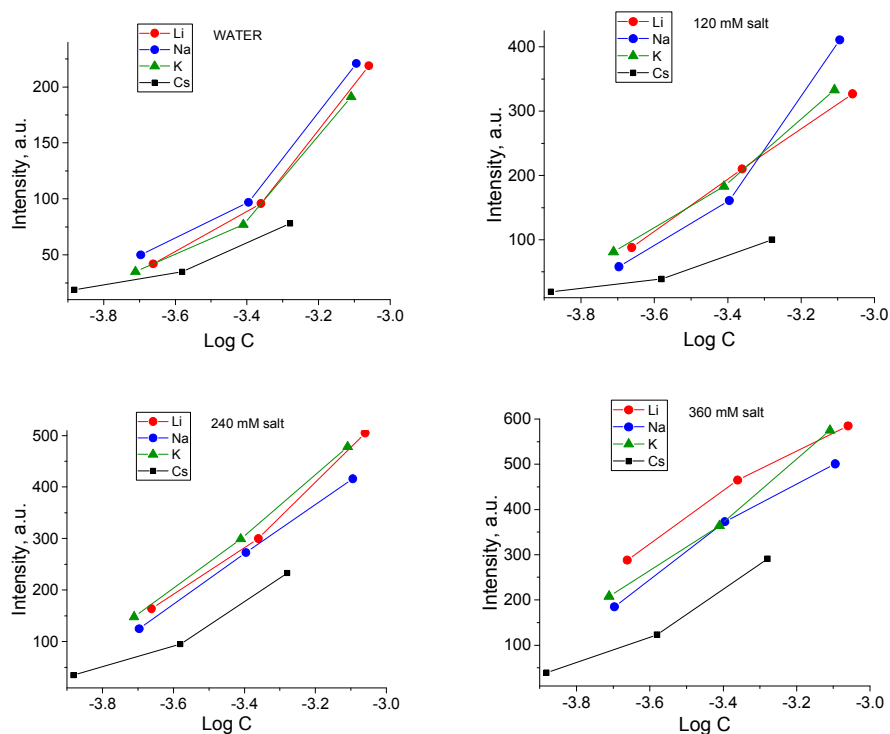


Figure 2.40. Dependence of NR peak maximum of **F3E10** with different counterions on the Log C of the polymer in 0-640 mM solution of corresponding salts.

For **F3E10 NH₄**, we unexpectedly observed a much stronger signal and a much lower CAC value when compared to any other counterion. When we performed the study at 0h and 72 h after preparation (**Fig. 2.41**), we observed a robust increase in intensity, meaning that the system takes longer to reach equilibrium.

SAXS experiments, in general, confirmed these results; in pure water (**Fig. 2.42 A,B**), we found SAXS profiles typical for polyelectrolyte solutions, with one peak around 0.7 nm^{-1} . The peak position varied slightly, with counterion size, changing from 0.74 to 0.61 nm^{-1} in agreement with a molecule size increase with increasing counterion size due to chain swelling. Upon an increase in the concentration of corresponding chloride salt from 120 to 640 mM (**Fig. 2.42 C-H**), we observed a change in the peak profile shape and the appearance of a -1 power law dependence corresponding to the formation of rod-like particles. For Li, Na, and K, the curves practically overlap, while for Cs, the intensity of the profiles was always lower and failed to reach -1 even at 640 mM cesium chloride.

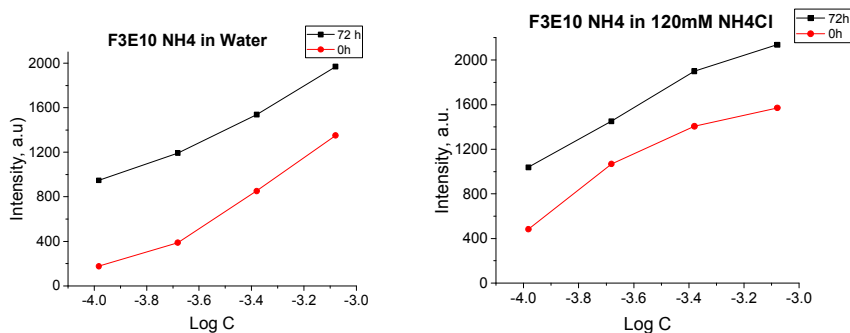


Figure 2.41 Dependence of NR peak maximum on the Log C of F3E10 NH4 the polymer in 0-120 mM solution of ammonium chloride immediately after preparation and after 72 h.

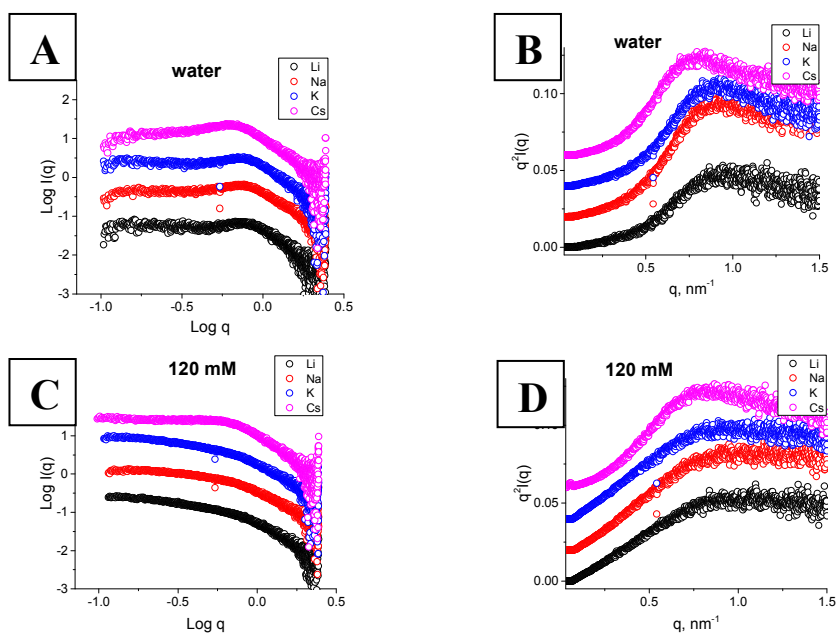


Figure 2.42. SAXS profiles and corresponding Kratky plots of **F3E10** with different counterions in 0 mM (A,B), 120 mM (C,D), 320 mM (E,F), and 640 mM (G,H) solution of corresponding salts.

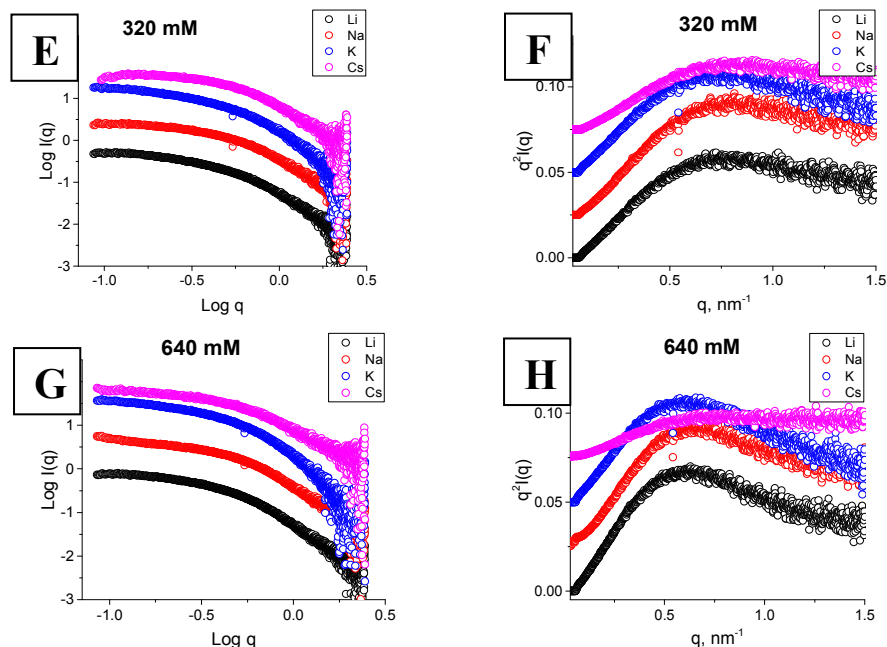
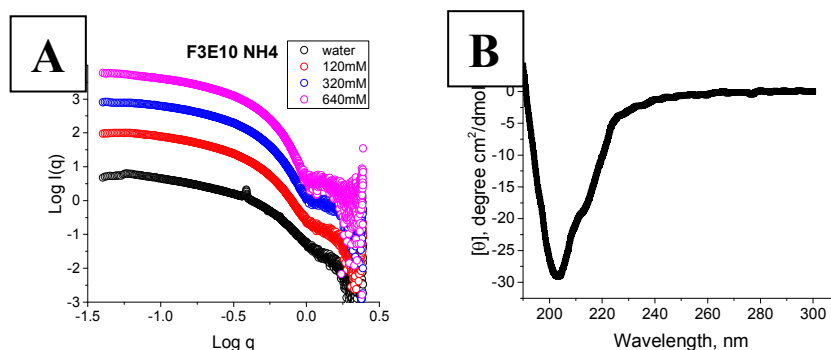


Figure 2.42. Continued.

For **F3E10-NH4**, the profiles displayed a similar appearance with slightly lower intensity in water (**Fig. 2.43A**); however, in all the cases, we observed a power law dependence of -1. Upon an increase in ionic strength, we also observed a transition with an isosbestic point around $q=1$ nm⁻¹ and the appearance of a second peak with a maximum at 1.41 nm⁻¹. Overall, the ammonium counterion strongly prompted the assembly. This may be due to the weakly acidic character of ammonium chloride; however, this is not the case, as **F3E10** also strongly assembled in pure water, which has a pH level of 8.0.

Figure 2.43. SAXS profiles (A) and CD spectrum (B) of **F3E10 NH4**.

The CD spectrum of **F3E10-NH4** displayed two minima at 213 nm and 203 nm (**Fig. 2.43B**); this represents the first direct observation of self-assembly obtained by CD for the polymer, suggesting the formation of very long fibers in solution.

Finally, we performed TEM studies of **F3E10 NH4** and observed the presence of very long fibers, reaching tens of micrometers in length with a diameter of around 5 nm (**Fig. 2.44**).

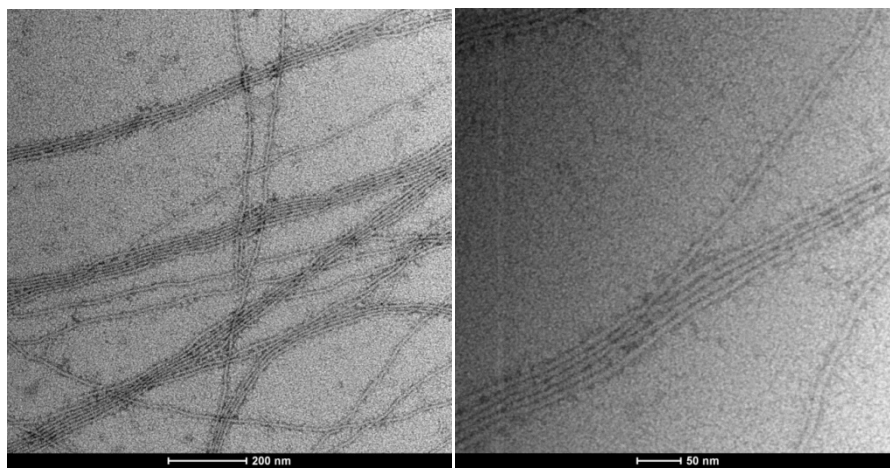


Figure 2.44. Representative TEM images of **F3E10 NH4** in water at 1 mg/ml.

Most of the fibers aggregated into bundles of a few to more than ten fibers that sometimes split apart and connected with other bundles. All fibers remained entirely separated and straight and never coalesced or twisted around each other. From TEM image analysis, we conclude that the ammonium ions participate in multivalent interactions with the PGA chains to stabilize the bundles. Of note, we failed to observe typical uranyl acetate artifacts, confirming that all the molecules assembled into fibers rather than remaining in solution.

2.9. Conclusion

We synthesized and studied stPGA families with oligophenylalanine cores and an increasing number of glutamic acid residues. We established that the correlation between the hydrophobicity of the core and the length of the polyglutamic chain has a critical role in determining self-assembly behavior - all compounds with a Phe:Glu ratio above 1:5 self-assembled into rods or fibers.

When we plotted Log CAC against the number of glutamic units per arm for **F2E₀₋₁₅** and **F3E₀₋₁₅** families, we observed that, in both cases, compounds with one glutamic unit per arm possessed a much lower CAC value than for the corresponding core (**Fig. 2.45**). This phenomenon occurs because the charged group becomes removed further away from the center of the core, and repulsive interactions diminish. For

compounds with 1-15 glutamic units per arm, we observed linear dependence of Log CAC on the number of Glu units, with a slightly lower slope in the case of a more hydrophobic core.

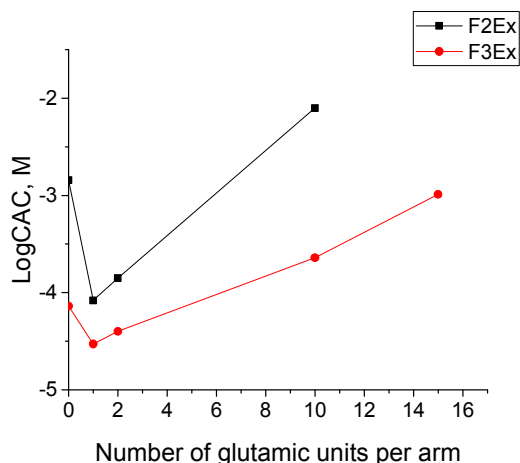


Figure 2.45. Dependence of Log CAC on the number of glutamic units per arm for **F2Ex** and **F3Ex** (x=0-15).

We report the first polyelectrolyte compound **F3E10**, whose self-assembly is directed by the supramolecular interactions of the core. Unlike previous reports, all functional groups were charged, and all compounds behaved as a classical polyelectrolyte in very diluted solutions, as shown by SAXS.

Through TEM and SAXS analyses, we also determined that the **F3E10** assembled into a helical fiber and not an expected 1D assembly; however, we could not differentiate between the presence of a single or a double helix.

2.10. Supplementary information

SI-2.1. Materials

SI-2.2. Experimental methods

SI-2.3. General procedure for the synthesis of peptides

SI-2.4. General procedure for the deprotection of Z-protected Peptides

SI-2.5. General procedure for the synthesis of the IC07-08 Cores

SI-2.6. General procedure for the synthesis of the F2 and F3

SI-2.7. General procedure for the synthesis of compounds $F_{2-3}E_1$

SI-2.8. General procedure for the polymerization

SI-2.1. Materials

All reagent grade chemicals were used without any purification. Doxorubicin hydrochloride salt was purchased from Xingcheng Chempharm Co. Ltd (Zhejiang, China). Anhydrous N,N-dimethylformamide (DMF, $\geq 99.8\%$ anhydrous), methanol (HPLC grade), tetrahydrofuran anhydrous (99.8%) was purchased from Scharlab SL (Sentmenat, Spain). Z-L-phenylalanine was purchased from Iris Biotech. NCA-Glu(OBz) was provided by PMC Isochem.

SI-2.2. Experimental Methods

Nuclear Magnetic Resonance Spectroscopy

NMR measurements were performed on Bruker 300 UltrashieldTM (Bruker, Billerica, United States) with a Bruker B-ACS 60 automation system. 2D experiments were performed with a Bruker 500 Ultrashield plus (Bruker, Billerica, United States) with Bruker sample case cooled automation system. All the measurements were performed at room temperature. The spectra were processed and analyzed using TopSpin software.

Circular Dichroism Spectroscopy

In order to measure the absorption of polarized light, the prepared solution was transferred in a quartz cuvette with a light path length of 1 cm or 0.1 mm and measured five times at room temperature with a J-1500 spectrometer (JASCO corporation, Easton, United States). A nitrogen flow of 2.7 L/min was led through the spectrometer.

Gel Permeation Chromatography

The GPC experiment was performed on a VISCOTEK GPCmax coupled to a VISCOTEK TDA302 detector system (Malvern, Malvern, England) - a dual LS detector (7 and 90°), viscosimeter, and RI detector. Experiment conditions: Column set: PW2500+3000+G (105/103/102 Å porosity), Flow: 0.8 ml/min, Solvent: 0.1% LiBr in DMF, Injection volume: 100 μ L. Temperature: 60°C. The GPC system was calibrated with well-defined poly(methyl methacrylate) (PMMA, 65kDa) standard, from Polymer Standards Service (PSS, Mainz Germany).

Fluorescent Spectroscopy

Fluorescence spectroscopy measurements were performed on an FP-6500 spectrofluorimeter (JASCO, Easton, United States) with an excitation wavelength of 550 nm and measured emission spectrum in a range from 575 to 740 nm. Polymer samples were dissolved in water or sodium chloride solution and, if not specified, otherwise allowed to equilibrate for 2 h. To 800 μ L of each solution, 1 μ L of 1 mg/ml NR solution in acetone was added.

Transmission Electron Microscopy

The TEM experiments were performed on the Transmission electron microscopy FEI Tecnai Spirit G2 with digital camera (Soft Image System, Morada, United States) and the image capture software (ITEMJ, Osaka, Japan). Samples were applied directly onto carbon film on 200 mesh copper grids. Excess of the sample was carefully removed by capillarity, and the grids were immediately stained with one drop of 0.1% phosphotungstic acid for 30s. Excess stain was removed by capillary action.

Cryo-TEM

Experiments were performed on Talos Arctica (ThermoFisher Scientific) operating at 200 kV at liquid nitrogen temperature. Images were recorded with a Falcon III Direct Detector Device in linear

mode with a pixel size of 1.42 Å/pixel at a nominal magnification of 73000X. Samples were vitrified on a Vitrobot (ThermoFisher Scientific) from a concentration of 1 mg/ml.

Dynamic Light Scattering

The DLS size measurements were performed on a Malvern Zetasizer nanoseries, nano ZS, ZEN3500 (Malvern Instruments, Malvern, UK). Samples of polymers were prepared in water at concentrations of 1 mg/ml and 10 mg/ml.

Small-Angle Neutron Scattering

Small-angle neutron scattering (SANS) measurements were performed on a SANS2D instrument at the ISIS spallation source (Rutherford Appleton Laboratory, Oxfordshire, UK). The observed q range was $2 \times 10^{-2} \text{ nm}^{-1} \leq q \leq 4.9 \text{ nm}^{-1}$. All scattering data were normalized for the sample transmission, empty cell, and solvent background.

Small-Angle X-Ray Scattering

The SAXS measurements were performed at the BL11 beamline of the Alba synchrotron in Barcelona, Spain. The observed q range was $4.24 \times 10^{-3} \text{ Å}^{-1} \leq q \leq 3.52 \text{ Å}^{-1}$, where q is the magnitude of the scattering vector $q = (4\pi/\lambda)\sin(\theta/2)$. If not specified otherwise, measurements were performed in Hilgenberg Mark-tubes made of glass N50 packed with green perforated plastic disk (length 80 mm, outer diameter 1.5mm, wall thickness 0.01 mm). All the solutions allowed to equilibrate 24h prior to measurement. Experiments were performed with the use of in-house cells and cell holders. Analysis and fitting were performed with ATSAS and Scatter software packages.

The radius of the gyration R_g can be calculated by plotting intensity $\text{Log } I(q)$ as a function of the square of scattering vector q , the so-called Guinier plot. The part of the graph at very low values of q is linear. Equation 3.1 describes the linear dependence from which R_g can be determined.

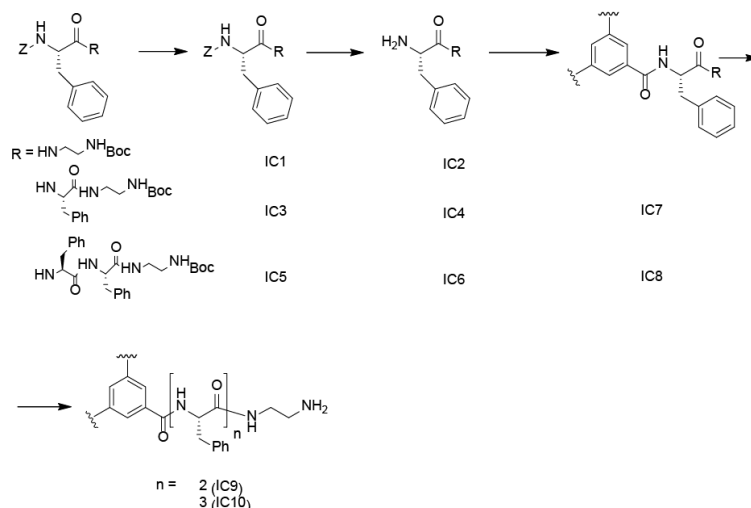
$$\text{Log}(I(q)) = \text{Log}(I(q)_0) - \frac{q^2 R_g^2}{3}$$

For the rod-like particles and fibers, a variation of the Guinier plot is used, which allows us to determine the radius of gyration of cross-section of the rod/fiber. The radius of cross-section can be determined by plotting $\text{Log}(qI(q))$ as a function of q . The intermediate part of this graph is linear, where the mathematic description is represented in equation. From this, the radius of gyration of cross-section R_c can be determined.

$$\text{Log}(I(q) \times q) = \text{Log}(I(q)_0 \times q) - \frac{q^2 R_c^2}{2}$$

R_g and R_c values correlate with the total length of the fibers L with relation 3.3, from which the length can be calculated

$$R_g^2 = R_c^2 + \frac{L^2}{12}$$

SI-2.3. General Procedure for The Synthesis of Peptides**Figure SI-2.1.** General scheme of the synthesis of BTA-based oligophenylalllanines.

In a round bottom flask with a stirrer, Z-L-Phenylalanine (4.48 g, 15 mmol), and DMTMM(Cl) (4.55 g, 0.165 mmol) were dissolved in 150 mL of methanol. The solution was stirred for 10 minutes, and the corresponding amine (0.165 mmol) in 10 ml of methanol was added dropwise. The reaction was allowed to proceed overnight. A white precipitate was filtered off and washed with methanol (3x50 ml) and the precipitate was dried under a vacuum. Yield = 90-95%.

IC-1: Product - white powder. Global yield: 12.7 g (92%). ¹H-NMR (300 MHz, DMSO-d₆): δ 1.37(s, 9H), 7.1-7.37(m, 10H), 2.68-3.21(m, 6H), 7.45(d, 1H), 4.17(m, 1H), 8.03(t, 1H), 4.94(s, 2H), 6.72(t, 1H).

IC-3: Product - white powder. Global yield: 8.14 g (94%). ¹H-NMR (300 MHz, DMSO-d₆): δ 1.36(s, 9H), 2.56-3.15(m, 8H), 4.23(h, 1H), 4.45(q, 1H), 4.94(s, 2H), 6.96(t, 1H), 7.14-7.36(m, 15H), 7.44(d, 1H), 7.94(t, 1H), 8.08(d, 1H).

IC-5: Product - white powder. Global yield: 5.8 g (91%). ¹H-NMR (300 MHz, DMSO-d₆): δ 1.37(s, 9H), 2.60-3.10(m, 10H), 4.22(dt, 1H), 4.44(dt, 1H), 4.53(dt, 1H), 4.92(s, 2H), 6.68(t, 1H), 7.10-7.36(m, 20H), 7.43(d, 1H), 7.86(t, 1H), 8.03(d, 1H), 8.17(d, 1H).

SI-2.4. General Procedure for the Deprotection of Z-protected Peptides

In a round bottom flask with a stirrer and nitrogen inlet and outlet, compound **01**, 10% (w/w) of Pd/C, and 250 mL methanol were added. The solution was purged with nitrogen for 10 min, followed by three vacuum/nitrogen cycles. A balloon with hydrogen was connected to the system, and the suspension was stirred for 6h. The mixture was filtered with celite. The obtained filtrate was concentrated in a vacuum. Yield = 85-92%.

IC-2: Product - white powder. Global yield: 8.67 g (87%). ¹H-NMR (300 MHz, DMSO-d₆): δ 1.37(s, 9H), 6.74(t, 1H), 2.86-3.12 (m, 5H), 7.04-7.39(m, 5H), 3.36(m, 1H), 7.87(t, 1H).

IC-4: Product - white powder. Global yield: 6.3 g (86%). ¹H-NMR (300 MHz, DMSO-d₆): δ 1.37(s, 9H), 2.71-3.22 (m, 8H), 4.47(q, 1H), 6.72(t, 1H), 7.09-7.29(m, 10H), 7.96(t, 1H), 8.03(d, 1H).

IC-6: Product - white powder. Global yield: 3.1 g (90%). ¹H-NMR (300 MHz, DMSO-d₆): δ 1.37(s, 9H), 2.45(dd, 1H), 2.70-3.17 (m, 9H), 3.34(dd, 1H), 4.43(dt, 1H), 4.54(m, 1H), 6.70(t, 1H), 7.03-7.29(m, 15H), 7.90-8.10(m, 2H), 8.25(d, 1H).

SI-2.5. General Procedure for the Synthesis of IC07-08 Cores

In a round-bottom flask with a stirrer, trimesic acid (174mg, 0.832 mmol) and DMTMM Cl (920 mg, 3.33 mmol) were dissolved in 30 ml of methanol. 3.32 mmol of the corresponding amine in 5 ml of methanol was added, and the mixture was stirred for 48h. The precipitate was filtered, washed with methanol, and dried.

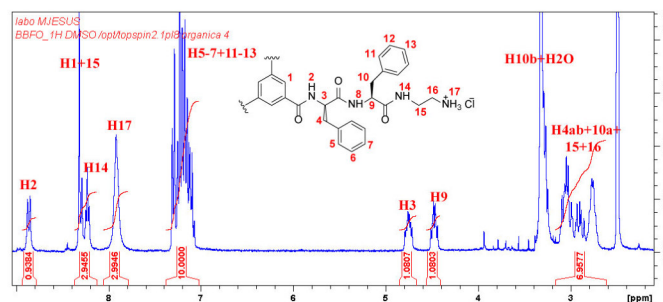
IC7. Product - white powder. Global yield: 1.24 g (79%). ¹H-NMR (300 MHz, DMSO- d₆): δ 1.37(s, 9H), 2.69-3.14 (m, 7H), 3.28 (dd, 1H), 4.48 (ddd, 1H), 4.76 (ddd, 1H), 7.06-7.34 (m, 10H), 8.23 (t, 1H), 8.29 (t, 1H), 8.31 (s, 1H), 8.86 (d, 1H).

IC8. Product - white powder. Global yield: 3.78 g (87%). ¹H-NMR (300 MHz, DMSO-d₆): δ 1.36 (s, 9H), 2.70-3.17 (m, 10H), 4.45 (dt, 1H), 4.57 (dt, 1H), 4.75 (ddd, 1H), 6.68 (t, 1H), 6.98-7.33 (m, 15H), 7.88 (t, 1H), 8.57 (d, 1H), 8.18 (s, 1H), 8.67 (d, 1H).

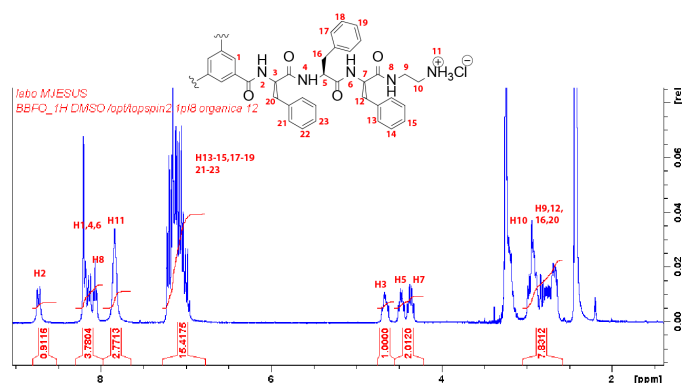
SI-2.6. General Procedure for the Synthesis of F2 and F3

In a round-bottom flask with a stirrer, 1g of compound 07 or 08 was suspended in 10 ml of methanol. 10 ml of 4M hydrogen chloride in dioxane was added, and the solution allowed to react for 4 h. Reaction completion was monitored by NMR. The mixture was precipitated in diethyl ether (100 ml), washed with the same solvent (2x200 ml), and dried in air. The compound was dissolved in water, 2M NaOH was added till pH 9.0, and the mixture was stirred for 30 min. The precipitate was filtered, washed with water until pH 5.5-6.0, and freeze-dried.

IC9. Product - white powder. Global yield: 3.71 g (90%). ¹H-NMR (300 MHz, DMSO-d₆): 2.47 (dd, 1H), 2.8-3.1 (m, 7H), 4.49 (ddd, 1H), 4.74 (ddd, 1H), 7.08-7.31 (m, 10H), 7.81 (t, 1H), 8.2 (t, 1H), 8.23 (s, 1H), 8.77 (d, 1H).



IC10. Product - white powder. Global yield: 2.11 g (97%). ¹H-NMR (300 MHz, DMSO-d₆): 2.68-3.08 (m, 8H), 3.18-3.33 (m, 2H), 4.44 (ddd, 1H), 4.56 (ddd, 1H), 4.76 (ddd, 1H), 7.00-7.33 (m, 15H), 7.77 (br.t., 3H), 8.15-8.33 (m, 3H).



SI-2.7. General Procedure for The Synthesis of Compounds F2-3E1

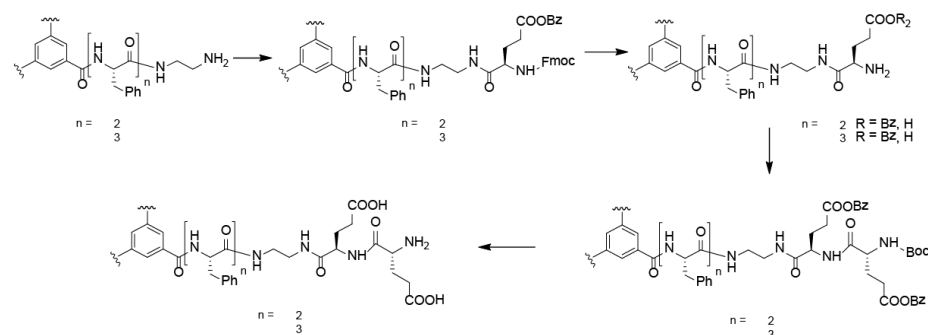


Figure SI-2.2. General scheme of the synthesis of FxEy.

In a round bottom flask with a stirrer, Z-L-(t-Bu)-Glu-OH (3.9 eq.), and DMTMM chloride (4.7 eq.) were dissolved in methanol, and the solution was allowed to stir for 10 min. **F2** or **F3** (1 eq.) was dissolved in methanol, TEA added (3.9 eq.), and the mixture allowed to stir for 10 min. Both solutions were combined, and the reaction was left to proceed for 48 h. The precipitate was filtered, washed with methanol and water and dried.

IC11. Product - white powder. Global yield: 560 mg (85%). ¹H-NMR (DMSO-d₆, 300 MHz): 1.36 (s, 9H), 1.68-1.98 (m, 2H), 2.22 (t, 2H), 2.77-3.22 (m, 8H), 3.95 (dt, 1H), 4.48 (dt, 1H), 4.80 (ddd, 1H), 5.01 (s, 2H), 7.03-7.44 (m, 15H), 7.87-8.02 (m, 2H), 8.12-8.30 (m, 2H), 8.67 (d, 1H).

IC12. Product - white powder. Global yield: 780 mg (89%). ¹H-NMR (DMSO-d₆, 300 MHz): 1.36 (s, 9H), 1.67-2.00 (m, 2H), 2.36 (t, 2H), 2.70-3.20 (m, 10H), 3.90 (dt, 1H), 4.45 (dt, 1H), 4.58 (ddd, 1H), 4.76 (ddd, 1H), 5.06 (s, 2H), 6.87 (d, 1H), 6.98-7.41 (m, 20H), 7.78-7.94 (m, 2H), 8.10-8.25 (m, 3H), 8.66 (d, 1H).

In a round-bottom flask with a stirrer, **IC11** or **IC12** was dissolved in TFA (final concentration 100 mg/ml), and the reaction allowed to proceed for 1 h. HBr (48%, aqueous solution, 3.3 eq.) was added, and the reaction was allowed to proceed for another 3 h. The solution was precipitated in diethyl ether, washed with diethyl ether till neutral pH, and then dried.

F2E1. Product - white powder. Global yield: 415 mg (98%). ¹H-NMR (300 MHz, DMSO-d₆): 1.96 (dt, 2H), 2.33 (t, 2H), 2.76-3.26 (m, 8H), 3.75 (dt, 1H), 4.48 (dt, 1H), 4.79 (ddd, 1H), 7.01-7.33 (m, 10H), 8.03 (t, 1H), 8.13 (br.s, 3H), 8.19-8.27 (m, 2H), 8.48 (t, 1H), 8.68 (d, 1H).

F3E1. Product - white powder. Global yield: 622 mg (99%). ¹H-NMR (300 MHz, DMSO-d₆): 1.88 (m, 2H), 2.17-2.30 (m, 2H), 2.62-3.13 (m, 10H), 3.65 (dt, 1H), 4.38 (dt, 1H), 4.49 (dt, 1H), 4.68 (dt, 1H), 6.90-7.27 (m, 15H), 7.90 (t, 1H), 7.98-8.19 (m, 5H), 8.39 (t, 1H), 8.59 (d, 1H).

SI-2.8. General Procedure for Polymerization

NCA-Glu-OBz (3g, 11.5 mmol) was transferred into a Schlenk tube fitted with a stirrer and a stopper. The tube was purged with three vacuum/nitrogen cycles, and 6 ml of anhydrous DMF was added. Initiator (0.383 mmol, 0.255 mmol or 0.153 mmol) was added, and the mixture was left stirring for three days under an inert atmosphere. 6 ml of THF was then added, and the mixture was precipitated in cold diethyl ether (100 ml), filtered, and washed with the same solvent (2x100 ml).

The corresponding protected stPGA was transferred to a round-bottom flask and dissolved in 25 ml of TFA. 48% HBr (2.5 ml) was added, and the mixture allowed to react overnight. The mixture was precipitated in diethyl ether (200 ml) filtered and washed with the same solvent (2x200 ml). The polymer was further purified by acidification of corresponding basic solution (pH 9) with 6M HCl followed by washing with water, second basification with saturated sodium bicarbonate solution, and further lyophilization.

For the preparation of other polyelectrolytes, the initiator was dissolved in 2 ml of anhydrous DMSO and purged with nitrogen. NCA-Lys*TFA, NCA-(Z)Orn, or NCA-Asp-OBz was placed in a Schlenk tube equipped with a stirrer under nitrogen and purged with three vacuum/nitrogen cycles. The monomer was dissolved in 2 ml of anhydrous DMSO. Afterward, the initiator solution was added to the monomer. The reaction was allowed to proceed overnight under vacuum. THF (5 ml) was then added to the solution. The polymer was precipitated in diethyl ether, filtered, and washed with diethyl ether (3x20 ml). The compound was then dried in air.

Deprotection of poly(benzyl aspartate) was performed using TFA/HBr in the following ratio: 1 g of the polymer, 10 ml of TFA, and 1 ml of 48% HBr. In a round bottom flask with a stirrer, the polymer was dissolved in TFA, and 48% HBr was added dropwise. The reaction was allowed to proceed overnight. The solution was then precipitated in diethyl ether. The precipitate was filtered and washed with diethyl ether (3x20 ml). After drying in air, the polymer was redissolved in 0.5 M NaHCO₃ and purified with a Float-A-Lyzer G2 dialysis device (Spectrum Laboratories, Compton, United States).

Deprotection of poly(lysine-trifluoroacetate) was performed using 2 eq. potassium carbonate in a mixture of water/methanol overnight. The reaction was quenched with 2M HBr, and the product was dialyzed and lyophilized.

Deprotection of poly(Z-ornithine) was performed in CHCl₃ (33 mg/mL), with 6 eq of HBr in acetic acid at 33% wt. The compound was precipitated in diethyl ether, dried, dialyzed, and lyophilized.

F0E10. ¹H-NMR (300 MHz, D₂O): 1.68-2.27 (m, 168H), 3.42 (m, 12H), 4.18 (m, 40H), 8.15 (br. s, 3H).

F2E10. ¹H-NMR (300 MHz, D₂O): 1.54-2.22 (m, 141H), 2.66-3.31 (m, 38H), 4.19 (m, 34H), 6.64-7.39 (m, 45H), 7.76 (br. s, 3H).

F2E25. ¹H-NMR (300 MHz, D₂O): 1.51-2.25 (m, 350H), 2.66-3.31 (m, 24H), 4.19 (m, 85H), 6.64-7.39 (m, 30H), 7.76 (br. s, 3H).

F3E10. ¹H-NMR (300 MHz, D₂O): 1.69-2.38 (m, 130H), 2.66-3.31 (m, 30H), 4.19 (m, 31H), 6.64-7.39 (m, 45H), 7.76 (br. s, 3H).

F3E15. ¹H-NMR (300 MHz, D₂O): 1.57-2.24 (m, 204H), 2.66-3.31 (m, 30H), 4.19 (m, 47H), 6.64-7.39 (m, 45H), 7.76 (br. s, 3H).

F3D10. ¹H-NMR (300 MHz, D₂O): 2.51 (m, 58H), 2.66-3.31 (m, 30H), 4.49 (m, 28H), 6.64-7.39 (m, 45H), 7.76 (br. s, 3H).

F3Orn10. ¹H-NMR (300 MHz, D₂O): 1.69-2.38 (m, 135H), 2.66-3.31 (m, 96H), 4.25 (m, 34H), 6.64-7.39 (m, 45H), 7.76 (br. s, 3H).

F3K10. ¹H-NMR (300 MHz, D₂O): 1.15-1.46 (m, 63H), 1.48-1.94 (m, 120H), 2.72-3.23 (m, 92H), 4.10-4.34 (m, 31H), 6.64-7.39 (m, 45H), 7.76 (br. s, 3H).

2.11. References

- Philp, D. and Stoddart, J. F. *Angew. Chemie Int. Ed.*, **35**, 1154–1196 (1996).
- Feng, H. *et al. Polymers*, **9**, (2017).
- Tritschler, U. *et al. Macromolecules* **50**, 3439–3463 (2017).
- Mendes, A. C., Baran, E. T., Reis, R. L. and Azevedo, H. S. *WIREs Nanomed. Nanobiotech.*, **5**, 582–612 (2013).
- Atkinson, S. P., Andreu, Z. and Vicent, M. J. *J. Pers. Med.*, **8**, E6 (2018).
- Deng, C., *et al. Prog. Polym. Sci.* **39**, 330–364 (2014).
- Gonz, C. M. and Sarabia-Vallejos, M. A. *Polymers*, **8**, 551 (2017).
- Zagorodko, O., Arroyo-Crespo, J. J., Nebot, V. J. and Vicent, M. J. *Macromol. Biosci.*, **17**, 1600316 (2016).
- Arroyo-Crespo, J. J. *et al. Biomaterials* **186**, 8–21 (2018).
- Apfelthaler, C., Anzengruber, M., Gabor, F. and Wirth, M. *Eur. J. Pharm. Biopharm.*, **115**, 131–139 (2017).
- Zhao, Y. *et al. Sci. Rep.*, **7**, 1–11 (2017).
- van Pomeroy, M. *et al. Nanotoxicology*, **13**, 558–571 (2019).
- Babin, J., Taton, D., Brinkmann, M. and Lecommandoux, S. *Macromolecules* **41**, 1384–1392 (2008).
- Agut, W. *et al. Langmuir* **26**, 10546–10554 (2010).
- Ahmad, Z. *et al. J. Biomater. Sci. Polym. Ed.*, **27**, 40–54 (2016).
- Armstrong, G. and Buggy, M. *J. Mat. Sci.*, **40**, 547–559 (2005).
- Greef, T. F. A. De *et al. Chem. Rev.*, 5687–5754 (2009).
- Krieg, E., Bastings, M. M. C., Besenius, P. and Rybtchinski, B. *Chem. Rev.*, **116**, 2414–2477 (2016).
- Cantekin, S., Greef, F. A. De and Palmans, A. R. A. *Chem. Soc. Rev.*, **41**, 6125–6137 (2012).
- Smulders, M. M. J., Schenning, A. P. H. J. and Meijer, E. W. *JACS*, **130**, 606–611 (2008).
- Kemper, B. *et al. JACS*, **140**, 534–537 (2017).
- Besenius, P. *et al. PNAS*, **107**, 17888–17893 (2010).
- Matsunaga Y, Miyajima N, Nakayasu Y, Sakai S, Y. M. *Bull. Chem. Soc. Jpn.*, 207–210 (1988).
- Fitié, C. F. C. *et al. Chem. Mater.*, 2394–2404 (2008).
- Fitié, C. F. C. *et al. J. Phys. Chem.*, **8**, 3928–3937 (2012).
- Fitié, C. F. C., Roelofs, W. S. C., Kemerink, M. and Sijbesma, R. P. *JACS* **132**, 6892–6893 (2010).
- Abraham, F. and Schmidt, H. *Polymer*, **51**, 913–921 (2010).
- Nakajima, H., Takahashi, M. and Kimura, Y. *Macromol. Mater. Eng.*, **295**, 460–468 (2010).
- Leenders, C. M. A. *et al. Chem. Commun.*, **49**, 1963–1965 (2013).

30. Bakker, M. H. et al. *ACS Nano*, **10**, 1845–1852 (2016).
31. Srinivasulu, G. et al. *J. Mol. Struct.*, **1006**, 180–184 (2011).
32. Loos, M. et al. *Tetrahedron*, **63**, 7285–7301 (2007).
33. Besenius, P. et al. *Contrast Media Mol. Imaging*, **7**, 356–361 (2012).
34. Holm, R. et al. *Biomacromolecules*, **20**, 375–388 (2019).
35. Ahlers, P. et al. *Macromol. Biosci.*, **17**, 1–7 (2017).
36. Duro-Castano, A. et al. *Mol. Pharm.*, **12**, 3639–3649 (2015).
37. Appel, R., Tacke, S., Klingauf, J. and Besenius, P. *Org. Biomol. Chem.*, **13**, 1030–1039 (2015).
38. Stergiou, N. et al. *ChemBioChem*, **19**, 912–916 (2018).
39. Kunishima, M. et al. *Tetrahedron*, **55**, 13159–13170 (1999).
40. Greene's Protective Groups In Organic Synthesis. (Wiley-Interscience, 2007).
41. Kurniasih, I. N. et al. *Langmuir*, **31**, 2639–2648 (2015).
42. Hayter, J. B. and Penfold, J. *Mol. Phys.*, **42**, 109–118 (1981).
43. Rex, P. H. J. *J. Appl. Cryst.*, (1985). **18**, 452–460 (1985).
44. F. Cavelier and Enjalbal, C. *Tetrahedron Lett.*, **37**, 5131–5134 (1996).
45. F. S. Gibson, S. C., Bergmeier, H. C. and Rapoport, H. *J. Org. Chem.*, **59**, 3216–3218 (1994).
46. Li, B. et al. *Tetrahedron Lett.*, **44**, 8113–8115 (2003).
47. Pincus, P. and Velasco, R. M. *J. Phys.*, **95**, 4506 (1976).
48. Ben, S., Essafi, W., Abidelli, A. and Rawiso, M. Q. *Arab. J. Chem.*, **10**, 1001–1014 (2017).
49. Dobrynin, A. V., Colby, R. H., Rubinstein, M. and York, N. *Macromolecules*, **28**, 1859–1871 (1996).
50. Burian, M. and Amenitsch, H. *IUCrJ*, **5**, 390–401 (2018).

Chapter 3

Role of aminoacid nature and order on the aqueous self-assembly of BTA-derivatives and corresponding polymers

3.1. Introduction

An intricate hierarchical system of non-covalent bond interactions regulates the self-assembly of natural molecules. Subtle changes to the molecular architecture may result in structural reinforcement or, in extreme cases, the complete disruption of the assembly due to secondary interactions even when primary interactions remain unmodified. With regards to BTA-based materials, many studies have evaluated various BTA substituent designs in the hope of tuning the properties of the final material.

Meijer et al. prepared a series of BTA-conjugates with dipeptides from L- or/and D-phenylalanine and glycine to study the role of amino acid sequence on secondary interactions.¹ Their studies in chloroform and heptane established the greater stability of BTA assemblies with a homochiral FF sequence compared to a heterochiral FF, with GF sequences and FG dipeptides displaying sequentially weaker assembling capabilities.

The Besenius group studies variations to the amino acid sequence in BTA-oligopeptides, finding that the incorporation of lysine and glutamate residues between phenylalanine sequences (i.e., BTA-FEFEF and BTA-FLFLF) permitted the preparation of pH-sensitive supramolecular copolymers.² Histidine insertions (BTA-FHFHF) also displayed pH-responsiveness, leading to their proposed application in siRNA delivery.³ Another study achieved responsiveness to ROS via the addition of methionine residues

(BTA-FMHHM); methionine residues oxidize in the presence of ROS to form charged sulfoxides.⁴ Interestingly, the incorporation of both glutamic acid and methionine (BTA-FEMEM) resulted in a double pH and redox responsive compound.⁵

In Chapter 2, we demonstrated that star-PGAs self-assemble in a different manner, which depends on the structure of the oligophenylalanine core. We hypothesized that we could decrease the CAC value of the core and the corresponding polymer by variation of the amino acid sequence, thereby providing access to supramolecular nanorods with enhanced stability.

Here, we evaluated the influence of amino acid sequence on the self-assembly of di-, tri- and tetra-peptide modified BTAs. Furthermore, we selected compounds with the most robust self-assembling properties as initiators for the synthesis of star-PGAs and assessed their self-assembly characteristics.

3.2. Synthesis and Self-assembly of Dipeptide Derivatives of BTA

In Chapter 2, we described the synthesis and properties of short star-PGAs based on hexa- and nona-phenylalanine derivatives of BTA and we used these compounds as a reference for all new compounds and polymers synthesized. First, we investigated dipeptide derivatives of BTA to determine if amino acid hydrophobicity influences self-assembly. We prepared three compounds based on BTA derivatives of diphenylalanine (**FF**), ditryptophane (**WW**), and dipentafluorophenylalanine (**ΦΦ** – see below for more information) (**Fig. 3.1**).

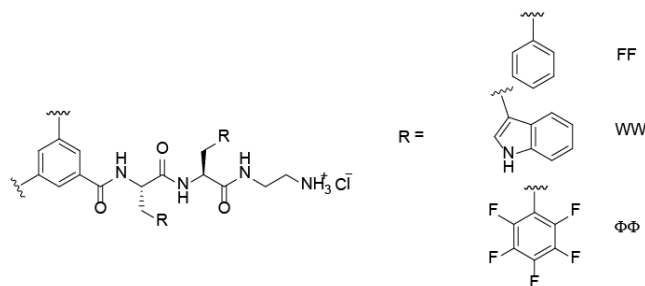


Figure 3.1. Structure of BTA-dipeptide Derivatives.

First, we prepared Z-L-pentafluorophenylalanine using the asymmetric alkylation of the glycine imine derivative. We prepared the catalyst for asymmetric alkylation in three steps according to a previously reported procedure, as shown in **Fig. 3.2**.⁶ We prepared Z-L-pentafluorophenylalanine in three steps, as shown in **Fig. 3.3**. In the first step, we prepared an imine derivative from glycine ethyl ester and benzophenoneimine at high to excellent yield.

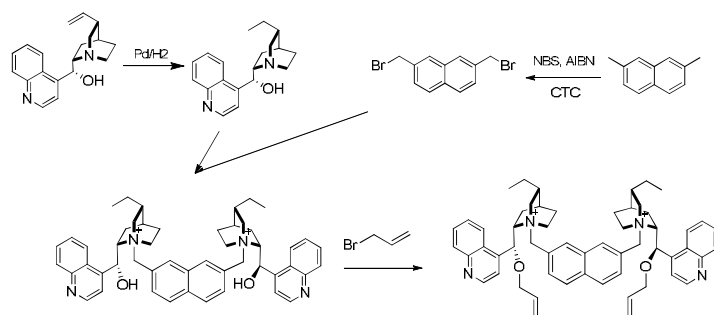


Figure 3.2. Scheme of synthesis of the catalyst for asymmetric alkylation.

We then alkylated bromopentafluorophenylalanine using a triple excess of chiral catalysts in comparison with the amount recommended in the study that originally described the protocol.⁶ Finally, we removed ethyl ester and benzophenone moieties by refluxing in 6M hydrochloric acid for five hours.

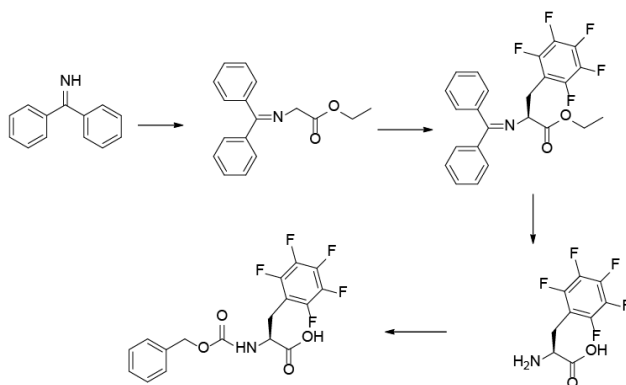


Figure 3.3. Synthetic Scheme of Pentafluorophenylalanine.

We tested the enantiomeric purity of L-pentafluorophenylalanine via polarimetry. Given the unreliability of the optical rotation of 5F-Phe hydrochloride, we prepared N-Fmoc-5F-Phe, which possesses a reported optical rotation equal to $-20.5 \pm 1.0^\circ$ in methanol. Polarimetry of N-Fmoc-5FPhe demonstrated an optical rotation of -19.6° , confirming an enantiomeric excess (ee) of above 95%. We used TLC and NMR for proof of compound purity, as melting temperatures for this compound have yet to be reported. Finally, we prepared Z-5F-Phe using a classical Z-OSu approach with a 96% yield.⁷ 5F-Phe, a non-natural amino acid, does not possess a specific one-letter code. For simplicity, we assigned the Greek letter Φ to this residue.

We prepared compounds **ΦΦ** and **WW** in comparable manner to that described for compound **FF**. However, we observed two complications in the synthesis of compound **ΦΦ**. First, we found that it was impossible to separate **Z-ΦΦ** from the starting material on normal-phase silica (independent of the solvent composition) due to strong non-specific interaction between fluorinated rings. As a solution, we separated compounds in the form of amines after Z-group deprotection. Second, we observed that Pd-catalyzed hydrogenolysis of **Z-ΦΦ** resulted in a parallel reaction of non-specific fluorine substitution with hydrogen in the aromatic ring (Fig. 3.4). We found it impossible to separate singly substituted compounds separate with column chromatography; however, we determined that decreasing the deprotection reaction time from 4-6 to 1-2 hours and adding 10% water to the reaction mixture completely suppressed the side reaction.

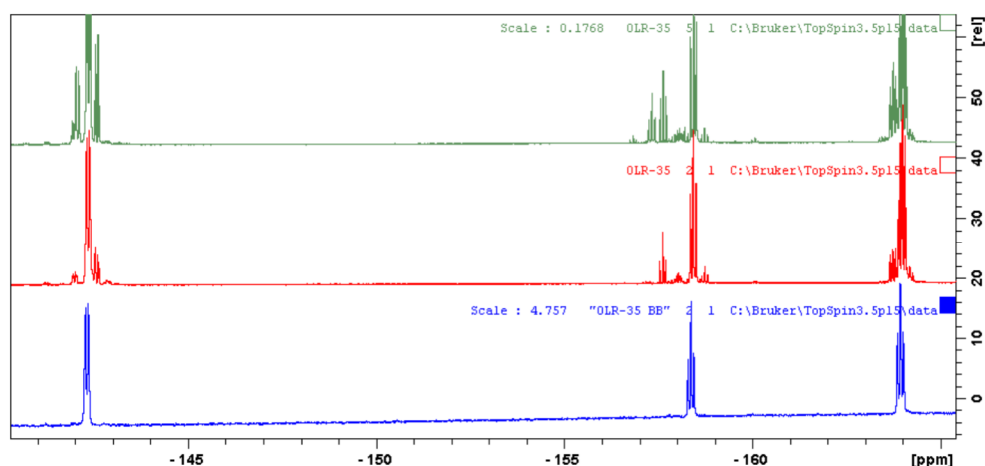


Figure 3.4. ^{19}F -NMR spectra of H- Φ -EDA after 6-hour (green), 2-hour (red), and modified (blue) deprotection procedures.

We performed fluorescent spectroscopy tests with Nile Red (NR) dye and determined CAC values for each compound, as shown in the table (Fig. 3.5). The fluorimetry study of **ΦΦ** (0.125 mM) showed an almost 9-times decrease in the CAC value in relation to the non-fluorinated **FF** (1.11 mM). **WW** displayed a slightly lower CAC than **FF** (1.0 mM). We also found a lack of similarity in the hypsochromic shift and intensity change of NR for the compounds. For **FF** and **ΦΦ**, we found a shift equal to 630 nm with intensity increasing in proportion to concentration. For **WW**, we observed a shift to 605-610 nm, and the intensity increase did not reach a significant level even at a high concentration close to the gelation point. Such a strong shift occurs due to the formation of highly hydrophobic microdomains and/or aromatic interaction with the core.^{8,9} Such strong blue shifts result in partial self-quenching of NR, and so, we only used the peak shift to determine CAC values.

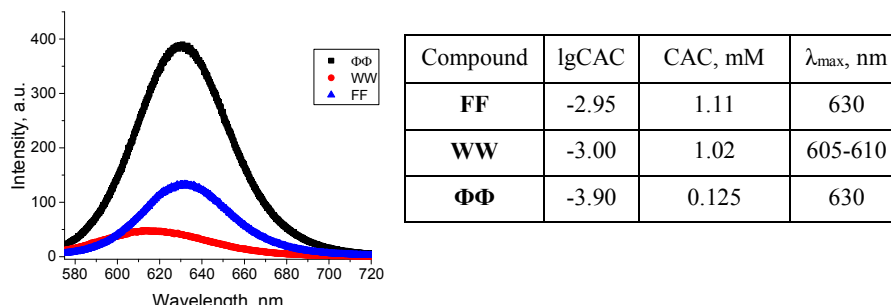


Figure 3.5. Representative NR spectra in 0.25 mM $\Phi\Phi$, 1.5 mM FF, and 1.5 mM WW. Table with CAC values and NR peak maximum wavelength for compounds

TEM with phosphotungstic acid staining demonstrated that both **FF** and **WW** (**Fig 3.6 A and B**) formed long flexible fibers and dense gels at higher concentrations. Morphologically, **FF** formed straight fibers with a uniform thickness of 8.2 ± 1 nm, as discussed in Chapter 2. **WW** fibers had a varying thickness of 11 ± 4 nm, with some of the thin fibers helically twisted. Cryo-TEM analysis of the compound confirmed the formation of fibers with varied thicknesses and an average length of 100-200 nm (**Fig 3.6 C**).

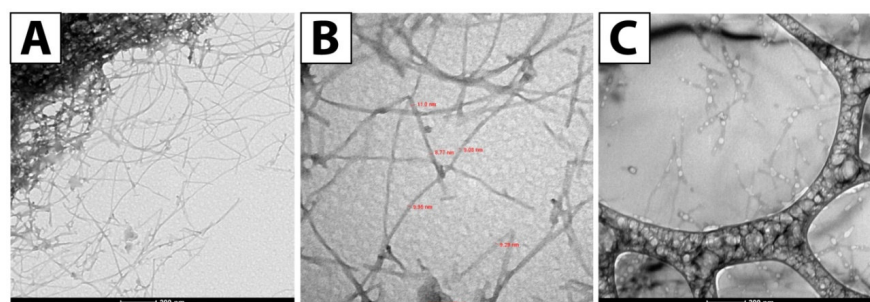


Figure 3.6. TEM images (**A and B**) of 2.0 mM WW in water and cryo-TEM images (**C**) of 1.1 mM of WW in water.

$\Phi\Phi$ in water formed short but rather thick rods (11.1 ± 0.7 nm) with variable length (**Fig 3.7 A,B**). In the presence of 120 mM salt, $\Phi\Phi$ formed a distinct type of fiber - aggregates of 9.1 ± 0.6 nm thick and 50-200 nm long displaying a defined helicity with full twist length of around 50 nm (**Fig 3.7 C-E**).

Of particular interest, the thickness of the generated fibers far exceeded the theoretically calculated diameter of the molecules in all cases - fully stretched, each molecule has a diameter of approximately 3 nm. This observation suggests that BTA-self-assembly might occur via a mechanism other than simple one-dimensional (1D) stacking. While defining the exact mechanism with this data remains difficult, we can consider two possibilities - thin fibers interact with each other forming bundles, or hexapeptides form more complicated seed structures that further assemble into 1D fibers.

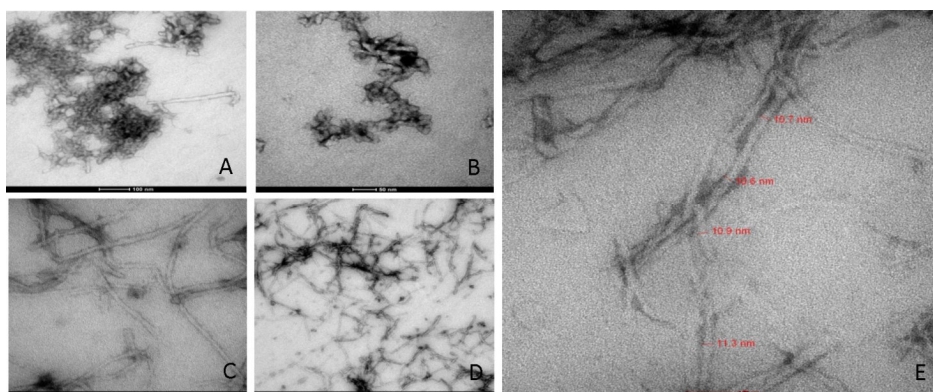


Figure 3.7. TEM images of $\Phi\Phi$ in water (A, B) and 120 mM NaCl (C-E).

In general, comparative SAXS studies in water and 20 mM NaCl of 1.2 mM, 1.2mM, and 0.25 mM solutions of **FF**, **WW**, and $\Phi\Phi$, respectively, confirmed the data obtained by TEM and fluorimetry (**Fig 3.8**). All curves in the intermediate q -range could be described by a -1 power law, confirming the presence of long cylindrical particles.

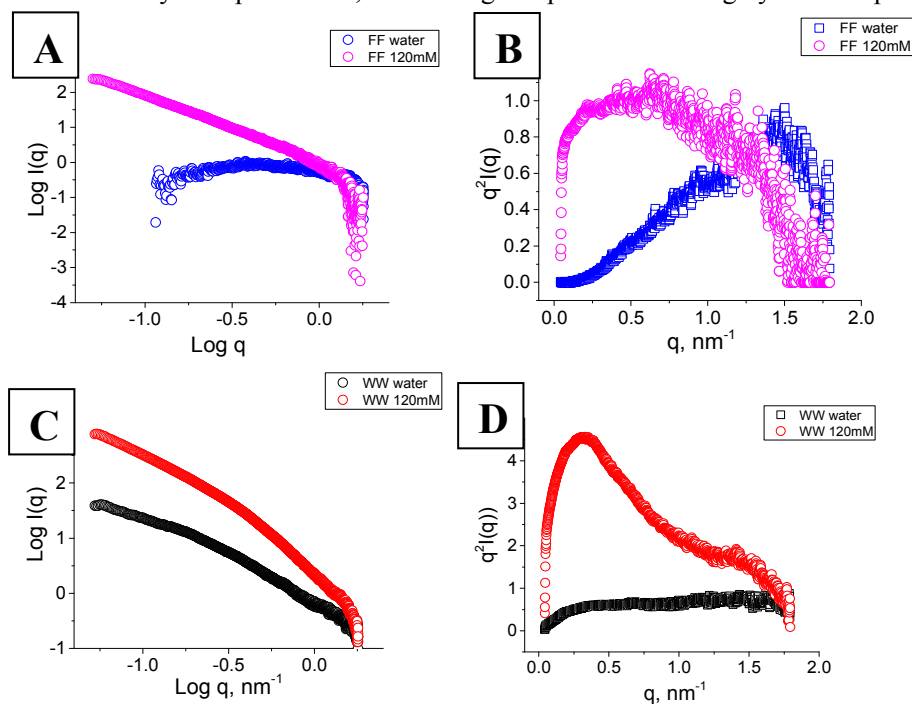


Figure 3.8. SAXS profiles and corresponding Kratky plots of **FF** (A, B), **WW** (C, D), and $\Phi\Phi$ (E, F) in water and 120 mM NaCl.

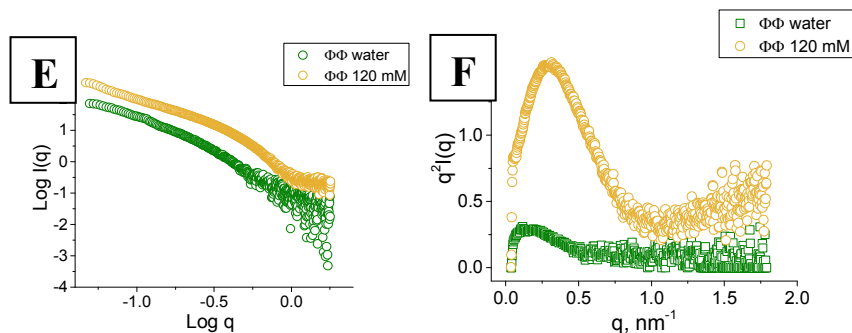


Figure 3.8 (continued).

From each scattering curve, we extracted the radius of gyration of the particle and of cross-section (**Table 3.1**). Overall, the radius of gyration of cross-section after the addition of salt decreased for **ΦΦ**, increased slightly for **WW**, and remained unchanged for **FF**, suggesting that each compound assembles in a similar but distinct manner.

$P(r)$ functions for **WW** have an appearance typical for rod-like particles with a varied rod diameter given the unclear identification of the first peak (**Fig. 3.9**). The corresponding function for **ΦΦ** has a defined peak at around 5 nm, corresponding to the fixed diameter of the rod and D_{\max} of 120 nm. The oscillations on the curve with a distance between the peak maxima of around 50 nm correspond to twisted fibers with the distance of the full 360-degree twist of 50 nm.

Table 3.1. Radii of gyration and cross-section calculated from SAXS data

| Compound | C salt, mM | R_g , nm | R_c , nm |
|-----------|------------|------------|------------|
| FF | 0 | 3.0 | - |
| FF | 20 | 25.2 | 4.28 |
| WW | 0 | 17.7 | 3.39 |
| WW | 20 | 22.1 | 3.94 |
| ΦΦ | 0 | 20.8 | 5.16 |
| ΦΦ | 20 | 28.5 | 3.61 |

Of note, it remains unclear whether the twist arises from a single helical fiber or from several straight fibers twisting around one another. From the fiber radius values, we hypothesize that a small number of fibers interact with each other and that a halogen ion or protonated amine group participates in the interactions, given the R_c values in water and the presence of salt.

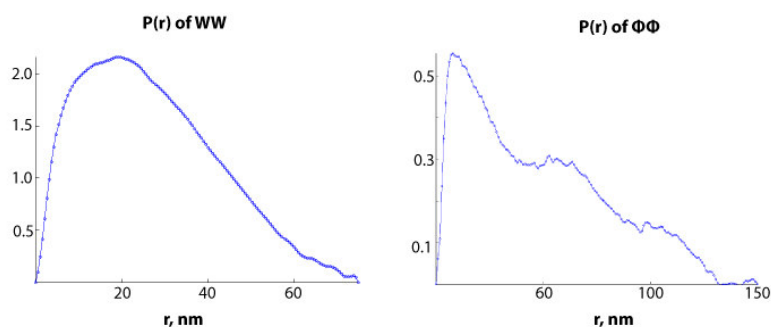


Figure 3.9. $P(r)$ functions of **WW** and **ΦΦ**.

3.3. Synthesis and Self-assembly of star-PGAs with cores based on Dipeptide Derivatives of BTA

For polymerization, we selected two candidate initiators - **FF** and **ΦΦ** - to prepare star-PGAs bearing 10 glutamic acid units per arm. As **WW** and **FF** compounds possess similar CAC values, we will not be able to observe differences between the corresponding polymers, and for this reason, we did not perform the polymerization of **WW**. We prepared polymers **FF-E10** and **ΦΦ-E10** by NCA-ROP polymerization, with their properties shown in with narrow polydispersity as was determined by GPC (**Fig. 3.10**).

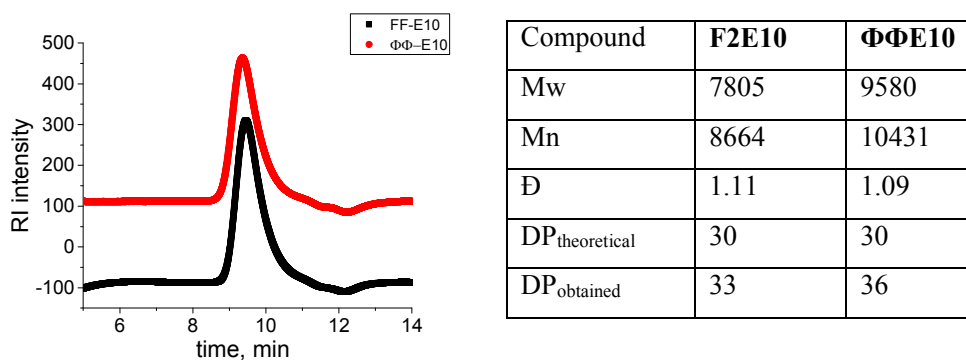


Figure 3.10. GPC chromatogram of **FF-E10** and **ΦΦ-E10** in benzyl ester form.

The fluorescence spectroscopy study of the corresponding polymers allowed us to determine CAC values of 7.86 mM for **FF-E10** and 1.77 mM for **ΦΦ-E10**. Interestingly, the ratio between CACs remained close for the cores and corresponding polymers (**Fig. 3.11A**).

We employed TEM of 43 mg/ml with 120 mM salt to study the morphology of self-assembled aggregates; however, we failed to observe any fiber formation for **FF-E10** at this concentration. For **ΦΦ-E10** at 25 mg/ml, we clearly observed the formation of fibers ranging in length from 100 to 250 nm; however, we noted a significantly lower width of the polymer fiber compared to the width of nanofiber formed by the corresponding core (**Fig. 3.11B**). The theoretically calculated diameter of the fully stretched polymer molecule is approximately 5 nm, and the observed fibers possess a comparable diameter, thereby correlating well with the classical mechanism of 1D polymerization. Of note, the generation of low numbers of fibers for high concentration results from the shifting of the system equilibrium towards small clusters.

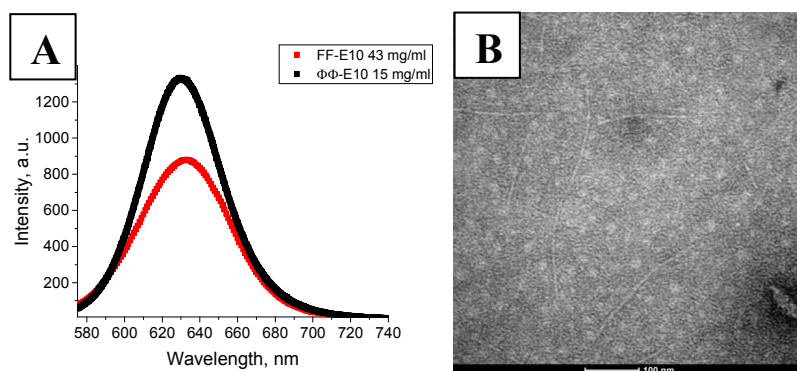


Figure 3.11. (A) Representative fluorescence spectra of **FF-E10** (43mg/ml) and **ΦΦ-E10** (15mg/ml) in water. (B) Representative TEM image of **ΦΦ-E10** (25 mg/ml) in water.

SAXS studies demonstrated that below the CAC (1.5 mM), polymers behave in an identical manner in water and 0.12 M NaCl. At 7.86 mM (**FF-E10**) and 7.06 mM (**ΦΦ-E10**), the slope of the curve was higher for **ΦΦ-E10** in water and 0.12 M NaCl confirming a stronger aggregation tendency (**Fig. 3.12 A,B**); however, the slope did not reach -1, which confirmed that the system represents a mixture of unimers and fibers.

The Guinier plot of **ΦΦ-E10** solution in 0.12 M NaCl demonstrated a R_g of 39.2 nm; however, as the percentage of unimeric molecules exceeds the number of molecules in fibers, we cannot directly extract the radius of gyration of the cross-section from the graph. To determine the R_c we subtracted **F0E10** scattering from the **ΦΦ-E10** curve. While imprecise, due to subtraction providing a noisier signal, this method suffices to estimate the R_c of the fibers in a complex mixture. This allowed us to determine an $R_{c,g}$ of 2.65 nm, or a R_c of 3.7 nm; values relatively close to the TEM results.

The $P(r)$ distribution function has an appearance typical for cylindrical particles, with a well-defined maximum corresponding to fiber diameter (**Fig. 3.12 C,D**). The appearance of a dip at 7.5 nm signifies that a small population of particles of average length 5-10 nm. For **F2E10**, the $P(r)$ function possesses only one maximum and D_{\max} of around 5 nm corresponding to unimers and small clusters of a few molecules.

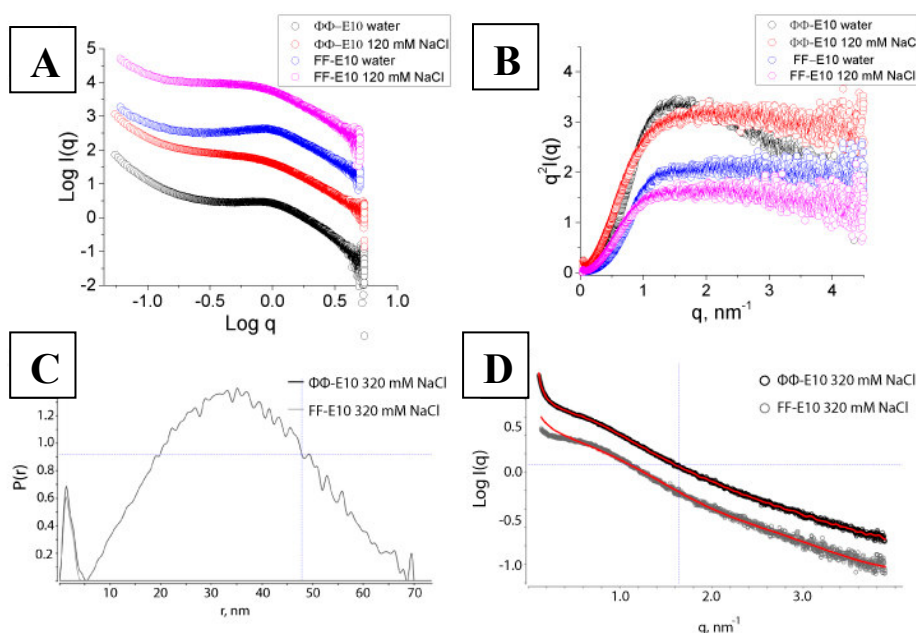


Figure 3.12. SAXS profiles of **FF-E10** and **$\Phi\Phi$ -E10** in water (A) and 120 mM NaCl (B). $P(r)$ distribution function (C) and corresponding curve fitting (D) of **FF-E10** and **$\Phi\Phi$ -E10** in 320 mM NaCl.

3.4. Self-assembling of Tripeptide Derivatives of BTA

We next studied the effect of amino acid nature and position in the core on self-assembly by preparing a family of seven compounds containing tripeptide sequences XFF, where X = phenylalanine (F), tryptophan (W), leucine (L), glycine (G), tyrosine (Y) or pentafluorophenylalanine (Φ), and one compound with an FWW sequence (**Fig. 3.13**). We prepared compounds with sequential liquid peptide synthesis in a similar manner as was described for the **F3** derivative.

Fluorimetry studies of hydrochloride salts in water revealed that the CAC of the compounds decreased in the order **FWW**>**WFF**>**FFF**> **Φ FF**>**LFF**~**YFF**>**GFF**. In 120 mM NaCl solution, the order changed slightly to **FWW**> **Φ FF**>**WFF**>**FFF**~**LFF**>**YFF**>**GFF**, although CAC values in all cases decreased due to charge screening (**Fig. 3.14 A,B**).

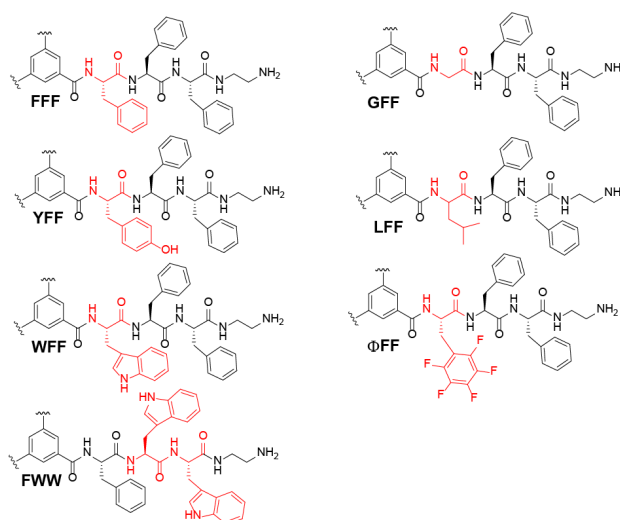
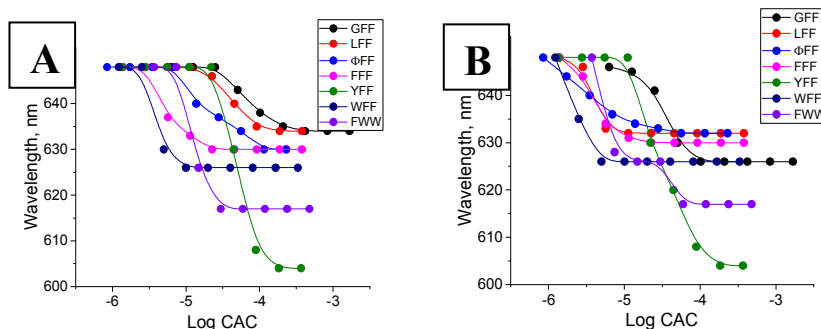


Figure 3.13. General structure of BTA-tripeptide Derivatives.

As expected, tryptophan-containing compounds exhibited higher CAC values due to the higher hydrophobicity of this residue. We expected that pentafluorophenylalanine replacement, as the most hydrophobic residue of all, would result in the highest decrease in the CAC value; however, on the contrary, the CAC value for **ΦFF** remained lower than for **FFF** in pure water. In the presence of salt, we observed the lowest CAC value within the studied compounds for **ΦFF**; however, the curve incline for **ΦFF** was also the lowest, suggesting a lower amount of non-covalent interactions. Existing models of pentafluorophenyl and benzyl ring interaction state that the π - π interactions are more efficient in the parallel-displaced orientation, which might result in a molecule distortion that partially disrupts directional network of non-covalent interactions.¹⁰

Tyr and Gly residues displayed a more destabilizing effect on self-assembly, with CACs of 0.125 mM and 0.835 mM, respectively. **LFF** possessed a CAC value higher than **YFF** and lower than **FFF** of 0.045 mM. For Leu and Gly containing residues, a decrease in CAC values can be correlated with weaker (in case of Leu) or absent (for Gly) non-covalent interactions in proximity to the core. In the case of **YFF**, we do not fully understand why we see such a decrease in the CAC value, taking into account that the wavelength shift of NR for **YFF** was almost 25 nm bigger than for the other compounds, suggesting an extremely hydrophobic microenvironment.

FWW exhibited CAC values of 0.03 mM and 0.014 mM in water and 0.12 M NaCl, respectively. The low value compared to **FFF** and **WFF** might relate to strong NR self-quenching due to the formation of highly hydrophobic microdomains or aromatic interactions with the core and the subsequent distortion of the results at low concentrations.



| Compound | CAC (water), mM | CAC (120mM NaCl), mM | λ_{max} , nm |
|------------|-----------------|----------------------|----------------------|
| FFF | 0.0058 | 0.0028 | 630 |
| LFF | 0.0451 | 0.0035 | 631 |
| WFF | 0.0052 | 0.0032 | 626 |
| GFF | 0.8350 | 0.4671 | 630 |
| YFF | 0.1250 | 0.0712 | 605 |
| ΦFF | 0.0320 | 0.0019 | 632 |
| FWW | 0.0313 | 0.0144 | 615 |

Figure 3.14. NR peak maximum dependence on the concentration of BTA-tripeptide derivatives in water (A) and 120 mM NaCl (B). Table with CAC values of all the compounds.

To characterize the dependence of CAC on the sequence of amino acids in the core, we tried to correlate CAC values with the hydrophobicity of the molecules. To calculate free energies of transfer (ΔG), we used an established Wimley-White whole residue hydrophobicity with both octanol and interface scales.¹¹ We calculated the Gibbs energy as $\Delta G = 3 \sum_{i=1}^3 \Delta G_i$, where i is an aminoacid residue position in the tripeptide. When we plotted $-\text{LogCAC}$ against ΔG for the corresponding compounds, we observed that all the compounds follow similar trends of decreasing CAC proportionally to the free energy of transfer from water to n-octanol (so-called octanol scale) in water and 120 mM NaCl (**Fig.3.15**). We observed that **YFF** and **LFF** slightly deviate from the general trend, possibly due to the formation of a system of directional non-covalent bonds rather than hydrophobicity.

To evaluate the applicability of the proposed approach, we plotted ΔG vs. $-\text{LogCAC}$ and observed an almost linear dependence in 120 mM NaCl solutions, with the strong deviation for **YFF** from the expected value the only exception. In pure water, however, dependence strongly varied from linear dependence. In salt-free solutions, the balance of directional non-covalent and non-directional hydrophobic interactions in the core and repulsive Coulomb and solvation interactions with water controls self-assembly. Unlike **FFF** and **WFF**, **GFF**, **LFF**, and **YFF** cannot form a third pair of directional π - π interactions, and the increase in CAC is proportional exclusively to the hydrophobic interactions, correlating with residue hydrophobicity. For **FFF** and **WFF**, the aromatic group provides additional stabilization through π - π bonds, thereby

explaining the spiked increase in CACs. In salt solution, however, Coulomb interactions are screened, and the dependence is closer to linear.

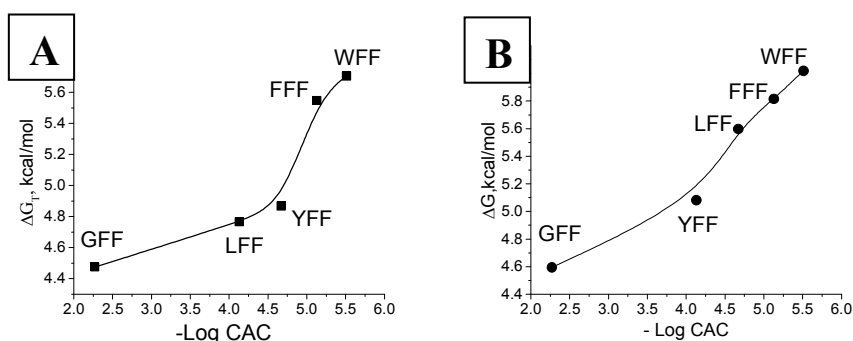


Figure 3.15. Dependence of Gibbs energy of transfer on $-\text{LogCAC}$ in water (A) and 0.12 M NaCl (B).

Next, we performed SAXS studies for all compounds; scattering curves demonstrate that all compounds assemble into defined structures and the corresponding Kratky plots confirmed the formation of the defined aggregates, as can be seen from the bell-like shape of the curve at low and intermediate q -range (**Fig. 3.16**). YFF represented the only exception – we found a Kratky plot close to zero for the whole q -range. While we observed Kratky plots for ΦFF and GFF typical for the lamellar objects due to a shifted maximum of the peak, the plots simultaneously displayed a defined maximum typical for rod-like particles, overall suggesting that these two compounds display distinct aggregation mechanisms.

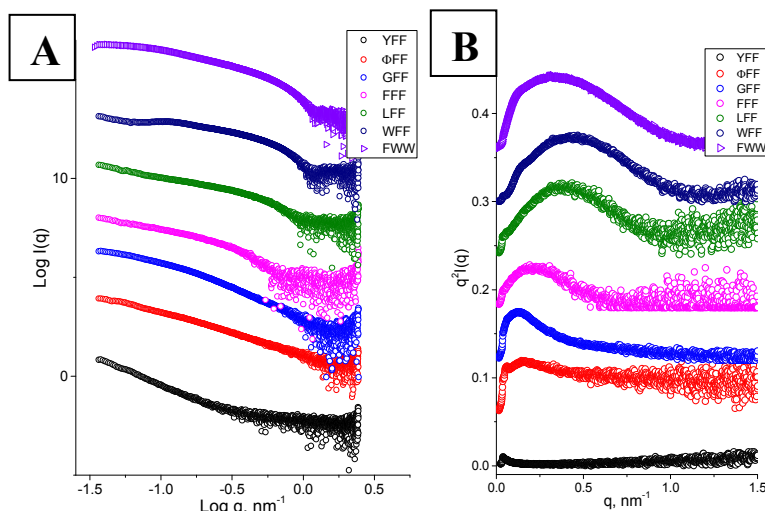


Figure 3.16. SAXS profiles and corresponding Kratky plots for XFF compounds and FWW.

SAXS data confirmed the self-assembly strength of the compounds in the order **FWW>WFF~FFF>LFF>ΦFF>GFF>>YFF**. By applying the Guinier approximation for rod-like and flat particles, we determined the radius of gyration of cross-section or of lamella thickness, as shown in **Table 3.2**. While we observed a significant deviation between these radii, the diameter of the fibers exceeds those theoretically predicted in all the cases. In the case of **YFF**, we could not properly define the linear range of the Guinier plot in qR_c limits; however, the radius seems to exceed 6.2 nm. Surprisingly, for compounds **ΦFF** and **GFF**, we could apply both types of Guinier equation (rod-like and flat particles) with equal success. This does not occur due to the formation of lamellae, and is more likely to occur via interparticle interactions with the formation of fractal structures. In both cases, we observed a power law dependence of -2. For **FWW**, we observed a power law dependence of -1.67 also typical for mass fractals.

Table 3.2. Some parameters of BTA derived tripeptides extracted from SAXS data

| Compounds | Power law | Power law (Porod) | Model | $R_{g, c}$, nm | R_c , nm |
|-----------------------------|--------------|-------------------|-------|-----------------|------------|
| FFF | -1 | -4 | rod | 6.92 | 9.6 |
| LFF | -1 | -4 | rod | 2.62 | 3.67 |
| GFF (in 120 mM NaCl) | -2 | -3 | rod | 8.7 | 12.2 |
| YFF | -2 | - | - | - | - |
| ΦFF | -2 | - | rod | 6.8 | 9.5 |
| WFF | -1 | -4 | rod | 3.41 | 4.77 |
| FWW | -1.67 (-5/3) | -4 | rod | 5.63 | 7.88 |

Next, we studied $P(r)$ functions of the corresponding supramolecular polymers in concentrated solutions to determine internal structure (**Fig. 3.17**). We observed that **LFF** and **WFF** (as well as **FFF**, as shown in Chapter 2) have $P(r)$ functions typical for cylindrical particles, which also correlate with the obtained power law -1. In the case of **LFF**, $P(r)$ functions oscillate strongly, and D_{max} is underestimated but sufficient to understand particle morphology. To some extent, **FWW** possesses partially similar $P(r)$ functions typical for cylindrical particles; however, the power law decay of -5/3 is typical for mass fractal where particles do not interact with each other. Of particular note, we observed identical oscillation of $P(r)$ function for **WFF** as for **FFF**, suggesting the formation of twisted helical assemblies.

All other compounds displayed $P(r)$ functions more characteristic of lamellar objects; however, the power law -2 obtained for all compounds is also characteristic of mass fractals with interacting particles. **YFF** possesses a distinct $P(r)$ function that starts from 10 nm and not from zero, as for other compounds; thus, **YFF** might form a porous

structure with a pore diameter from 10 to 110 nm. Due to the failure to fit to modified Guinier equations, we assume that **YFF** self-assembles into disordered aggregates due to phase separation, with a lack of non-covalent bond formation into a directional network.

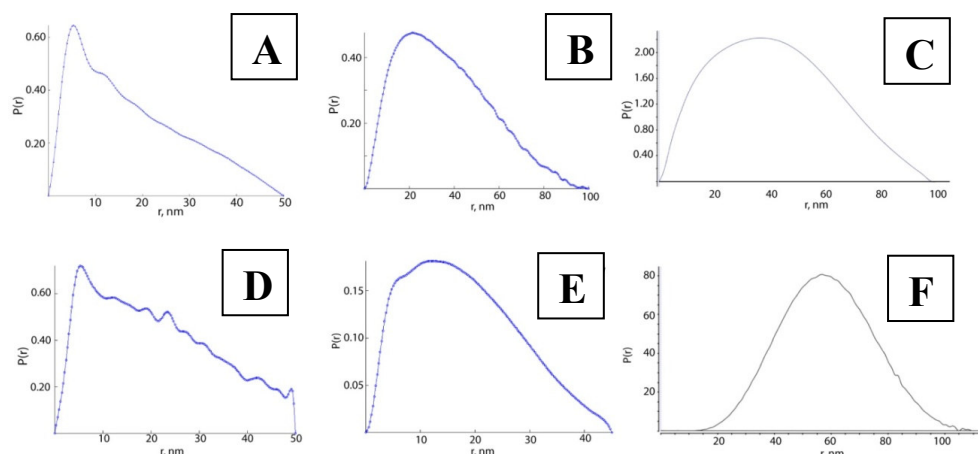


Figure 3.17. $P(r)$ distribution functions for **WFF** (A), **GFF** (B), **ΦFF** (C), **LFF** (D), **FWW** (E) and **YFF** (F).

We next performed circular dichroism studies for the compounds in water and 120 mM NaCl, and we found that all compounds exhibited distinct CD-spectra (**Fig. 3.18**). The spectrum of **FFF** displays two minima at 204 and 214 nm and another small minimum at 250 nm with a sharp increase at 190 nm in water (**Fig. 3.18A**). While the spectrum strongly resembles that of an alpha-helix observed in proteins, the spectrum remains distinct due to a shift in both minima. We also measured the CD spectrum of **FFF** at a concentration below the CAC and found it to be identical to the spectrum of the concentrated solution. Furthermore, we also observed an identical CD spectrum for a solution of **FFF** heated to 80 °C for 20 min, confirming that the obtained CD spectrum arises from the molecule itself rather than from the secondary structure. SAXS, TEM, and fluorimetry confirmed the presence of self-assembled fibers in concentrated solution and their absence in the diluted solution, suggestive of a weak helical signal. In 120 mM NaCl, the minimum at 204 nm becomes less pronounced while the peak at 214 increases in intensity. In this case, salt-induced increase in the fiber length and helix content results in an increased signal corresponding to helical assembly. A CD peak at 215-220 nm was already reported for BTA-based helices.¹² Spectra of **LFF** and **ΦFF** in water display a single minima at 206 and 214 nm, while in 120 mM NaCl the second minimum appears at 218 and 220 nm, respectively (**Fig. 3.18 C,E**). We observed similar spectra for the diluted solutions (below CAC) to the spectrum of a concentrated solution in water at 25 °C and 120 mM NaCl at 80 °C. A small peak at 195 nm present in both spectra in water disappeared in the presence of salt.

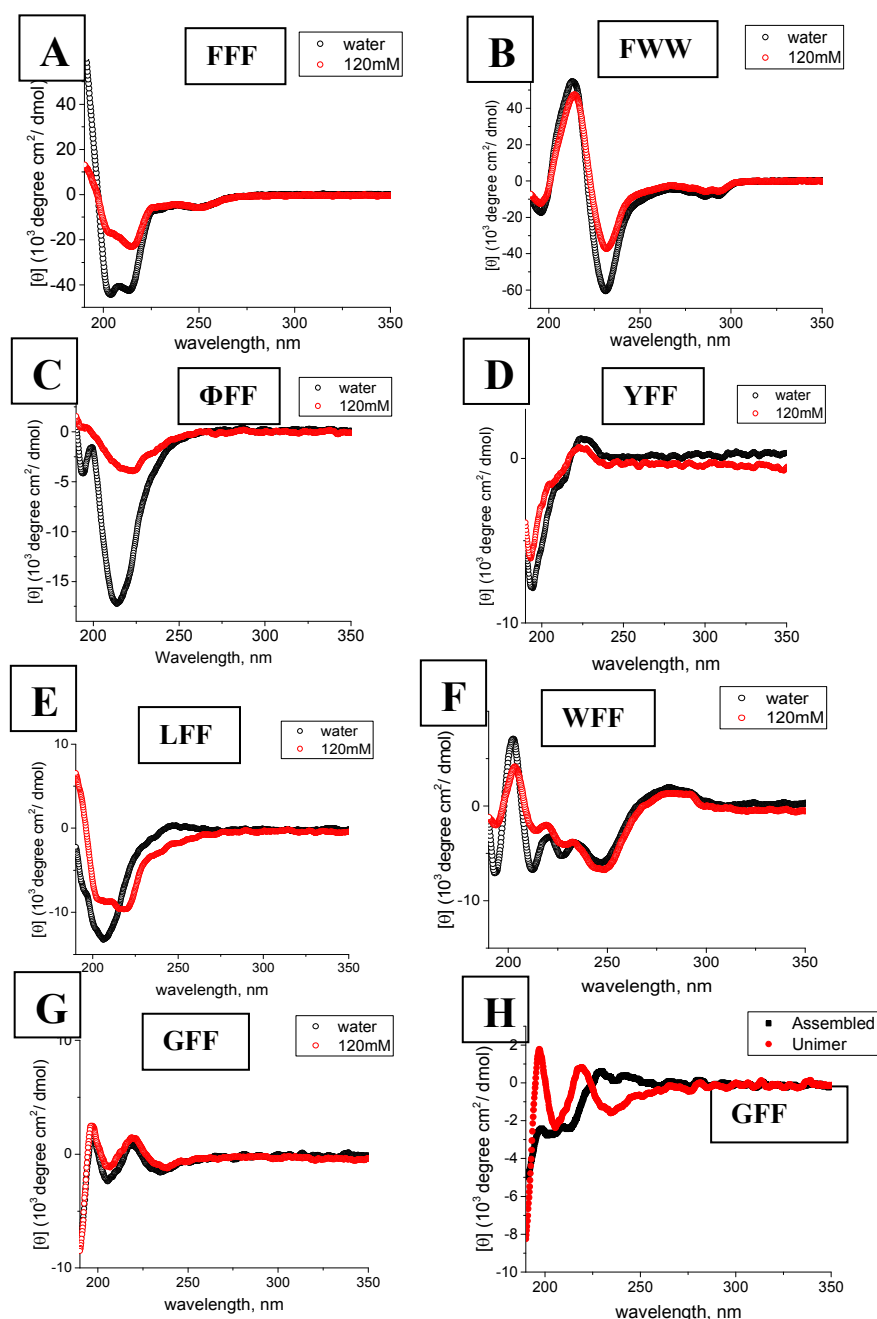


Figure 3.18. CD spectra of BTA-nonapeptide derivatives in water and 0.12 M NaCl (FFF (A), FWW (B), ΦFF (C), YFF (D), LFF (E), WFF (F), GFF (G)). The CD spectrum of freshly diluted GFF gel and after 24 hours (E).

We observed a similar spectrum for **FWW** to an antiparallel beta-sheet with a strong minimum at 231 nm with equal amplitude maximum at 213 nm (**Fig. 3.18 B**). Upon addition of salt, the intensity of the maximum at 213 nm increased slightly. Meanwhile, we found a complicated spectrum for **WFF** with four distinct maxima and minima that changed intensity upon addition of salt, perhaps due to the appearance of another BTA-related peak overlapping with the original spectrum (**Fig. 3.18 F**). Finally, we observed identical spectra of **YFF** and **GFF** independent of temperature, concentration, and salt content (**Fig. 3.18 D,G**). When we performed CD of the diluted **GFF** gel we observed a distinct spectrum (**Fig. 3.18E**), however its intensity remains low and it is hard to assign a known structure to it.

Finally, we performed TEM studies for all compounds; in general, image analysis confirmed SAXS findings (**Fig. 3.19**).

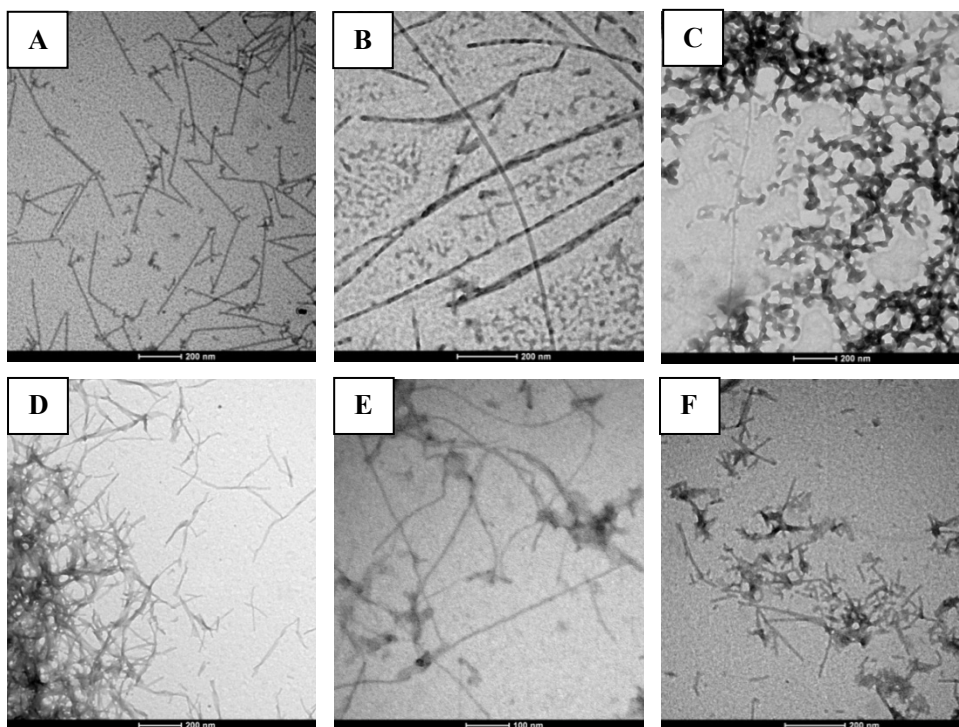


Figure 3.19. TEM images of BTA-tripeptide derivatives. A) **LFF**, B) **GFF**, C) **YFF**, D) **WFF**, E) **ΦFF**, F) **FWW**.

LFF assembled into very thin defined perfectly separated rods that never exceeded 500 nm length (**Fig. 3.19 A**). **GFF** formed very thick fibers with a diameter of 15 to 30 nm with a variety of different morphologies simultaneously present, including simple long and short fibers as well as twisted fibers (**Fig. 3.19 B**). We also observed direct evidence of interactions between two fibers with the formation of a thicker twisted

fiber. **WFF** assembled into defined mostly twisted particles; however, we did not observe any interaction between particles (**Fig. 3.19 D**). **ΦFF** and **FWW** both formed fractal structures, with the majority of the particles interacting with each other in gel-like networks (**Fig. 3.19 E,F**). **YFF** formed unusual gel-like structures lacking any defined morphology (**Fig. 3.19 C**). We did observe a few long thin fibers connected with the gel masses; however, we failed to observe any separate fibers. While we believe that this represents to first report of this type of aggregate in aqueous solution for BTA-based systems, Jana et al reported a similar example for BTA with an attached tyrosine methyl ester that formed a porous organic material in methanol, which is much less polar than water.¹³

In summary, our data suggests that each compound displays a different mechanism of self-assembly, which is influenced by the nature, hydrophobicity, and the order of amino acids. For the **XFF** sequence, the first amino acid exclusively determines the self-assembly behavior; we observed a pronounced effect in the case of **YFF**, which formed porous organic materials in water exclusively due to tyrosine non-directional assembly.

3.5. Synthesis and Self-assembly of star-PGAs with cores based on tripeptide Derivatives of BTA

Despite the peculiar properties of each tripeptide derivative, their applicability as initiators for the synthesis of star-PGA is limited. As almost all compounds possessed CAC values below the CAC of **FFF**, we selected only two initiators - **FFF** and **WFF** - for the synthesis of polymers. Using NCA-ROP, we prepared polymer **WFF-E10** with 10 glutamic units per arm, while the preparation of **FFF-E10** was described in **Chapter 2**.

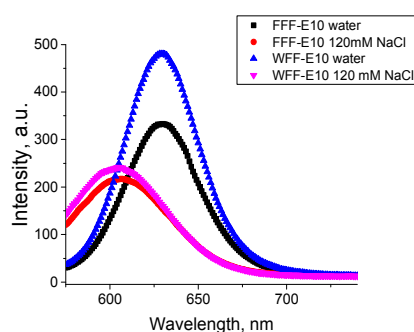


Figure 3.20. Fluorescent spectra of NR with 1.6 mM **FFF-E10** and **WFF-E10** in water and 0.12 M NaCl.

Fluorimetry studies of the corresponding polymers revealed a similar peak shift for NR to that observed for the corresponding cores - equal to 630 nm and 610 nm for **FFF-E10** and **WFF-E10**, respectively (**Fig. 3.20**). However, we observed very close

CAC values due to the polydisperse nature of the polymer smearing the difference between core CACs. Due to these findings, we did not continue studying tripeptide-based polymers.

3.6. Self-assembling of tetrapeptide derivatives of BTA

To obtain a more obvious effect of amino acid nature on polymer self-assembly, we prepared cores with tetrapeptides consisting of phenylalanine and tryptophan in differing orders, as shown in **Fig. 3.21**.

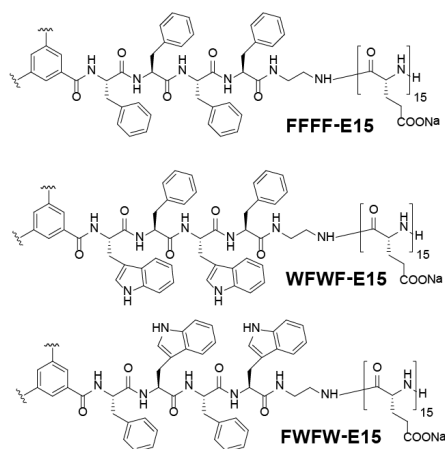


Figure 3.21. General structure of the BTA derivative of tetrapeptides.

These cores failed to display solubility in water independently of pH; therefore, we prepared the corresponding polymers using the already established NCA-ROP strategy. Taking into account previously-defined relationships, we synthesized polymers with 15 units per arm and compared them with **F3E10** to keep CAC values within the same range. All the polymers had narrow dispersity (1.06-1.08) as measured by GPC (**Fig. 3.22**).

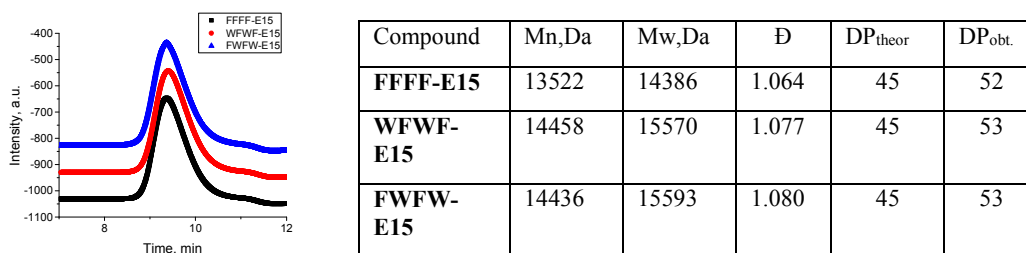


Figure 3.22. GPC chromatograms of **FFFF-E15**, **FWFW-E15** and **WFWF-E15** in the benzyl ester form. Table with the properties of the polymers

Of particular interest, we noted a difference in the color of initiators and corresponding polymers in acidic conditions. In the presence of 2M HCl in methanol, we observed pink and violet colored initiators (**Fig.3.23 A-C**), while in a solution of TFA, we observed light pink and dark violet corresponding polymers (**Fig.3.23 D,E**). Upon deprotection with TFA/HBr, these colors changed to a greyish light green and a greenish deep blue, respectively (**Fig.3.23 F,G**). All compounds consisting of phenylalanines were white.

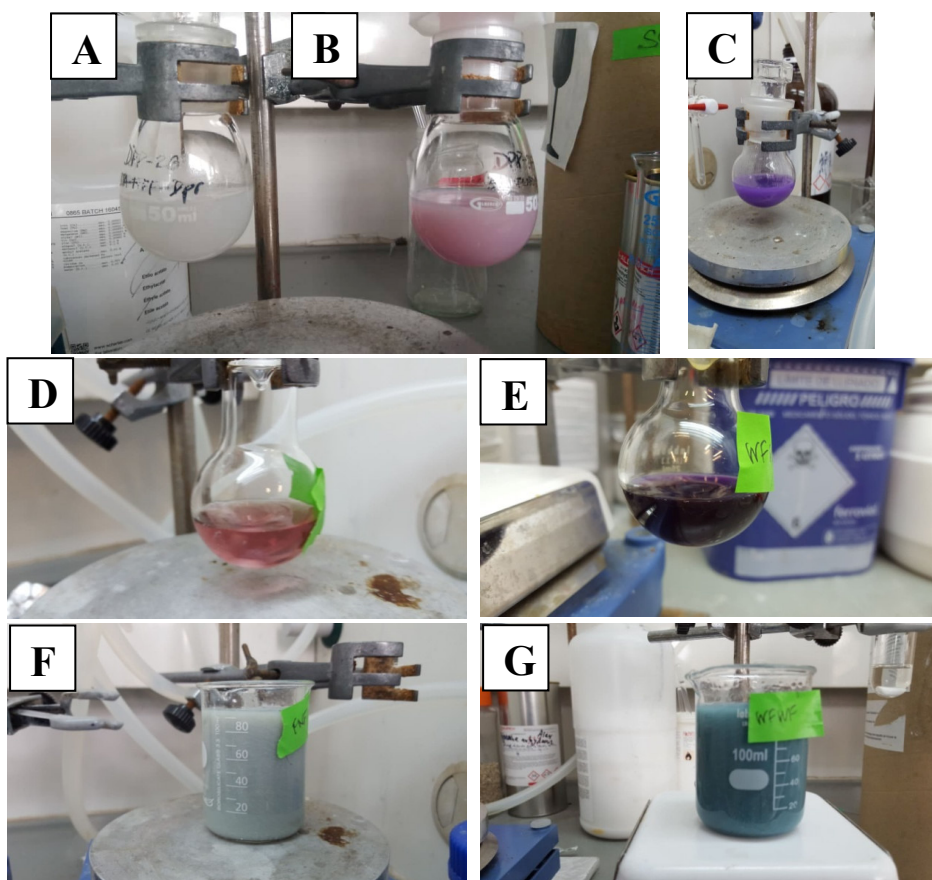


Figure 3.23. Photos of tryptophane-containing compounds in acidic conditions. A) **FFFF**; B) **FFWF**; C) **WFWF**; D) **FFWF-E15** in TFA; E) **WFWF-E15** in TFA; F) **FFWF-E15** in TFA/HBr; G) **WFWF-E15** in TFA/HBr.

Fluorimetry studies didn't demonstrate the difference of CACs of tryptophane containing polymers (0.16 mM and 0.17 mM for **WFWF-E15** and **FFWF-E15**, respectively), while being higher for **FFFF-E15** (0.79 mM). In 120 mM NaCl CAC values were equal to 0.31, 0.08, and 0.08 mM for **FFFF-E15**, **WFWF-E15**, and **FFWF-E15**, respectively (**Fig. 3.24**). Of interest, we observed a smooth decrease in the

wavelength of NR maximum in pure water, signifying a lack of defined CAC value and the existence of a system in dynamic equilibrium shifted towards fiber formation by concentration increase, similar to the behavior observed for block-copolymer micelles. However, all the curves decrease sharply with a defined CAC value in the presence of salt. We additionally checked if the cores interfered with NR fluorescence by performing blank measurements of the polymer solutions without NR. In all cases, we only observed background noise.

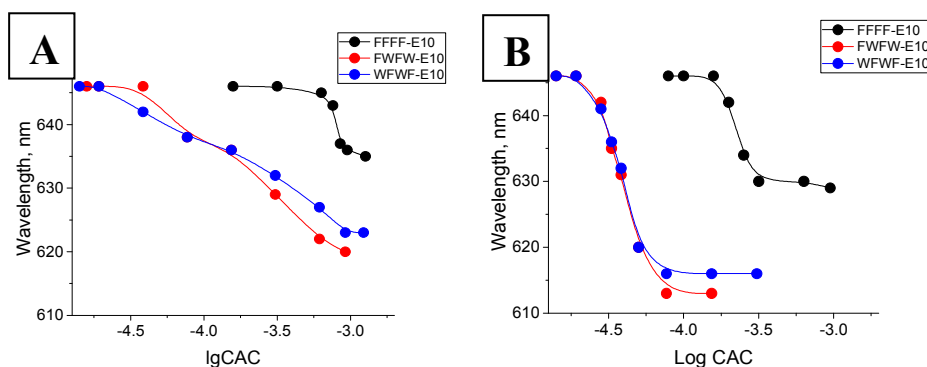


Figure 3.24. Dependence of NR peak maximum on Log CAC values in water (A) and 120 mM NaCl (B).

In the next step, we performed negative TEM studies in which we observed small spherical particles rather than nanorods (**Fig. 3.25**). In all the images, we observed similar worm-like network artifacts as described for **F3E10** in **Chapter 2**.

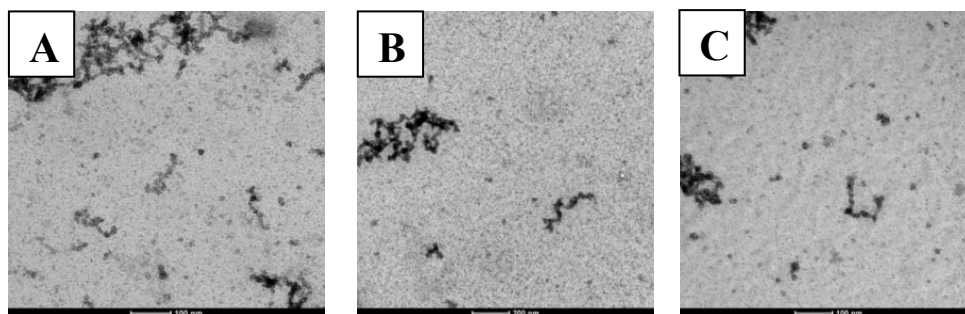


Figure 3.25. TEM images for **FFFF-E10** (A), **FWFW-E10** (B), and **WFWF-E10** (C).

To study polymer aggregation, we performed SAXS studies with similar concentrations of polymer and varying concentrations of salt (0 to 640 mM) (**Fig. 3.26**). We confirmed that tryptophan-containing compounds possessed higher CAC values as 2-3 defined peak maxima started to appear in pure water on the Kratky plot. **WFWF-E15** appeared to assemble in a stronger manner to **FWFW-E15** as we observed an almost

complete transition at 120 mM and 320 mM NaCl for **WFWF-E15** and **FWWF-E15**, respectively.

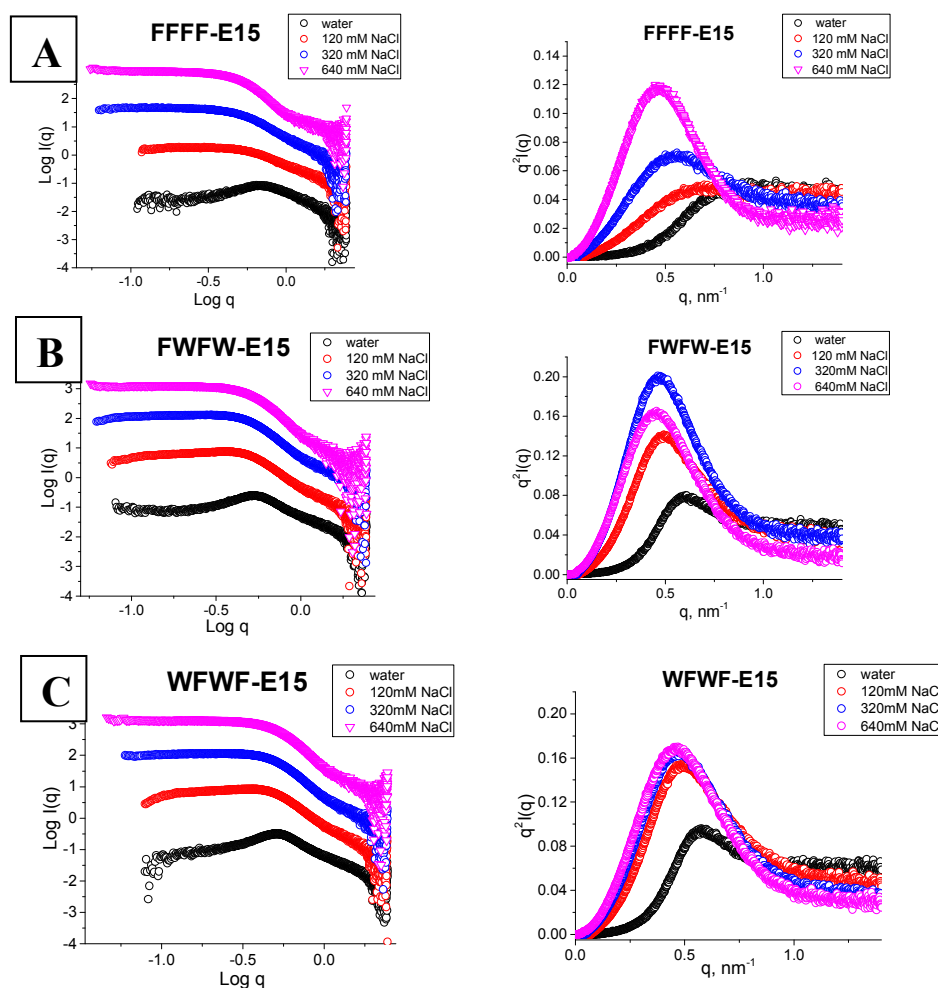


Figure 3.26. SAXS profiles and corresponding Kratky plots for **FFFF-E15** (A), **FWWF-E15** (B), and **WFWF-E15** (C).

Modified Guinier plots for rod-like particles allowed us to determine the R_g of cross-section as 2.62 nm, 2.70 nm, and 2.69 nm for **FFFF-E15**, **FWWF-E15**, and **WFWF-E15**, respectively. These values correspond to R_c values of 3.67, 3.78, and 3.76 nm, respectively. As in the case of **F3E10**, these values are slightly higher than the diameter of the theoretically predicted molecule.

Following a more detailed study of SAXS plots, we observed that for all the compounds the power law dependence at low q -range changed from negative (repulsive

interactions) to zero or just slightly deviating from 0 to -0.15 upon an increase of ionic strength. Furthermore, we found a Power law in the medium q -range equal to approximately -4, sometimes extending to between -4 and -5. The latter values do not fit to any existing dependencies, neither defined nor fractal, although studies have identified such behavior for dendrimers and core-shell micelles that display overlap between the chain scattering and sphere scattering.^{14,15}

Thermal studies of **WFWF-E15** demonstrated a decrease in the scattering intensity of the curve and a decrease of Kratky plot peak with a slight shift of its maximum towards higher q -values (Fig. 3.27A). $P(r)$ functions of three polymers in 320 mM NaCl are very similar (Fig. 3.27B) with D_{\max} of around 8 nm.

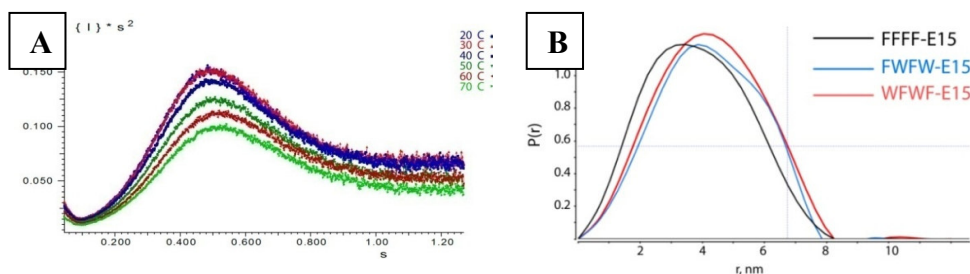


Figure 3.27. SAXS profiles of **WFWF-E15** at different temperatures (A). $P(r)$ functions of **FFFF-E15** (black), **FWWF-E15** (blue) and **WFWF-E15** (red) in 320 mM NaCl (B).

These data confirm that BTA-tetrapeptide derived polymers fail to assemble in water in 1D structures, and instead forming small core-shell micelles below 10 nm in diameter.

3.7. Self-assembly of Tripeptide-derivatives of BTA with Different Chiralities

A recent study reported that phenylalanine tripeptides consisting of L-L-L and L-D-L sequences of amino acids demonstrated a completely different pattern of self-assembly.¹⁶ Therefore, we decided to evaluate whether similar variations in sequence affect the self-assembly of corresponding BTA-based molecules.

First, we prepared a compound (*L,D,L*)-**FFF** in a similar way to (*L,L,L*)-**FFF** (Fig. 3.28).

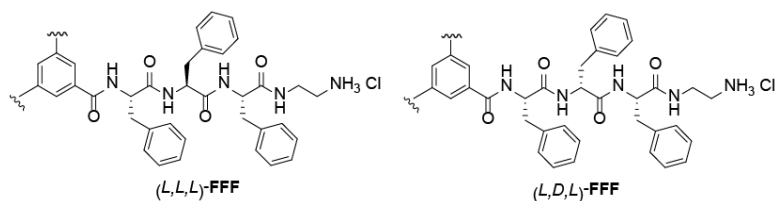


Figure 3.28. General structure of (*L,L,L*) and (*L,D,L*)-triphenylalanine derivatives.

Fluorimetry studies found CAC values of (L,D,L) -FFF 1.5 orders of magnitude lower than for (L,L,L) -FFF. The corresponding CD spectra in water displayed a weak signal, with two minima at 206 and 197 nm, while in 0.12 M NaCl, one minimum at 195 nm resembles a random coil. Furthermore, SAXS and TEM studies of (L,D,L) -FFF failed to uncover any evidence of the formation of organized structures (Fig. 3.29).

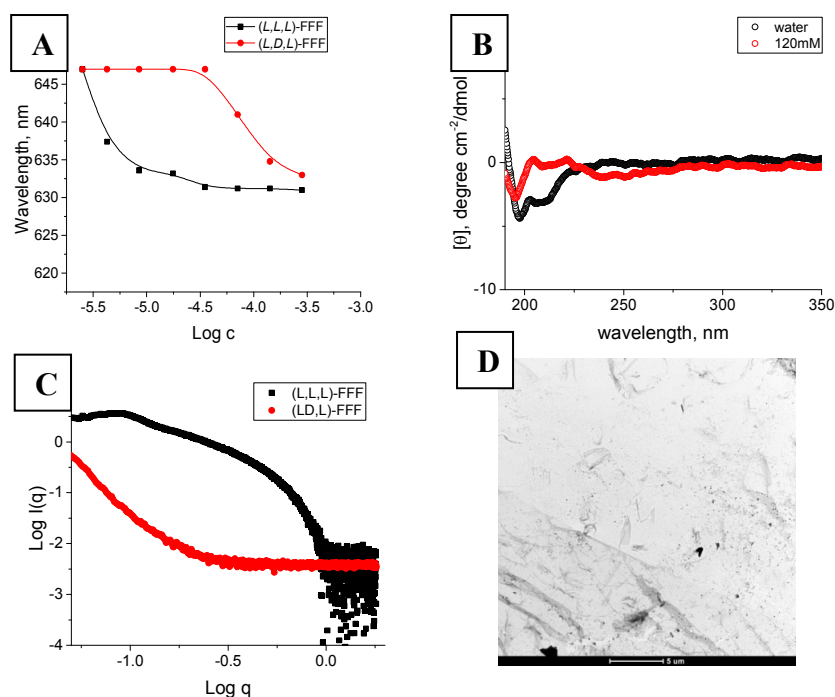


Figure 3.29. Dependence of NR peak maximum on Log C of (L,L,L) - and (L,D,L) -FFF (A). CD spectra of (L,D,L) -FFF in water and 0.12 M NaCl (B). SAXS (C) and TEM (D) of (L,D,L) -FFF and (L,L,L) -FFF at 5mg/ml.

3.8. Conclusion

In this chapter, we studied a series of BTA-based compounds with varied sequence and nature of amino acids. From the analysis of BTA-dipeptide derivatives, we determined that the higher hydrophobicity of amino acids increases the strength of self-assembly; this was more pronounced for phenylalanines with and without a fluorinated aromatic ring. However, the morphology of self-assembled particles of the cores also changed from separate fibers to thick rods and mass fractals. A comparison of the pair of corresponding star-PGAs demonstrated that compounds with a more hydrophobic core (**ΦΦ-E10**) displayed higher CAC values and assembled into defined long thin fibers.

Comparative analyses of tripeptide-derivatives of BTA demonstrated that the nature of the first amino acid in the sequence plays a crucial role in self-assembly and determines the morphology of the final particle. In addition to the order of amino acids, the ability to form a directional system of non-covalent bonds is also of high importance. When we replaced the second L-phenylalanine in an *(L,L,L)*-FFF to a D-isomer, we observed complete disruption of self-assembly and a lack of formation of defined structures. This can be explained in terms of tripeptide conformation; for *(L,L,L)*-FFF, the aromatic rings are situated on a plane, while in *(L,D,L)*-FFF, the rings interact with each other in the tripeptide.

Finally, we provide evidence that star-PGAs with cores consisting of tetrapeptide BTA- derivatives do not assemble into fiber-like structures. We hypothesize that tetrapeptides, but not tripeptides, display higher chain flexibility and can form small core-shell micelles.

Overall, we demonstrate that star-PGAs can assemble into rod-like particles only when amino acid hydrophobicity, order, and chirality favor the formation of a strong and directional system of hydrogen bonds, and under conditions of minimal core flexibility.

3.9. Supplementary information

- SI-3.1. Synthesis of Chiral Catalyst 2,7-Bis{O(9)-a-N-allyl-hydrocinchonidinium-N-methyl}naphthalene Dibromide
- SI-3.2. Synthesis of 2,3,4,5,6-pentafluorophenylalanine and its N-protected Derivatives
- SI-3.3. Synthesis of Dipeptide-ethylenediamine-Boc Derivatives
- SI-3.4. Synthesis of **H-(L,D,L)-FFF-Boc**
- SI-3.5. Synthesis of **H-XFF-EDA-Boc** Tripeptides
- SI-3.6. Synthesis of Tetrapeptides-ethylenediamine-Boc Derivatives
- SI-3.7. Synthesis of BTA-derivatives of Di-, Tri-, and Tetrapeptides
- SI-3.7. Star-polyglutamate Synthesis
- SI-3.8. Experimental methods

SI-3.1. Synthesis of Chiral Catalyst 2,7-Bis{O(9)-a-N-allyl-hydrocinchonidinium-N-methyl}naphthalene Dibromide

We prepared the catalyst in four steps, as previously described by Leenders et al.⁶

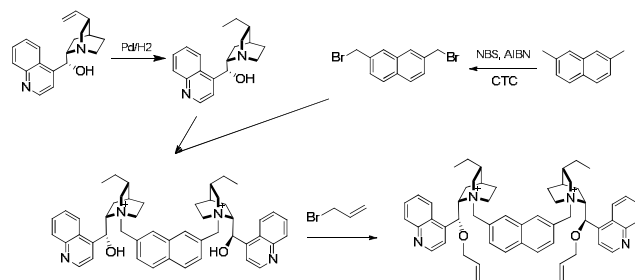


Figure SI-3.1. Synthetic scheme for 2,7-Bis{O(9)-a-N-allyl-hydrocinchonidinium-N-methyl}-naphthalene Dibromide.

3.1.1. Synthesis of 2,7-bis(bromomethyl)naphthalene

A mixture of 2,7-dimethylnaphthalene (2.0 g, 12.8 mmol), N-bromosuccinimide (5.0 g, 28.16 mmol), and 2,2'-azobisisobutyronitrile (190 mg, 1.15 mmol) in carbon tetrachloride (160 mL) was stirred under reflux for 10 minutes, after which the mixture was cooled to 0°C. The precipitated succinimide was filtered off and the filtrate was evaporated under reduced pressure. The residue was recrystallized from chloroform. Product - white solid. Global yield: 3.82 g (95 %).

¹H NMR (300 MHz, CHCl₃-d): 7.80 (d, J = 8.3 Hz, 2H), 7.78 (s, 2H), 7.49 (d, J = 8.3 Hz, 2H), 4.63 (s, 4H).

3.1.2. Synthesis of (-)-hydrocinchonidine

A mixture of (-)-cinchonidine (5 g, 16.98 mmol) and a 10% Pd/C catalyst (1 g) was stirred in methanol (130 mL) under a hydrogen atmosphere at room temperature for 10 hours. The reaction mixture was filtered through a celite pad. The obtained residue was suspended in hexane (200 mL), stirred at room temperature for 1 hour, and filtered. Product - white solid. Global yield: 4.07 g (81 %).

¹H NMR (300 MHz, d-MeOH): 8.81 (d, J = 4.4 Hz, 1H), 8.22 (d, J = 7.5 Hz, 1H), 8.05 (d, J = 8.3 Hz, 1H), 7.77 (t, J = 7.0 Hz, 1H), 7.71 (d, J = 4.6 Hz, 1H), 7.65 (t, J = 7.0 Hz, 1H), 5.62 (d, J = 3.9 Hz, 1H), 3.63-3.54 (m, 1H), 3.10-3.02 (m, 2H), 2.68-2.59 (m, 1H), 2.37-2.30 (m, 1H), 1.88-1.76 (m, 3H), 1.53-1.40 (m, 2H), 0.81 (t, J = 7.3 Hz, 3H).

3.1.3. Synthesis of 2,7-Bis(hydrocinchonidinium-N-methyl) naphthalene dibromide

(-)-Hydrocinchonidine (1.57 g, 5.3 mmol) and 2,7-bis(bromomethyl)naphthalene (0.82 g, 2.61 mmol) were mixed in 8 mL of a mixture of ethanol, DMF, and chloroform (5:6:2). The mixture was stirred at 100°C for 6 hours. After cooling to room temperature, the resulting suspension was diluted with 20 mL of methanol and 60 mL of ether and stirred for 1 hour. The precipitate was filtered and washed with ether. The residue was recrystallized from methanol-ether. Product - pink solid. Global yield: 3.3 g (69 %).

¹H-NMR (300 MHz, DMSO-d₆): 9.00 (d, J = 4.4 Hz, 2H), 8.37-8.31 (m, 4H), 8.21 (d, J = 8.6 Hz, 2H), 8.12 (d, J = 8.6 Hz, 2H), 7.93 (d, J = 7.8 Hz, 2H), 7.88-7.82 (m, 4H), 7.76-7.71 (m, 2H), 6.77 (d, J = 4.6 Hz, 2H), 6.63 (s, 2H), 5.36 (d, J = 12.4 Hz, 2H), 5.15 (d, J = 12.7 Hz, 2H), 4.43-4.32 (m, 2H), 4.02-3.96 (m, 2H), 3.54-3.41 (m, 2H), 3.39-3.27 (m, 4H), 2.20-2.05 (m, 4H), 2.01-1.92 (m, 2H), 1.73-1.61

(m, 4H), 1.48-1.36 (m, 2H), 1.31-1.23 (m, 4H), 0.71 (t, $J = 7.3$ Hz, 6H)

3.1.4. Synthesis of 2,7-Bis{O(9)- α -N-allyl-hydrocinchonidinium-N-methyl}naphthalene Dibromide

To a suspension of the previous compound (1.60 g, 1.77 mmol) in dichloromethane (8.90 mL), allyl bromide (0.91 mL, 10.58 mmol) and a 50% (m/m) KOH solution (1.98 mL) was added. This mixture was stirred for 4 hours in which time all the solids were dissolved. The obtained mixture was diluted with 20 mL of ultrapure water. The mixture was then extracted three times with 50 mL dichloromethane. The combined organic extracts were first dried with magnesium sulphate and concentrated on a rotary evaporator (Heidolph, Schwabach, Germany). The crude solid was recrystallized from dichloromethane-hexane. Product - yellow solid. Global yield: 1.59 g (90 %).

$^1\text{H NMR}$ (300 MHz, $\text{DMSO-}d_6$): 9.05 (d, $J = 4.3$ Hz, 2H), 8.45 (s, 2H), 8.34 (d, $J = 7.9$ Hz, 2H), 8.25 (d, $J = 8.2$ Hz, 2H), 8.17 (d, $J = 7.8$ Hz, 2H), 7.97 (d, $J = 7.6$ Hz, 2H), 7.90 (t, $J = 7.2$, 2H), 7.80 (t, $J = 7.0$ Hz, 2H), 7.74 (d, $J = 4.1$ Hz, 2H), 6.54 (s, 2H), 6.25-6.18 (m, 2H), 5.53 (d, $J = 17.2$ Hz, 2H), 5.38-5.33 (m, 4H), 5.14 (d, $J = 12.2$, 2H), 4.46 (d, $J = 7.8$ Hz, 2H), 4.20-4.12 (m, 2H), 4.09-4.01 (m, 4H), 3.60-3.52 (m, 2H), 3.42-3.39 (m, 2H), 2.33-2.29 (m, 2H), 2.17-2.10 (m, 2H), 2.07-1.99 (m, 2H), 1.81-1.76 (m, 4H), 1.56-1.48 (m, 2H), 1.29-1.16 (m, 6H), 0.72 (t, $J = 7.1$ Hz, 6H).

SI-3.2. Synthesis of 2,3,4,5,6-pentafluorophenylalanine and its N-protected derivatives

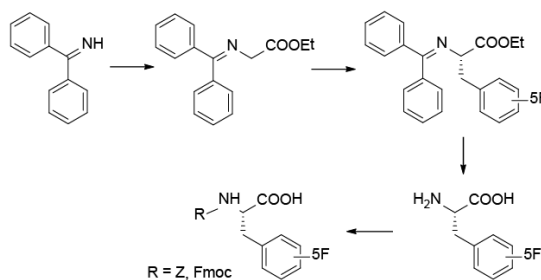


Figure SI-3.2. Synthetic Scheme for 2,3,4,5,6-pentafluorophenylalanine and its N-protected Derivatives

3.2.1. Synthesis of N-(diphenylmethylene)glycine Ethyl Ester

Benzophenone imine (20.26 g, 0.11 mol), glycine ethyl ester (15.60 g, 0.10 mol), and a small amount of magnesium sulfate (as a desiccant) were mixed in dichloromethane (400 mL) with a calcium chloride tube connected and the mixture was stirred for 24 hours. The mixture was filtered and the filtrate dried on a rotary evaporator (Heidolph, Schwabach, Germany). The obtained residue was dissolved in 200 mL of diethyl ether and washed twice with 200 mL of water. The organic phase was dried using magnesium sulfate and filtered. The filtrate was dried using a rotary evaporator (Heidolph, Schwabach, Germany) and the obtained residue recrystallized from diethyl ether with hexane. Product - white solid. Yield: 29.6 g (quantitative).

$^1\text{H NMR}$ (300 MHz, $\text{DMSO-}d_6$): 7.59-7.36 (m, 8H), 7.22-7.16 (m, 2H), 4.13 (s, 2H), 4.10 (q, $J = 7.1$, 2H), 1.17 (t, $J = 7.1$, 3H).

3.2.2. Synthesis of 5F-Phe

N-(diphenylmethylene) glycine ethyl ester (5.2 g, 18.7 mmol) and chiral catalyst (333 mg, 0.32 mmol) were mixed in toluene/chloroform (75 mL, 7:3 v/v). 2,3,4,5,6-pentafluorobenzyl bromide (25 g, 93.5 mmol) was added, and the reaction mixture was cooled to 0°C. A 50% aqueous solution of

KOH (25 mL) was added, and the mixture was left stirring at 0°C for 10 hours. The obtained suspension was diluted with ether (750 mL) and washed with water (3 x 500 mL). The organic phase was dried with magnesium sulfate, filtered through a celite pad, and concentrated in vacuo. Hydrogen chloride 6M (100 mL) was added, and the solution was stirred under reflux for 5 hours at 108°C. The solution got washed three times with diethyl ether (400 mL), and the aqueous phase dried *in vacuo*. Product - white solid. Yield: 1.88 g (63 %).

¹H NMR (300 MHz, D₂O): 4.30 (t, J = 7.01 Hz, 1H), 3.43 (dttd, J = 6.91, 14.95, 21.86 Hz, 2H); ¹⁹F NMR (300 MHz, CHCl₃-d): -141.5 (dd, J = 22.52, 8.06 Hz, 2F), -156.6 (t, J = 20.58 Hz, 1F), -161.2 (td, J = 22.09, 8.73 Hz, 2F).

3.2.3. Synthesis of Z-L-2,3,4,5,6-pentafluorophenylalanine

L-2,3,4,5,6-pentafluorophenylalanine was protected at the amino-terminus using N-(benzyloxycarbonyloxy)succinimide (Z-OSu). In a round bottom flask, L-2,3,4,5,6-pentafluorophenylalanine (4.950 g, 19.4 mmol) was dissolved in an acetone: water (50:50) mixture (100 mL). The pH was adjusted to pH 7 using a saturated NaHCO₃ solution. Z-OSu (4.239 g, 19.4 mmol) was added, and the reaction was left stirring overnight. Acetone was evaporated from the solution using a rotary evaporator (Heidolph, Schwabach, Germany), after which the aqueous solution was washed with dichloromethane (100 mL x2). The aqueous layer was then acidified to pH 2.5 using concentrated hydrogen chloride, causing the compound to precipitate as a white solid. The compound was extracted from the aqueous layer using ethyl acetate (100 mL x 3). The combined organic layers were washed with water (150 mL). The organic phase was then dried using magnesium sulfate and filtered. The solution was concentrated using a rotary evaporator (Heidolph, Schwabach, Germany) and further dried with a deep vacuum. Product - white powder. Product - white solid. Yield: 7.08 g (94 %).

¹H NMR (300 MHz, DMSO-d₆): 7.75 (d, J = 9.62 Hz, 1H), 7.42-7.22 (m, 5H), 4.24 (qd, J = 5.58 Hz, 14.14 Hz 1H), 3.24-2.98 (m, 3H). ¹⁹F NMR (300 MHz, DMSO-d₆): -142.5 (dd, J = 17.03, 6.49 Hz, 2F), -157.2 (t, J = 21.90 Hz, 1F), -161.2 (td, J = 22.71, 7.73 Hz, 2F).

3.2.4. Synthesis of Fmoc-L-2,3,4,5,6-pentafluorophenylalanine

Fmoc-OSu (129 mg, 0.38 mmol) was added to a solution of 5F-Phe (100 mg, 0.392 mmol) and sodium carbonate (91.5 mg, 0.392 mmol) in H₂O/acetone (1:1) over a period of 1 h while the pH was kept at 9.0–10.0 by the addition of 1 M sodium carbonate solution. The mixture was allowed to react overnight. EtOAc was added, and the mixture was acidified with 6 M HCl. The organic layer was washed with water, dried, and concentrated. On the addition of petroleum ether, the product crystallized. Product - white solid. Global yield: 168 mg (90 %).

¹H NMR (300 MHz, DMSO-d₆): 7.88 (m, 3H), 7.66 (d, 2H), 7.46-7.26 (m, 4H), 4.34-4.12 (m, 3H), 3.27-3.05 (m, 2H); ¹⁹F NMR (300 MHz, DMSO-d₆): -142.3 (dd, 2F), -157.2 (t, 1F), -163.4 (td, 2F).

SI-3.3. Synthesis of Dipeptide-ethylenediamine-Boc Derivatives

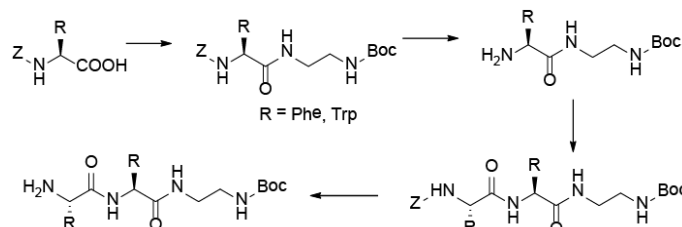


Figure SI-3.3. Synthetic scheme for Dipeptide-ethylenediamine-Boc Derivatives

3.3.1. Synthesis of Ethylenediamine-Boc Derivatives of Amino Acids

In a round bottom flask, Z-protected amino acid (1 eq.) and DMTMM*Cl (1.2 eq.) were dissolved in methanol. After 10 minutes, N-BOC-diaminoethane (1.1 eq.) was added, and the reaction left to continue overnight. The product was precipitated in water and filtered. The compound was further dried for 3 hours on a vacuum pump.

Z-Φ-EDA-Boc. Product - white solid. Global yield: 1.31 g (95 %). ¹H NMR (300 MHz, DMSO-d₆): 8.03 (t, 2H), 7.55 (d, 1H), 7.39-7.20 (m, 5 H), 6.73 (t, 1H), 5.06-4.86 (m, 2H), 4.31-4.21 (m, 1H), 3.17-2.87 (m, 6H), 1.36 (s, 9H); ¹⁹F NMR (300 MHz, DMSO-d₆): -142.83 (dd, 6.49 Hz, 2F), -157.42 (t, 1F), -163.7 (td, 2F)

Z-W-EDA-Boc. Product - yellowish solid. Global yield: 1.47 g (95 %). ¹H NMR (300 MHz, DMSO-d₆): 10.88(s, 1H), 8.02 (t, 2H), 7.61 (d, 1H), 7.37-7.20 (m, 7 H), 7.13 (d, 1H), 7.00 (ddt, 1H), 6.73 (t, 1H), 4.94 (s, 2H), 4.21 (m, 1H), 3.17-2.82 (m, 6H), 1.37 (s, 9H).

In a round bottom flask, Z-X-EDA-Boc was dissolved in methanol (150 mL). The solution was mixed with a palladium catalyst (150 mg) and purged (3 x N₂/ vacuum cycle) to remove moisture and oxygen. The system was then placed under hydrogen. After the reaction completed (checked with a ninhydrin test as described in the frame below), the solution was filtered over a celite pad and dried using a rotary evaporator (Heidolph, Schwabach, Germany).

H-Φ-EDA-Boc: Product - white solid. Global yield: 920 mg (86 %). ¹H NMR (300 MHz, DMSO-d₆): 7.84 (t, J = 5.47Hz, 1H), 6.68 (t, J = 4.45Hz, 1H), 3.11-2.80 (m, 7H), 1.29 (s, 11H). ¹⁹F NMR (300 MHz, DMSO-d₆): -142.83 (dd, J = 17.03, 6.49 Hz, 2F), -158.36 (t, J = 21.90 Hz, 1F), -163.7 (td, J = 6.88 Hz, 2F). m/z: 397.2 Da (Expected: 397 Da).

H-W-EDA-Boc: Product - yellowish viscous liquid. Global yield: 1.01 g (88 %). ¹H NMR (300 MHz, DMSO-d₆): 10.83 (s, 1H), 7.93 (t, 1H), 7.55 (d, 1H), 7.33 (d, 1H), 7.14 (d, 1 H), 7.00 (ddt, 1H), 6.77 (t, 1H), 3.43 (dd, 1H), 3.13-2.91 (m, 6H), 2.74 (dd, 1H), 1.37 (s, 9H).

3.3.2. Synthesis of N-Boc-N'-(dipeptide) Ethylenediamine

In a round bottom flask, the corresponding Z-L-amino acid (1.1 eq.) and DMTMM*Cl (1.2 eq.) were dissolved in methanol. After 10 minutes, H-X-EDA-Boc (1.0 eq) dissolved in methanol was added. The reaction was allowed to proceed overnight. An excess amount of water was then added to the flask. The mixture was filtered, washed with water, and dried.

Z-WW-EDA-Boc: Product - white to pinkish powder. Global yield: 1.40 g (79 %). ¹H NMR (300 MHz, DMSO-d₆): 10.81(s, 1H), 10.78(s, 1H), 8.02 (d, 1H), 7.92 (t, 1H), 7.60 (d, 1H), 7.57 (d, 1H), 7.39-6.91 (m, 15 H), 6.70 (t, 1H), 4.94 (s, 2H), 4.50 (m, 1H), 4.29 (m, 1H), 3.18-2.80 (m, 8H), 1.36 (s, 9H).

Directly after filtration, compound Z-XX-EDA-Boc was mixed in a flask together with a Pd/C catalyst (150 mg) in methanol (100 mL) and water (10 mL). After purging the flask (three cycles of N₂/ vacuum) of moisture and oxygen, the system was put under hydrogen pressure and allowed to react for two hours. The solution was filtered through a celite pad and the filtrate was dried on a rotary evaporator followed by a deep vacuum.

H-ΦΦ-EDA-Boc: Purification of the residue was carried out by column chromatography with Ethyl acetate: dichloromethane (9:1) as the mobile phase. Two fractions eluted shortly after each other with the last eluted fraction containing the deprotected dipeptide. Product - white powder. Global yield after two steps: 1.33 g (68 %). ¹H NMR (300 MHz, DMSO-d₆): 8.26 (m, 1H), 8.11 (t, J = 4.64 Hz, 1H), 6.71 (m, 1H), 4.51 (m, 1H), 3.21-2.78 (m, 7H), 2.75-2.61 (m, 1), 1.37 (s, 9H). ¹⁹F NMR (300 MHz, DMSO-d₆): -141.87 (dd, J = 25.29, 7.33 Hz, 2F), -142.57 (dd, J = 8.17, 24.47Hz, 2F), -

157.48 (t, $J = 22.84$ Hz, 1H), -158.36 (t, $J = 21.21$ Hz, 1F), -163.54 - -164.13 (m, 4F). m/z : 783.3 Da

H-WW-EDA-Boc: Product - white powder. Global yield: 744 mg (85 %). ^1H NMR (300 MHz, DMSO- d_6): 10.84(d, 1H), 10.78(d, 1H), 8.02 (d, 1H), 7.92 (t, 1H), 7.53 (d, 1H), 7.41 (d, 1H), 7.33 (d, 1H), 7.30 (d, 1H), 7.15-6.86 (m, 6 H), 6.72 (t, 1H), 4.50 (m, 1H), 3.47 (dd, 1H), 3.07-2.85 (m, 7H), 2.66 (dd, 1H), 1.36 (s, 9H).

SI-3.4. Synthesis of H-(L,D,L)-FFF-Boc

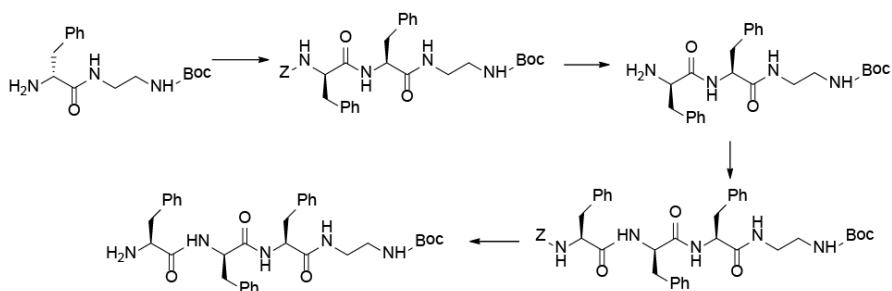


Figure SI-3.4. Synthetic scheme for H-(L,D,L)-FFF-Boc

H-(L,D,L)-FFF-EDA-Boc was synthesized in a similar manner to H-(L,L,L)-FFF-EDA-Boc, as described in Chapter 2.

H-(D,L)-FF-EDA-Boc: Product - white powder. Global yield: 1.25 g (80 %). ^1H NMR (300 MHz, DMSO- d_6): 8.12 (d, 1H), 8.00 (t, 1H), 7.30-7.03 (m, 10H), 6.72 (t, 1H), 4.46 (m, 1H), 3.37 (dd, 1H), 3.20-2.70 (m, 7H), 2.42 (dd, 1H), 1.54 (br.s, 2H), 1.37 (s, 9H).

Z-(L,D,L)-FFF-EDA-Boc: Product - white powder. Global yield: 2.01 g (93 %). ^1H NMR (300 MHz, DMSO- d_6): 8.46 (d, 1H), 8.20 (d, 1H), 8.11 (t, 1H), 7.36-6.98 (m, 20H), 6.74 (t, 1H), 4.89 (s, 2H), 4.55 (m, 2H), 4.21 (m, 1H), 3.10-2.22 (m, 8H), 1.37 (s, 9H).

H-(L,D,L)-FFF-EDA-Boc: Product - white powder. Global yield: 1.37 g (86 %). ^1H NMR (300 MHz, DMSO- d_6): 8.47 (d, 1H), 8.08 (m, 2H), 7.31-6.90 (m, 15H), 6.77 (t, 1H), 4.55 (m, 1H), 4.45 (m, 1H), 3.39 (dd, 1H), 3.21-2.31 (m, 8H), 1.51 (br. s, 2H), 1.37 (s, 9H).

SI-3.5. Synthesis of H-XFF-EDA-Boc tripeptides.

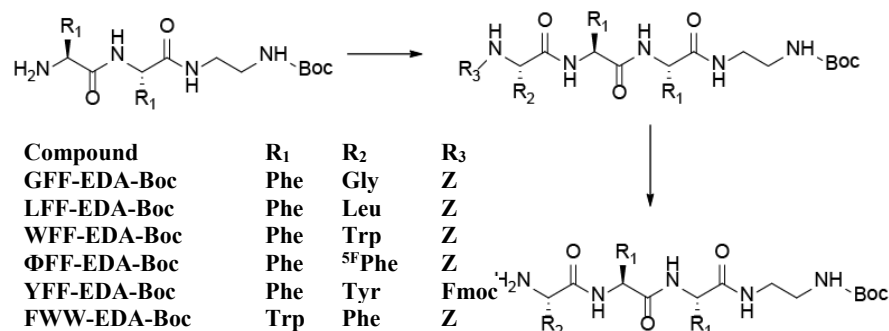


Figure SI-3.5. Synthetic scheme for H-XFF-EDA-Boc and H-XWW-EDA-Boc Tripeptides.

SI-3.5.1. Synthesis of Z-protected Tripeptides with Terminal EDA-Boc

In a round bottom flask, a corresponding Z-amino acid (1.1 eq.) and DMTMM*Cl (1.2 eq) were dissolved in methanol. After 10 minutes, H-FF-EDA-Boc (1.0 eq) or H-WW-EDA-Boc dissolved in methanol was added. The reaction was allowed to proceed overnight.

Z-GFF-EDA-Boc: Product - white powder. Global yield: 1.76 g (71 %). ¹H NMR (300 MHz, DMSO-d₆): 8.16 (d, 1H), 7.94 (d, 1H), 7.82 (t, 1H), 7.43-7.11 (m, 16H), 6.67 (t, 1H), 5.01 (d, 2H), 4.49 (m, 1H), 4.42 (m, 1H), 4.11 (m, 1H), 3.56 (m, 2H), 3.12-2.67 (m, 10H), 1.36 (s, 9H).

Z-LFF-EDA-Boc: Product - white powder. Global yield: 1.91 g (93 %). ¹H NMR (300 MHz, DMSO-d₆): 8.11 (d, 1H), 7.83 (m, 2H), 7.39-7.10 (m, 16H), 6.67 (t, 1H), 5.01 (d, 2H), 4.50 (m, 1H), 4.41 (m, 1H), 3.97 (m, 1H), 3.14-2.70 (m, 8H), 1.59-1.81 (m, 11H), 0.81 (dd, 6H).

Z-ΦFF-EDA-Boc. An excess amount of water was added to the flask. The solution was filtered and washed with water. Product - white powder. Global yield: 1.29 g (63 %).

¹H NMR (300 MHz, DMSO-d₆): 8.19 (d, 1H), 8.04 (d, 1H), 7.83 (t, 1H), 7.49 (d, 1H), 7.38-7.09 (m, 15H), 6.66 (t, 1H), 4.96 (q, 2H), 4.54 (m, 1H), 4.43 (m, 1H), 4.31 (m, 1H), 3.97 (m, 1H), 3.13-2.70 (m, 12H), 1.36 (s, 9H). ¹⁹F NMR (300 MHz, DMSO-d₆): -141.9 (dd, J = 24.4, 6.7 Hz, 2F), -157.4 (t, J = 22.3 Hz, 1F), -163.5 (ddd, J = 6.7 Hz, 22.3 Hz, 2F).

Fmoc-Y(OtBu)FF-EDA-Boc: Product - white powder. Global yield: 1.03 g (50 %). ¹H NMR (300 MHz, DMSO-d₆): 8.17 (d, 1H), 8.04 (d, 1H), 7.88 (m, 3H), 7.63 (d, 2H), 7.52 (d, 1H), 7.41 (t, 2H), 7.33-6.97 (m, 15H), 6.77 (d, 2H), 6.69 (t, 1H), 5.75 (s, 4H), 4.55 (m, 1H), 4.48 (m, 1H), 4.27-3.92 (m, 4H), 3.15-2.57 (m, 10H), 1.36 (s, 9H), 1.17 (s, 9H).

Z-WFF-EDA-Boc: Product - yellowish powder. Global yield: 1.71 g (91 %). ¹H NMR (300 MHz, DMSO-d₆): 10.77 (s, 1H), 8.16 (d, 1H), 7.31 (d, 1H), 7.87 (t, 1H), 7.58 (d, 1H), 7.49 (t, 2H), 7.46-6.83 (m, 19H), 6.69 (t, 1H), 4.92 (s, 2H), 4.54 (m, 1H), 4.45 (m, 1H), 4.52 (m, 1H), 3.08-2.67 (m, 10H), 1.37 (s, 9H).

Z-FWW-EDA-Boc: Product - yellowish powder. Global yield: 2.15 g (73 %). ¹H NMR (300 MHz, DMSO-d₆): 10.81 (s, 1H), 10.78 (s, 1H), 8.13 (d, 1H), 8.04 (d, 1H), 7.80 (t, 1H), 7.59 (d, 1H), 7.55 (d, 1H), 7.42 (d, 1H), 7.36-6.92 (m, 21H), 6.68 (t, 1H), 4.92 (q, 2H), 4.57 (m, 1H), 4.46 (m, 1H), 4.25 (m, 1H), 3.88-2.82 (m, 9H), 2.64 (dd, 1H), 1.36 (s, 9H).

SI-3.5.2. Synthesis of Tripeptides with Terminal EDA-Boc

In a round bottom flask, the intermediate compound Z-XFF-EDA-Boc was dissolved in methanol (150 mL). The solution was mixed with a palladium catalyst (10% w/w) and purged (3 x N₂/vacuum cycle). Hereafter the system was put under hydrogen pressure. After the reaction was completed (checked with a ninhydrin test as described in the frame below), the solution was filtered over a celite pad and dried using a rotary evaporator (Heidolph, Schwabach, Germany).

H-WFF-EDA-Boc: Product - yellowish powder. Global yield: 1.03 g (85 %). ¹H NMR (300 MHz, DMSO-d₆): 10.85 (d, 1H), 8.28 (d, 1H), 7.96 (t, 1H), 7.52 (d, 1H), 7.33 (d, 1H), 7.29-6.94 (m, 15H), 6.71 (t, 1H), 4.54 (m, 1H), 4.44 (m, 1H), 3.40 (dd, 1H), 3.15-2.58 (m, 12H), 1.16 (br.s, 2H), 1.37 (s, 9H).

H-ΦFF-EDA-Boc: Product - white powder. Global yield: 0.92 g (87 %). ¹H NMR (300 MHz, DMSO-d₆): 8.23 (d, 1H), 8.03 (d, 1H), 7.88 (t, 1H), 7.30-7.09 (m, 10H), 6.69 (t, 1H), 4.52 (m, 1H), 4.43 (m, 1H), 3.13-2.66 (m, 11H), 2.57 (dd, 1H), 1.73 (br.s, 2H), 1.36 (s, 9H). ¹⁹F NMR (300 MHz, DMSO-d₆): -142.2 (dd, J = 24.0, 7.1 Hz, 2F), -158.4 (t, J = 22.2 Hz, 1F), -163.8 (ddd, J = 6.7 Hz, 22.2 Hz, 2F).

H-LFF-EDA-Boc: Product - white powder. Global yield: 1.55 g (90 %). $^1\text{H NMR}$ (300 MHz, DMSO- d_6): 8.19 (d, 1H), 7.93 (m, 2H), 7.30-7.08 (m, 11H), 6.70 (t, 1H), 4.50 (m, 1H), 4.43 (m, 1H), 3.15-2.70 (m, 9H), 1.60 (m, 2H), 1.37 (s, 9H), 1.27-0.98 (m, 2H), 0.79 (dd, 6H).

H-GFF-EDA-Boc: Product - white powder. Global yield: 1.34 g (87 %). $^1\text{H NMR}$ (300 MHz, DMSO- d_6): 8.22 (d, 1H), 7.91 (d, 1H), 7.31-7.08 (m, 11H), 6.70 (t, 1H), 4.51 (m, 1H), 4.43 (m, 1H), 3.19-2.69 (m, 12H), 1.69 (br.s, 2H), 1.36 (s, 9H).

H-FWW-EDA-Boc: Product - yellowish powder. Global yield: 1.67 g (83 %). $^1\text{H NMR}$ (300 MHz, DMSO- d_6): 10.79 (s, 2H), 8.09 (m, 2H), 7.86 (t, 1H), 7.55 (d, 1H), 7.50 (d, 1H), 7.42 (d, 1H), 7.33-6.89 (m, 12H), 6.71 (t, 1H), 4.58 (m, 1H), 4.47 (m, 1H), 3.40 (m, 1H), 3.12-2.81 (m, 10H), 1.36 (s, 9H).

SI-3.5.3. Deprotection of Fmoc-YFF-EDA-Boc

H-Y(OBoc)FF-EDA-Boc: Product - white powder. Global yield: 0.44 g (95 %). $^1\text{H NMR}$ (300 MHz, DMSO- d_6): 8.23 (d, 1H), 8.00-7.89 (m, 2H), 7.86 (d, 1H), 7.68 (d, 1H), 7.41-6.99 (m, 16H), 6.70 (t, 1H), 4.54 (m, 1H), 4.44 (m, 1H), 3.17-2.69 (m, 11H), 2.42 (dd, 1H), 1.60 (br.s, 2H), 1.37 (s, 9H), 1.25 (s, 9H).

SI-3.6. Synthesis of tetrapeptides-ethylenediamine-Boc derivatives.

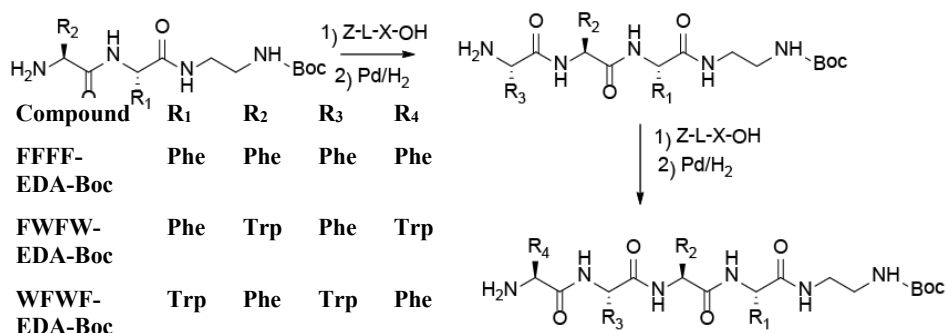


Figure SI-3.6. General scheme of synthesis of EDA-Boc terminal tetrapeptides.

Tetrapeptides FFFF, FWFW, and WFWF were prepared in a similar way to tripeptides, using DMTMM chemistry and Pd/H₂ deprotection.

H-FFFF-EDA-Boc: Product - white powder. Global yield: 1.66 g (97 %). $^1\text{H NMR}$ (300 MHz, DMSO- d_6): 1.37 (s, 9H), 1.53 (br.s, 2H), 2.40 (dd, 1H), 2.68-3.14 (m, 11H), 3.25 (m, 1H), 4.40-4.61 (m, 3H), 6.68 (t, 1H), 7.01-7.31 (m, 20H), 7.89 (t, 1H), 8.18 (d, 2H).

H-WFWF-EDA-Boc: Product - yellowish powder. Global yield: 1.72 g (93 %). $^1\text{H NMR}$ (300 MHz, DMSO- d_6): 1.37 (s, 9H), 1.99 (br.s, 2H), 2.58 (dd, 1H), 2.71-3.24 (m, 11H), 3.39 (m, 1H), 4.48 (dt, 1H), 4.55 (m, 2H), 6.68 (t, 1H), 6.89-7.37 (m, 18H), 7.52 (d, 1H), 7.58 (d, 1H), 7.86 (t, 1H), 8.10 (d, 1H), 8.20 (d, 1H), 10.78 (s, 1H), 10.82 (s, 1H).

H-FWFW-EDA-Boc: Product - yellowish powder. Global yield: 1.26 g (95 %). $^1\text{H NMR}$ (300 MHz, DMSO- d_6): 1.36 (s, 9H), 2.14 (br.s, 2H), 2.36 (dd, 1H), 2.74-3.19 (m, 11H), 3.34 (dd, 1H), 4.41-4.63 (m, 3H), 6.68 (t, 1H), 6.89-7.36 (m, 18H), 7.49 (d, 1H), 7.57 (d, 1H), 7.85 (t, 1H), 8.00 (d, 1H), 8.08 (d, 1H), 8.11 (d, 1H), 10.72 (s, 1H), 10.81 (s, 1H).

SI-3.7. Synthesis of BTA-derivatives of di- tri- and tetrapeptides.

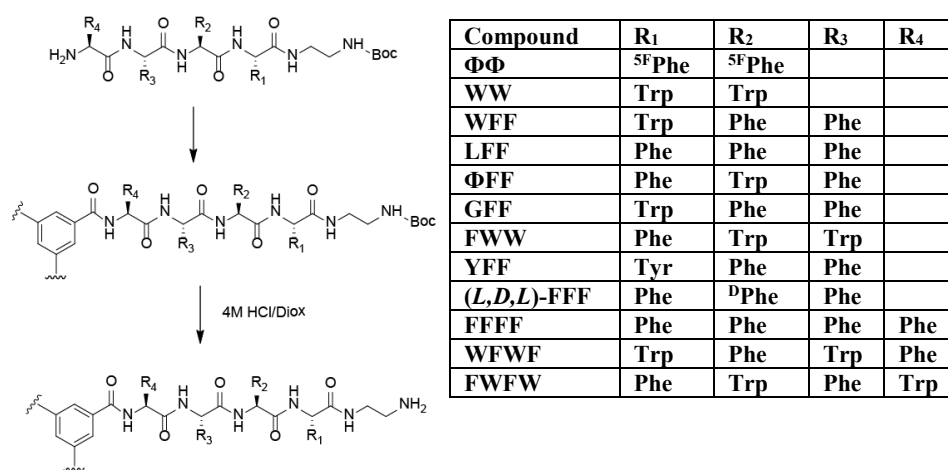


Figure SI-3.7. General scheme of synthesis of BTA-derivatives of di- tri- and tetrapeptides.

SI-3.7.1. Synthesis of Boc-protected BTA derivatives

Corresponding amine (4.5 eq.) was dissolved in DMF. The solution was added to a mixture of DMTMM*BF₄ (4.5 eq.) and trimesic acid (1.0 eq). The reaction mixture was stirred for 48 hours. This was followed by precipitation in 50 mL of diethyl ether. The solids were collected by filtration and washed with diethyl ether. The product was further dried on a vacuum pump to obtain a white powder.

BTA-ΦΦ-EDA-Boc: Product - white powder. Global yield: 520 mg (70 %). ¹H NMR (300 MHz, DMSO-d₆): 8.71 (d, J=5.40, 1H), 8.42-8.22 (m, 2H), 4.75 (m, 1H), 2.95-2.69 (m, 9H), 1.37 (s, 9H). ¹⁹F NMR (300 MHz, DMSO-d₆): -141.93 (dd, J = 20.67, 61.93 Hz, 2F), -157.79 (dd, J = 38.75, 20.73 Hz, 1F), -163.70 (m, 2F). m/z: 1758.2 Da (Expected: 1755 Da)

BTA-WFF-EDA-Boc: Product - white powder. Global yield: 715 mg (87 %). ¹H NMR (300 MHz, DMSO-d₆): 10.65 (d, 1H), 8.67 (d, 1H), 8.29 (s, 1H), 8.14 (d, 1H), 7.87 (t, 1H), 7.64 (d, 1H), 7.31-6.90 (m, 15H), 6.68 (t, 1H), 4.80 (m, 1H), 4.57 (m, 1H), 4.45 (m, 1H), 3.20-2.75 (m, 10H), 1.37 (s, 9H).

BTA-YFF-EDA-Boc: Product - white powder. Global yield: 140 mg (34 %). ¹H NMR (300 MHz, DMSO-d₆): 8.12 (d, 1H), 8.00 (d, 1H), 7.80 (t, 1H), 7.27-7.08 (m, 12H), 6.99 (d, 2H), 6.74 (d, 2H), 6.66 (t, 1H), 6.27 (d, 1H), 4.49 (m, 1H), 4.44 (m, 1H), 4.26 (m, 1H), 3.13-2.75 (m, 11H), 2.62 (dd, 1H), 1.36 (s, 9H), 1.21 (s, 9H).

BTA-ΦFF-EDA-Boc: Product - white powder. Global yield: 470 mg (70 %). ¹H NMR (300 MHz, DMSO-d₆): 8.81 (d, 1H), 8.30 (s, 1H), 8.15 (d, 1H), 7.95 (s, 1H), 7.83 (t, 1H), 7.28-6.93 (m, 10H), 6.65 (t, 1H), 4.85 (m, 1H), 4.56 (m, 1H), 4.44 (m, 1H), 3.12-2.74 (m, 10H), 1.36 (s, 9H).

BTA-LFF-EDA-Boc: Product - white powder. Global yield: 955 mg (89 %). ¹H NMR (300 MHz, DMSO-d₆): 8.61 (d, 1H), 8.39 (s, 1H), 8.08 (d, 1H), 8.02 (d, 1H), 7.84 (t, 1H), 7.28-7.03 (m, 11H), 6.67 (t, 1H), 4.55 (m, 2H), 4.42 (m, 1H), 3.14-2.70 (m, 9H), 1.60 (m, 2H), 1.36 (s, 9H), 0.87 (t, 6H).

BTA-GFF-EDA-Boc: Product - white powder. Global yield: 830 mg (77 %). ¹H NMR (300 MHz, DMSO-d₆): 8.83 (t, 1H), 8.48 (s, 1H), 8.18 (d, 1H), 8.07 (d, 1H), 7.84 (t, 1H), 7.30-7.08 (m, 10H), 6.66 (t, 1H), 4.54 (m, 1H), 4.44 (m, 1H), 4.87 (ddd, 2H), 3.16-2.70 (m, 10H), 1.36 (s, 9H).

BTA-WW-EDA-Boc: Product - yellowish powder. Global yield: 417 mg (83 %). ¹H NMR (300 MHz, DMSO-d₆): 10.77 (d, 1H), 10.68 (d, 1H), 8.69 (d, 1H), 8.30 (s, 1H), 8.23 (d, 1H), 7.90 (t, 1H), 7.66 (d, 1H), 7.56 (d, 1H), 7.27 (m, 2H), 7.13 (m, 2H), 7.98 (ddt, 4H), 6.67 (t, 1H), 4.84 (m, 1H), 4.52 (m, 1H), 3.27-2.83 (m, 8H), 1.36 (s, 9H).

BTA-FWW-EDA-Boc: Product - yellowish powder. Global yield: 1.05 g (65 %). ¹H NMR (300 MHz, DMSO-d₆): 10.77 (s, 2H), 8.66 (d, 1H), 8.32 (d, 1H), 8.17 (s, 1H), 8.03 (d, 1H), 7.82 (t, 1H), 7.56 (m, 2H), 7.33-6.88 (m, 12H), 6.67 (t, 1H), 4.78 (m, 1H), 4.61 (m, 1H), 4.47 (m, 1H), 3.40 (m, 1H), 3.20-2.82 (m, 10H), 1.35 (s, 9H).

BTA-(L,D,L)-FFF-EDA-Boc: Product - white powder. Global yield: 902 mg (85 %). ¹H NMR (300 MHz, DMSO-d₆): 8.52 (d, 1H), 8.48 (d, 1H), 8.12 (m, 2H), 7.31-6.99 (m, 15H), 6.72 (t, 1H), 4.68 (m, 1H), 4.52 (m, 1H), 4.54 (m, 1H), 3.22-2.33 (m, 10H), 1.35 (s, 9H).

BTA-FFFF-EDA-Boc: Product - white powder. Global yield: 720 mg (78 %). ¹H NMR (300 MHz, DMSO-d₆): 1.37 (s, 9H), 2.66-3.20 (m, 12H), 4.40-4.64 (m, 3H), 4.74 (dt, 1H), 6.67 (t, 1H), 6.99-7.32 (m, 20H), 7.87 (t, 1H), 8.04-8.24 (m, 3H), 8.27 (d, 2H).

BTA-WFWF-EDA-Boc: Product - yellowish powder. Global yield 920 mg (76 %). ¹H NMR (300 MHz, DMSO-d₆): 1.36 (s, 9H), 2.70-3.19 (m, 12H), 4.45 (dt, 1H), 4.57 (m, 2H), 4.81 (dt, 1H), 6.67 (t, 1H), 6.87-7.32 (m, 18H), 7.55 (d, 1H), 7.63 (d, 1H), 7.79 (t, 1H), 8.02-8.20 (m, 3H), 8.62 (d, 2H), 10.60 (s, 1H), 10.76 (s, 1H).

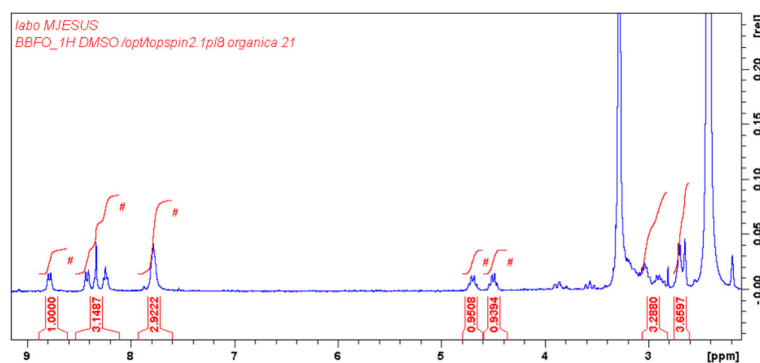
BTA-FWWF-EDA-Boc: Product - yellowish powder. Global yield: 750 mg (84 %). ¹H NMR (300 MHz, DMSO-d₆): 1.36 (s, 9H), 2.75-3.21 (m, 12H), 4.47 (dt, 1H), 4.57 (m, 2H), 4.78 (dt, 1H), 6.67 (t, 1H), 6.86-7.34 (m, 18H), 7.55 (d, 1H), 7.58 (d, 1H), 7.84 (t, 1H), 8.02 (d, 1H), 8.10 (d, 1H), 8.14 (s, 1H), 8.34 (d, 1H), 8.64 (d, 1H), 10.72 (s, 1H), 10.78 (s, 1H).

SI-3.7.2. Synthesis of BTA derivatives of di-, tri- and tetrapeptides

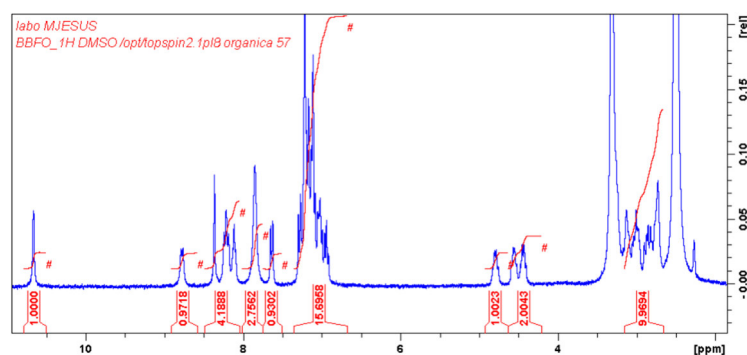
Corresponding Boc-protected BTA derivatives were suspended in methanol (to reach a final concentration of 100 mg/ml). After 5 minutes, a hydrogen chloride solution in dioxane (1 ml per 1 ml of methanol solution) was added and the reaction allowed to proceed for 5 hours. The compound mixture was precipitated in diethyl ether, followed by filtration, and then washing with diethyl ether.

For the synthesis of initiators, the compound was solubilized in water, after which the pH was increased to 10 using NaOH (0.5 M). A white precipitate was filtered on a paper filter. To remove the residual base, the compound was washed with purified water until the pH of the filtrate was 6-7. The obtained product was dried using lyophilization.

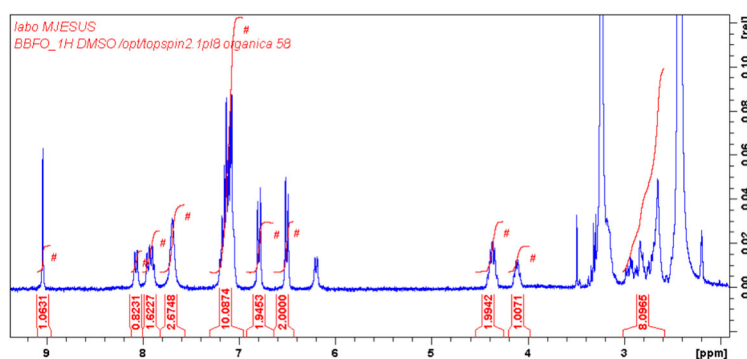
BTA-ΦΦ-EDA-NH₂. Product - yellow powder. Global yield: 395 mg (98 %). ¹H NMR (300 MHz, DMSO-d₆): 9.10 (d, J = 6.73, 1H), 8.42 (t, J = 5.45, 1H), 4.70 (m, 2H), 4.35-3.15 (m, 4H), 2.85-2.74 (m, 2H). ¹⁹F NMR (300 MHz, DMSO-d₆): -142.10 (qd, J = 6.66, 23.69 Hz, 2F), -157.76- -158.01 (m, 1F), -163.48- -163.90 (m, 2F).



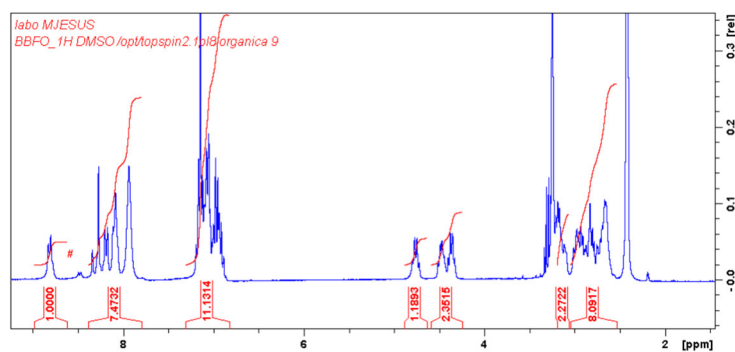
BTA-WFF-EDA-NH2: Product - yellow powder. Global yield: 670 mg (99 %). ^1H NMR (300 MHz, $\text{DMSO}-d_6$): 10.66 (s, 1H), 8.78 (d, 1H), 8.36 (s, 1H), 8.22 (m, 2H), 8.12 (t, 1H), 7.85 (br. s, 3H), 7.64 (d, 1H), 7.35-6.88 (m, 15H), 4.79 (m, 1H), 4.56 (m, 1H), 4.44 (m, 1H), 3.18-2.67 (m, 10H).



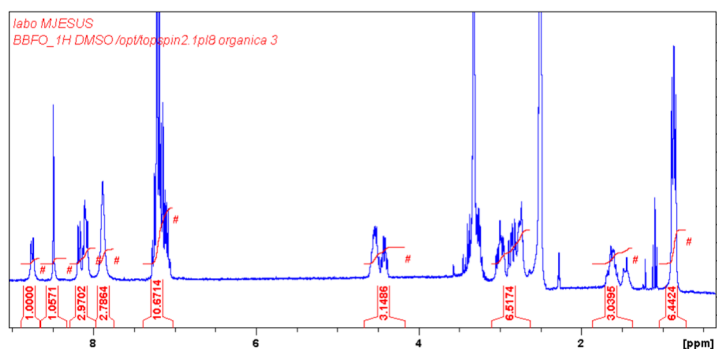
BTA-YFF-EDA-NH2: Product - white powder. Global yield: 120 mg (91 %). ^1H NMR (300 MHz, $\text{DMSO}-d_6$): 9.04 (s, 1H), 8.07 (d, 1H), 7.92 (m, 2H), 7.70 (br. t, 3H), 7.22-7.03 (m, 12H), 6.79 (d, 2H), 6.51 (d, 2H), 6.20 (d, 1H), 4.37 (m, 2H), 4.11 (m, 1H), 3.00-2.57 (m, 10H).



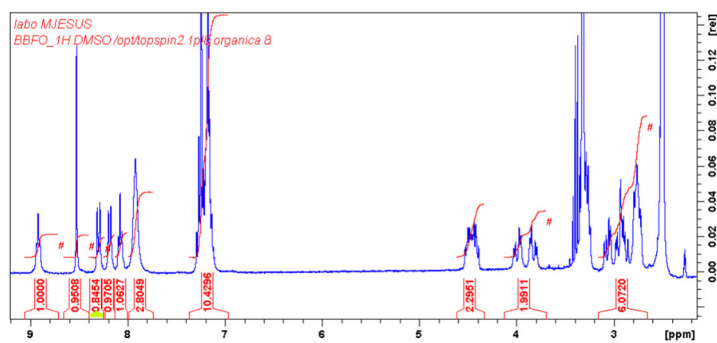
BTA-ΦFF-EDA-NH2: Product - white powder. Global yield: 410 mg (94 %). ^1H NMR (300 MHz, $\text{DMSO}-d_6$): 8.85 (d, $J = 8.04$, 3H), 8.31 (s, 3H), 8.21 (t, $J = 5.47$, 3H), 7.88 (s, 9H), 7.32-7.04 (m, 36H), 4.75 (dt, 3H), 4.48 (dt, 3H), 3.14-2.69 (m, 8H).



BTA-LFF-EDA- NH2: Product - white powder. Global yield: 810 mg (95 %). ^1H NMR (300 MHz, $\text{DMSO}-d_6$): 8.75 (d, 1H), 8.49 (s, 1H), 8.18 (d, 1H), 8.09 (m, 2H), 7.88 (br.t, 3H), 7.28-7.03 (m, 12H), 4.53 (m, 2H), 4.42 (m, 1H), 3.05-2.68 (m, 8H), 1.71-1.37(m, 3H), 0.86 (dd, 6H).

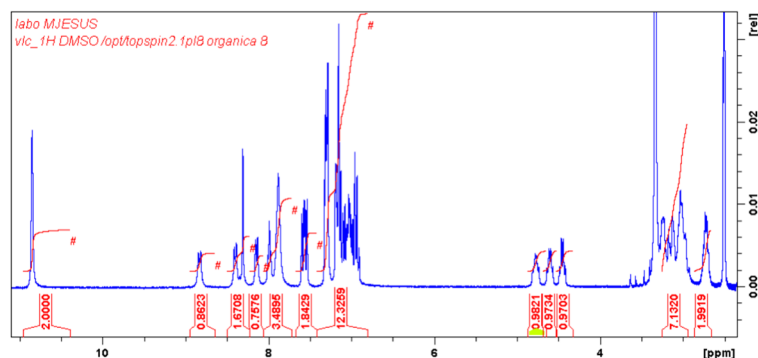


BTA-GFF-EDA-NH2: Product - white powder. Global yield: 695 mg (93 %). ^1H NMR (300 MHz, $\text{DMSO}-d_6$): 8.92 (t, 1H), 8.53 (s, 1H), 8.30 (d, 1H), 8.18 (d, 1H), 8.08 (t, 1H), 7.92 (br. t, 3H), 7.30-7.08 (m, 10H), 4.46 (m, 2H), 3.90 (ddd, 2H), 3.11-2.66(m, 10H).

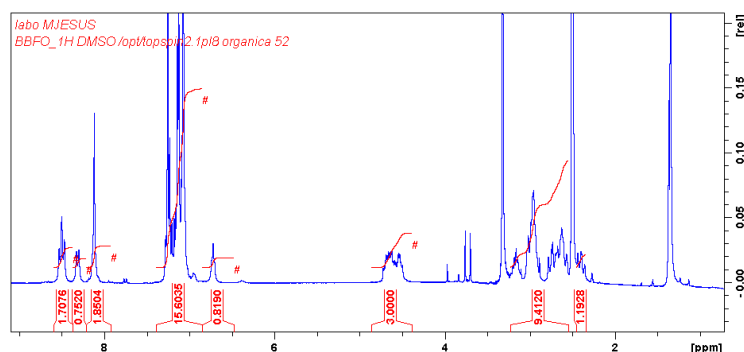


BTA-WW-EDA- NH2: Product - pinkish powder. Global yield: 300 mg (90 %). ^1H NMR (300 MHz, $\text{DMSO}-d_6$): 10.82 (d, 1H), 10.72 (d, 1H), 8.83 (d, 1H), 8.38 (s, 1H), 8.34 (d, 1H), 8.09 (t, 1H), 7.82 (br. t, 3H), 7.66 (d, 1H), 7.56 (d, 1H), 7.28 (dd, 2H), 7.17 (dd, 2H), 6.98 (ddt, 4H), 4.84 (m, 1H), 4.52 (m, 1H), 3.27-2.99 (m, 6H), 2.73 (m, 2H).

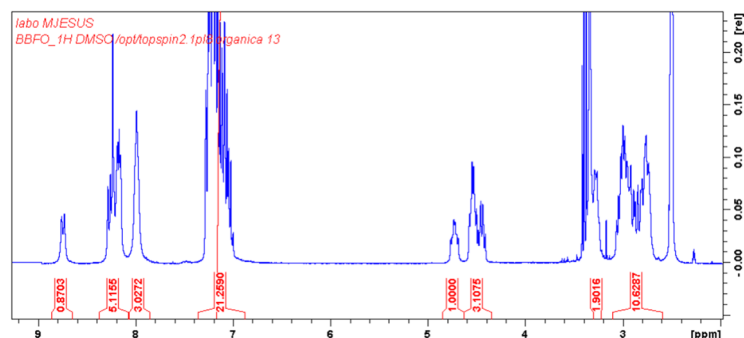
BTA-FWW-EDA-NH2: Product - brownish powder. Global yield: 423 mg (91 %). ^1H NMR (300 MHz, $\text{DMSO}-d_6$): 10.85 (s, 2H), 8.83 (d, 1H), 8.40 (d, 1H), 8.31 (s, 1H), 8.14 (d, 1H), 7.99 (t, 1H), 7.88 (br. t, 1H), 7.58 (d, 2H), 7.54 (d, 2H), 7.35-6.88 (m, 12H), 4.77 (m, 1H), 4.60 (m, 1H), 4.45 (m, 1H), 3.28-2.88 (m, 8H), 2.72 (m, 2H).



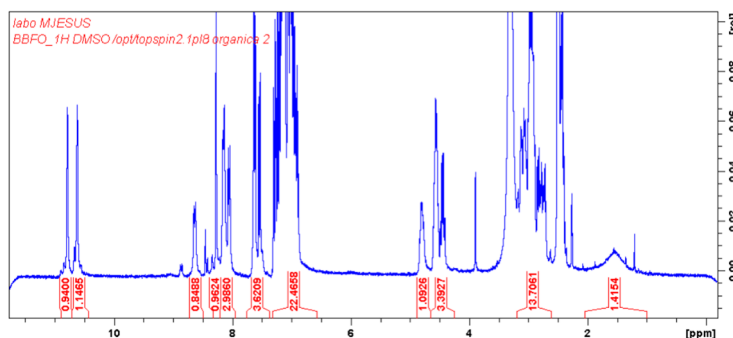
BTA-(L,D,L)-FFF-EDA-NH2: Product - white powder. Global yield: 170 mg (98 %). ^1H NMR (300 MHz, $\text{DMSO}-d_6$): 8.64 (d, 1H), 8.57 (d, 1H), 8.43 (m, 2H), 8.21 (s, 1H), 8.02 (br. t, 3H), 7.31-7.03 (m, 15H), 4.68 (m, 1H), 4.57 (m, 2H), 3.34-2.40 (m, 10H).



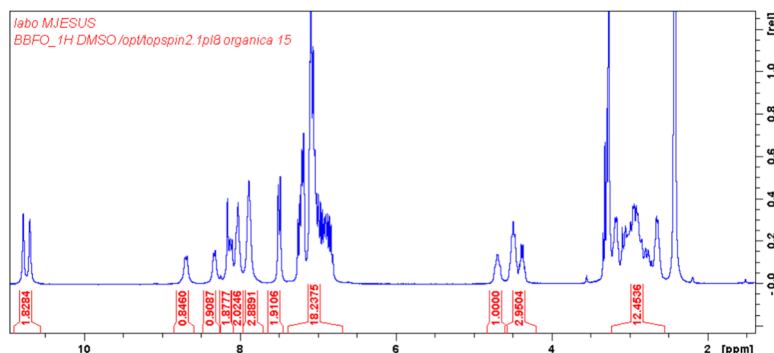
BTA-FFFF-EDA-NH2: Product - white powder. Global yield: 770 mg (98 %). ^1H NMR (300 MHz, $\text{DMSO}-d_6$): 2.68-3.08 (m, 10H), 3.19-3.30 (m, 2H), 4.45 (dt, 1H), 4.54 (m, 2H), 4.73 (dt, 1H), 6.99-7.30 (m, 20H), 7.99 (t, 3H), 8.11-8.31 (m, 5H), 8.74 (d, 1H). Yield: 98 %.



BTA-WFWF-EDA-NH2: Product - yellow powder. Global yield: 650 mg (97 %). ^1H NMR (300 MHz, $\text{DMSO}-d_6$): 1.56 (br.s, 2H), 2.39-2.47 (m, 2H), 2.74-3.19 (m, 10H), 4.45 (dt, 1H), 4.56 (m, 2H), 4.81 (dt, 1H), 6.87-7.35 (m, 18H), 7.55 (d, 1H), 7.63 (m, 2H), 8.06 (d, 1H), 8.16 (m, 2H), 8.28 (s, 1H), 8.64 (d, 1H), 10.63 (s, 1H), 10.79 (s, 1H).



BTA-FWFW-EDA-NH2: Product - yellow powder. Global yield: 556 mg (97 %). ^1H NMR (300 MHz, $\text{DMSO}-d_6$): 2.55-3.23 (m, 12H), 4.38 (dt, 1H), 4.49 (m, 2H), 4.70 (dt, 1H), 6.78-7.30 (m, 18H), 7.49 (d, 2H), 7.89 (br.s, 3H), 8.03 (m, 2H), 8.11 (d, 1H), 8.16 (s, 1H), 8.34 (d, 1H), 8.69 (d, 1H), 10.70 (s, 1H), 10.78 (s, 1H).



SI-3.7. Star-polyglutamate Synthesis

NCA-glutamic acid γ -benzyl ester was added to a Shlenk tube submerged in an ice bath. After purging the tube (3 nitrogen/vacuum cycles), the monomer was dissolved in anhydrous DMF (4 mL). The initiator was dissolved in DMF (2 mL) before addition to the Shlenk tube. The reaction was left stirring for three days at 10°C in an inert atmosphere. After completion of the reaction, THF was added and the mixture was precipitated in cold diethyl ether (150 mL). The compound was recovered upon filtration. Product - white or yellowish powder.

Per 100 mg of polymer, 1 mL of trifluoroacetic acid and 0.1 mL of 48% hydrobromic acid were added to the polymer in a round bottom flask. The reaction was allowed to proceed for 16 hours under stirring. The polymer was precipitated in ether (15 mL / 100 mg) and recovered as a white solid upon filtration and further dried and suspended in water. NaOH (1 M) was added until the full dissolution of the suspension. The solution was filtered through a PES membrane with a pore size of 0.22 μm (Millipore, Burlington, U.S.A.) and acidified using 6M hydrochloric acid to a pH of 3.0-3.5. The precipitate was filtered and washed with purified water until a pH 5.5-6.0 was reached. The

compound was suspended in water, the pH adjusted to 8.5 with 0.5 M NaHCO₃, and dialyzed for 48 hours. Finally, the solution was lyophilized to obtain pure polymer.

ΦΦ-E10: ¹H-NMR (300 MHz, D₂O): 1.54-2.22 (m, 102H), 2.66-3.31 (m, 24H), 4.19 (m, 34H), 7.76 (br. s, 3H). ¹⁹F-NMR (300 MHz, D₂O): -143.2 (m, 18H), -156.1 (m, 9H), -162.6 (m, 18H).

WFF-E10: ¹H-NMR (300 MHz, D₂O): 1.53-2.21 (m, 96H), 2.65-3.31 (m, 30H), 4.18 (m, 31H), 7.35-7.18 (m, 20H), 7.75 (br. s, 3H).

WFW-E10: ¹H-NMR (300 MHz, D₂O): 1.67-2.24 (m, 288H), 2.65-3.31 (br. m, 30H), 4.18 (m, 54H), 7.31-7.19 (m, 20H), 7.85 (br. s, 3H).

FWFW-E10: ¹H-NMR (300 MHz, D₂O): 1.64-2.24 (m, 288H), 2.64-3.27 (br. m, 30H), 4.18 (m, 54H), 7.40-7.21 (m, 20H), 8.01 (br. s, 3H).

FFFF-E10: ¹H-NMR (300 MHz, D₂O): 1.64-2.24 (m, 288H), 2.64-3.27 (br. m, 30H), 4.20 (m, 51H), 7.45-6.67 (m, 20H), 7.79 (br. s, 3H).

SI-3.8. Experimental methods

Optical rotation

To obtain a value of optical rotation for compound Fmoc-Φ, an experiment was performed at room temperature (25°C) using an automated polarimeter (Jasco P-1020, Oklahoma City, USA) at a wavelength of 589 nm, a concentration of 1g/100 mL in methanol with a polarimetry cell of 1 dm.

3.10. References

1. Van Den Hout, K. P., Martín-Rapún, R., Vekemans, J. A. J. M. and Meijer, E. W. *Chem.-A Eur. J.* **13**, 8111–8123 (2007).
2. Ahlers, P., Fischer, K., Spitzer, D. and Besenius, P. *Macromolecules*, **50**, 7712–7720 (2017).
3. Ahlers, P. *et al. Macromol. Biosci.*, **17**, 1–7 (2017).
4. Otter, R., Marijan, C., Seiffert, S. and Besenius, P. *Eur. Polym. J.*, **110**, 90–96 (2019).
5. Spitzer, A. D. *et al. Angew. Chemie Int. Ed.*, **56**, 15461–15465 (2018).
6. Park, H. *et al. Angew. Chem.*, **6**, 3162–3164 (2002).
7. Hughes, A. B. *Amino Acids, Peptides and Proteins in Organic chemistry Vol.4.* (2011).
8. Kurniasih, I. N. *et al. Langmuir*, **31**, 2639–2648 (2015).
9. Stuart, M. C. A., Van De Pas, J. C. and Engberts, J. B. F. N. *J. Phys. Org. Chem.*, **18**, 929–934 (2005).
10. Neel, A. J., Hilton, M. J., Sigman, M. S. and Toste, F. D. *Nature*, **543**, 637–646 (2017).
11. Wimley, W. C., Creamer, T. P. and White, S. H. *Biochemistry*, **35**, 5109–5124 (1996).
12. Appel, R., Tacke, S., Klingauf, J. and Besenius, P. *Org. Biomol. Chem.*, **13**, 1030–1039 (2015).
13. Jana, P., Paikar, A., Bera, S., Maity, S. K. and Haldar, D. *Org. Lett.*, **16**, 38–41 (2014).
14. Doncom, K. E. B. *et al. Soft Matter*, **11**, 3666–3676 (2015).
15. Rathgeber, S. *et al. J. Chem. Phys.*, **117**, 4047–4062 (2002).
16. Garcia, A. M. *et al. Chem*, **4**, 1862–1876 (2018).

Chapter 4

Role of core and chain structure variations on star-PGA self-assembly

4.1. Introduction

Supramolecular assembly of BTA-based systems is highly sensitive to subtle changes in the molecule structure. The addition of structural elements of different classes to BTA-based compounds has been employed to obtain materials with new properties. Compounds with p-carboxybenzoic moieties attached directly to BTA behave as hydrogelators,¹ with X-ray powder diffraction (XRD) analysis demonstrating that compounds became organized in two-dimensional (2D) sheets interacting through π - π -interactions. Studies of benzene-1,3,5-triyl tris(cyclohexyl-carbamate) and BTA-phenylacetic derivatives also reported similar packing.^{2,3} P-aminobenzoate moiety has been commonly used in combination with other blocks, including pentafluorophenylalanines or urea, to increase control over self-assembly.^{4,5} Direct conjugation of alkyl chains to BTA usually results in the formation of organogels and hydrogels; very often, mechanism of self-assembly for these compounds deviate from simple columnar stacking, including, for example, interstack interactions.⁶

The BTA-based core studied in this thesis comprises three structural elements: BTA itself, a short aminoacid sequence, and a short alkyl chain. While Chapter 3 evaluated the effect of the amino acid sequence on star stPGA self-assembly, the overall goal of this chapter is to identify how changes of the other two structural elements in the

core affect self-assembly. In this way, we hope to develop systems with lower critical aggregation concentration (CAC) values and improved or novel morphologies. In this chapter, we studied the effect of (1) flat aromatic insertions (p-aminobenzoyl and m,m-aminoisophthaloyl), (2) aliphatic chains at terminal ends of the core, and (3) the composition of polypeptide chains on self-assembly of supramolecular stPGA.

4.2. Self-assembly of BTA Derivatives with Aromatic Insertions

4.2.1. Self-assembly of BTA Derivatives with Aromatic Insertions as Hydrochloric Salts

Flat aromatic compounds attached directly to the BTA through amide bonds should increase the trend of the compound to self-assemble and, thus, increase the stability of the corresponding stPGA. To test this hypothesis, we prepared two BTA derivatives with p-aminobenzoic acid (ABA) and 5-aminoisophthalic acid (AIP) (**Fig.4.1**) decorated with diphenylalanines.

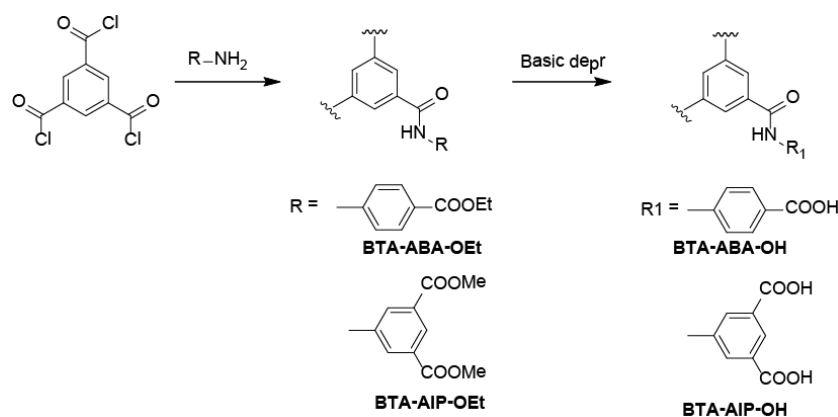


Figure 4.1. General scheme of synthesis of BTA derivatives of aromatic carboxylic acids.

We prepared the **BTA-ABA-OH** and **BTA-AIP-OH** intermediates using a two-step synthesis. In the first step, we performed the alkylation of trimesyl chloride with the corresponding ethyl aminobenzoate or dimethyl aminoisophthalate in anhydrous dimethylacetamide (DMA). When we tried to perform a similar reaction in DMF, the compounds gelled and the product was a mixture of mono-, di- and tri-substituted derivatives, as demonstrated by NMR (**Fig. 4.2**).

We synthesized **BTA-AIP-OH** by the basic deprotection of the methyl ester group. We tested various methods to achieve a sufficient yield of deprotection with the lowest possible amide hydrolysis. **Table 4.1** provides an overview of the methods evaluated. Initially, we employed a two-step deprotection protocol which included an overnight reflux in 19.5 mg/ml NaOH in DMF followed by mild basic hydrolysis with an aqueous solution of 0.56 mg/ml NaOH.⁷ We reached up to 76% deprotection after the

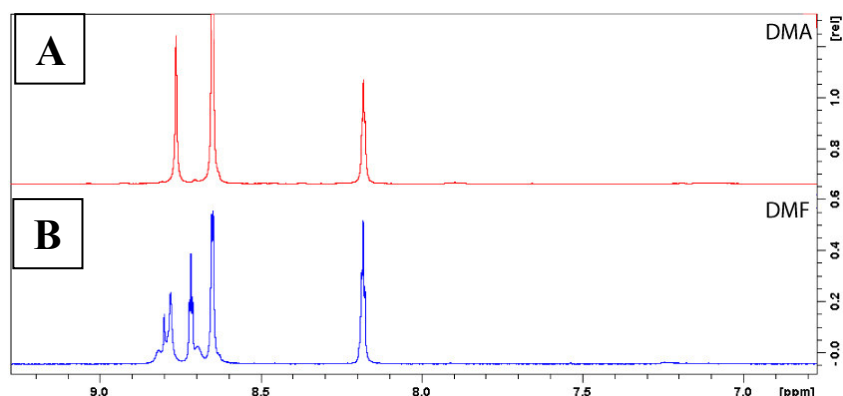


Figure 4.2. NMR spectra of **BTA-AIP-OMe** synthesized in DMA (A) and DMF (B).

first step and no improvement after the second one (Table 4.1, Entry 1). Therefore, we tried more harsh two-step basic hydrolysis with 19.2 mg/ml of KOH in MeOH, which resulted in 51% deprotection after the first step and a slight increase in deprotection (63%) after the second step. We found that acidic hydrolysis with TFA/HBr was less efficient, reaching 50% after 24h at RT. Next, we modified the original two-step protocol, increasing NaOH concentration in DMF to 38.4 mg/ml; after an overnight reaction under reflux, we achieved 93% deprotected of the compound. For the second step, we used a 0.25 g/mL suspension of LiOH in methanol at RT for 2h; we obtained almost quantitative deprotection (Table 4.1, Entry 4). Further increases in the concentration of NaOH resulted in DMF hydrolysis and the formation of non-identified yellow impurities. When we attempted to deprotect the compound with LiOH in methanol in one step, we observed partial hydrolysis of the amide bond with the formation of a complex mixture of products.

Table 4.1. Ester Deprotection Strategies.

| Entry | Method | Conditions | Yield of Deprotection |
|----------|--|--|-----------------------|
| 1 | Double reflux according to | | |
| | 1) Reflux 1st deprotection 2) Reflux 2nd deprotection | 110°C, 24h, DMF, 19.5 mg/mlNaOH 90°C, 24h, DMF, 0.56 mg/mlNaOH | 76% 73% |
| 2 | 1) KOH /methanol 2) KOH /methanol | RT,24h, methanol, 19.2 mg/mlKOH RT, 24h, methanol, +2 mL 2M KOH | 51% 63% |
| 3 | Acids (TFA, HBr) | RT | 50% |
| 4 | Reflux with NaOH | 110°C, 24h, DMF, 38.4 mg/mlNaOH | 93% |
| | LiOH/MeOH | RT, 2h, MeOH, 0.25 g/mL LiOH. | 98% |

To confirm the structure of the obtained compound (**Fig. 4.3A**), we performed a series of 2D NMR experiments. From the heteronuclear single quantum coherence (HSQC) spectra (**Fig. 4.3B**), we identified C9-H9 (125.75 ppm-8.26 ppm), C6-H6 (125.08 ppm-8.74 ppm), and C1-H1 (130.72 ppm-8.87 ppm). With the heteronuclear multiple bond correlation HMBC spectra (**Fig. 4.3C**), we obtained C3-H4 and C8-H6 correlations and a sharply shifted H4 amide peak at 11.02 ppm. Finally, from 2D nuclear Overhauser effect spectroscopy (NOESY) (**Fig. 4.3D**), H4-H1 and H4-H6 crosspeaks unambiguously confirmed that the structure of the compound corresponds to that which we expected.

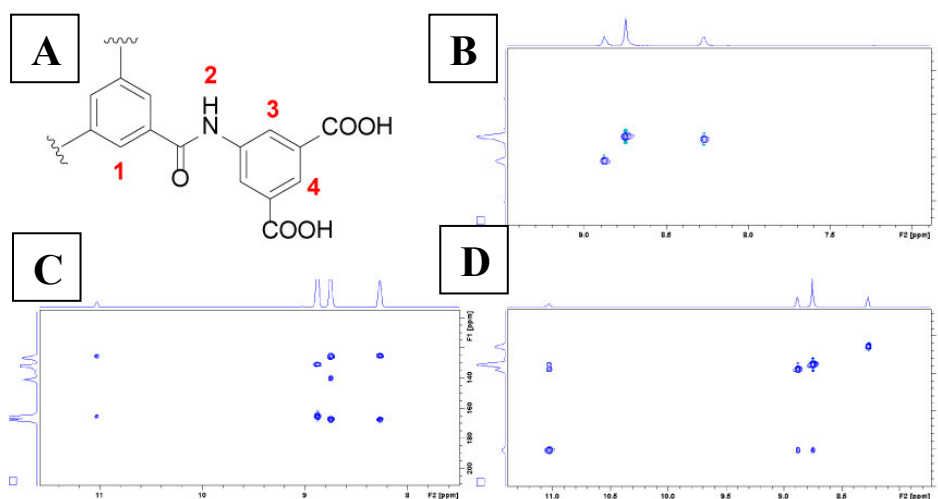


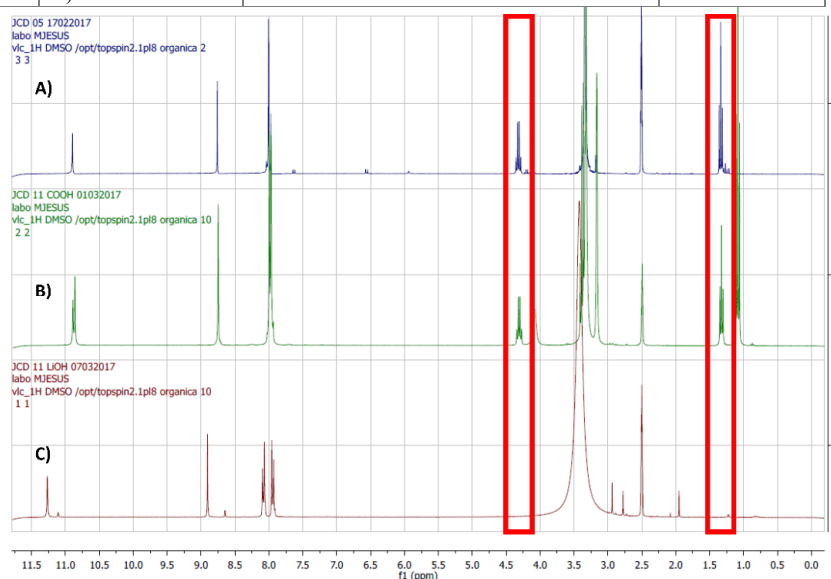
Figure 4.3. A) Structure of BTA-AIP-OH. HSQC (B), HMBC (C) and NOESY (D) spectra.

We obtained **BTA-ABA-OH** by hydrolysis of the ethyl ester; usually, ethyl esters are harder to deprotect than methyl esters. As a first trial, we used the procedure developed for **BTA-ABA-OMe**, and basic deprotection of 38.4 mg/ml NaOH in DMF under reflux resulted in 64% deprotection, while treatment with 0.25 g/ml solution of LiOH in methanol for 2h resulted in 89% deprotection. To achieve an increase in de-esterification efficiency, we performed a second deprotection with LiOH in the same conditions, which provided a deprotection of 98%. We then increased the reaction time to 3.5 h, which resulted directly in 100% deprotection. Table 4.2. provides an overview of the methods employed.

The NMR spectra (**Fig. 4.4**) display a decrease in the signal corresponding to the ethyl groups upon deprotection. Spectra A represents compound **BTA-ABA-OEt**, Spectra B shows the NMR of the compound after deprotection with NaOH, and Spectrum C shows full deprotection.

Table 4.2. Distinct methods and conditions used to achieve the required deprotection yield

| Entry | Method | Conditions | Yield Deprotected |
|----------|---------------------|---------------------------------|-------------------|
| 1 | 1) Reflux with NaOH | 110°C, 24h, DMF, 1.2 mL 4M NaOH | 64% |
| | 2) LiOH/MeOH | RT, 2h, MeOH, 0.25 g/mL LiOH. | 89% |
| | 3) LiOH/MeOH | RT, 2h, MeOH, 0.25 g/mL LiOH | 98% |
| 2 | 1) Reflux with NaOH | 110°C, 24h, DMF, 1.2 mL 4M NaOH | 65% |
| | 2) LiOH/MeOH | RT, 3.5h, MeOH, 0.25 g/mL LiOH. | 100% |

**Figure 4.4.** NMR spectra of **BTA-ABA-OH** before deprotection (A) and after the first (B) and second (C) deprotection steps.

We confirmed the structure of the **BTA-ABA-OH** (**Fig. 4.5A**) by 2D NMR experiments; the HSQC spectra (**Fig. 4.4B**) shows C7-H7 (130.23 ppm-7.93 ppm), C6-H6 (119.46 ppm-8.00 ppm), and C1-H1 (130.69 ppm, 8.90 ppm) couples. From the HMBC spectrum (**Fig. 4.5C**), we observed C8-H9, C3-H4, C3-H1, and C6-H4 crosspeaks and amide H4 at 11.2 ppm.

2D NOESY confirms previous assumptions by identifying H4-H1, H4-H6, and H1-H6 crosspeaks (**Fig. 4.5 D**).

We then performed the synthesis of corresponding phenylalanine derivatives in a similar manner to **F3** described in Chapter 2. DMTMM BF₄ coupling with the corresponding amine and further deprotection with 4M HCl in dioxane provided for the generation of pure compounds (**Fig. 4.6**).



119

F1 and **AIP-F1**, we observed an intensity increase of NR peak without a shift in peak maximum, perhaps explained by the fact that the solution is more apolar than pure water, although we failed to observe the formation of hydrophobic microdomains. There appears to be a shift from 648 nm to 639 nm and to 630 nm in 37.5 mM and 150 mM NaCl solution, respectively (**Fig. 4.7**). In both cases, we observed the same peak shift, but with a higher intensity for **AIP-F1**.

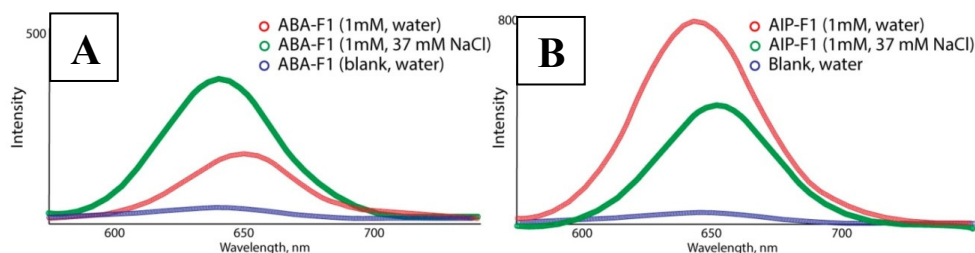


Figure 4.7. Nile red fluorometry of **ABA-F1** and **AIP-F1**.

In the case of **ABA-F2** and **AIP-F2**, we observed a more pronounced difference (**Fig. 4.8**). For 0.5 mM solutions, we found that **ABA-F2** readily assembled in water, and the addition of salt resulted in an insignificant increase in intensity. We also observed a peak shift to 630 nm for both solutions; the NR peak maximum shift for **AIP-F2** in water was 638 nm, which shifted further to 630 nm with an increase in intensity in 37.5 mM NaCl.

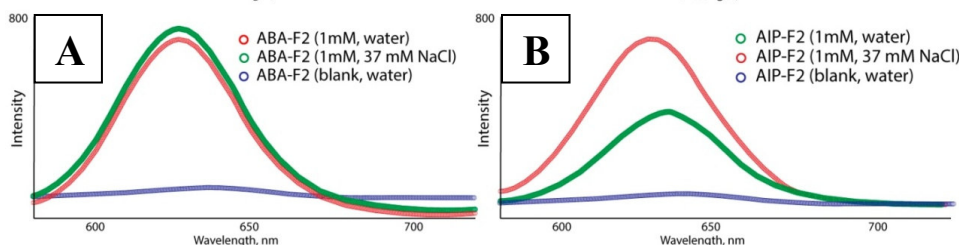


Figure 4.8. Nile red fluorometry results of A) **ABA-F2** and B) **AIP-F2**.

We established CAC values for **AIP-F2** and **ABA-F2** in water of 0.63 mM and 0.057 mM, respectively, and in 120 mM NaCl solution of 0.023 and 0.006 mM, respectively. In both cases, the insertion of aminobenzoate moiety seems highly beneficial for self-assembly behaviour. In aqueous solutions, six-arm compound bears six positive charges, and the Coulomb repulsions are much stronger. In a salty solution, the repulsive interactions become screened, and a rather small difference in CAC can be explained purely by steric hindrance (**Fig. 4.9**).

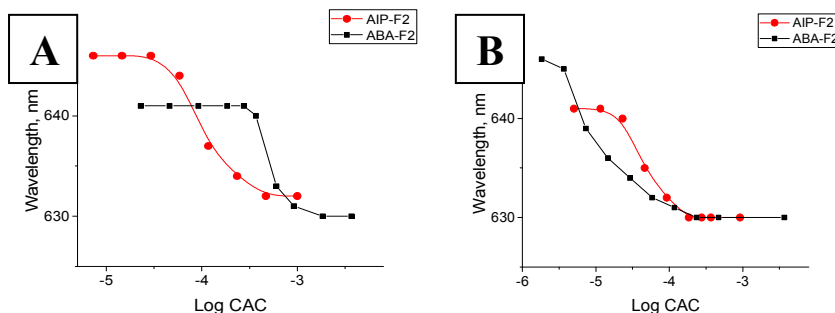


Figure 4.9. Dependence of NR peak maximum on Log CAC values in water (A) and 120 mM NaCl (B).

We measured circular dichroism (CD) spectra of both compounds **ABA-F1** and **AIP-F1** with and without the addition of salt. Spectrum A in Fig. 4.10 demonstrates that compound **ABA-F1** does not possess a secondary structure in pure water. When we increased the ionic strength to 37.5 and 75 mM, we observed a spectrum with two positive peaks at 223 and 319 nm and two negative peaks at 203 and 292 nm. Most probably, in addition to supramolecular polymerization of the compound, another secondary structure appears (extra helices or twisted fibers) similar to that reported by Anuradha et al.⁸ Compound **AIP-F1** provided a very weak CD signal which slightly increased in the presence of salt, suggesting that no measurable secondary structure formed.

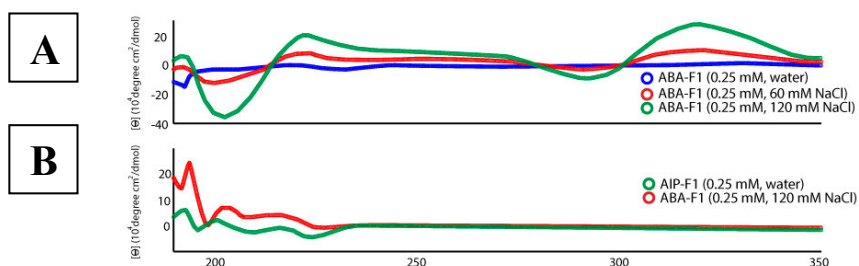


Figure 4.10. CD spectra of **ABA-F1** (A) and **AIP-F1** (B).

Upon heating a solution of **ABA-F1** from 10 to 40 °C, we failed to observe a spectrum, thereby signifying full disassembly (Fig. 4.11).

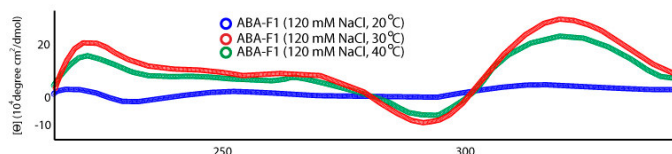


Figure 4.11. CD spectra of **ABA-F1** at different temperatures.

The CD spectra of **ABA-F2** in water (Fig. 4.12A) possesses two maxima at 197 nm and 290 nm and a minimum at 220 nm. The addition of salt resulted in a slight increase in the maximum at 290 nm, while the peak at 195 nm increased more significantly. Compound **AIP-F2** in water (Fig. 4.12B) provides a very weak CD signal; a finding that correlates nicely with fluorimetry results, overall suggesting the formation of small assembled structures. After the addition of salt, a strong minimum appears at 218 nm, which confirms the self-assembly of the compound with the formation of a left-handed spiral (M-helix).

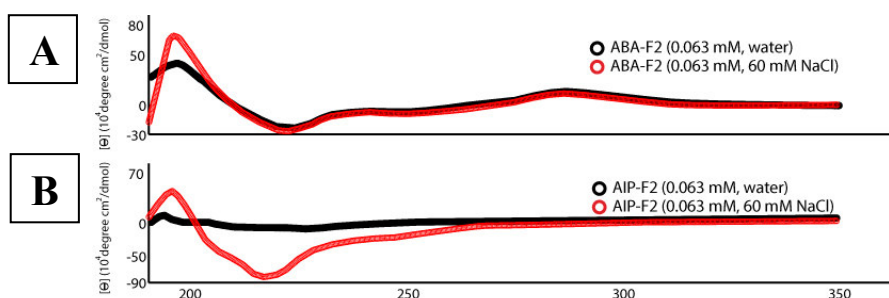


Figure 4.12. CD spectra of **ABA-F2** (A) and **AIP-F2** (B) in water and 60 mM NaCl.

First we performed SAXS experiments for 2.5 mM, 1 mM and 0.5 mM solutions of **ABA-F1** and **AIP-F1** (Fig. 4.13); after data reduction, we used normal and modified Guinier approximation to extract R_g and $R_{g,c}$ values and fiber length (Table 4.3).

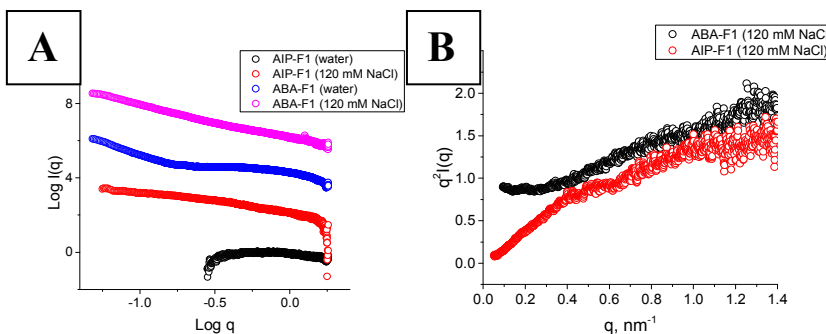


Figure 4.13. SAXS profiles of **ABA-F1** and **AIP-F1** (A) and corresponding Kratky plots (B).

We found ample evidence that compound **AIP-F1** fails to form aggregates in water, given the power law dependence of zero. After the addition of NaCl, we observed a power law dependence of -1, corresponding to rod-like particles with an approximate length of 55 nm. While we already observed some clusterization in water for **ABA-F1**, a more pronounced power law dependence of -2 appeared after the addition of salt. We calculated rod length as 121 nm (in water) and 99 nm (with NaCl). Analysis of $P(r)$ functions for compounds (Fig. 4.14) in water confirmed the absence of aggregation of compound **AIP-F1**; the observed D_{max} of 2.5 nm corresponds to unimolecular species

of, possibly, small clusters (**Fig. 4.14**). For **ABA-F1** in water and in the presence of salt, the $P(r)$ function is typical for rod-like particles; however, in water, it displays strong oscillations due to interference of interparticle repulsions.

Table 4.3. SAXS results of compounds **ABA-F1** and **AIP-F1**, both with and without NaCl.

| Compound | R_g (nm) | R_c (nm) | L (nm) | Power law |
|----------------------|------------|------------|----------|-----------|
| ABA-F1 | 34.8 | 0.81 | 121 | - |
| ABA-F1 - NaCl | 28.6 | 0.82 | 99 | -2 |
| AIP-F1 | 1.1 | 0 | 0 | - |
| AIP-F1 - NaCl | 15.9 | 0.9 | 55 | -1 |

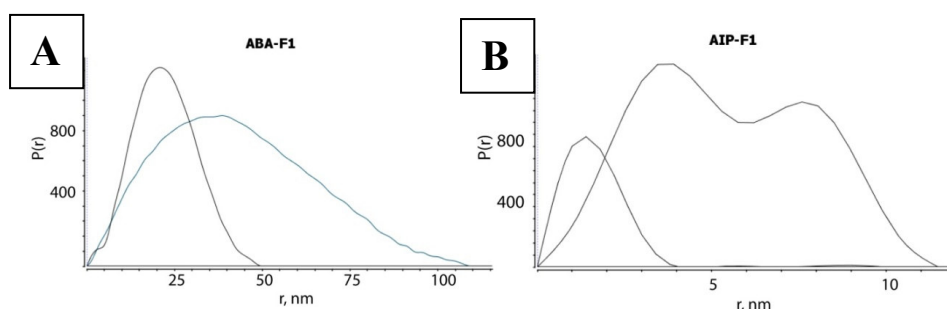


Figure 4.14. $P(r)$ functions for compounds **ABA-F1** and **AIP-F1** in water and 120 mM NaCl.

For **AIP-F1** in water, the $P(r)$ function corresponds to unimolecular species. However, the $P(r)$ function possesses a strange appearance with two defined maxima in the presence of salt, which is probably related to the partial overlap of the molecules during self-assembly or the formation of spherical micelles. **Fig. 4.15** displays the SAXS profiles of compounds **AIP-F2** and **ABA-F2**; we calculated R_g and $R_{g,c}$ values using standard and modified Guinier approximation (**Table 4.4**).

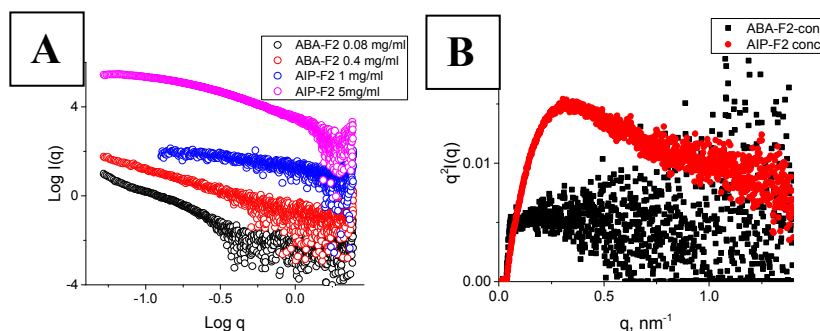


Figure 4.15. SAXS profiles for compounds **AIP-F2** and **ABA-F2** (A) and comparative Kratky plot (B).

We found that the R_c values for compounds **AIP-F2** and **ABA-F2** were close to 4.5 nm each. In the case of **ABA-F2**, we observed high nanorod length dispersity; therefore, the results of length measurements cannot be considered precise as the qR_g

value (the parameter used to check the validity of the Guinier approximation) exceeds the upper limit of 1.5. The power law dependence at low to medium q -range for **AIP-F2** (as mentioned above) is typical for either lamellae or mass fractals. In the case of **ABA-F2**, we observed a change in the power law from -1 to -2 upon an increase in concentration, probably signifying the formation of separated rods or fibers at lower concentrations. Upon an increase in concentration, mass fractals form and particles interact with each other.

Table 4.4. SAXS Values for compounds **AIP-F2** and **ABA-F2**

| Compound | R_g (nm) | R_c (nm) | L (nm) | Power law |
|---------------|------------|------------|----------|-----------|
| AIP-F2 | 13.8 | 4.52 | 46 | -2 |
| ABA-F2 | 18.4 | 4.69 | 63 | -1/-2 |

We found relatively similar $P(r)$ functions for **AIP-F2** and **ABA-F2** (Fig. 4.16), with a weakly defined peak at 3-6 nm as would be expected for cylindrical particles. When comparing the appearance of the function at higher distances, **ABA-F2** seems to assemble into rod-like particles, while **AIP-F2** forms fractal structures.

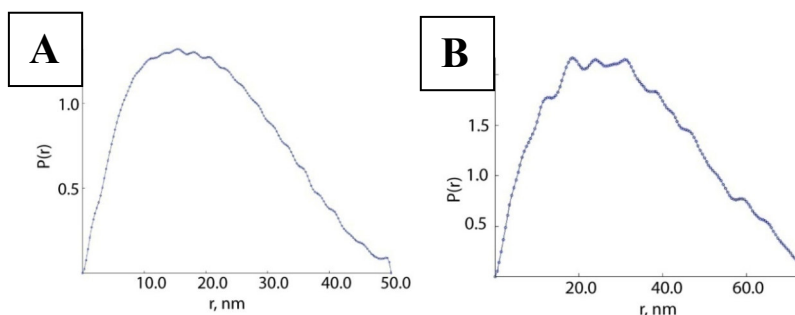


Figure 4.16. $P(r)$ functions for compounds **AIP-F2** (A) and **ABA-F2** (B).

TEM with negative staining of **AIP-F2** and **ABA-F2** confirmed these suggestions; **ABA-F2** formed rod-like objects with a length of 50-150 nm that interacted with each other (Fig. 4.17). Unexpectedly, even at high concentrations, we never observed long fibers as in the case of **F3**, and the **ABA-F2** formed only short rods. We determined a fiber width of 9-11 nm, which agrees well with SAXS data. The image of compound **AIP-F2** at the same concentration (Fig. 4.17B) provides evidence of the existence of aggregates with no defined structure, suggesting that the mechanism of aggregation must differ from the usual stacking. **ABA-F2** may form stacks stabilized by H-bonds between the amides of *p*-dibenzamide. For **AIP-F2** with diphenylalanine arms in meta position (*m,m*-tribenzamide), those amides may not form a directional system of H-bonds or π - π stacking; therefore, the stack formation may not be favored. Another explanation for the lack of defined structures is that **AIP-F2** requires more energy to bring the six arms in a plane and that, therefore, the concentration employed here remains below the critical aggregation point.

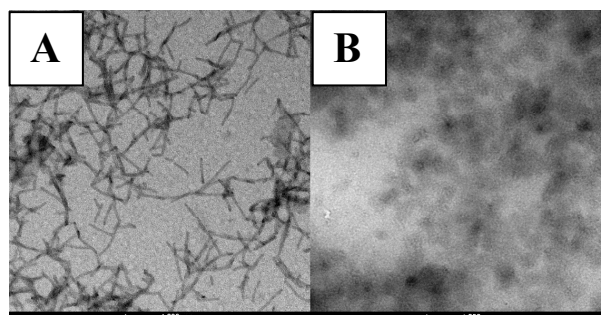


Figure 4.17. TEM images of 0.5 mM **ABA-F2** (A) and 0.5 mM **AIP-F2** (B) in water with uranyl acetate staining.

Fig. 4.18 depicts TEM images of **ABA-F2** with a concentration of 0.1-0.5 mM. At 0.1 mM, we failed to observe any defined structures; however, at concentrations 0.25 mM and 0.5 mM, we observed the clear formation of linear rods. At a concentration of 0.5 mM, as determined by SAXS, we discovered that rods interact with each other forming mass fractals.

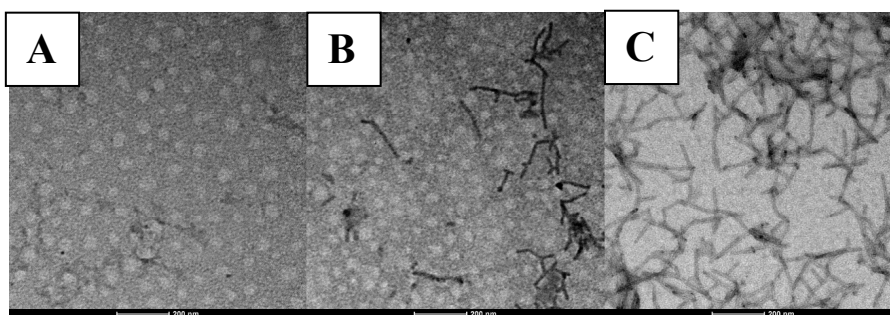


Figure 4.18. TEM images of **ABA-F2** at 0.1 mM (A), 0.25 mM (B) and 0.5 mM (C).

4.2.2. Self-assembly of *stPGA* based on **ABA-F2** and **AIP-F2**

The results presented above established compounds **ABA-F2** and **AIP-F2** as the most interesting prospective molecules for use as polymerization initiators. We next prepared five polymers with varied polymerization degree: **ABA-F2E10**, **AIP-F2E10**, **AIP-F2E25**, **ABA-F2E50**, and **AIP-F2E50** (Fig. 4.19-4.20).

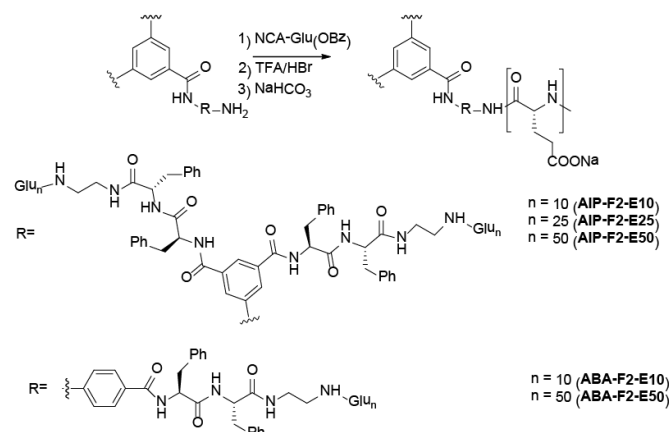


Figure 4.19. General scheme of polymer synthesis and structures of corresponding polymers.

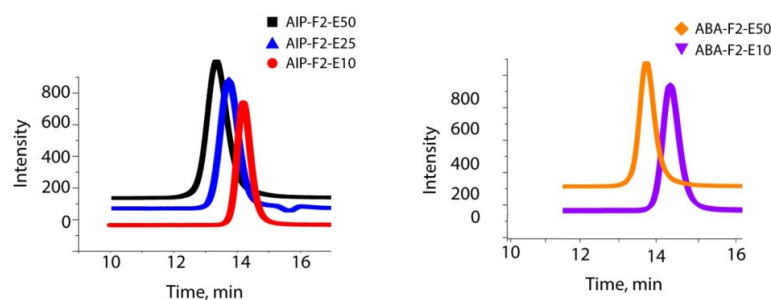


Figure 4.20. GPC chromatograms of the corresponding polymers.

Table 4.5. Properties of prepared polymers.

| Compound | M _n ^a , Da | Đ ^a | DP theor. | DP obtained | DP/arm |
|------------------|----------------------------------|----------------|-----------|-------------|--------|
| ABA-F2E10 | 8149 | 1.07 | 30 | 30 | 10 |
| AIP-F2E10 | 13954 | 1.09 | 60 | 51 | 8-9 |
| AIP-F2E25 | 33716 | 1.15 | 150 | 142 | 47 |
| ABA-F2E50 | 31997 | 1.09 | 150 | 139 | 46 |
| AIP-F2E50 | 60329 | 1.17 | 300 | 264 | 44 |

^aas determined by GPC

Initially, we performed fluorimetry studies only for those polymers with ten monomer units per arm (**ABA-F2E10** and **AIP-F2E10**), which we selected for further studies because of structural similarity with **F3E10**. **Fig. 4.21 A** and **B** show typical fluorescence spectra for increasing concentrations of **ABA-F2E10** and **AIP-F2E10**. In a 0.188 M NaCl solution, we also observed an increase in intensity for both polymers.

Furthermore, a shift in the NR peak from 648 to 641 nm appears for compound **ABA-F2E10**, indicating the formation of more hydrophobic microdomains.

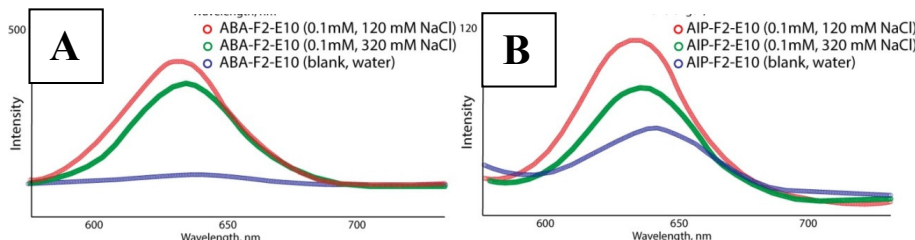


Figure 4.21. Fluorescence spectra of NR in **ABA-F2E10** (A) and **AIP-F2E10** (B).

We studied all synthesized polymers using CD spectroscopy (**Fig. 4.22**); the compounds in diluted solutions possessed identical spectra with a small positive peak at 217 nm and a strong negative peak at 196 nm typical for a random coiled secondary structure.

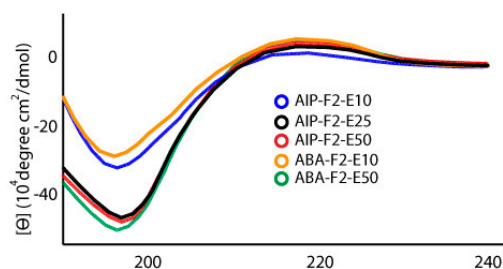


Figure 4.22. CD spectra of synthesized polymers with a concentration of 0.25 mg/ml.

Considering the rather weak six-armed polymer self-assembly, we performed SAXS studies only for compound **ABA-F2E10** and **ABA-F2E50** (as control) at different concentrations of polymers and salt (**Fig. 4.23**).

Upon an increase of salt concentration (from 0 to 320 mM) in a low concentration polymer solution (10 mg/ml), we observed the a transition from a curve typical for polyelectrolyte solutions to a slightly uphill curve. Power law analysis revealed a value of -0.3, corresponding to a solution comprising a mixture of unimolecular particles and a small fraction of rods. At a higher concentration of polymer, we found a power law closer to 0 in the low-q region and -3 in the Porod region (usually observed for collapsed Gaussian polymer chains); this was the expected result as PGA chains collapse at a relatively high concentration of salt. Unexpectedly, we failed to observe the appearance of a curve with a slope of -1, as observed for **F3E10**, suggesting that the formed particles lack the tendency to assemble into fibers. Nevertheless, the Guinier plot modified for rod-like particles was applicable, and for both concentrations, we determined similar $R_{g,c}$ of 1.56 nm, which corresponds to R_c of 2.18 nm. This

corresponds to the formation of very short nanorods as, for spherical micelles, this approach gives non-defined curves.

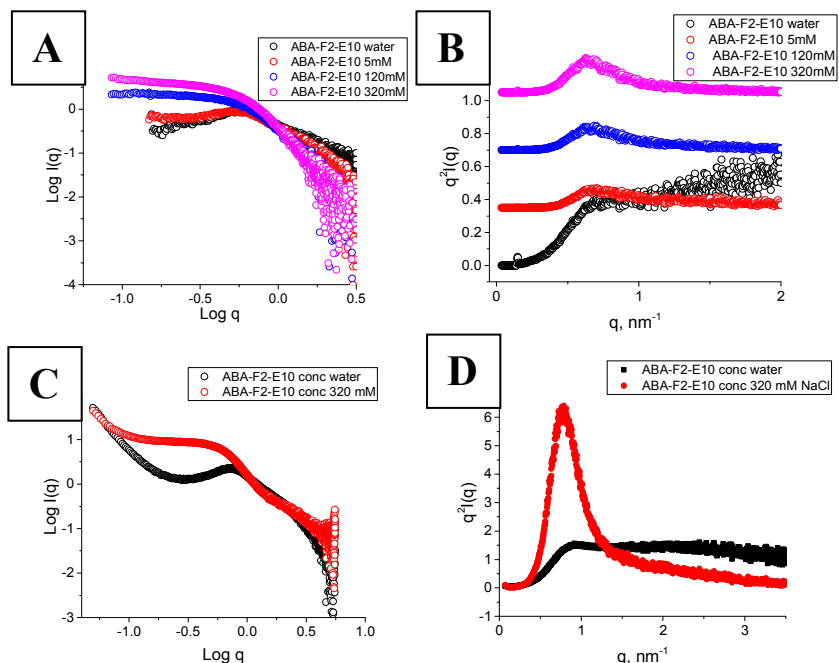


Figure 4.23. SAXS profiles and corresponding Kratky plots of **ABA-F2E10** at 10 mg/ml (A, B) and 40 mg/ml (C, D) and varied salt concentrations.

On the SAXS curves for compound **ABA-F2-E50**, we observed the appearance of a power law dependence between -1 and -2 (**Fig. 4.24**). When we analyzed $P(r)$ distribution functions for **ABA-F2E10** and **ABA-F2E50**, we observed that for the shorter polymer, the function corresponded to mainly small objects with a diameter of around 9 nm and a low fraction of longer particles. For **ABA-F2E50**, we observed a function typical for short rods of 15 nm in length and radius of cross-section of around 2 nm.

4.3. Effect of Aliphatic Chain Hydrophobicity on Self-assembly of BTA-based Diphenylalanines

To study the role of aliphatic chain length at the initiator termini, we prepared compounds with end-modified diamines with 2, 6, and 12 methylene units, named for simplicity as **F2C2**, **F2C6**, and **F2C12** (**Fig. 4.25**). The synthetic strategy employed for these compounds is detailed in Chapter 2.

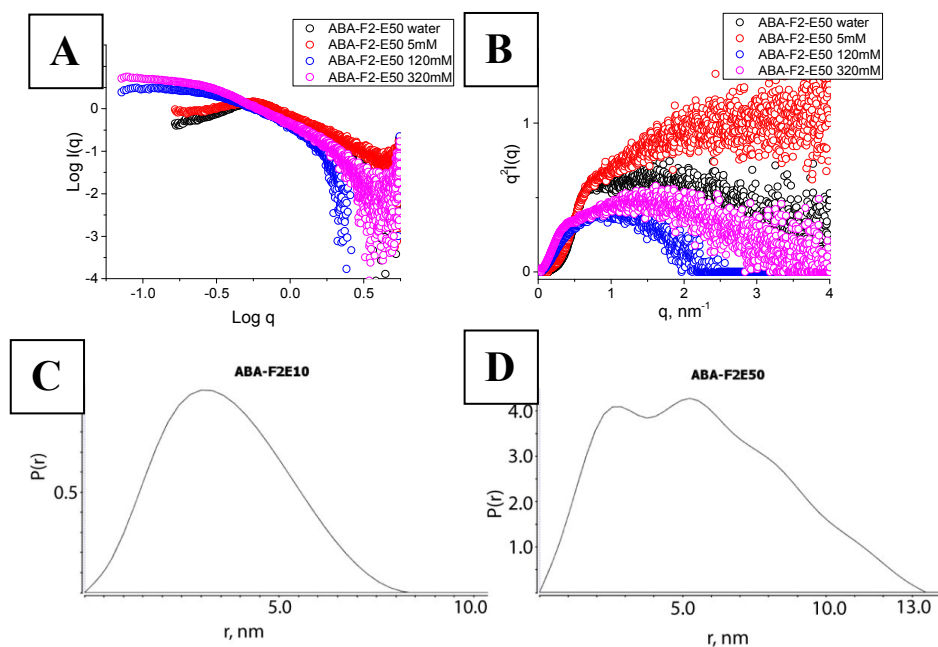


Figure 4.24. SAXS profiles and (A-B) Kratky plots of ABA-F2-E50 at 10 mg/ml and varied salt concentration. (C-D) $P(r)$ distribution functions of ABA-F2E10 and ABA-F2E50.

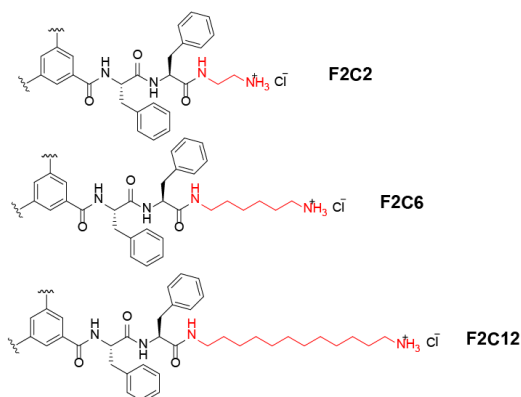


Figure 4.25. The general structure of compounds F2C2-F2C12.

As N-Boc-dodecamethylenediamine is not commercially available, we synthesized (in a one-step protocol from DiBoc and C12-diamine) and isolated it at high yield after column purification. We synthesized the compounds F2C2-F2C12 in a similar manner as for compound FF, using the corresponding monoprotected diamines.

We determined CAC values for three compounds by NR fluorescence spectroscopy in water and 120 mM NaCl solution, as shown in **Fig.4.26**.

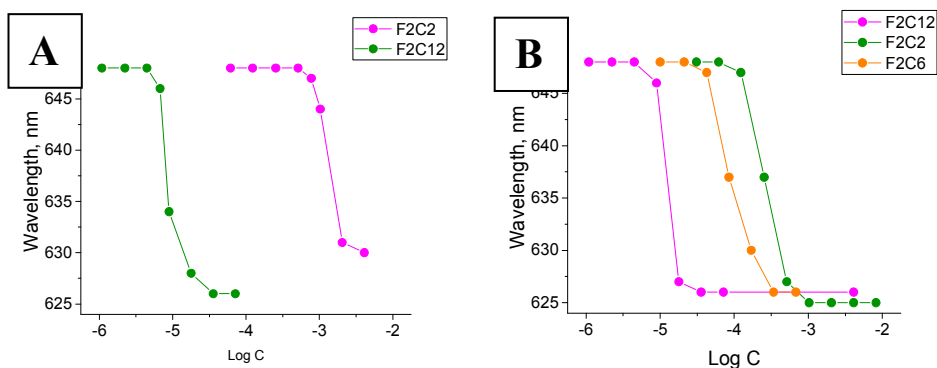


Figure 4.26. Dependence of NR peak maximum on the concentration of compounds **F2C2-F2C12** in water (A) and 120 mM NaCl (B).

We observed that CAC values decrease in the order **F2C12**<<**F2C2**<**F2C6** in pure water. In 120 mM NaCl, the CAC values decreased in the order **F2C12**<**F2C6**<**F2C2** (**Fig. 4.26**). We plotted the obtained values as Log CAC against the number of methylene units (**Fig.4.27A**). For salt solutions, we found a linear dependence. When the terminal charges are screened, self-assembly increase proportionally to the increase of hydrophobic chain length; however, the dependence strongly deviated from linear in pure water. Of note, in case of **F2C12**, we determined equal CAC values in both water and 120 mM NaCl, as the distance from the core to the charge is high and the flexibility of the dodecamethylene chain suffices to negate the repulsions of charged groups at the end of the chain.

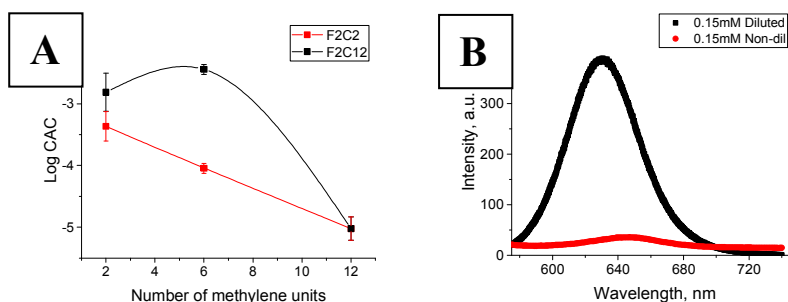


Figure 4.27. Dependence of Log CAC on the number of methylene units (A); Fluorescence spectra of NR in **F2C6** prepared from gel dilution and direct dissolution after 24 h (B).

Interestingly, we observed unexpected behavior for **F2C6**. At concentrations below 2 mg/ml, we failed to detect self-assembly by fluorescence studies neither immediately nor 24 h after preparation; however, at a concentration of 5 mg/ml, the

compound gelled after a few hours. Upon dilution, we observed an increased in both peak intensities and a blue shift of NR, even at concentrations that provided for negative results for directly dissolved samples (**Fig. 4.27B**)

We next performed TEM studies for **F2C6** and **F2C12** (similar data for **F2C2** is demonstrated in Chapter 2) (**Fig. 4.28**).

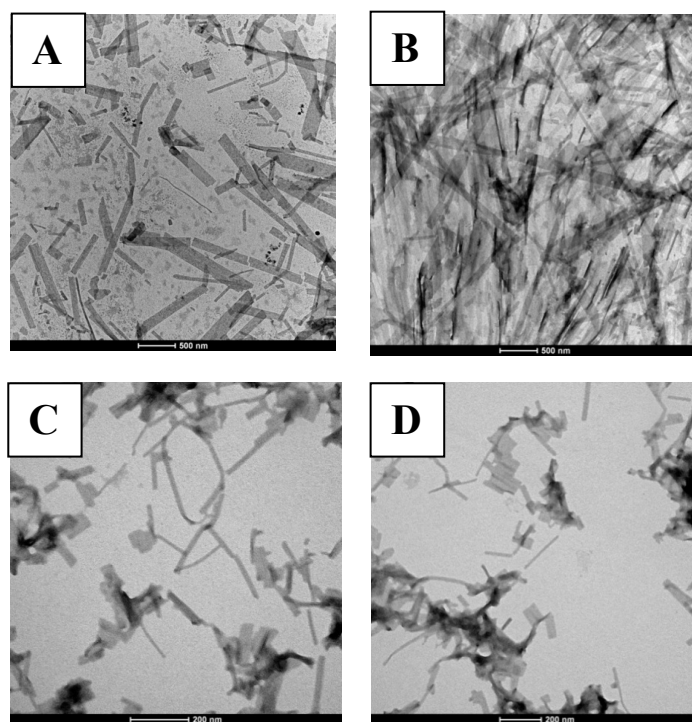


Figure 4.28. TEM images of compounds **F2C6** (A, B) and **F2C12** (C, D) in water stained with uranyl acetate.

Unlike **F2C2**, which assembled into long fibers, **F2C6** and **F2C12** displayed a more complicated assembling behavior; in the case of **F2C6**, we observed mainly 2D flat objects from 250 nm to a few microns in length and from 20 to 200 nm in width. More concentrated solutions also consist of longer flat objects. Unexpectedly, we observed the formation of inflexible objects with sharp edges that remained well separated from each other in general. For **F2C12**, we observed the presence of different objects; from 1D rods to 2D nanosheets with varied thickness and width. Analysis of the images revealed that the flat objects interact with each other and with themselves, rolling into 1D rods, while other objects displayed a rectangular size with well-defined edges.

We measured the CD spectra of **F2C6** at a concentration of 0.5 mg/ml prepared by simple dissolution and dilution of the compound at 5 mg/ml (**Fig. 4.29**). We observed very different CD spectra; while the spectra for the non-diluted compound generally

lacked any significant signals other than a small minimum at 208 nm, the diluted compound provided a robust signal with three minima at 202, 215, and 251 nm. We hope that deeper analysis of this data will allow the understanding of the mechanism of self-assembly of this compound.

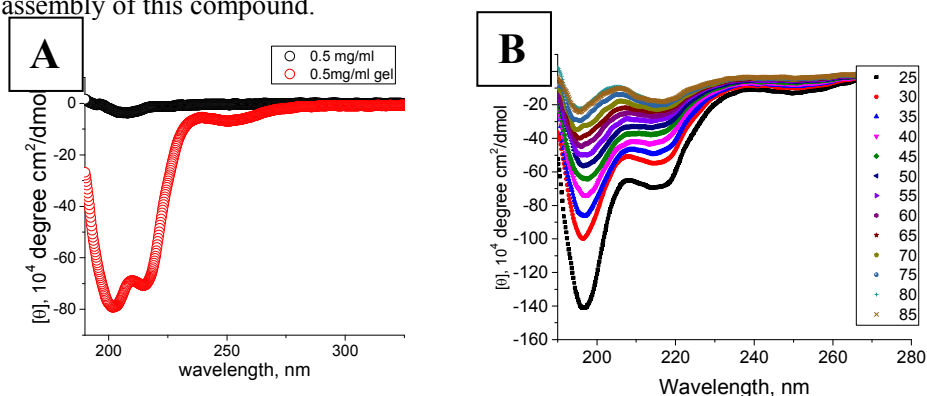


Figure 4.29. A) CD spectra of **F2C6** at 0.5 mg/ml directly dissolved (black) and diluted from 5 mg/ml (red). B) CD spectra of **F2C6** at 25-85 °C.

Temperature variation experiments on freshly diluted **F2C6** demonstrated the rapid disappearance of the peak, corresponding to complete disassembly of the supramolecular polymers. The final spectrum at 85 °C possesses two minima at 197 and 215 nm, which corresponds to the unimeric compound itself.

We attempted to study **F2C12** by SAXS, but we failed to extract reliable R_g values due to the presence of a wide morphological polydispersity. However, we extracted a power law dependence in the low to medium q -range equal to -2, corresponding to lamellar particles. When we applied a Guinier approximation for flat particles, we determined an R_g of 0.96 nm. Taking into account that the cross-sectional radius of gyration of a randomly oriented lamella of thickness T is given by $R_g = T/\sqrt{12}$, we determined a lamellar thickness of 3.32 nm. While this data cannot be considered as precise, considering the particular nature of the system, it does provide a maximum possible thickness of the lamella.

The $P(r)$ distribution function of the **F2C12** corresponds to that expected for lamellar objects with no defined maximum corresponding to molecule diameter (**Fig. 4.30**). The D_{max} estimated from the $P(r)$ of around 100 nm correlates with the TEM data. Kratky plot appearance also unambiguously confirms the presence of flat objects due to typical plateau in low q -region without defined maximum.

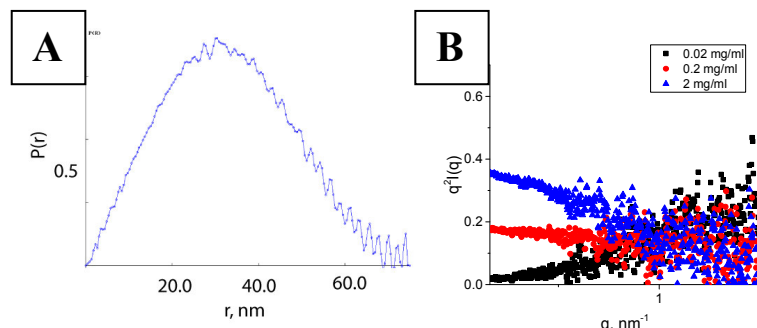


Figure 4.30. $P(r)$ distribution functions for **F2C12** (A) and the corresponding Kratky plot (B).

4.3.1. Self-assembly of stPGA Based on **F2C2** and **F2C12**

Based on the obtained data, we selected compounds **F2C2** and **F2C12** as initiators for polymerization and prepared compounds **F2C12-E10** (Fig. 4.31) with 10 glutamic units per arm (total degree of polymerization of 30). We described the synthesis of **F2C2-E10** in Chapter 2.

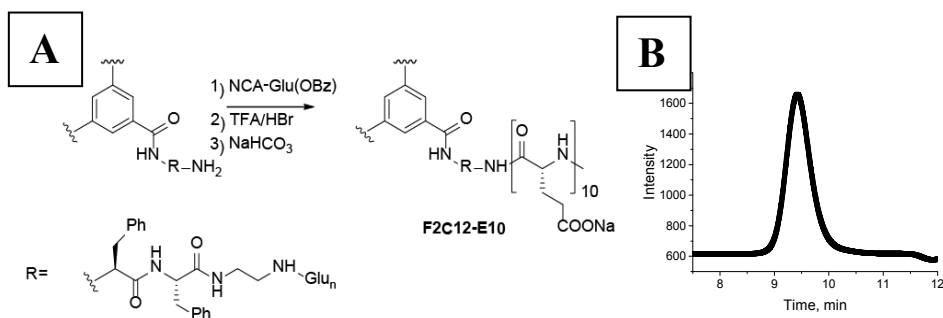


Figure 4.31. A) General scheme of **F2C12** polymerization. B) GPC chromatogram of **F2C12-E10** as benzyl ester.

Both polymers obtained possessed low PDI values of 1.08 and 1.11 for **F2C2-E10** and **F2C12-E10**, respectively. We determined CAC values of both polymers by fluorimetry in water, and 120 mM NaCl solution, with the resulting data displayed in Fig. 4.32. For **F2C12-E10**, we found CAC values almost two orders of magnitude lower in the presence and absence of salts. Charge screening with salt additionally decreased CAC values almost five times.

Next, we performed SAXS analysis to establish the shapes of the formed particles. We studied polymer solutions at concentrations of 10 mg/ml and 20 mg/ml and varied salt content from 0 to 320 mM. We observed a distinct transition in the middle q -range of the doubly logarithmic plot, corresponding to directional polymer self-assembly. The Kratky plot possesses a bell-shaped curve in the low q -region, which

corresponds to the formation of frozen aggregates (as in supramolecular gels) or organized particles. We note that, in contrast to **F2C12**, the Kratky plot of the polymer does not correspond to lamellar objects.

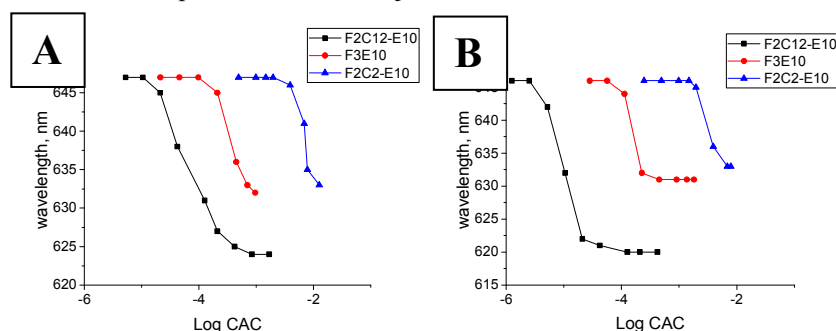


Figure 4.32. NR peak maximum dependence on Log C of **F2C12-E10**, **F2C2-E10**, and **F3E10** in water (A) and 0.12 M NaCl (B).

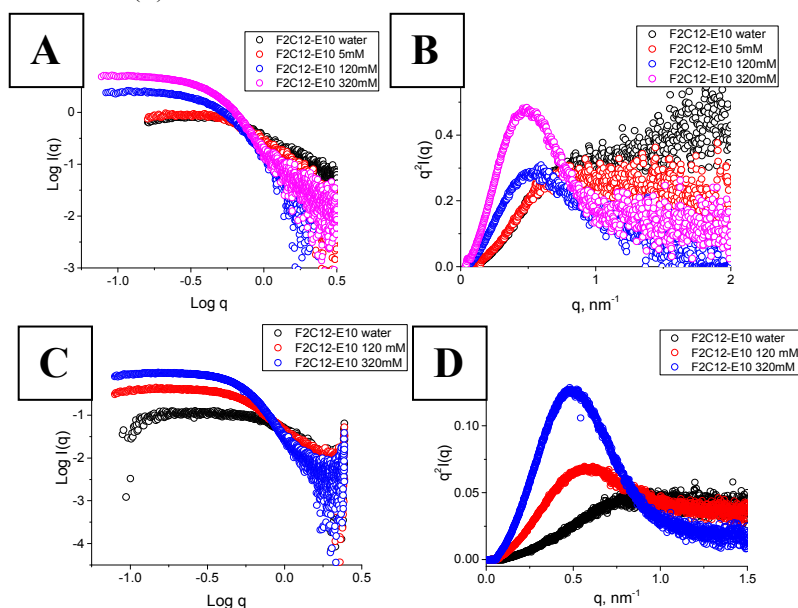


Figure 4.33. SAXS profiles and corresponding Kratky plots of **F2C12-E10** at 10 (A, B) and 20 mg/ml (C, D) with varied salt concentration.

Analysis of a Guinier plot of **F2C12-E10** modified for rod-like objects demonstrated that upon an increase in salt concentration, the R_g of cross-section increased and remained steady at 2.3 nm for both polymer concentrations, a value that corresponds to an R_c of 3.2 nm. Finally, we built a pair of distance distribution functions – we obtained a D_{max} from the function of around 10 nm and an R_g of 3.74 nm, a value lower than estimated from the Porod plot.

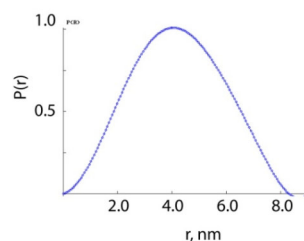


Figure 4.34. $P(r)$ functions of **F2C12E10** at 20 mg/ml in 320 mM NaCl.

We obtained a defined $P(r)$ distribution function only for **F2C12-E10** in 320 mM salt solution due to strong repulsive interferences of the chains at lower ionic strength. We estimated D_{\max} at 9.5 nm and R_g as 3.2 nm.

TEM analysis of **F2C12-E10** failed to reveal the presence of particles or rods. By combining data, we assume that the structures formed in this case are clusters whose size does not exceed 6.5 nm in diameter. We observed power law dependence of -4 in the intermediate q -range that corresponds to defined spherical particles. The fact that Guinier approximation for rod-like particles also remained valid maybe explained by considering the dimensions of the rods. From the calculations, the rods fitting this model possess a radius of 3.2 nm and a length of 10 nm, which will provide a similar scattering pattern as spherical particles.

We do not fully understand if the high flexibility of the dodecamethylene chains that stimulate the formation of micellar clusters or its specific assembly, which requires an overlap of the chains, dictates this behavior.

4.4. Self-assembly of Complex BTA-based Derivatives

Using the previously collected data, we designed two initiators combining the previously described structural elements in an attempt to increase the length of the PGA chains. We employed an aminobenzoate moiety to increase the planarity of the central part of the molecule and a sequence of triphenylalanine or tri-(pentafluoro)-phenylalanine for comparison, as the Φ -based compounds are among the strongest known assembling units. Finally, we used a terminal dodecamethylenediamine moiety in the hope that the increased core planarity will overcome the tendency of 2D objects to form (**Fig. 4.35**).

We prepared N-Boc, N'-triphenylalanine dodecamethylenediamine in a similar manner to the **F2C12** compound, although with an additional Z-L-phenylalanine coupling step. We prepare N-Boc, N'-tri (pentafluorophenylalanine) dodecamethylenediamine in a similar manner to the non-fluorinated analog. In the latter case, we employed a shorter hydrogenation time due to the previously highlighted side reaction of fluorine replacement with hydrogen.

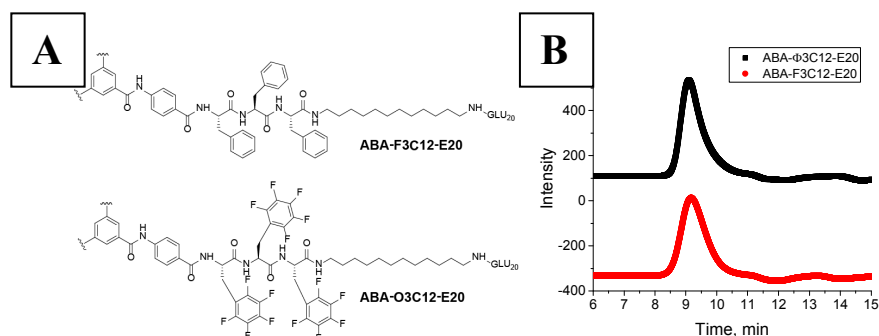


Figure 4.35. A) General structure of compounds **ABA-F3C12-E20** and **ABA-Φ3C12-E20**. B) GPC chromatograms of **ABA-F3C12-E20** and **ABA-Φ3C12-E20**.

Due to the low reactivity of the **BTA-ABA** compound in the DMTMM coupling reaction, we transformed **BTA-ABA** into the corresponding chloroanhydride by refluxing with thionyl chloride. We then removed residual thionyl chloride with the sequential addition of dichloromethane and evaporation under vacuum, and then used the compound for amine coupling without further purification. Finally, we removed terminal Boc groups with 4M HCl/dioxane. We did not study self-assembly of the cores due to extremely low solubility.

Considering the strong decrease in CAC observed for the addition of each building block, we decided to increase the length of the polymeric chains (**Fig. 4.35A**). Using NCA-ROP, we prepared polymers with 20 glutamic units per arm (DP 60 in total) with low polydispersity (1.11 and 1.15), as shown by GPC (**Fig. 4.35B**). Due to the limited solubility of both initiators in DMF and other organic solvents, we performed the reaction in anhydrous DMSO.

We determined the CAC of polymers by fluorimetry using **F3G10** as a control; we observed a tremendous decrease in CAC for both **ABA-F3C12-E20** and **ABA-Φ3C12-E20** in comparison to **F3G10** (**Fig. 4.36**). We determined CAC values for **ABA-F3C12-E20** and **ABA-Φ3C12-E20** in pure water of 28 μM and 7.2 μM, respectively, while in the presence of 120 mM, polymers displayed an equal CAC value of 2 μM.

The difference between CAC values between **ABA-F3C12-E20** and **ABA-Φ3C12-E20** in pure water derives purely from tripeptide sequence variation. In the presence of fluorinated triphenylalanine, the CAC decreases almost an order of magnitude, while in 120 mM solution, we observed identical CAC values for both compounds due to charge screening.

Next, we performed SAXS studies to understand the mechanism of assembly (**Fig. 4.37**).

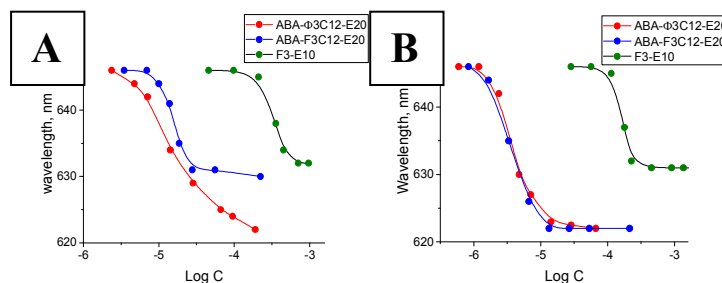


Figure 4.36. NR peak maximum dependence on LogC of ABA-F3C12-E20, ABA-Φ3C12-E20, and F3E10 in water (A) and 0.12 M NaCl (B).

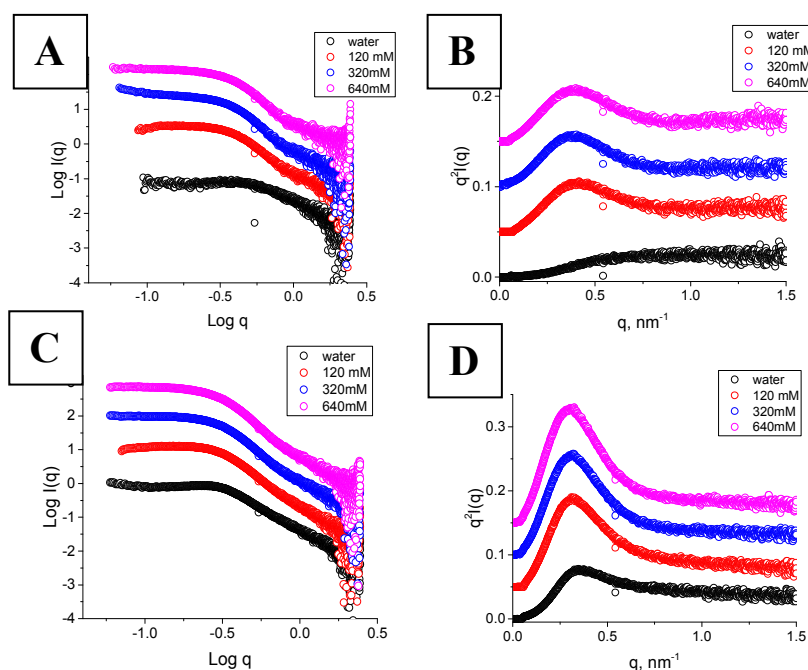


Figure 4.37. SAXS profiles and Kratky plots of ABA-F3C12-E20 (A, B) and ABA-Φ3C12-E10 (C, D).

In both cases, we observed a sharp transition upon increase in ionic strength to 120 mM; however, further increases in ionic strength had an insignificant effect on transition. Applying normal and modified Guinier plots for rod-like particles and standard processing of the data allowed us to extract R_g , R_c , and length of the particles, as described in **Table 4.6**.

Table 4.6. Structural parameters extracted from SAXS data

| Compound | $R_{c,g}$, nm | R_c , nm | R_g , nm | L , nm | D_{max} , nm |
|----------------------|----------------|------------|------------|----------|----------------|
| ABA-F3C12-E20 | 2.76 | 3.86 | 4.2 | 12.9 | 13 |
| ABA-Φ3C12-E20 | 3.67 | 5.1 | 5.05 | 15.0 | 15 |

$P(r)$ distribution functions allowed us to determine D_{max} values for **ABA-F3C12-E20** and **ABA-Φ3C12-E20** of 13 and 15 nm, in good agreement with previous calculations (Fig. 4.38). Finally, we found a power law dependence in the intermediate q -region equal to -4 , typical for particles with a spherical shape or close to spherical shape. TEM analysis confirmed the presence of small particles with a shape close to spherical (Fig. 4.38).

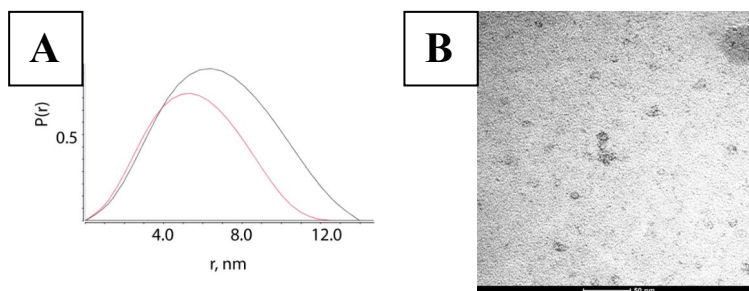


Figure 4.38. A) $P(r)$ functions for **ABA-F3C12-E20** (red) and **ABA-Φ3C12-E20** (black). B) TEM of **ABA-Φ3C12-E20**.

Overall, both compounds seem to assemble into very small, prolonged objects, consisting of a relatively small number of molecules. As in previous studies, it remains unclear if high core flexibility or increased length of glutamic acid units limits the growth of the nanorods. These results are better than for **F2C12**- and tetrapeptide-based polymers, probably due to the presence of *p*-aminobenzoate moiety, which by increasing the planarity of the core favors the formation of 1D self-assembly. Of significant note, small core-shell micelles represent fascinating materials for drug delivery, and the study of Dox encapsulation in **ABA-Φ3C12-E20** micelles will be presented in Chapter 6.

4.5. Effect of Charge Density on Self-assembly of BTA-based PGAs

We previously determined that an increase in core hydrophobicity fails to allow for the synthesis of self-assembling star-polyelectrolytes with a higher degree of polymerization due to the formation of small spherical micelles. Therefore, we kept the core relatively small and varied the length of star arms by controlling polyelectrolyte arm composition. Coulomb repulsions of PGA chains represent the main force opposing the attracting interactions of the synthesized polymers; one possible strategy to diminish those repulsions is to decrease chain density with a neutral monomer. We selected sarcosine and glutamate for the preparation of a series of random copolymers with the

ratio between the monomers 2:1, 1:1, and 1:2 using **F3** NH₂ as initiator. We employed **F3E10** and **F3E15** as control.

Using similar NCA-ROP protocols as described for the preparation of PGA, we prepared compounds **F3ExSy** (Fig. 4.39); the Table within Fig. 4.39 describes these properties.

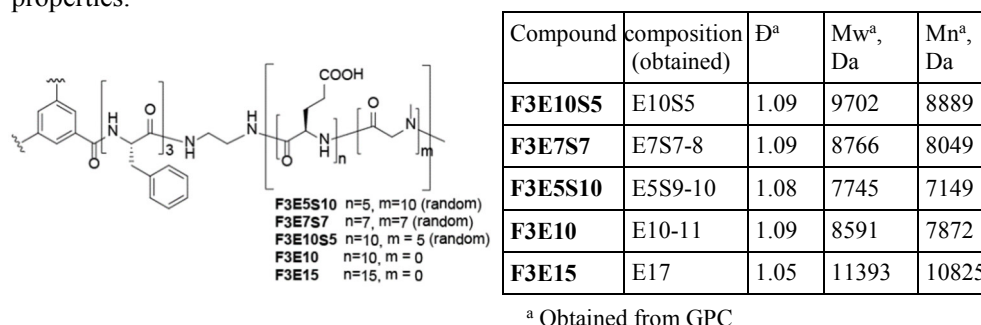


Figure 4.39. The general structure of prepared copolymers and a table with their properties.

We determined CAC of copolymers by NR fluorimetry in water and in 120 mM NaCl (Fig. 4.40). Plotting the logCAC values in the water against glutamic acid content established an almost linear dependence, thereby confirming the strong destructive effect of multiple charges on polymer self-assembly (Fig. 4.41).

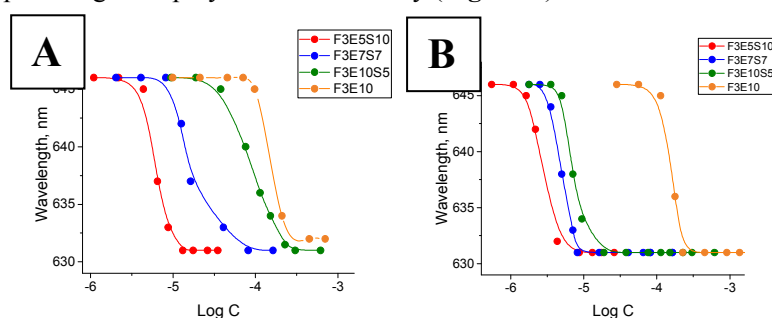


Figure 4.40. NR peak maximum dependence on Log C of copolymers in water (A) and 0.12 M NaCl (B).

In a 120 mM NaCl solution, we found an evident deviation from the linearity of log CAC dependence on glutamic acid content that can be explained in terms of charge screening - increasing the number of charges requires a higher concentration of salt for sufficient screening. **F3E5S10** possesses only five randomly distributed glutamic units per arm, and we observed full charge screening in a 120 mM NaCl solution. Extrapolation of both graphs to zero Glu content provides a practically identical value CAC of 1.9 μ M for star-polysarcosine.

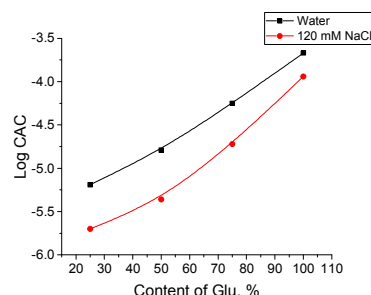


Figure 4.41. Log CAC dependence on the fraction of the charged chain in water and 120 mM NaCl.

We next performed a TEM study of the compounds stained with uranyl acetate (**Fig. 4.42**) using a concentration equal to five times higher than the CAC. We observed an obvious morphological transition from wormlike particles to rods, thereby confirming the hypothesis that the appearance of wormlike particles is an artifact appearing from the induced aggregation of PGA with positively charged uranyl. Despite this problem, this approach remains beneficial for the study of polymeric morphologies.

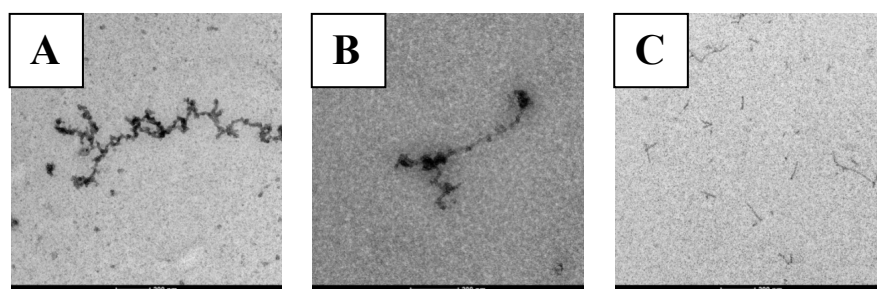


Figure 4.42. TEM images of **F3E10S5** (A), **F3E7S7** (B) and **F3E5S10** (C) at concentration five times higher than CAC.

We next performed SAXS studies for all polymers in water and solutions with varied ionic strength; we used gradually decreasing concentrations of the polymers due to a stronger tendency to self-assemble. We found robust evidence for a decreased effect of salt when the density of charged monomer decreases, reaching a state when salt produces no effect for the polymers with the highest Sar content.

After spectral analysis and the extraction of the main characteristic data (**Table 4.7**), we observed that all polymers in the low q -region possess a power law dependence of -1 confirming the formation of rod-like particles. We found that a power law dependence in Porod region changed from -2 to -4, corresponding to a transition from disordered polymer chains to a particle with a flat surface.

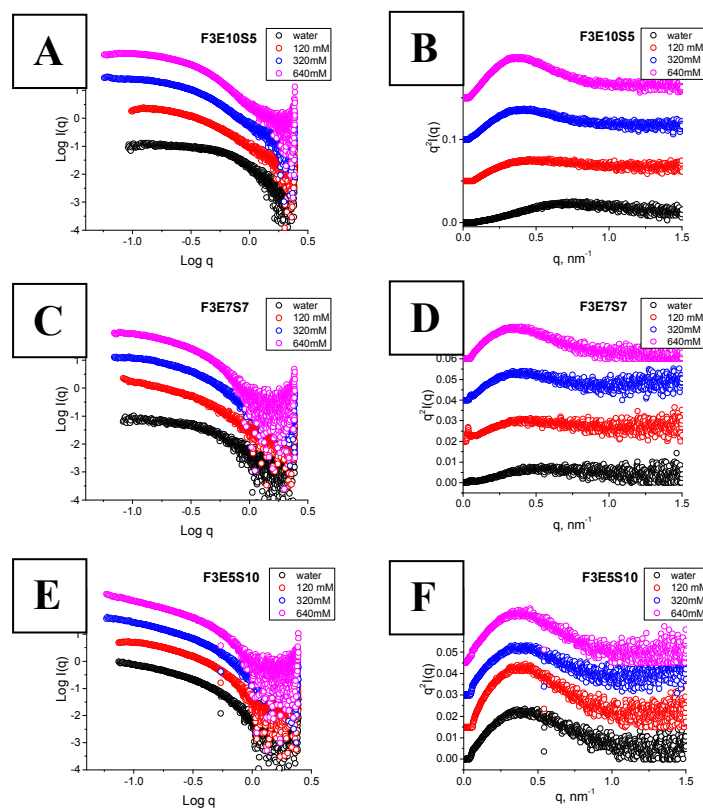


Figure 4.43. SAXS profiles and Kratky plots of **F3E10S5** (A, B), **F3E7S7** (C, D), **F3E5S10** (E, F).

Table 4.7. Structural properties of copolymers determined from SAXS data

| Compound | Power law 1 | Power law 2 | $R_{c,g}$, nm | R_c , nm |
|---------------|-------------|-------------|----------------|------------|
| F3G10 | -1 | -2 | 1.17 | 1.64 |
| F3G15 | -1 | -2 | 1.70 | 2.48 |
| F3G2S1 | -1 | -3 | 2.41 | 3.37 |
| F3G1S1 | -1 | -4 | 2.79 | 3.91 |
| F3G1S2 | -1 | -4 | 2.62 | 3.67 |

Next, we extracted $P(r)$ distance distribution functions (**Fig. 4.44**); the $P(r)$ function possesses a typical appearance for rod-like particles with increased length upon an increase in compound concentration. There exist some function oscillations caused by a lack of fully screened repulsive interactions (as in case of **F3E15**) or due to helical inner structure of the particles.

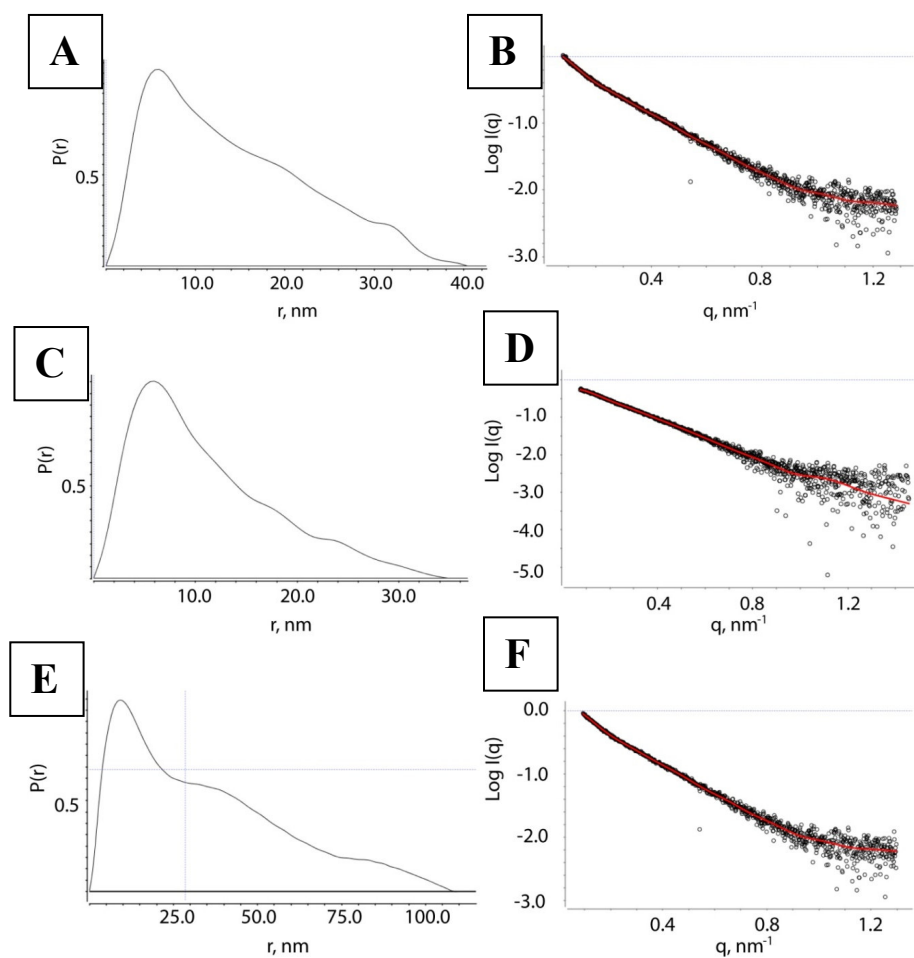


Figure 4.44. $P(r)$ functions and corresponding fits of **F3E10S5** (A, B), **F3E7S7** (C, D) and **F3E5S10** (E, F).

4.6. Conclusion

Following the structure-activity relationship studies described in Chapters 2 and 3 during the development of stPGAs as efficient drug delivery carriers, we synthesized and studied new families of stPGA with diphenylalanine BTA-derivatives cores with *p*-aminobenzoate or *m,m*-aminoisophthalate insertions and different lengths of terminal methylene chains.

While p-aminobenzoate addition resulted in the formation of short nanorods that interacted at higher concentrations to form mass fractals, m-aminoisophthalate insertion resulted in the formation of disordered aggregates. We believe that the difference in assembly derives from the higher steric complexity of m,m-aminoisophthalate derivatives that restricts phenyl rings orientation in a single plane. For corresponding polymers, we observed the formation of core-shell micelles similar to those discussed in Chapter 3. We hypothesize that when the flexibility of the molecule increases, energetically more favourable micelles form due to phase separation.

Incorporation of hexamethylene and dodecamethylene terminal chains in BTA-diphenylalanine derivatives resulted in the formation of flat 2D objects, a previously unreported finding for BTA-based compounds before. Considering the extremely thin nature of the 2D objects and the very high flexibility of the chains, we suggest that the formed membranes consist of a few layers of molecules with charged groups exposed to the surface. Corresponding polymers assembled into small core-shell micelles, correlating well with high chain flexibility.

A combination of the most hydrophobic elements in a single stPGA core (p-aminobenzoate and dodecamethylene terminal groups) also resulted in the formation of core shell-micelles. By analyzing data from Chapters 2-4, we conclude that stPGAs with relatively small cores with sufficient hydrophobicity can assemble into 1D nanorods. When the flexibility of the core increases, phase separation with the formation of core-shell micelles becomes more energetically favourable.

When we evaluated a variation of charge density along the polymer chain using **F3** cores and glutamate-sarcosine copolymers of different ratios, we observed that a decrease of Glu density along the chain resulted in a substantial decrease in CAC values. This strategy could be applied for the preparation of larger polymers with an increased number of functional groups that self-assemble by a supramolecular mechanism or larger self-assembling stPGA that will allow an increase in the diameter of the core and number of available functional groups.

4.7. Supplementary Information

SI-4.1. Synthesis of BTA-based tetraphenylalanines with p-aminobenzoic and m,m-aminodisophthalate insertions

SI-4.2. Synthesis of **BTA-F2C6** and **BTA-F2C12**

SI-4.3. Synthesis of **BTA-ABA-F2C12** and **BTA-ABA-Φ3C12**

SI-4.4. Star-polyglutamate Synthesis

SI-4.1. Synthesis of BTA-based Tetraphenylalanines with *p*-aminobenzoic and *m,m*-aminodiisophthalate Insertions

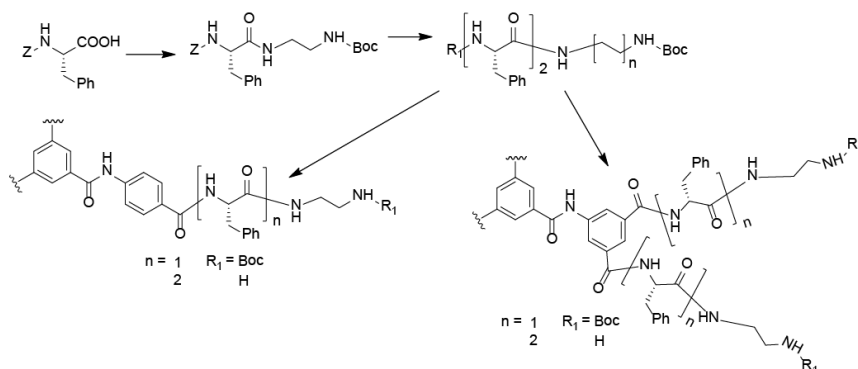


Fig. SI-4.1. General synthetic scheme for ABA-F2 and AIP-F2.

Synthesis of Triethyl 4,4',4''(benzene-tricarbonyl tris(azanediyl)tribenzoate)

In a round bottom flask with a stirrer and nitrogen inlet and outlet, 5.91 g of ethyl-4-aminobenzoate and 4.94 g of potassium carbonate were dissolved in 60 ml of anhydrous DMA. After the dissolution of ethyl-4-aminobenzoate, 2.1 g of benzene-1,3,5-tricarbonyl-trichloride was added under a nitrogen atmosphere and the mixture was stirred overnight, during which time the suspension turned yellow. The compound was precipitated in water and washed sequentially with water (3x60 ml), methanol (100 ml), and diethyl ether (100 ml). The compound was dried under vacuum.

Product - white solid. Global yield: 9.52 g (96.5 %). ¹H-NMR (300 MHz, DMSO-d₆): δ 1.34 (t,9H), 8.76 (s,3H), 4.32 (q,6H), 10.89 (s,3H), 7.95-8.07 (m,12H).

Synthesis of 4,4',4''-(benzenetricarbonyltris(azanediyl)tribenzoate)

In a round bottom flask with a stirrer, BTA-ABA-OEt was dissolved in 250 ml of DMF and then 16.8 mL of 4M NaOH was added dropwise. The mixture was stirred under reflux overnight, where it formed a yellow-clear solution. The mixture was acidified to pH 1-2 with a 1M solution of HCl. A white precipitate was filtered off and washed with water until pH 4. Afterward, the precipitate was washed with methanol (100 ml) and diethylether (100ml) and air dried. 5 g of the obtained compound was added to a suspension of 37.5 g LiOH in 150 mL methanol and the mixture stirred for 3.5h, and then acidified with HCl till pH 1. A white precipitate was filtered off and washed with water till pH 4, and then with methanol (100 ml) and diethylether (100 ml). The compound was then air dried.

Product - white solid. Global yield: 7.25 g (84 %). ¹H-NMR (500 MHz, DMSO-d₆): δ 7.93 (d,6H), 8.00 (d,6H), 8.89 (s,3H), 11.20 (s,3H). ¹³C-NMR (500MHz, DMSO-d₆): δ 119.46 (t), 130.23 (t), 130.69 (t), 133.14 (q), 135.31 (q), 141.46 (q), 164.94 (q), 169.52 (q).

Synthesis of Tetramethyl 5,5'-((2,2'-(5-((3,5-bis(methoxycarbonyl) phenyl) carbamoyl)-1,3 phenylene)bis(acetyl))bis(azanediyl))-diisophthalate

In a round bottom flask with a stirrer and nitrogen inlet and outlet, 7.5 g dimethyl-5-aminoisophthalate and 5 g potassium carbonate were dissolved in 60 ml of DMA (anhydrous) under a

nitrogen atmosphere. When dimethyl-5-aminoisophthalate was dissolved, 2.1 g of benzene-1,3,5-tricarbonyl trichloride was added dropwise and the mixture was stirred overnight, during which time a white precipitate formed. The precipitate was filtered off and washed sequentially with DMA (3x60ml), water (3x150 ml), methanol (100 ml), and diethyl ether (100 ml). The compound was dried under vacuum.

Product - white solid. Global yield: 6.55 g (79 %). ¹H-NMR (300 MHz, DMSO-d₆): δ 3.92 (s, 18H), 8.88 (s, 3H), 8.27 (t, 3H), 11.02 (s, 3H), 8.80 (d, 3H).

Synthesis of 5,5',5''-(benzenetricarbonyltris(azanediyl))triisophthalate

In a round bottom flask with a stirrer, 5g of BTA-AIP-OMe was suspended in 230 mL DMF and then 12 mL of 4M NaOH was added dropwise. The mixture was stirred under reflux overnight. Afterward, the precipitate was filtered off and washed with acetonitrile (3x100 ml) and acetone (3x100ml). The precipitate was dissolved in water and acidified till pH 1-2 with 1 M solution of HCl and a white precipitate formed. The precipitate was filtered off and washed with water until pH 4, and then with methanol (100 ml) and diethylether (100 ml). 2g of the obtained compound was added to a suspension of 15g LiOH in 60 mL methanol. This mixture was stirred for 2h and then acidified with HCl till pH 1. A precipitate formed, which was filtered off and washed with water till pH 4 and then with methanol (100 ml) and diethyl ether (100 ml). The compound was air dried.

Product - white solid. Global yield: 3.94 g (67 %). ¹H-NMR (300 MHz, DMSO-d₆): δ 8.26 (s, 3H), 8.87 (s, 3H), 8.74 (s, 3H), 11.02 (s, 3H). ¹³C-NMR (500 MHz, DMSO-d₆): δ 125.08(t), 132.5(q), 165.14(q), 125.75(t), 135.5(q), 167.05(q), 130.72(t), 140(q).

Synthesis of N-1,N3,N5-tris(4-(((S)-1-((2-aminoethyl)amino)-1-oxo-3-phenylpropan-2-yl)carbamoyl)phenyl)benzene-1,3,5-tricarboxamide (ABA-F1)

In a round bottom flask with stirrer, BTA-ABA-OH (0.1 g, 0.196 mmol) and DMTMM (BF₄) (0.29 g, 0.88 mmol) were dissolved in 3 mL of DMF. When the mixture became clear, H-F-EDA-Boc (0.27 g, 0.88 mmol) was added and the reaction allowed to proceed overnight. The mixture turned yellow and cloudy and was subsequently precipitated in water. The precipitate was filtered off and washed sequentially with water (3x20 ml), acidic water (pH 3, 3x20 ml), and acetonitrile (3x 20 ml). The compound was air dried.

Product - white solid. Global yield: 65mg (12 %). ¹H-NMR (300 MHz, DMSO-d₆): δ 1.36 (s, 27H), 2.91-3.20 (m, 18H), 4.65 (q, 3H), 6.76 (t, 3H), 7.12-7.36 (m, 15H), 7.87 (s, 12H), 8.11 (t, 3H), 8.47 (d, 3H), 8.73 (s, 3H), 10.76 (s, 3H).

30 mg of the compound was dissolved in methanol (0.5 ml) and 4M HCl in dioxane (0.5 ml) was added. The mixture was stirred for 5h at RT and then precipitated in diethyl ether. The compound was washed with diethyl ether until neutral pH and the product airdried.

Product - white solid. Global yield: 23mg (92 %). ¹H-NMR (300 MHz, DMSO-d₆): δ 2.72-3.19 (m, 12H), 4.67 (q, 3H), 7.12-7.40 (m, 15H), 7.86 (s, 6H), 7.89 (s, 6H), 7.98 (s, 3H), 8.01 (s, 6H), 8.33 (t, 3H), 8.61 (d, 3H).

Synthesis of N1,N3,N5-tris(3,5-bis(((S)-1-((2-aminoethyl) amino)-1-oxo-3-phenylpropan-2-yl)carbamoyl)phenyl)benzene-1,3,5-tricarboxamide (AIP-F1)

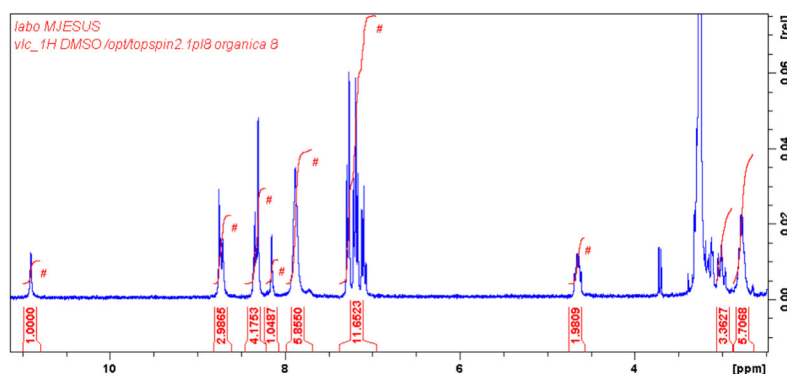
In a round bottom flask with a stirrer, BTA-AIP-OH (0.1 g, 0.23 mmol) and DMTMM (BF₄) (0.47 g, 1.40 mmol) were dissolved in 3 mL of DMSO. When the mixture became clear, H-F-EDA-Boc (0.66 g, 2.14 mmol) was added and the reaction allowed to proceed overnight. The mixture was precipitated in water and the precipitate was filtered off and washed with water (3x20 ml). The mixture

was dissolved in acetone and precipitated in acidic water (pH 3) and washed with acidic water of the same pH (3x20 ml) and then water (3x20 ml). The compound was freeze-dried.

Product - white solid. Global yield: 256mg (52 %). ¹H-NMR (300 MHz, DMSO-d₆): δ 1.36(s,54H), 2.91-3.21(m,36H), 4.72(q,6H), 6.74(t,6H), 7.11-7.34(m,30H), 7.99(s,3H), 8.17(t,6H), 8.33(s,6H), 8.57(d,6H), 8.78(s,3H), 10.82(s,3H).

150 mg of compound was dissolved in methanol (1.5 ml) and 4M HCl in dioxane (1.5 ml) added. The mixture was stirred for 6h at RT and precipitated in diethyl ether. The compound was washed with diethyl ether till neutral pH and the product airdried.

Product - white solid. Global yield: 115mg (82 %). ¹H-NMR (300 MHz, DMSO-d₆): δ 2.85(q,12H), 3.02-3.40(m,24H), 4.73(q,6H), 7.12-7.40(m,30H), 8.23(s,3H), 8.38 (s, 6H), 8.41(t,6H), 8.80(d, 6H), 8.83(s,9H), 10.98(s,3H).



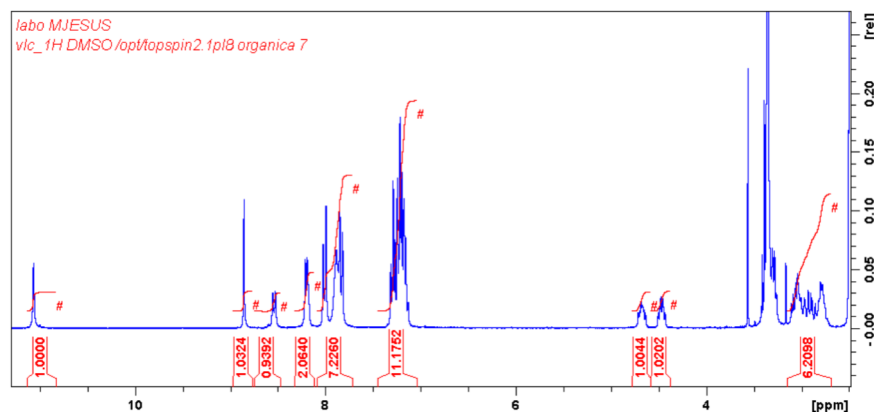
Synthesis of *N1,N3,N5-tris(4-(((S)-1-(((S)-1-((2-aminoethyl)amino)-1-oxo-3-phenylpropan-2-yl)amino)-1-oxo-3-phenylpropan-2-yl)carbamoyl) phenyl)benzene-1,3,5-tricarboxamide (ABA-F2)*

In a round bottom flask with a stirrer, BTA-ABA-OH (0.1 g, 0.196 mmol) and DMTMM(BF₄)(0.29 g, 0.88 mmol) were dissolved in 3 mL of DMF. When the mixture became clear, H-F2-EDA-Boc (0.53 g, 0.88 mmol) was added and the reaction was allowed to proceed overnight. The mixture turned yellow and cloudy and was precipitated in methanol. The precipitate was filtered off and washed sequentially with methanol (3x20 ml) and diethyl ether (20 ml). The compound was airdried.

Product - white solid. Global yield: 233mg (34 %). ¹H-NMR (300 MHz, DMSO-d₆): δ 1.37(s,27H), 2.79-3.16(m,24H), 4.47(q,3H), 4.69(q,3H), 6.71(t,3H), 7.11-7.32(m,30H), 7.79-7.93(m,12H), 7.96(t,3H), 8.12(d,3H), 8.46(d,3H), 8.74(s,3H), 10.78(s,3H).

230 mg of compound was dissolved in methanol (1.5 ml) and 4M HCl in dioxane (1.5 ml) was added. The mixture was stirred for 6h at RT and then precipitated in diethyl ether. The compound was washed with diethyl ether till neutral pH and the product airdried.

Product - white solid. Global yield: 101mg (51 %). ¹H-NMR (300 MHz, DMSO-d₆): δ 2.75-3.12(m,18H), 4.48(q,3H), 4.68(q,3H), 7.15-7.33(m,30H), 7.79-7.96(m,15H), 8.01(d,6H), 8.20(d,6H), 8.55(d,3H), 8.86(s,3H), 11.07(s,3H).

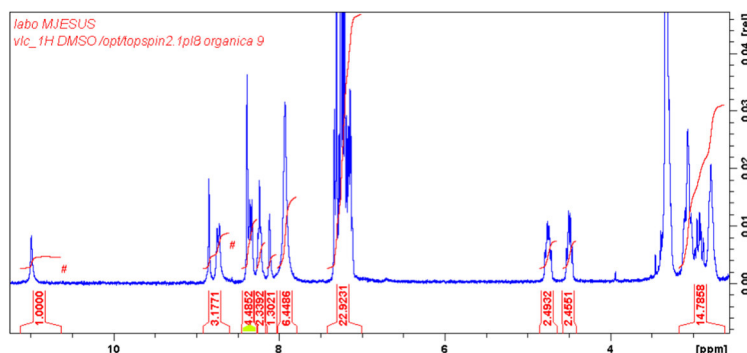


Synthesis of *N1,N3,N5-tris(3,5-bis(((S)-1-(((S)-1-((2-aminoethyl)amino)-1-oxo-3-phenylpropan-2-yl)amino)-1-oxo-3-phenylpropan-2-yl)carbamoyl)phenyl)benzene-1,3,5-tricarboxamide (AIP-F2)*

In a round bottom flask with a stirrer, BTA-AIP-OH (90 mg, 0.21 mmol) and DMTMM BF₄ (0.47 g, 2.0 mmol) were dissolved in 3 mL of DMSO. When the mixture became clear, H-F2-EDA-Boc (0.84 g, 2.0 mmol) was added and the reaction allowed to proceed overnight. The mixture turned yellow and remained clear and was precipitated in water. The precipitate was filtered off and washed with water (3x20 ml). The residue was redissolved in acetone and precipitated in acetonitrile. The precipitate was filtered off and washed with acetonitrile (3x50 ml). The compound was air dried.

Product - white solid. Global yield: 367mg (57 %). ¹H-NMR (300 MHz, DMSO-d₆): δ 1.36(s, 54H), 2.81-3.15(m, 48H), 4.49(q, 6H), 4.78(q, 6H), 6.68(t, 6H), 7.09-7.32(m, 60H), 7.91(s, 3H), 7.96(t, 6H), 8.22(d, 6H), 8.33(s, 6H), 8.54(d, 6H), 8.79(s, 3H), 10.85(s, 3H).

350 mg of compound 12 (270 mg) was dissolved in methanol (3 ml) and 4M HCl in dioxane (3 ml) added. The mixture was stirred for 6h at RT and was then precipitated in diethyl ether. The compound was washed with diethyl ether till neutral pH. The product was air dried. Product - white solid. Global yield: 295mg (89 %). ¹H-NMR (300 MHz, DMSO-d₆): δ 2.71-3.11(m, 36H), 4.49(q, 6H), 4.74(q, 6H), 7.10-7.35(m, 60H), 7.95(s, 18H), 8.12(s, 3H), 8.24(t, 6H), 8.34(d, 6H), 8.39(s, 6H), 8.74(d, 6H), 8.85(s, 3H), 10.99(s, 3H).



Prior to polymerization, the initiators were synthesized in amine form by redissolving in water and adding 4M NaOH till pH 9. The white precipitate formed was filtered off and the compound was washed with water (3x20 ml) till neutral pH and freeze-dried.

SI-4.2. Synthesis of BTA-F2C6 and BTA-F2C12

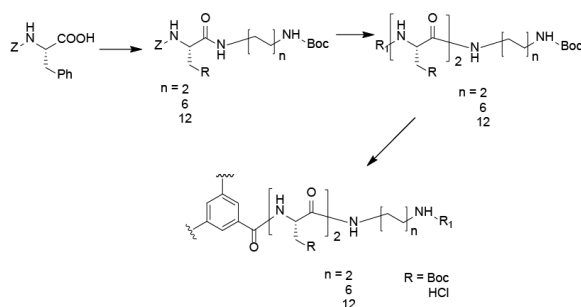
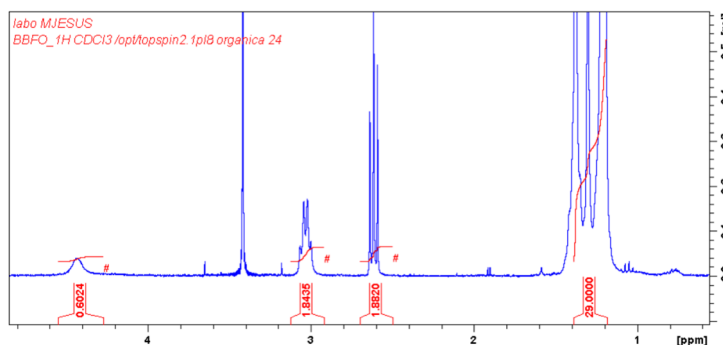


Fig. SI-4.2. General scheme of the synthesis of **BTA-F2C6** and **BTA-F2C12**.

Synthesis of *N*-Boc-dodecamethylenediamine

In a round-bottom flask with a stirrer, 1,12-dodecamethyldiamine was dissolved in 50 ml of chloroform. Boc₂O (0.5g, 2.29mmol) was dissolved in chloroform (10ml) and added dropwise to the solution of diamine, and the mixture was stirred overnight. The mixture was concentrated and purified with column chromatography (chloroform-methanol 1:9 (v/v), 1% TEA).

Product: white powder. Global yield: 2.52 g (75 %). ¹H NMR (CDCl₃, 300MHz): 4.43 (br.s., 1H), 3.04 (dt, 2H), 1.13-1.54 (m, 31H).



The synthesis of **BTA-F2C6** and **BTA-F2C12** was performed identically to the synthesis of **BTA-F2C2**.

Z-F-C6-Boc: Product - white solid. Global yield: 3.37 g (88.5 %). ¹H (DMSO-d₆): 7.83 (t, 1H), 7.36 (d, 1H), 7.30-7.05 (m, 10H), 6.67 (t, 1H), 4.87 (s, 2H), 4.11 (m, 1H), 3.05-2.60 (m, 6H), 1.33-1.03 (m, 17H).

Z-F-C12-Boc: Product - white solid. Global yield: 3.12 g (79 %). ¹H (DMSO-d₆): 1.15-1.41 (m, 29H), 2.67-3.14 (m, 6H), 4.19 (dt, 1H), 4.94 (s, 1H), 6.73 (t, 1H), 7.11-7.38 (m, 10H), 7.43 (d, 1H), 7.90 (d, 1H).

H-F-C6-Boc: Product - white solid. Global yield: 2.79 g (91 %). ¹H (DMSO-d₆): 7.74 (t, 1H), 7.31-7.10 (m, 5H), 6.75 (t, 1H), 3.34 (dd, 1H), 3.00 (n, 2H), 2.96-2.83 (m, 3H), 2.61 (dd, 1H), 1.61 (br.s., 2H), 1.41-1.25 (m, 13H), 1.24-1.11 (m., 4H).

H-FC12-Boc: Product - white solid. Global yield: 2.55 g (89 %). ¹H (DMSO-d₆, 300 MHz): 1.09-1.42 (m, 29H), 1.61 (br.s, 2H), 2.61 (dd, 1H), 2.88-3.12 (m, 5H), 3.34 (dd, 1H), 6.73 (t, 1H), 7.10-7.30 (m, 5H), 7.73 (t, 1H).

Z-F2-C6-Boc: Product - white solid. Global yield: 4.15 g (90 %). ¹H (DMSO-d₆): 8.00 (d, 1H), 7.76 (t, 1H), 7.37 (d, 1H), 7.30-7.00 (m, 15H), 6.67 (t, 1H), 4.94 (s, 2H), 4.47 (m, 1H), 4.24 (m, 1H), 3.11-2.61 (m, 8H), 1.41-1.11 (m, 17H).

Z-F2C12-Boc: Product - white solid. Global yield: 3.95 g (85 %). ¹H (DMSO-d₆, 300 MHz): 1.09-1.42 (m, 29H), 2.67 (dd, 1H), 2.76-3.09 (m, 7H), 4.23 (dt, 1H), 4.47 (dt, 1H), 4.93 (s, 2H), 6.72 (t, 1H), 7.07-7.37 (m, 15H), 7.43 (d, 1H), 7.83 (t, 1H), 8.08 (d, 1H).

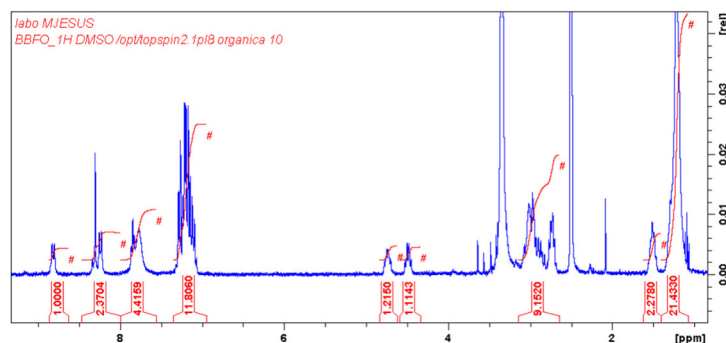
H-F2-C6-Boc: Product - white solid. Global yield: 3.43 g (86 %). ¹H (DMSO-d₆): 8.02 (d, 1H), 7.87 (t, 1H), 7.36-7.05 (m, 10H), 6.75 (t, 1H), 4.49 (m, 1H), 4.37 (m, 1H), 3.10-2.76 (m, 8H), 1.62 (br.s., 2H), 1.46-1.08 (m, 17H).

H-F2-C12-Boc: Product - white solid. Global yield: 3.27 g (92 %). ¹H (DMSO-d₆, 300 MHz): 1.07-1.49 (m, 29H), 1.62 (br.s, 2H), 2.77-3.09 (m, 8H), 3.37 (dd, 1H), 4.49 (dt, 1H), 6.73 (t, 1H), 7.08-7.30 (m, 10H), 7.87 (t, 1H), 8.02 (d, 1H).

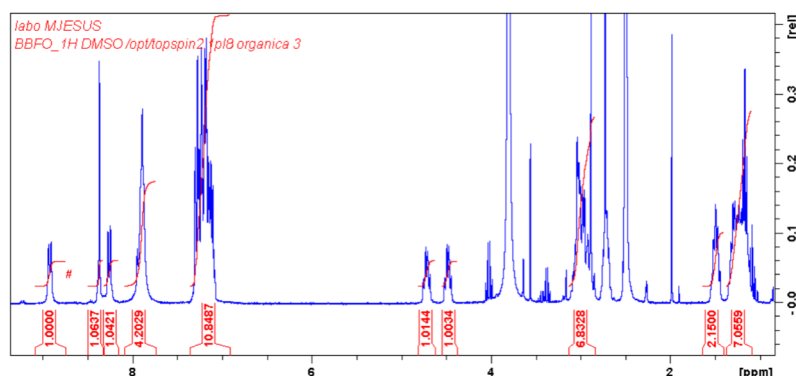
BTA-F2C12-Boc: Product - white solid. Global yield: 2.19 g (64 %). ¹H (DMSO-d₆): 1.08-1.41 (m, 29H), 2.77-3.10 (m, 8H), 4.49 (dt, 1H), 4.76 (dt, 1H), 6.71 (t, 1H), 7.04-7.33 (m, 10H), 7.81 (t, 1H), 8.19 (d, 1H), 8.21 (s, 1H), 8.70 (d, 1H).

BTA-F2-C6-Boc: Product - white solid. Global yield: 2.52 g (77 %). ¹H (DMSO-d₆): 8.70 (d, 1H), 8.22 (s, 1H), 8.20 (d, 1H), 7.82 (t, 1H), 7.31-7.06 (m, 10H), 6.75 (t, 1H), 4.77 (m, 1H), 4.50 (m, 1H), 3.12-2.78 (m, 8H), 1.40-1.07 (m, 17H).

BTA-F2C12-HCl: Product - white solid. Global yield: 1.85 g (95.7 %). ¹H (DMSO-d₆): 1.05-1.39 (m, 18H), 1.51 (m, 2H), 2.74 (m, 2H), 2.82-3.13 (m, 4H), 4.49 (dt, 1H), 4.72 (dt, 1H), 7.05-7.35 (m, 10H), 7.77 (br.s, 3H), 7.84 (t, 1H), 8.24 (d, 1H), 8.30 (s, 1H), 8.82 (d, 1H).



BTA-F2-C6-HCl: Product - white solid. Global yield: 1.77 g (94 %). ¹H (DMSO-d₆): 8.93 (d, 1H), 8.37 (s, 1H), 8.27 (d, 1H), 7.90 (m, 4H), 7.35-7.06 (m, 10H), 4.72 (m, 1H), 4.48 (m, 1H), 3.12-2.83 (m, 6H), 2.72 (m, 2H), 1.50 (m, 2H), 1.37-1.09 (m, 6H).



SI-4.3. Synthesis of BTA-ABA-F2C12 and BTA-ABA-Φ3C12.

Synthesis of **BTA-ABA-F2C12** and **BTA-ABA-Φ3C12** was performed identically to the synthesis of **BTA-ABA-F2**, with the synthesis of N-Boc-dodecadiamine and H-F2-C12 reported above.

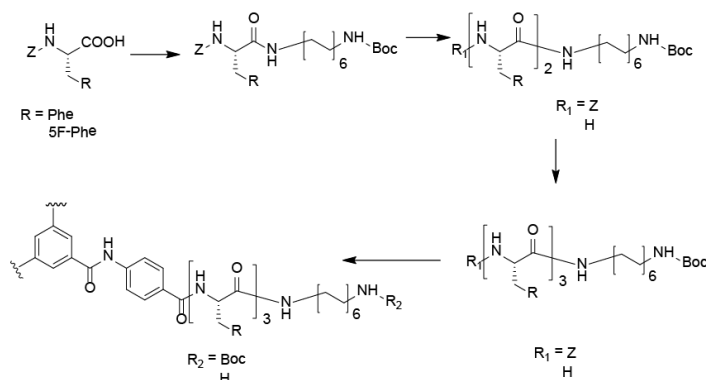


Fig. SI-4.3. General Synthetic Scheme for **BTA-ABA-Φ3C12** and **BTA-ABA-F3C12**.

Z-Φ1-C12-Boc: Product - white solid. Global yield: 2.26 g (81 %). ¹H-NMR (DMSO-d₆): 7.92 (t, 1H), 7.57 (d, 1H), 7.39-7.2 (m, 5H), 6.72 (t, 1H), 4.99 (q, 2H), 4.25 (m, 1H), 3.06 (m, 2H), 2.96-2.82 (m, 4H), 1.45-1.03 (m, 29H). ¹⁹F-NMR (DMSO-d₆): -141.7 (dd, 2F), -157.6 (t, 1F), -163.7 (dt, 2F).

H-Φ1-C12-Boc: Product - white solid. Global yield: 1.71 g (85 %). ¹H-NMR (DMSO-d₆): 7.79 (t, 1H), 6.71 (t, 1H), 3.33 (m, 1H), 3.09-2.71 (m, 4H), 1.43-1.09 (m, 29H). ¹⁹F-NMR (DMSO-d₆): -142.1 (dd, 2F), -158.6 (t, 1F), -164.0 (dt, 2F).

Z-Φ2-C12-Boc: Product - white solid. Global yield: 3.01 g (87 %). ¹H-NMR (DMSO-d₆): 8.23 (d, 1H), 7.99 (t, 1H), 7.58 (d, 1H), 7.40-7.21 (m, 5H), 6.72 (t, 1H), 4.98 (q, 2H), 4.53 (m, 1H), 4.28 (m, 1H), 3.11-2.77 (m, 8H), 1.45-1.03 (m, 29H). ¹⁹F-NMR (DMSO-d₆): -141.7 (dd, 2F), -142.0 (dd, 2F), -157.6 (t, 1F), -158.2 (t, 1F), -163.7 (m, 4F).

H-Φ2-C12-Boc: Product - white solid. Global yield: 2.35 g (83 %). ¹H-NMR (DMSO-d₆): 8.65 (d, 1H), 8.46 (t, 1H), 8.08 (d, 1H), 4.56 (m, 1H), 3.90 (m, 1H), 3.18-2.75 (m, 6H), 1.45-1.01 (m, 29H). ¹⁹F-NMR (DMSO-d₆): -141.3 (dd, 4F), -157.0 (t, 1F), -157.6 (t, 1F), -163.2 (dt, 2F), -163.6 (dt, 2F).

Z-Φ3-C12-Boc: Product - white solid. Global yield: 3.34 g (88 %). ¹H-NMR (DMSO-d₆): 8.42 (d, 1H), 8.21 (d, 1H), 7.96 (t, 1H), 7.56 (d, 1H), 7.39-7.21 (m, 5H), 6.72 (t, 1H), 4.96 (q, 2H), 4.63 (m, 1H), 4.53 (m, 1H), 4.61 (m, 1H), 3.13-2.77 (m, 10H), 1.51-1.02 (m, 29H). ¹⁹F-NMR (DMSO-d₆): -141.5 (dd, 2F), -141.7 (dd, 2F), -142.1 (dd, 2F), -157.5 (t, 1F), -158.0 (t, 1F), -158.2 (t, 1F), -163.7 (m, 6F).

H-Φ3-C12-Boc: Product - white solid. Global yield: 2.81 g (93 %). ¹H-NMR (DMSO-d₆): 8.45 (d, 1H), 8.20 (d, 1H), 8.97 (t, 1H), 6.72 (t, 1H), 4.60 (m, 1H), 4.52 (m, 1H), 3.39 (dd, 1H), 3.10-2.78 (m, 7H), 2.66 (dd, 1H), 1.43-1.03 (m, 29H). ¹⁹F-NMR (DMSO-d₆): -141.5 (dd, 2F), -141.8 (dd, 2F), -142.5 (dd, 2F), 157.90 (t, 1F), -158.0 (t, 1F), 158.50 (t, 1F), -163.8 (m, 6F).

Z-F3-C12-Boc: Product - white solid. Global yield: 2.01 g (94 %). ¹H-NMR (DMSO-d₆): 8.15 (d, 1H), 8.03 (d, 1H), 7.76 (t, 1H), 7.25 (d, 1H), 7.35-7.10 (m, 20H), 6.71 (t, 1H), 4.92 (s, 2H), 4.52 (m, 1H), 4.45 (m, 1H), 4.21 (m, 1H), 3.04-2.71 (m, 9H), 2.63 (dd, 1H), 1.44-1.06 (m, 29H).

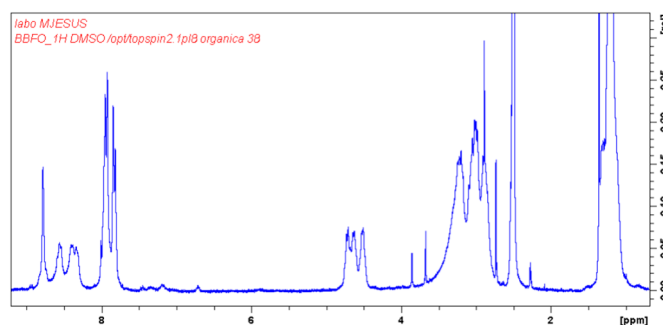
H-F3-C12-Boc: Product - white solid. Global yield: 1.55 g (80 %). ¹H-NMR (DMSO-d₆): 8.15 (d, 1H), 7.89 (d, 1H), 7.75 (t, 1H), 7.21-6.88 (m, 15H), 6.65 (t, 1H), 4.46 (m, 1H), 4.38 (m, 1H), 3.26 (m, 1H), 3.01-2.62 (m, 9H), 2.37 (dd, 1H), 1.61 (br.s, 2H), 1.39-0.98 (m, 29H).

BTA-ABA-chloroanhydride: BTA-ABA (100 mg) was suspended in 2 ml of dichloromethane. Thionyl chloride (0.5 ml) was added, and the mixture was refluxed for 30 min. The mixture was allowed to cool down to RT, and the solvent was removed under vacuum. 2 ml of DCM were added, and the solvent was removed under vacuum. After three solvent removal cycles, chloroanhydride was obtained as a white powder and used further without additional purification.

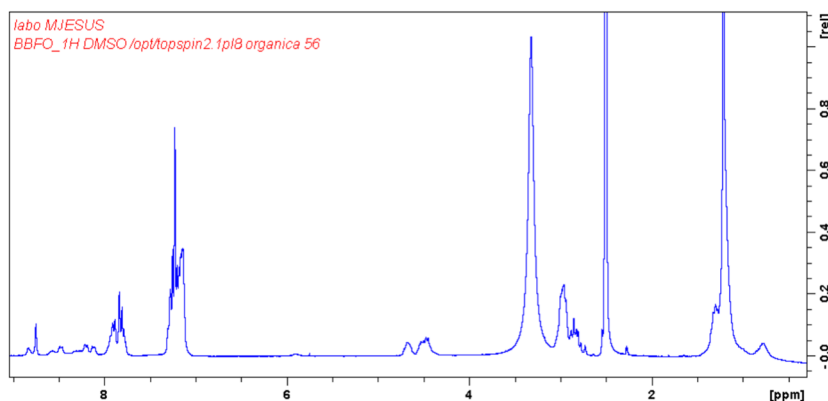
BTA-ABA-Φ3-C12Boc: Product - white solid. Global yield: 170 g (53 %). ¹H-NMR (DMSO-d₆): 10.80 (s, 1H), 8.77 (s, 1H), 8.53 (d, 1H), 8.37 (d, 1H), 8.30 (d, 1H), 7.99-7.79 (m, 6H), 6.72 (t, 1H), 4.72 (m, 1H), 4.63 (m, 1H), 4.52 (m, 1H), 3.11-2.78 (m, 10H), 1.41-1.05 (m, 29H). ¹⁹F-NMR (DMSO-d₆): -141.5 (dd, 2F), -141.7 (dd, 2F), -142.3 (dd, 2F), 157.70 (t, 1F), -158.0 (t, 1F), 158.20 (t, 1F), -163.8 (m, 6F).

BTA-ABA-F3-C12Boc: Product - white solid. Global yield: 370mg (48 %). ¹H-NMR (DMSO-d₆): 10.80 (s, 1H), 8.74 (s, 1H), 8.46 (d, 1H), 8.17 (d, 1H), 8.08 (d, 1H), 7.89 (d, 2H), 7.81 (d, 2H), 7.77 (t, 1H), 7.35-7.10 (m, 15H), 6.72 (t, 1H), 4.68 (m, 1H), 4.54 (m, 1H), 4.50 (m, 1H), 3.12-2.48 (m, 10H), 1.42-1.09 (m, 29H).

BTA-ABA-Φ3-C12-H: Product - white solid. Global yield: 140 g (99 %). ¹H-NMR (DMSO-d₆): 8.78 (s, 1H), 8.56 (d, 1H), 8.39 (d, 1H), 8.33 (m, 1H), 8.03-7.76 (m, 6H), 4.72 (m, 1H), 4.63 (m, 1H), 4.52 (m, 1H), 3.45-2.78 (m, 10H), 1.49-0.99 (m, 20H). ¹⁹F-NMR (DMSO-d₆): -141.5 (dd, 2F), -141.8 (dd, 2F), -142.2 (dd, 2F), 157.70 (t, 1F), -158.0 (t, 1F), 158.20 (t, 1F), -163.8 (m, 6F).



BTA-ABA-F3-C12-H: Product - white solid. Global yield: 335 g (98 %). ¹H-NMR (DMSO-d₆): 8.75 (s, 1H), 8.48 (d, 1H), 8.20 (d, 1H), 8.11 (d, 1H), 7.99-7.72 (m, 6H), 7.33-7.08 (m, 15H), 4.68 (m, 1H), 4.52 (m, 1H), 4.46 (m, 1H), 3.09-2.75 (m, 10H), 1.40-1.06 (m, 20H), 0.78 (br.s, 2H).



SI-4.4. Star-polyglutamate Synthesis

Polymerization was performed as already described in Chapter 2.

4.8. References

1. Howe, R. C. T. *et al. Chem Comm.*, **49**, 4268–4270 (2013).
2. Online, V. A. *et al. Chem. Comm.*, **50**, 5209–5211 (2014).
3. Lynes, A. D., Hawes, C. S., Byrne, K. and Schmitt, W. *Dalt. Trans.*, **47**, 5259–5268 (2018).
4. Baker, B. C. *et al. ChemistrySelect*, **1**, 1641–1649 (2016).
5. Besenius, P. *et al. PNAS*, **107**, 17888–17893 (2010).
6. Lynes, A. D. *et al. Cryst Eng Comm*, **19**, 1427–1438 (2017).
7. Zhang, Y. *et al. Polyhedron*, **33**, 127–136 (2012).
8. Anuradha, D. D., Al Kobaisi, M. and Bhosale, S. V. *Sci. Rep.*, **5**, 15652 (2015).

Chapter 5

Development of PGA based combination conjugates designed as triple negative breast cancer therapy

5.1. Introduction

Cancer is a family of diseases characterized by abnormal cell growth and the subsequent spread of the primary tumor throughout the body. Each cancer subtype possesses its own unique features and properties, such as proliferation rate, tendency to metastasize, treatment responsiveness, and therapy resistance. Treatment strategies have evolved from single-agent approaches to combination-based strategies using several drugs with differing targets or combinations of different therapeutic approaches.¹

Breast cancer, the most frequently diagnosed cancer in women, is a complex and heterogeneous disease that exhibits a high risk of developing metastasis and resistance mechanisms² and, therefore, represents a significant cause of death. Among the different breast cancer subtypes, triple negative breast cancer (TNBC) represents between 10-20% of all cases and displays poor clinical prognosis.³ While chemotherapy represents the most commonly chosen treatment for TNBC patients due to its high chemosensitivity compared to other subtypes⁴, patients with advanced disease exhibit poor responses, thereby triggering the requirement for new therapies.

Polymer-based Combination Therapy. Nanomedicine-based combination therapies may represent an efficient means to treat breast cancer^{5,6} with the approval of CombiPlex technology (Vyxeos, previously known as CPX-351)⁷ by the US FDA the

most relevant clinical milestone underling the importance of combination nanomedicines. This strategy involves the encapsulation of two clinically-approved chemotherapeutic drugs into a liposomal formulation.

As opposed to simple encapsulation of drugs, the conjugation of drugs or drug combinations to a polymeric backbone offers numerous advantages, which include passive tumor accumulation via the enhanced permeability and retention (EPR) effect in well-vascularized tumors⁸ and the ability to cross specific biological barriers to reach previously unreachable sites.⁹ Furthermore, polymer conjugation of drugs offers additional advantages,^{10,11} such as improved pharmacokinetics, overall multivalency,^{6,12} and the co-delivery of drugs at the desired ratio, and the specific release/activation at the required site of action via the application of polymer-drug linkers that respond to physiological stimuli.^{13,14} Overall, polymer based-combination therapy represents a more efficient anti-tumor strategy, and preclinical data has begun to underline the effectiveness of this approach.^{12,15–17}

The development of polypeptide and polymer conjugates recently started to shift from monotherapies towards combination therapeutics.¹⁸ Polypeptide combinations include either a physical mixture of a conjugate with another conjugate or free drug(s) or chemically conjugated drugs on the same polymer.^{19–21} Other strategies include combinations of the conjugate with immunotherapy, radiotherapy etc.^{22,23} The Polymer Therapeutics Laboratory at the CIPF developed the first polymeric combination conjugate for advanced hormone-dependent breast cancer; a conjugate of 2-(hydroxypropyl) methacrylamide-aminoglutethimide-doxorubicin (HPMA-AGM-Dox) that combines endocrine therapy (aromatase inhibitor) and chemotherapy, respectively.^{15–17} The development of this combination conjugate derived from the demonstrated activity of HPMA-Dox in chemoresistant breast tumors²⁴ and the observed synergism of aromatase inhibitors²⁵ with chemotherapy.^{26–28} The HPMA-AGM-Dox combination conjugate displayed increased *in vitro* and *in vivo* cytotoxicity in a metastatic breast cancer model (4T1),¹⁶ with the improvements deriving from altered biodistribution, differential release kinetics, and an altered molecular mechanism of action of the drug combination. We further corroborated the utility of similar combination conjugates findings via the generation of a new family of biodegradable polyglutamate (PGA)-based combination conjugates that displayed improved clinical relevance.^{17,29}

This Ph.D. thesis forms part of the European Research project “Towards the design of Personalised Polymer-based Combination Nanomedicines for Advanced Stage Breast Cancer Patients” (MyNano)” to continue breast cancer treatment research within the realms of polymer-based combination therapy. Within the framework of this project, we have screened different breast cancer lines representing the four main subtypes and detected subtype-specific synergic drug combinations that can reduce cancer cell viability and modulate tumor exosome biogenesis/release. Exosomes represent a molecular target that we are exploring as part of antimetastatic therapies.³⁰ For the TNBC

subtype, we discovered synergies between primaquine/fulvestrant, dinaciclib/fasudil, and neratinib/biscurcumin. While this thesis has been mainly focused on the well-defined polypeptidic biodegradable architectures that combine controlled polymerization techniques, biosensitive linkers, and cross-linking agents, as seen in the previous chapters, the final goal is to generate advanced combination conjugates,^{31,32} and this is the focus of this chapter.

This chapter describes the development of a combination therapy based on Rho-associated protein kinase (ROCK) (fasudil) and cyclin-dependent kinase (CDK) inhibitors (dinaciclib) for the treatment of metastatic TNBC, with both drugs previously identified as a synergistic pairing in TNBC treatment via a screening approach. We prepared a small family of compounds for each drug by applying different linking strategies that displayed responsiveness to enzymes, pH, or redox agents. We developed a family of single conjugates for each drug towards the main aim of constructing a combination conjugate with an adequate drug ratio and drug release kinetics (optimization of the linking chemistry). Other than TNBC cells (murine 4T1, human MDA-MB-231), we also evaluated each conjugate in MDA-MB-453 and ZR-75-1 cells, which represent other breast cancer subtypes positive for Her2, given that this subtype also displayed sensitivity to this combination.

5.2. Optimization Of PGA-Fasudil Conjugates As Anticancer Therapeutics

In Chapter 1, we described that polypeptide conjugates consist of the polymeric backbone, the linking moiety, drug(s), and, potentially, surface modifications. The nature of the polymer-drug linker plays a crucial role in the performance of the conjugate, determining release kinetics, and the overall activity of the drug. In this chapter, we evaluated several different responsive linkers to obtain optimal drug release. Additionally, we considered the role of PGA architecture in influencing the activity of the selected conjugates *in vitro*.

5.2.1. Synthesis and Characterization of PGA-Fasudil Conjugates - Polymer-drug Linker Optimization

Fasudil, an inhibitor of ROCK already approved for use in China and Japan,³³ belongs to a larger family of serine-threonine kinases.³⁴ ROCK is mainly involved in the regulation of the cytoskeleton, cell migration, and motility (**Fig. 5.1**), although many studies have observed the overexpression of ROCK in many cancer types, thereby providing support for ROCK inhibitors in anti-cancer therapeutics.³⁵ The ROCK inhibitor Y27632 decreased metastasis of breast cancer to the bone *in vivo*,³⁶ while fasudil, another ROCK inhibitor, also inhibited cell migration in the MDA-MB-231 breast cancer cell line³⁷ as well as in many other cancer types.³⁸⁻⁴¹ Fasudil-polymer conjugates have yet to be reported, so we prepared a family of Fas-PGA conjugates and studied their properties as a single agent and as a combination polymer conjugate therapy with dinaciclib.

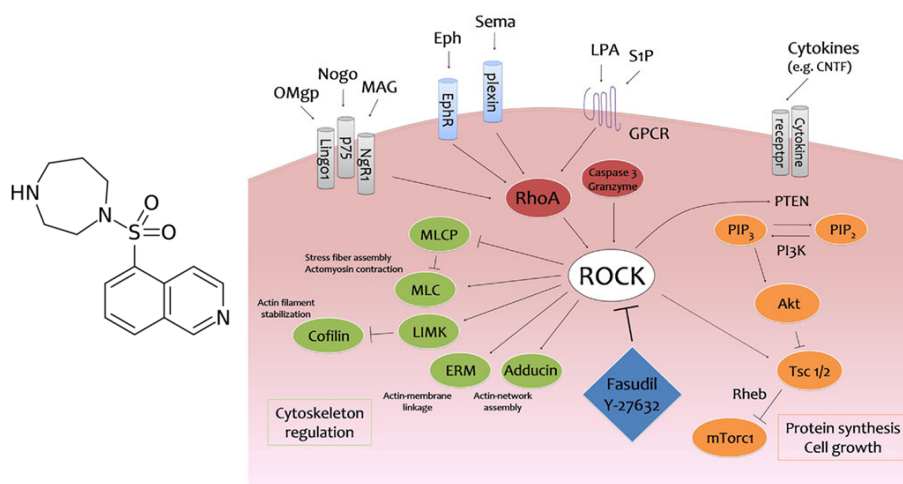


Figure 5.1. Chemical structure of fasudil and ROCK signaling pathway (adapted from⁴²).

Fasudil possess just one easily accessible functional group: the secondary amine in the diazepine ring. We prepared a small family of PGA-Fasudil conjugates connected through secondary amine with different linkers in an attempt to achieve optimized drug release kinetics. We attached fasudil through amide (PGA-FAS), carbamate (PGA-O-FAS), and disulfide self-immolative (PGA-SS-FAS) linkers. We prepared the amide linker by direct conjugation of the fasudil secondary amide to the carboxylic groups of PGA using DMTMM as a coupling agent. We prepared the carbamate linker in two steps using 2-propyn-2-ol carbamate derivative of fasudil further conjugated to azide-modified PGA using click reaction (Fig.5.2).

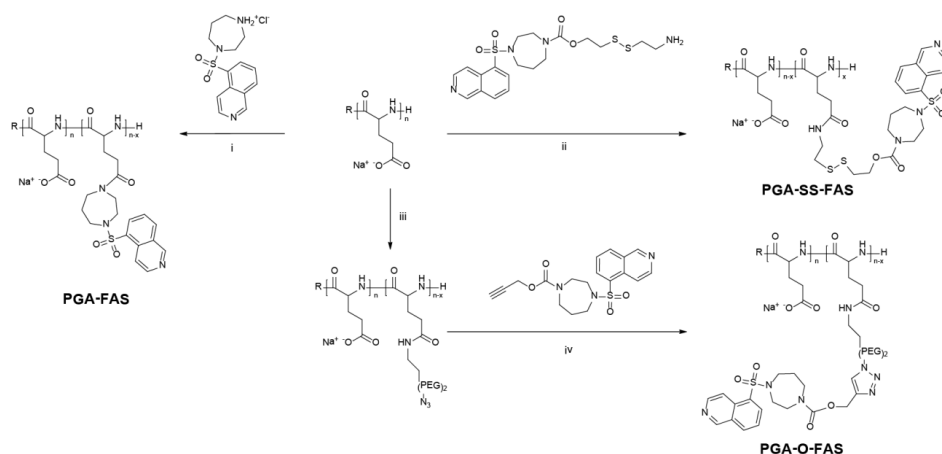


Figure 5.2. Synthesis of PGA-FAS, PGA-O-FAS, and PGA-SS-FAS. i) DMTMM Cl, NaHCO₃; ii) DMTMM BF₄, DIEA; iii) DMTMM Cl, DIEA, H₂N-PEG₂-N₃; iv) CuSO₄, Na Ascorbate.

We prepared an alternative self-immolative disulfide linker in four steps, as shown in **Fig.5.3**. The first step comprised the thiol exchange between pyridyl disulfide with mercaptoethanol, while the next two steps involved alcohol activation with *p*-nitrophenyl chloroformate and the consequent reaction with fasudil, giving the product **IC3**. The final step comprised the second thiol exchange with cysteamine hydrochloride and compound conjugation to PGA through amide coupling. We observed general instability for product **IC4**, with significant degradation after 48 h even at -80 °C; therefore, we performed the last coupling step immediately after compound preparation.

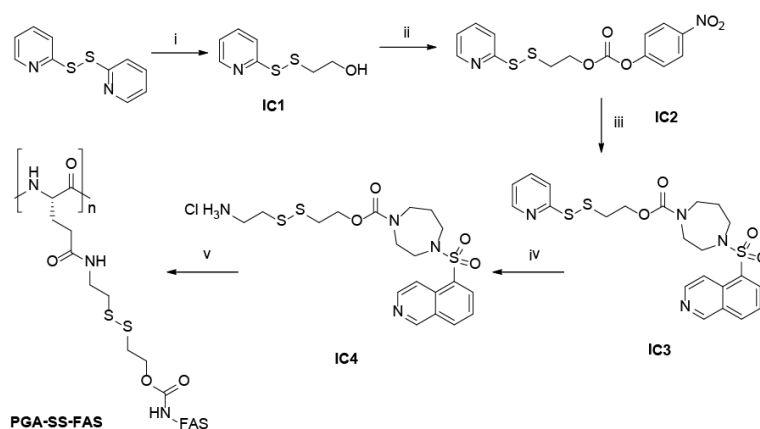


Figure 5.3. Synthesis of PGA-SS-FAS conjugates. i) $\text{HSCH}_2\text{CH}_2\text{OH}$, MeOH; ii) *p*-nitrochloroformate, TEA, THF; iii) Fas*HCl, TEA, DCM; iv) $\text{HSCH}_2\text{CH}_2\text{NH}_2$, MeOH; v) PGA, DMTMM BF_4 , DIEA.

We obtained the desired conjugates with high purity, as demonstrated by ^1H NMR experiments (**Fig.5.4**). UV-Vis analysis allowed us to determine total drug loading (% wt), which we found to be in good agreement with the estimated value obtained from NMR analysis (% molar) (**Fig. 5.5**).

We found a free drug content of below 0.1% wt of total drug loading using HPLC. **Table 5.1** summarizes the most relevant parameters for the physicochemical characterization of polymer-drug conjugates. DLS studies demonstrated that all the conjugates have a hydrodynamic radius in PBS close to 5nm and a negative value of z-potential close to -20 mV.

Table 5.1. Physicochemical Characterization of PGA-Fas conjugates.

| Conjugate | Linker | Yield, % | Conj. eff., % | TDL, %wt | FD, %wt | R_h , nm | Z-pot., mV |
|------------|---------------------------|----------|---------------|----------|---------|------------|------------|
| PGA-Fas | Amide | 89 | 92 | 13.7 | 0.01 | 4 | -21.5 |
| PGA-O-Fas | Carbamate | 76 | 87 | 12.4 | 0.1 | 5 | -19.4 |
| PGA-SS-Fas | Self-immolative disulfide | 79 | 85 | 10.5 | 0.1 | 5 | -23.4 |

^aDetermined by UV-Vis. ^bDetermined by HPLC (UV-Vis) and calculated as % of the total drug loading.

^cHydrodynamic radius and z-potential measured via DLS instrument in 1mM KCl.

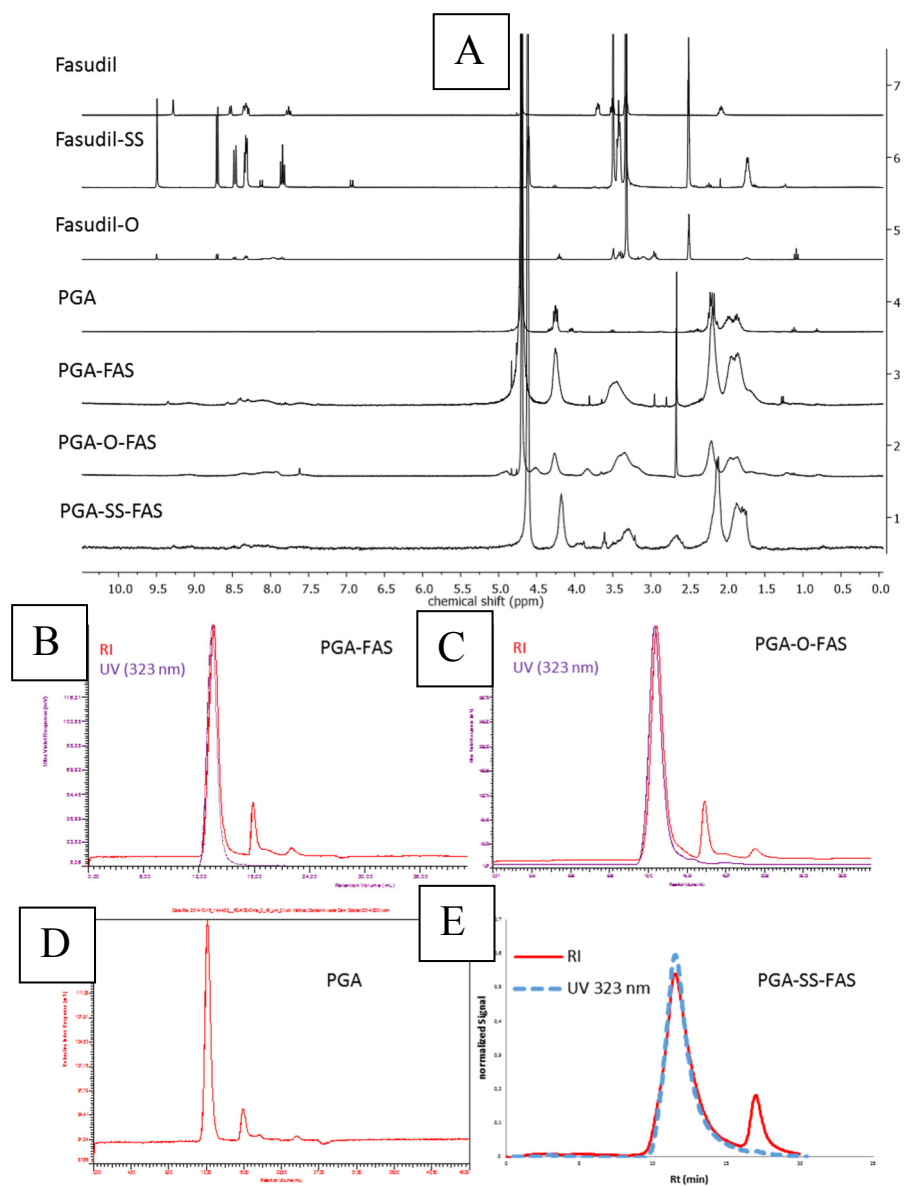


Figure 5.4. Characterization of PGA-Fasudil conjugates: A) Chemical identity and purity assessed via ^1H NMR spectroscopy. Size-exclusion chromatograms for PGA-Fas (B), PGA-O-Fas (C), the parent polymer (D) and PGA-SS-Fas (E).

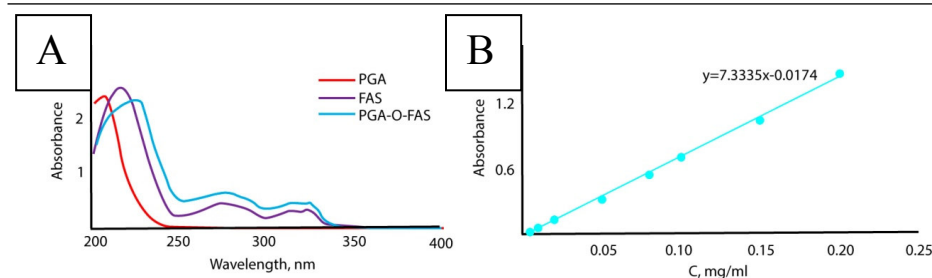


Figure 5.5. UV-Vis spectra of each conjugate (A) and the calibration curve for the free drug (B).

5.2.2. Drug Release Kinetics of PGA-Fasudil Conjugates

Next, we had studied the kinetics of fasudil release in conditions corresponding to the responsive nature of the linker. We designed the amide linker of PGA-Fas to be cleaved by proteases, and so, we studied release in the presence of Cathepsin B. We observed a prolonged drug release, reaching only 1.5 % after 3 days (**Fig.5.6A**) and, for that reason, we discontinued further studies of these conjugates.

The carbamate linkers of PGA-O-Fas cleave in responsive to basic pH conditions, so we studied drug release at pH 6.0 and 7.4. At pH 7.4, we detected less than 1% release during the first 5 days; however, at pH 6, we observed somewhat better release, reaching 5% after 5 days (**Fig.5.6B**).

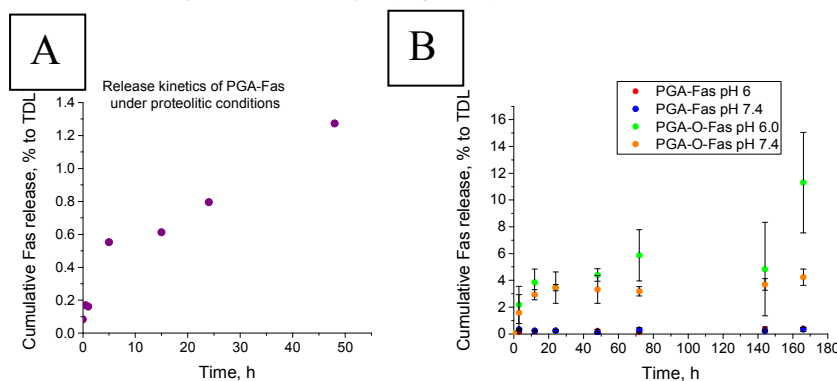


Figure 5.6. Drug release kinetics under different hydrolytic conditions found in the endocytic pathway: Hydrolytic acid conditions for PGA-O-Fas and PGA-Fas (A), Data as mean \pm SEM (n=3); Proteolytic conditions (Cathepsin B) for PGA-Fas (B).

The self-immolative disulfide linker of PGA-SS-FAS displays redox-responsiveness, and we studied release in the presence of 5 mM and 10 μ M DTT, mimicking intra and extracellular concentration of GSH. In the presence of 5 mM DTT, we observed very rapid drug release, reaching 80 % after 8 hours and close to 100 % after 24 h. During the first 6 hours, we detected linear release kinetics characteristics of

for zero-order kinetics. In the presence of 10 μ M DTT, we failed to observe any drug release, even after 72 h (**Fig. 5.7**).

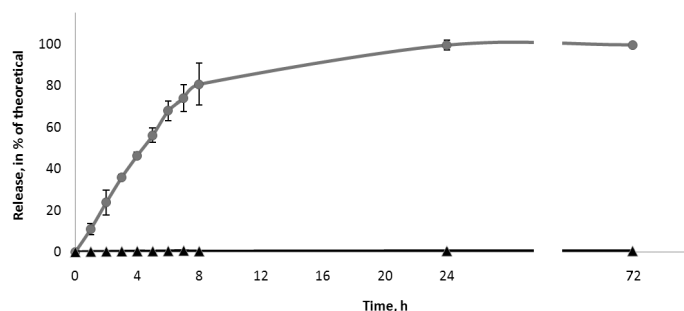


Figure 5.7. Release kinetics in 5 mM (gray circles) and 10 μ M (black triangles) DTT.

5.2.3. *In vitro* Studies of PGA-Fasudil Conjugates

We next studied toxicity profiles for PGA-FAS, PGA-O-FAS, and PGA-SS-FAS in three breast cancer cell lines: 4T1 (murine TNBC), MDA-MB-231 (human TNBC), and MDA-MB-453 (Human Her2-positive) using the MTT cell viability assay at 72h post-treatment.

We observed the complete inactivity of conjugates with amide (PGA-Fas) and carbamate linkers (PGA-O-Fas) in the 4T1 cell line (**Fig.5.8A**), while in MDA-MB-231 cells, the carbamate linker (PGA-O-Fas) showed weak activity, while PGA-Fas also remained inactive (**Fig.5.8B**). Overall, this behavior correlates well with release kinetics results. Amide bonds generally take a prolonged time to cleave,⁴³ while the pH-dependent cleavage of carbamate depends on each particular molecule and may vary in a broad range.⁴⁴ Taking into account the release kinetics from PGA-O-Fas (i.e., slow-release in acidic medium), the activity profile might be explained either by much lower pH in the endosomes of MDA-MB-231 or by enhanced expression of specific enzymes which can cleave carbamates. Conjugates with self-immolative disulfide linkers (PGA-SS-Fas) displayed significantly higher activity, vastly exceeding the activity of free fasudil in MDA-MB-231, although displaying lower activity than the free drug in 4T1 cells (**Fig. 5.8C-D**). We performed an additional study of PGA-SS-Fas in MDA-MB-453 cells and observed the slightly higher activity of the PGA-SS-Fas than free fasudil (**Fig.5.8E**). The substantial differences between the activity of PGA-SS-Fas in different cell lines might correlate with altered GSH levels or different modes of conjugate internalization. Data in the literature concerning GSH levels in the selected cell lines establish GSH levels in MDA-MB-231 cells of 7-12 mM,⁴⁵ in 4T1 of ~2mM,⁴⁶ and in MDA-MB-453 of ~4 mM.⁴⁷

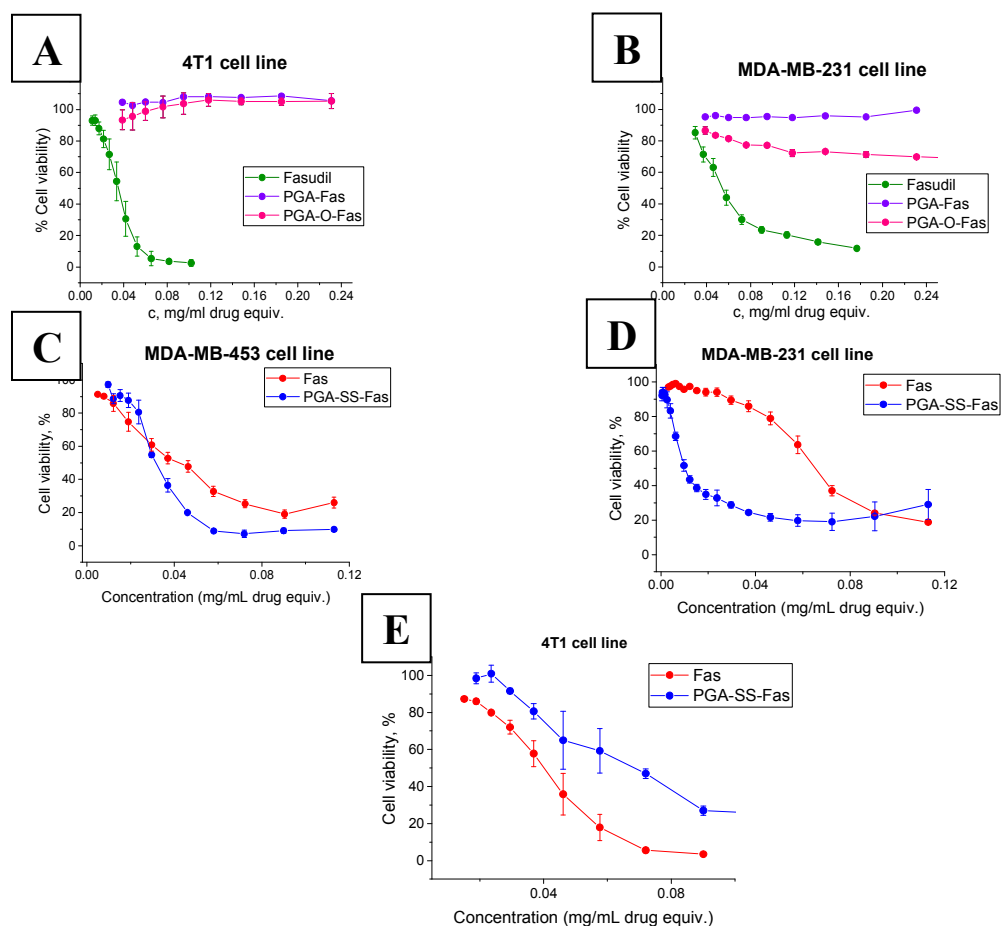


Figure 5.8. Cell viability studies at 72h by MTT assay following treatment with PGA-Fas and PGA-O-Fas in 4T1 (A) and MDA-MB-231 (B), and PGA-SS-Fas in MDA-MB-453 (C), MDA-MB-231, (D) and 4T1 (E) cell lines.

Studies have reported significantly lower levels of both ROCK1 and 2 in luminal breast cancers than in HER2-positive cancers and TNBCs.⁴⁸ Nuclear ROCKII signal correlated negatively with estrogen receptor (ER) and progesterone receptor (PR) expression and positively with HER2 overexpression. HER2 activates multiple signaling pathways, including ERK1/2, MAPK, and PI3K/Akt. ERK1/2 is an upstream effector of GTP-activating proteins and guanine exchange factors, which in turn activate ROCK. We observed a similar correlation for free drug between MDA-MB-231 and MDA-MB-453; the IC₅₀ values for fasudil were 0.04 and 0.065 mg/ml, respectively. Nevertheless, even after combining the data on GSH and ROCK levels, we do not observe a clear correlation between activity levels and fasudil conjugates in breast cancer cell lines. In

4T1 cells, the lower activity of the conjugate may be due to lower GSH levels and slower linker cleavage.

From the previous study we determined that PGA-SS-Fas is the most active conjugate in the family with unexpectedly high activity in MDA-MB-231 cell line. In order to check if the drug and the conjugate act in a similar way we assessed the migration of MDA-MB-231 cells following treatment with fasudil the PGA-SS-Fas. We discovered that both free drug (**Fig. 6.9D**) and conjugate (**Fig. 6.9E**) inhibited cell migration. PGA itself, used as a control, failed to inhibit cell migration (**Fig. 6.9C**). However, PGA-SS-FAS inhibited cell migration to a lesser degree than the free drug (**Fig. 6.9G**) (42% vs. 20%, respectively). Taking into account higher toxicity of the conjugate and its lower migration inhibition we can conclude that the mechanism of action of the drug and the conjugate are not identical, which can be caused by different internalization pathways.

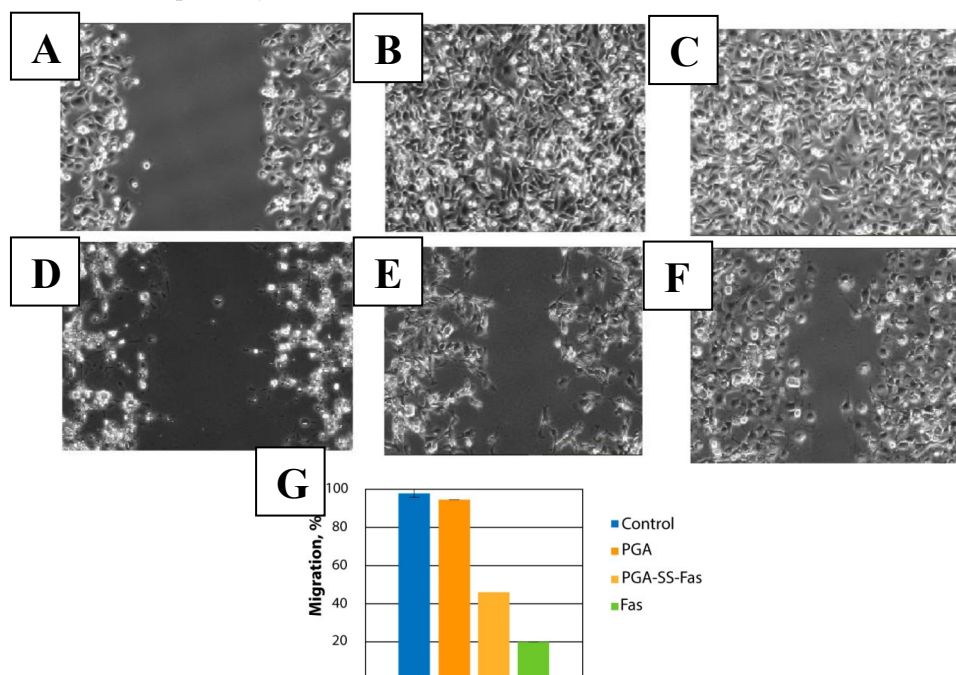


Figure 5.9. Migration assay in MDA-MB-231. Data corresponding to the migration assay performed under different treatments. Data expressed as mean \pm SEM, n=2. Statistical analysis was performed using Student's t-test, * $p < 0.05$, ** $p < 0.01$, *** $p < 0.001$, relative to the control. A) Migration of cells at t=0h. B) Migration of cells at 24h in control conditions. C) Migration of cells at 24h under PGA treatment. D) Migration of cells at 24h under Fas IC₅₀ treatment. E) Migration of cells at 24h under PGA-SS-Fas treatment. F) Migration of cells at 24 h under Fas treatment. G) Quantification of migration. Data expressed as mean \pm SEM, n=2.

Given these results, we selected the conjugate containing the self-immolative disulfide linker (PGA-SS-Fas) as the most promising candidate for further studies.

5.2.4. Synthesis and Characterization of PGA-Fasudil Conjugates – Architectural Optimization

Maintaining the self-immolative disulfide linker as the polymer-drug linking moiety, we next evaluated stPGA polymers with different architectures (linear, three- and six-arm polymers) and polymerization degree (30-600) to study the effect of architecture on drug performance *in vitro*.

We prepared five stPGA-SS-Fas conjugates with self-immolative disulfide linkers using the methodology described above (Fig. 5.10). We obtained the three-branched stPGAs (F3E10, F2E50, and F2E200 compounds) used as carriers, as reported in Chapter 2, and the six-branched PGAs (AIP-F2E10 and AIP-F2E25) as reported in Chapter 4. Figure 5.10 provides a general scheme of PGA-SS-FAS conjugates with different architectures. Conjugates were extensively characterized and their main physicochemical properties are shown in Table 5.2.

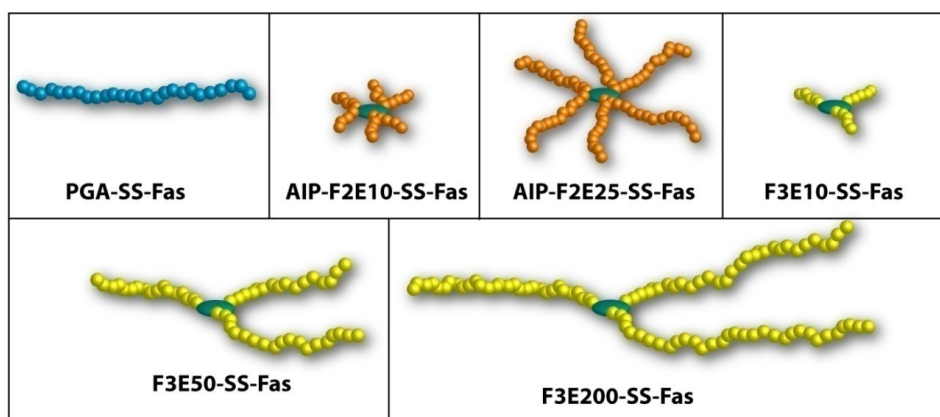


Figure 5.10. General scheme of the PGA-SS-FAS conjugates with different architectures.

Table 5.2. Structure and characterization of the prepared conjugates.

| Conjugate | N arms | Glu/arm | DP ^a | TDL ^b , % | Free drug ^c , % | Size ^d , nm |
|------------------|--------|---------|-----------------|----------------------|----------------------------|------------------------|
| PGA-SS-Fas | - | 100 | 100 | 12.5 | 0.5 | 4.1 |
| F3E10-SS-Fas | 3 | 10 | 30 | 16.8 | 0.5 | 2.8 |
| AIP-F2E10-SS-Fas | 6 | 10 | 60 | 14.1 | 0.5 | 3.2 |
| F3E50-SS-Fas | 3 | 50 | 150 | 14.8 | 0.5 | 4.7 |
| AIP-F2E25-SS-Fas | 6 | 25 | 150 | 10.7 | 0.5 | 4.5 |
| F3E200-SS-Fas | 3 | 200 | 600 | 11.5 | 0.5 | 8.6 |

^aDetermined by GPC. ^bDetermined by UV-Vis. ^cDetermined by HPLC (UV-Vis) and calculated as % of the total drug loading. ^dHydrodynamic radius measured via DLS instrument in 1mM KCl.

Toxicity of all the conjugates was studied *in vitro* on the MDA-MB-231 cell line, and IC₅₀ values are present in **Fig. 5.11**. Overall, we discovered that polymer architecture has a pronounced effect on conjugate toxicity. The linear conjugate (PGA-SS-Fas) presented the highest cytotoxicity (lowest IC₅₀), and both **F2E200-SS-Fas** and **F2E50-SS-Fas** displayed comparable IC₅₀ values. Compounds **F3E10-SS-Fas**, **AIP-F2E10-SS-Fas**, and **AIP-F2E25-SS-Fas** also displayed comparable toxicities, at an approximately three times higher IC₅₀ value when compared to the linear analog. However, all conjugates displayed better toxicity profiles when compared to the free drug independent of architecture.

The toxicity difference between the polymers with different architectures may be explained in terms of spatial charge density. While cell membranes display a negative charge, PGA cannot freely diffuse through the membrane due to electrostatic repulsion and becomes internalized by endocytosis. The spatial charge density of the polymers is highest for short polymers (**F3E10-SS-Fas** and **AIP-F2E10-SS-Fas**) and decreases with an increase in the degree of polymerization.

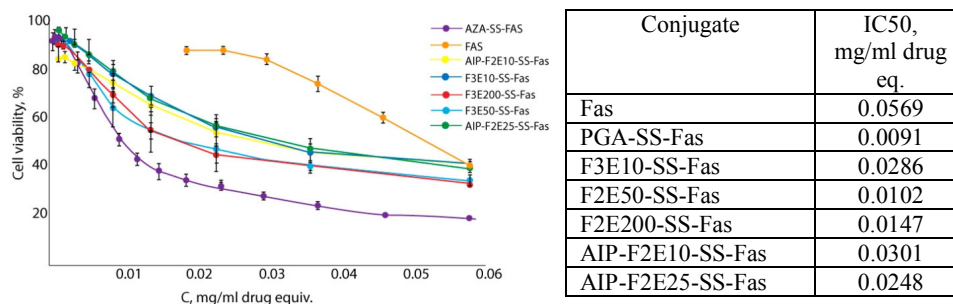


Figure 5.11. Cell viability studies of PGA-SS-Fas conjugates with different polymer architecture in the MDA-MB-231 cell line, 72h MTT assay. Data represented as mean \pm SD (n>3).

5.2.5. Plasma Stability of Selected Conjugates

Prior to moving to *in vivo* experiments, we studied the stability of the conjugate in blood plasma. This research included a close collaboration with Snežana Dordevic, a Ph.D. student in the laboratory. We developed a method for the liquid chromatography-mass spectrometry (LC-MS) determination of fasudil levels using triple quadrupole ion trap MS with electrospray ionization. Validation of analytical data obtained from biological sample analysis is of fundamental importance since they are used to make critical decisions supporting the safety and efficacy of a medicinal drug substance or product.

5.2.5.1. Method Validation

5.2.5.1.1. Linearity

We plotted calibration curves for fasudil and ranitidine (internal standard) peak area ratio versus fasudil and ranitidine concentration ratio. We found a linear calibration curve over a concentration range of 5 ng/ml to 1000 ng/ml. The linearity was represented by a linear regression equation as follows (see below) with an R^2 value of 0.9994.

$$y = 0.3225 x + 0.4908$$

We present the values used for the calibration curve, together with back-calculated concentrations and % accuracy, which ranges from 91.99 % to 101.0 %, in **Table 5.3**. Limit of detection and limit of quantification values calculated from the LINEST function were 5.31 ng/ml and 16.09 ng/ml, respectively. We employed this calibration curve for the calculation of fasudil concentration in all plasma samples and in the comparison of results obtained from other validation parameters.

Table 5.3. Calibration solutions used for the construction of calibration curve, their back-calculated concentrations and accuracy

| $C_{\text{fas}}/C_{\text{ran}}$ (ng/ml) | $S_{\text{fas}}/S_{\text{ran}}$ | Back-calculated C (ng/ml) | Accuracy (%) |
|--|---------------------------------|------------------------------|-----------------|
| 10 | 3.4575 | 9.1991 | 91.99 |
| 20 | 6.7825 | 19.5091 | 97.55 |
| 50 | 16.0296 | 48.1823 | 96.36 |
| 100 | 32.7640 | 100.0722 | 100.07 |
| 200 | 65.6327 | 201.9905 | 101.00 |
| 400 | 130.3232 | 402.5811 | 100.65 |
| 800 | 258.2984 | 799.4034 | 99.93 |
| 1000 | 322.7873 | 999.3690 | 99.94 |

C_{fas} – concentration of fasudil, C_{ran} – concentration of ranitidine, S_{fas} – peak area of fasudil peak, S_{ran} – peak area of ranitidine peak

5.2.5.1.2. Stability

The second step in LC-MS/MS method validation was the evaluation of stock (1 mg/ml) and working (10 µg/ml) solutions of fasudil and ranitidine for 48h at -20 °C. The results shown in **Fig. 5.12** establish the stability of stock and working solutions of fasudil and ranitidine over 48h. Nevertheless, we still suggest the preparation of sample/calibration solutions for analysis from fresh stock and working solutions, if possible.

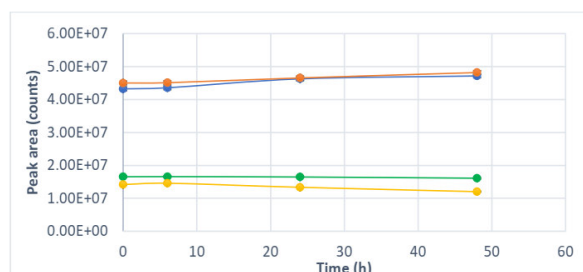


Figure 5.12. Stability of stock and working solutions of fasudil (1 mg/ml [red] and 10 µg/ml [blue] and ranitidine (1 mg/ml [green] and 10 µg/ml [yellow] color)

5.2.5.1.3. Selectivity

We assessed the selectivity of our method by comparing the chromatogram of blank plasma and spiked plasma. We found retention times of 1.27 min for fasudil and 1.22 for ranitidine as represented in **Fig. 5.13A,B**. In the blank plasma chromatogram (**Fig. 5.13C**), we failed to observe any significant endogenous peaks that could interfere with a retention time of analyte and internal standard, overall indicating that the method displayed good selectivity. Additionally, we injected the blank plasma sample after the ULOQ control sample and used this to evaluate any potential carry-over effect of the analyte or internal standard from one sample to another. The obtained blank chromatogram established a lack of carry-over effect, thereby permitting the continued further validation of the method.

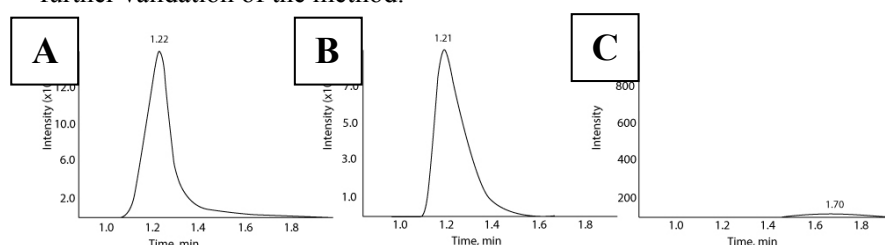


Figure 5.13. Chromatograms obtained from fasudil (A), ranitidine (B), and blank plasma (C) detected in positive electrospray ionization mode with multiple reaction monitorings cans and by following two mass transitions $292.4 \text{ m/z} \rightarrow 99.2 \text{ m/z}$ and $292.4 \rightarrow 129.0 \text{ m/z}$ for fasudil, and $315.2 \text{ m/z} \rightarrow 101.9 \text{ m/z}$ and $315.2 \text{ m/z} \rightarrow 130.0 \text{ m/z}$ for ranitidine

5.2.5.1.4. Precision and Accuracy

We calculated the precision of the LC-MS/MS method as the pooled relative standard deviation according to Equation 2, Equation 3, and Equation 4:

$$RSD_{pooled} = \sqrt{\frac{RSD_1^2 + RSD_2^2 + \dots + RSD_k^2}{k}}$$

Equation 2

$$RSD = \frac{Sd}{C_{mean}}$$

Equation 3

$$Sd = \sqrt{\frac{\sum_{i=1}^n (C_i - C_{mean})^2}{n - 1}}$$

Equation 4

where RSD_{pooled} represents the pooled relative standard deviation, RSD the relative standard deviation, k the number of groups, Sd the standard deviation, C_{mean} the mean concentration of fasudil, and C_i the concentration of fasudil for a specific sample, while n is the number of replicates. In this project, we were not able to perform this number of replicate measurements due to the limited amount of available plasma samples; therefore, we calculated the RSD_{pooled} value instead of the RSD .

We also calculated the accuracy of the developed LC-MS/MS method at four QC levels (LLOQ, low, medium, and ULOQ) and presented this accuracy as the percentage difference between fasudil concentration in QC levels and nominal value (fasudil concentration from calibration solutions).

We determined both within-run and between-run accuracy and precision; these data are presented in **Table 5.5**. According to these results, the accuracy and precision are appropriate and with the acceptance level recommended by validation guidelines ($\pm 20\%$ for LLOQ and $\pm 10\%$ for the rest of the QC levels). Both precision and accuracy improve as the concentration of the analyte increases, as expected for LC-MS/MS-based analysis.

Overall, we confirm the accuracy and precision of the developed method for the determination of fasudil concentration in plasma.

Table 5.4. Parameters obtained for within-run and between-run accuracy and precision

| | | Within-run | | Between-run | |
|-----------|-----------|-----------------------|------------------------|-----------------------|------------------------|
| Sample | C (ng/ml) | Accuracy ^a | Precision ^b | Accuracy ^a | Precision ^b |
| LLOQ | 10 | -11.49% | 10.68% | -10.10% | 9.52% |
| Low QC | 30 | -4.21% | 8.48% | -4.28% | 9.17% |
| Medium QC | 500 | -3.01% | 5.21% | -3.01% | 5.83% |
| High QC | 1000 | -2.89% | 3.18% | -2.88% | 3.15% |

^adifference from nominal value

^b RSD_{pooled}

5.2.5.1.5. Matrix Effect

After performing the LC-MS/MS analysis of blank plasma spiked with fasudil and ranitidine at LLOQ, medium QC, and ULOQ levels after sample preparation, we calculated the matrix effect values (the effect of plasma as a solvent) as the ratio of the peak area in the presence of matrix and the peak area in the absence of matrix.

We encountered matrix factor values of 0.9106, 0.9278, and 0.9492 for fasudil at the low, medium, and elevated levels of QC sample, 0.9370 for ranitidine (Table 6.6) indicating a lack of coeluting substances that could significantly influence the signal of the analyte and internal standard. To achieve more precise concentration results, we will use matrix-matched calibration solutions in the plasma stability study.

Table 5.5. Matrix effect values obtained for fasudil and internal standard

| | MF _{fas} | MF _{ran} | MF _{fas} /MF _{ran} | RSD |
|-----------|-------------------|-------------------|--------------------------------------|--------|
| LLOQ | 0.9106 | 0.9370 | 0.9612 | 2.829% |
| Medium QC | 0.9278 | 0.9370 | 0.9902 | 2.012% |
| ULOQ | 0.9492 | 0.9370 | 1.0130 | 1.805% |

MF_{fas}- matrix effect for fasudil, MF_{ran}- matrix effect for ranitidine, RSD - relative standard deviation

5.2.5.1.6. Recovery

The calculation of the recovery for three replicates at low-, medium-, and high-QC levels (10 ng/ml, 500 ng/ml and 1000 ng/ml) represents the last step in the validation of the LC-MS/MS method for the determination of fasudil in plasma. We found mean extraction recoveries for fasudil of 76.5±3.2 %, 78.9±5.1 %, and 81.3±1.5 % for all three QC levels. The mean recovery for ranitidine as internal standard (1 ng/ml) was 79.04±2.5 %.

In the stability studies that will be performed later, we employed an internal standard to take said recovery values into consideration and to ensure the trueness of this method.

5.2.5.1.7. Process Efficiency

Process efficiency is a general term used to express the “trueness” of LC-MS methods. In this study, we calculated the process efficiency for LLOQ, medium QC and ULOQ level in two different cases. First, we calculated the process efficiency for the LC-MS/MS method without using internal standard, according to Equation 5:

$$\%PE = \frac{\%R * \%ME}{100}$$

Equation 5

where %PE represents the process efficiency, %R the recovery for fasudil, and %ME the matrix effect for fasudil. Then, we calculated the process efficiency when using an internal standard, according to Equation 6:

$$\%PE = \frac{\left(\% \frac{R_{fas}}{R_{ran}} * \% \frac{ME_{fas}}{ME_{ran}} \right)}{100}$$

Equation 6

where %PE represents the process efficiency expressed as a percentage and so %R the recovery value for fasudil (% R_{fas}) and ranitidine (% R_{ran}) and %ME the percentage of matrix effect for fasudil (% ME_{fas}) and ranitidine (% ME_{ran}).

Fig. 5.14 depicts the obtained results for process efficiencies, where the values rise from 68.90% to 93.03%, then from 73.20% to 98.84% and from 77.17% to 104.20% at the three QC levels when employing an internal standard. Again, these results highlight the importance of employing an internal standard in quantitative analysis, which allows the better trueness of the method.

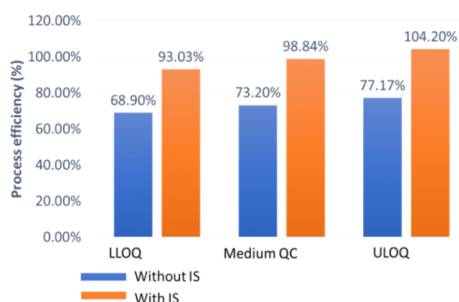


Figure 5.14. Process efficiency values obtained with (blue) and without (orange) an internal standard (IS) at three QC levels (LLOQ- 10 ng/ml; medium QC- 500 ng/ml; ULOQ - 1000 ng/ml).

5.2.5.2. Plasma Stability of the PGA-SS-FAS Conjugate

Both the polymer and the linker used for drug conjugation must remain stable in the bloodstream to allow for targeted delivery; therefore, stability studies will provide insight into the fate of PGA-SS-Fas conjugates in the bloodstream and subcellular compartments. Given the analytical applications of LC-MS methods and the low concentrations of free drug in this situation, we explored LC-MS as a means to analyze the stability of PGA-SS-Fas conjugates.

We analyzed the samples with the previously developed and validated LC-MS/MS method. We calculated the concentration of free fasudil in plasma solutions, sampled at defined time points, and presented the values as a percentage of the free drug compared to the total concentration of conjugated fasudil (Figure 5.15).

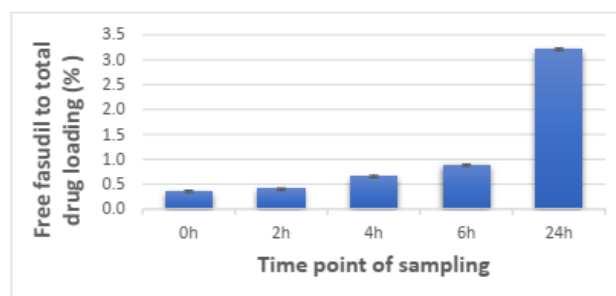


Figure 5.15. Percentage of free fasudil in plasma, during stability studies of the PGA-SS-FAS conjugate

While the percentage of free drug in plasma increased from 0.35 % to 3.21 % over the 24h of the stability study, this finding still suggests the high stability of the PGA-SS-FAS conjugate, as expected due to disulfide linking moiety. Following administration, conjugates will normally accumulate within tumors via the EPR effect within 24 hours; therefore, a 3% loss of total drug loading will not alter the therapeutic performance.

Thus, we conclude that the PGA-SS-FAS conjugate is stable in plasma, thereby providing the impetus for further *in vivo* studies.

5.2.6. *In vivo* Studies of the PGA-SS-FAS Conjugate

We performed *in vivo* studies using an MDA-MB-231-Luc-based TNBC mouse model⁴⁹ with two dosage regimens of either 12 mg/kg and 40 mg/kg of linear PGA-SS-FAS. Injection of the MDA-MB-231-Luc cell line is used to model late-stage breast cancer and is one of the most popular animal models of TNBC. Furthermore, Luc transfection allows the tracking of tumor cells post-inoculation. We induced tumor growth by subdermal inoculation of 3×10^6 early passage MDA-MB-231-Luc cells suspended in 100 μ L of MatrigelTM (10%) in the mammary fat pad of NOD/SCID mice under inhalatory anesthesia (3% sevoflurane in pure oxygen). We started treatment after 2 weeks of cellular injection with periodicity of 2 injections per week two each week during 3 weeks.

42 days after inoculation, we sacrificed animals using CO₂ inhalation, and extracted and weighed tumors. In both cases, we failed to observe a statistically significant difference in tumor volumes in animals treated with the conjugate, free drug and the control (PBS). We also failed to observe any loss in body weight over time in any of the treated animals, suggesting that the conjugate does not elicit any toxic effects (**Fig. 5.16**).

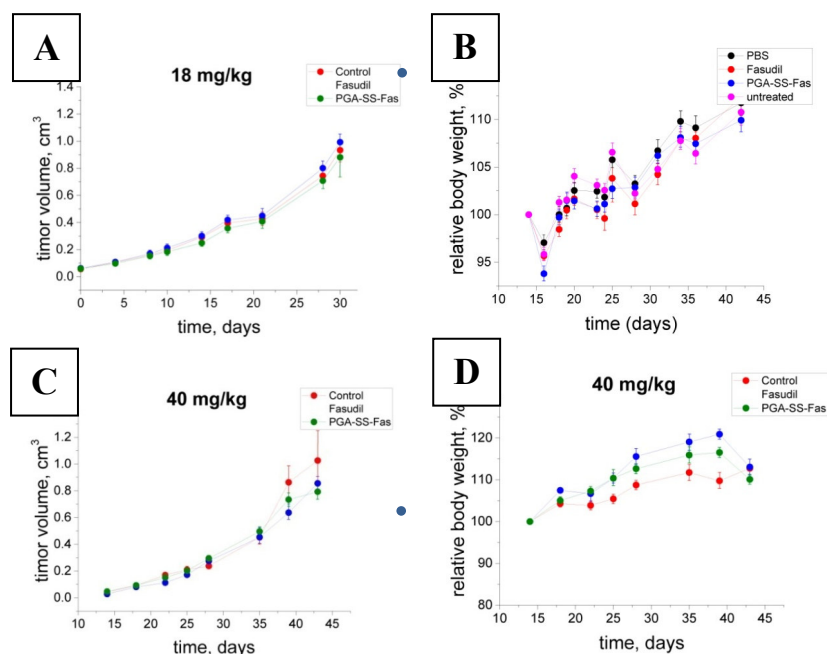


Figure 5.16. Tumor volume and body weight evolution for treatment regimens of 18 mg/kg (A, B) and 40 mg/kg (C, D) PGA-SS-Fas. Data represented as mean \pm SD ($n > 3$).

The MDA-MB-231-Luc model is also a suitable model for the study of antimetastatic effects of nanomedicines as lung and lymph node metastasis develop profoundly in this model.⁴⁹ We employed bioluminescence based imaging to monitor metastasis (**Fig. 5.17**); overall, we found that both PGA-SS-Fas and free Fas fail to significantly inhibit metastasis to the auxiliary lymph nodes or the lungs at any of the concentrations tested.

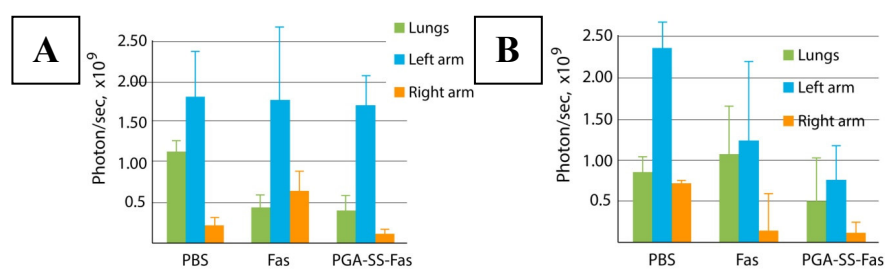


Figure 5.17. Metastasis in lungs and auxiliary lymph nodes following treatments with 18 mg/kg (A) and 40 mg/kg (B) dose regimens. Data represented as mean \pm SD ($n > 3$).

These results were not unexpected, considering that fasudil does not display cytotoxic or cytostatic properties. Migration assay also confirmed that fasudil and corresponding conjugate partially inhibited cell migration but did not restrict it (see sect.

5.2.3). Similar differences in the activity of the fasudil in vitro and in vivo have previously been reported.⁴⁰ In vitro, fasudil stimulates cell detachment and leads to partial actin filament disorganization, effects linked to attenuated RhoA/ROCK activation, and signaling.³⁷

Despite the relatively low efficiency of Fasudil as an anticancer agent alone due to lack of cytotoxic properties, Fasudil can increase the efficiency of cytotoxic or cytostatic drugs as part of combination therapies.^{50,51} Therefore, to achieve the desired therapeutic output, a combination approach was sought, as Fasudil, due to its molecular mechanism of action could nicely sensitize the cancer cells to be attacked by a second drug such as Dinaciclib. Synergistic combinations were identified within MyNano Project, as mentioned above.

5.3. Optimization Of PGA-Dinaciclib Conjugates

5.3.1. Synthesis and Characterization of the Conjugates - Optimization of Polymer-drug Linkers

Dinaciclib is a very potent inhibitor of the cyclin-dependent kinases (CDKs) that regulate of cell cycle and is currently being evaluated in several clinical trials against various cancer, including TNBC.^{52–54}

While dinaciclib possess a readily available primary alcohol that can be employed for direct modification (**Fig.5.18**), the presence of the pyridyl N-oxide group restricts the reaction conditions for dinaciclib modification, especially those involving reductive or alkylating agents. The effect of acids or bases on the stability of N-oxides depends on the type of molecule and may vary over a broad range. As the stability of dinaciclib under acidic and basic conditions has yet to be reported, we made a short study on the stability of dinaciclib in water and chloroform in the presence of acids and bases (pH 3.0 and 11.0) over 24h (**Fig. 5.19**) prior to synthesis.

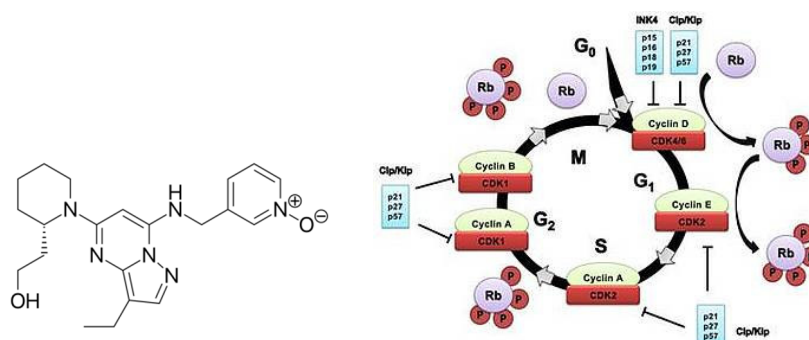


Figure 5.18. A) Chemical structure of dinaciclib. B) Schematic representation of cell cycle progression and involved CDKs (Adapted from ref.⁵⁵)

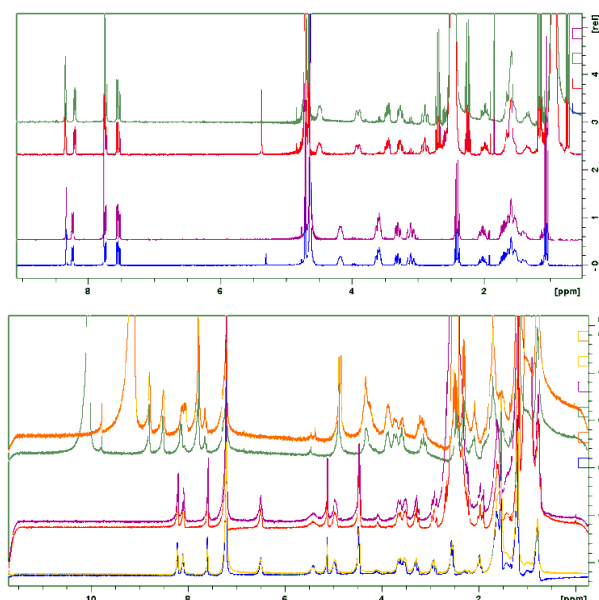


Figure 5.19. Stability studies of dinaciclib in water (upper spectra) and chloroform (lower spectra) at different pH levels.

In water at pH 3.0 and pH 11.0 and in chloroform at pH 11.0, dinaciclib remains stable during 24 h: however, we observed the appearance of new peaks that represent a signature of partial degradation of dinaciclib in chloroform at pH 3.0 after 24 h.

We prepared a small family of PGA-Dinaciclib conjugates employing various linking strategies - ester (PGA-O-Din), biphosphate (PGA-PP-Din), and disulfide self-immolative (PGA-SS-Din) linkers (see **Fig. 5.20**). We prepared the ester-linked conjugate by direct conjugation of dinaciclib to the carboxylic groups of PGAs using a DIC/DMAP coupling strategy.

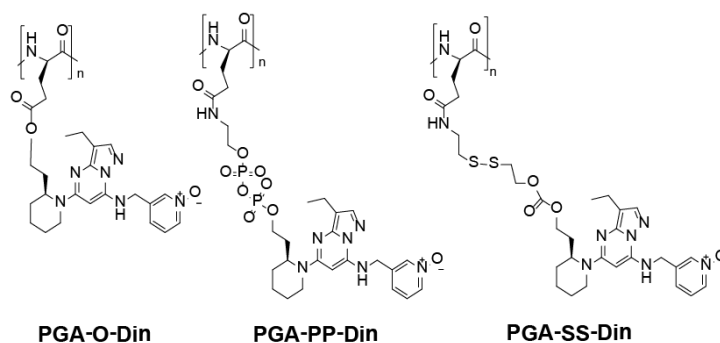


Figure 5.20. Structure of PGA-Din conjugates employing various linking strategies.

We prepared the biphosphate linker in four steps, as shown in **Fig. 5.21**. We prepared N-Fmoc-ethylenediamine monophosphate in two steps from ethanolamine by i) sequential protection of the amine group with Fmoc using standard procedure followed by ii) treatment with diphosphoryl chloride.

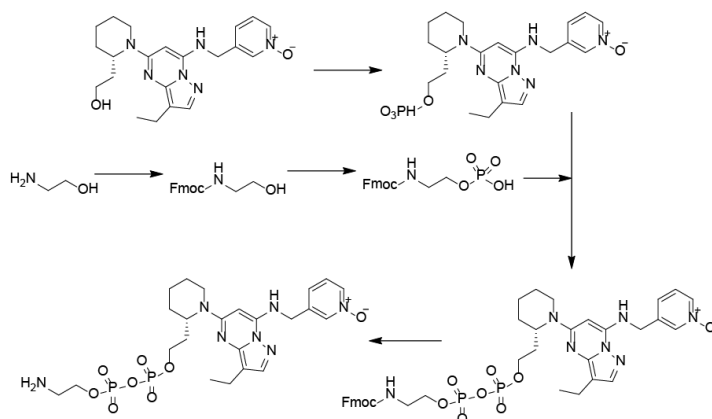


Figure 5.21. Synthetic Scheme of PGA-PP-Din.

We prepared dinaciclib monophosphate by the treatment of dinaciclib with diphosphoryl chloride and purification on normal phase silica in methanol. Next, we performed a coupling reaction between Din- and Fmoc-ethanolamine phosphates with CDI/ZnCl₂ reaction. Finally, we deprotected Fmoc using the standard 20% piperidine/DMF protocol and conjugated the obtained amine to PGA with DMTMM BF₄. We monitored compound and final conjugate synthesis using both ¹H and ³¹P NMR. From the ³¹P NMR analysis, we clearly observed the appearance of a single multiplet at -12 ppm corresponding to biphosphate instead of a singlet at 0 ppm corresponding to the monophosphate (**Fig. 5.22**). These data suggest that biphosphate does not degrade during synthesis or after polymer conjugation/purification.

Finally, we performed DOSY NMR to determine the diffusion coefficient of dinaciclib and polymer chains (**Fig. 5.23**); this analysis demonstrated that all the peaks corresponded to a single diffusion coefficient, thereby providing indirect support for stable conjugation.

We prepared the self-immolative disulfide carbonate linker in a four-step synthetic procedure similar to the one described for fasudil, as shown in **Fig. 5.3**. We used an identical alcohol activated with p-nitrophenyl chloroformate to prepare the carbonate derivative. The reaction did not proceed in the presence of 2 eq. of triethylamine and 1 eq. DIEA/0.1 eq. DMAP; therefore, we used 1 eq. of DMAP and obtained a pure product with high yield.

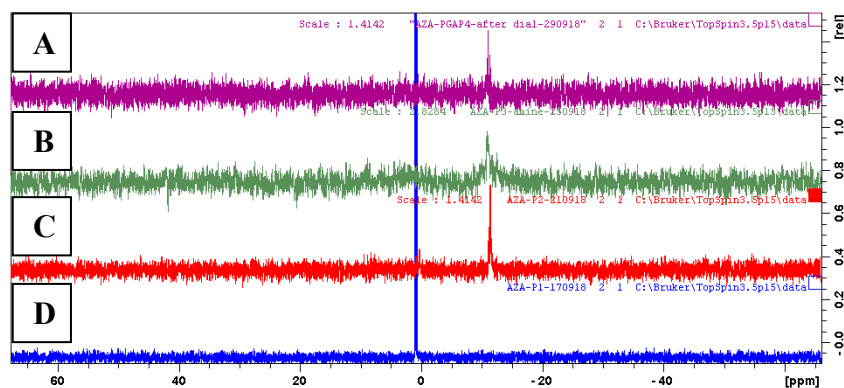


Figure 5.22. ^{31}P NMR spectra of Din-phosphate (A), Din-PP-(Fmoc-ethanolamine) (B), Din-PP-(ethanolamine) (C), and PGA-PP-Din (D).

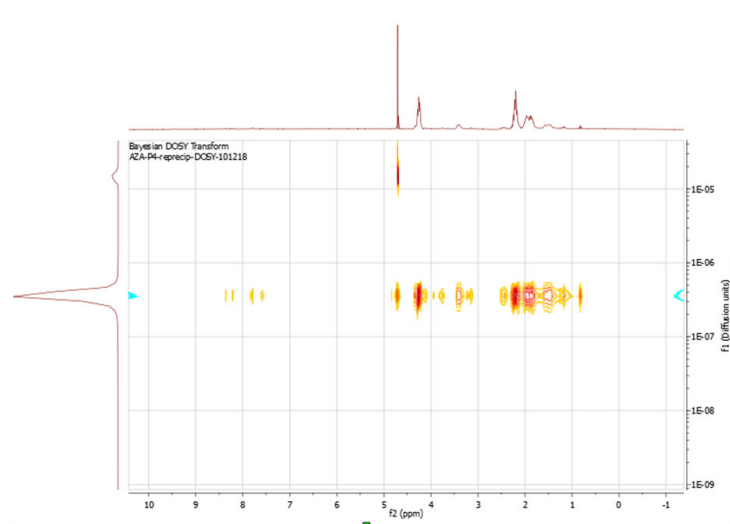


Figure 5.23. DOSY NMR spectra of PGA-PP-Din.

Finally, we performed a second thiol exchange with cysteamine hydrochloride, and then conjugated the compound to PGA through amide coupling with DMTMM. For the purification of the conjugates, we used a combination of size-exclusion chromatography and dialysis with further lyophilization.

We characterized three conjugates with NMR to prove compound identity (**Fig. 5.24**). We monitored conjugation by ^1H NMR, clearly observing a broadening of the peaks in the aromatic region corresponding to dinaciclib protons, which relates to the increased diffusion coefficient of the conjugate. We used UV-Vis to determine TDL, and HPLC to determine free drug content (See **Table 5.6**).

Overall, we obtained conjugates with 3.4-5.2 % modification (w/w) and extremely low content of the free drug (usually below the LOD of HPLC).

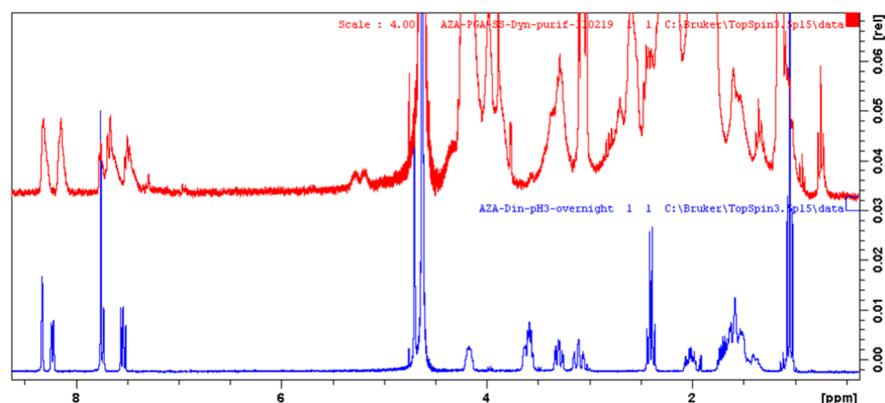


Figure 5.24. ^1H NMR spectra of dinaciclib and PGA-SS-Din.

Table 5.6. Characterization of three PGA-Din conjugates.

| Conjugate | DP ^{a,b} | TDL ^c , % | Free drug ^d , % | Diameter ^e , nm |
|------------|-------------------|----------------------|----------------------------|----------------------------|
| PGA-O-Din | 100 | 4.75 | <1.0 | 4.5 |
| PGA-PP-Din | 100 | 3.71 | <1.0 | 4.2 |
| PGA-SS-Din | 100 | 5.23 | <1.0 | 5.3 |

^aDetermined by GPC. ^bDetermined by NMR. ^cDetermined by UV-Vis. ^dDetermined by HPLC (UV-Vis) and calculated as % of the total drug loading. ^eHydrodynamic radius measured via DLS instrument in 1mM KCl.

5.3.2. Cell Viability studies with PGA-Dinaciclib Conjugates

We studied cell viability of all the conjugates synthesized *in vitro* in two human breast cancer cell lines: MDA-MB-231 (TNBC) and ZR-75-1 (Her2-positive) (**Fig. 5.25**).

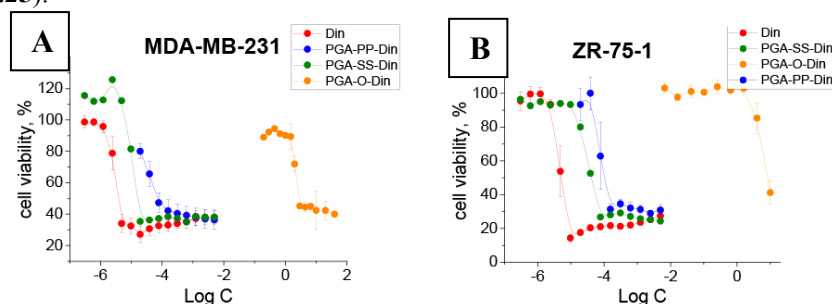


Figure 5.25. Toxicity curves for dinaciclib and corresponding conjugates in MDA-MB-231 (left) and ZR-75-1 (right).

The conjugate bearing an ester linker (PGA-O-Din – orange line) displayed extremely low toxicity in both cell lines compared to free dinaciclib, with an observed decrease of more than four orders of magnitude (**Fig. 5.25**). Taking into account the high activity of the free drug, we hypothesize that the observed activity derives from the slow hydrolysis of the ester linker or, alternatively, from the residual free drug, which may be present at a level below 0.1% (to total drug loading), which cannot be detected by HPLC.

Lysosomal enzymes can cleave biphosphate linkers, and we observed a decrease in toxicity for PGA-PP-Din by approximately 1-2 orders of magnitude when compared to the free drug in both cell lines, most probably because of different cell uptake.⁵⁶

The activity of the conjugate bearing a self-immolative disulfide linker (PGA-SS-Din) displayed the highest toxicity among conjugates, though remaining lower than that of free dinaciclib. We discovered similar IC₅₀ values for free dinaciclib and PGA-SS-Din in both cell lines, which probably relate to the similar levels of GSH and biphosphate-cleaving enzyme. The slightly lower IC₅₀ value of free dinaciclib in MDA-MB-231 may derive from the higher expression of CDKs in every stage of the cell cycle.

5.3.3. Drug Release Kinetics Of Selected Pga-Dinaciclib Conjugates

We next studied the release kinetics of dinaciclib from PGA-SS-Din with HPLC. One pressing problem with dinaciclib detection in this manner is the presence of the N-oxide group, which inhibits retention on reverse-phase columns. Previously published studies described the implementation of LC-MS in the determination of dinaciclib, and so, we used information from these studies as our starting point.⁵⁷

The release kinetics profile of dinaciclib from PGA-SS-Din in the presence of 5 mM DTT (promotes SS cleavage) (**Fig. 5.26**) strongly resembles the fasudil release kinetics profile obtained for PGA-SS-Fas (**Fig. 5.7**). The first part of the curve displays linearity (usual for zero-order kinetics), with 70% of the drug released during the first 8 h, which is close to the value obtained for fasudil analog (82%). We failed to observe any drug release in response to treatment with 10 μ M DTT (conditions mimicking extracellular levels).

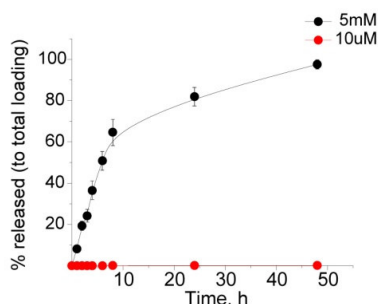


Figure 5.26. Release kinetics profile for PGA-SS-Din in 5 mM and 10 μ M DTT, respectively. Data represented as mean \pm SD (n=3).

Overall, the activity of the dinaciclib is limited exclusively by the speed of drug release, assuming that internationalization speed does not strongly depend on the type of linker employed. At the time of writing, we are also exploring drug release kinetics under hydrolytic conditions and in the presence of cathepsin B.

5.4. Optimization Of A Polymer-Based Combination Conjugate

We next sought to understand the potential for a combination treatment employing conjugated fasudil and dinaciclib. Given the encouraging results obtained, we chose to employ self-immolative disulfide linkers and tested a combination of single PGA-drug conjugates in the ZR75 and MDA-MB-231 breast cancer cell lines to evaluate synergy. In a second stage, we would develop a combination conjugate with both drugs conjugated at an optimal ratio to the same PGA carrier as a means to ensure that both drugs can act in the same cell at the same ratio and within the same time period.

In the ZR-75 cell line, PGA-SS-Fas appears to decrease the toxicity of PGA-SS-Din (**Fig. 5.27**). We also observed lower IC₅₀ values for PGA-SS-Fas than for free Fas, which suggests low intracellular levels of GSH. The IC₅₀ value for the combination of single PGA-drug conjugates was close to that obtained for free fasudil, which is related exclusively to the activity of dinaciclib activity. Furthermore, the IC₅₀ value for the combination of free drugs was the lowest of all compounds tested.

These results suggest that fasudil and dinaciclib do not synergize, independent of their conjugation status, in the ZR-75-1 model.

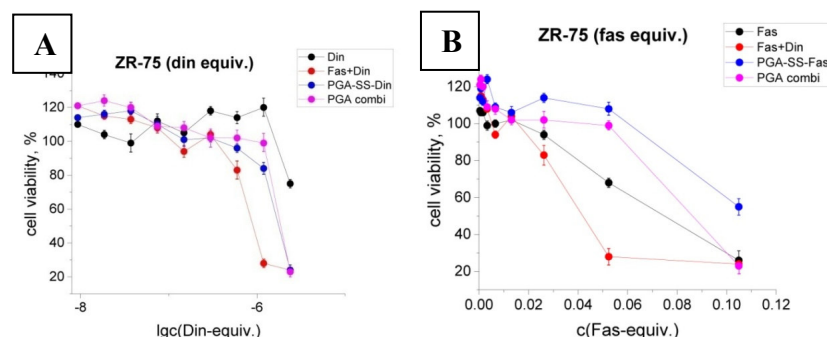


Figure 5.27. Toxicity curves for free drugs, corresponding conjugates, and their combination recalculated per drug equivalents of fasudil (A) and dinaciclib (B) in the ZR-75-1 model. Data represented as mean \pm SD ($n=3$).

For MDA-MB-231, we observed a comparable activity of a physical mixture of the single PGA-drug conjugates with PGA-SS-Din alone (**Fig. 5.28**); however, both PGA-SS-Din alone or the combination of PGA-SS-Din/PGA-SS-Fas displayed higher activity than the corresponding free drug and combination of free drugs. Unfortunately, the differences between the activity of single conjugates and in combination did not reach statistical significance, and we cannot claim synergism.

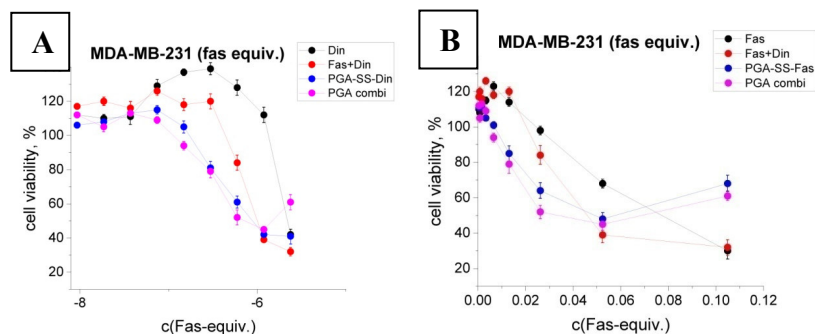


Figure 5.28. Toxicity curves for free drugs, corresponding conjugates, and their combination recalculated per drug equivalents of fasudil (A) and dinaciclib (B) in the MDA-MB-231 model. Data represented as mean \pm SD (n=3).

These results suggest that the concentration of fasudil employed is insufficient to foster synergism with dinaciclib. To explore this supposition, at the time of writing, we are evaluating a combination of PGA-SS-Din and elevated levels of free fasudil to evaluate drug synergism at higher fasudil concentrations as well as undertaking *in vivo* studies with dinaciclib conjugates.

5.5. Conclusion

We have prepared and studied two families of conjugates; a conjugate of the ROCK-inhibitor fasudil and a conjugate of the CDK-inhibitor dinaciclib. In each family, we evaluated three different linkers (ester, self-immolative disulfide, and either amide or biphosphate) for Fas and Din, and comparative analyses determined that conjugates with self-immolative linkers displayed optimal activity that correlated to intracellular levels of GSH and general sensitivity of the cells to the drug.

We observed robust activity of fasudil conjugates *in vitro*; however, it is rather inefficient *in vivo* and does not affect tumor growth or metastasis development, similar to the free drug. These results were expected, considering that fasudil does not possess cytotoxic or cytostatic activities and, as suggested by many authors, is more useful as an auxiliary agent in combination with more potent drugs.⁴⁰

Dinaciclib and the corresponding conjugates with disulfide and diphosphate linkers demonstrated very high activity *in vitro* in two cell line models (ZR-75 and MDA-MB-231), although conjugates displayed less activity than the free drug.

Finally, we studied the combination of the two drugs as a physical mixture of the polymers in two cell models (ZR-75 and MDA-MB-231), which provided evidence that the concentration of fasudil did not suffice to foster synergism.

5.6. Supplementary information

SI-5.1. Experimental methods

SI-5.2. Synthesis Of Compounds

SI-5.1. Experimental Methods

Ultraviolet-Visible Spectroscopy

UV-VIS measurements were performed using a JASCO V-630 spectrophotometer at 25 °C with 1.0 cm matched quartz cells and a spectral bandwidth of 0.5 nm.

Determination of total drug content by UV Spectroscopy. Fasudil or dinaciclib were used as calibration standards. To obtain a calibration curve, samples were diluted using MilliQ water to give a concentration range of 1.5-20 µg/mL. The total drug loading of the conjugates (0.5 mg/ml) was determined by measuring the absorbance at 323 nm in Milli-Q H₂O (for fasudil) or at 259 nm (for dinaciclib). PGA in the same concentration range as the conjugates was analyzed (0-5 mg/mL) and used as blank.

HPLC

HPLC analysis employed a Waters instrument equipped with an autosampler (Waters 717), two binary pumps, and a PDA detector (Waters 2996).

Determination of free drug content - fasudil. Detection was carried out at $\lambda = 323$ nm (peak characteristic of the drug, mobile phase: H₂O (1% NH₃)/MeOH (40/60), at a retention time of 6 minutes). The column used was a reversed-phase C18 InertSustain that lacked the silanol groups that might interfere and retain products. The calibration curve was built using commercial Fasudil, showing a linear response within the concentration range employed (1.5-20 µg/mL). Solid-liquid extraction was used to determine the free fasudil content in the PGA-drug conjugates. 2mg of the conjugates was suspended in MeOH (HPLC grade) and sonicated for 30 minutes. Then, the suspension was filtered (0.22µm) into HPLC vials for analysis. Two reference standards were employed in every experiment.

Determination of free drug content - dinaciclib. Detection was carried out at $\lambda = 259$ nm (peak characteristic of the drug, mobile phase: H₂O (0.1% HAc)/MeOH (25/75), at a retention time of 8.8 minutes). The column used was a reversed-phase ZORBAX C18, 150 x 4.6 mm, 3.5 µm modified with octadecylsilyl groups. The calibration curve was built using commercial dinaciclib showing a linear response within the concentration range employed (0.00156 – 0.1 mg/ml). Solid-liquid extraction was used to determine the free dinaciclib content in the PGA-drug conjugates. 2 mg of the conjugates were suspended in MeOH (HPLC grade) and sonicated for 30 minutes. Then, the suspension was filtered (0.22µm) into HPLC vials for analysis. Two reference standards were employed in every experiment.

Fasudil Release Kinetics:

Test solution 1: Solution containing 2 mg/ml of PGA-SS-Fas (equivalent of 0.236 mg/ml of fasudil) in PBS containing 5 mM of DTT. The solution was kept at 37 °C. Samples were analyzed at a fixed time point (1,2,3,4,6,8,24, and 48 h).

Test solution 2: Solution containing 2 mg/ml of PGA-SS-Fas (equivalent of 0.236 mg/ml of fasudil) in PBS containing 10 µM of DTT. The solution was kept at 37 °C. Samples were analyzed at a fixed time point (1,2,3,4,6,8,24, and 48 h).

Conditions: *Column*: InertSustain C18, 5 μ m, 4.6x250 mm modified with octadecylsilyl groups; *Mobile phase*: Methanol: acetate buffer 45:55; *Acetate buffer*: Aqueous solution containing 0.2 % acetic acid and 0.2 % ammonium acetate; *Wavelength*: 323 nm; *Flow*: 1 ml/min; *Injection volume*: 20 μ l; *Detector*: DAD.

For quantification of release kinetics calibration curve within the concentration range, 1.5-20 μ g/mL was used.

Dinaciclib Release Kinetics:

Test solution 1: Solution containing 2 mg/ml of PGA-SS-Din in PBS containing 5 mM of DTT. The solution was kept at 37 °C. Samples were analyzed at a fixed time point (1, 2, 3, 4, 6, 8, 24, and 48 h).

Test solution 2: Solution containing 2 mg/ml of PGA-SS-Din in PBS containing 10 μ M of DTT. The solution was kept at 37 °C. Samples were analyzed at a fixed time point (1, 2, 3, 4, 6, 8, 24, and 48 h).

Conditions: *Column*: ZORBAX C18, 150 x 4.6 mm, 3.5 μ m modified with octadecylsilyl groups; *Mobile phase*: Methanol: 0.1% HAc in water 75:25; *Wavelength*: 259 nm; *Flow*: 0.6 ml/min; *Injection volume*: 10 μ l; *Detector*: DAD.

For quantification of release kinetics calibration curve within the concentration range, 0.00156 – 0.1 mg/ml was used.

NMR Spectroscopy

NMR spectra were recorded at 27 °C (300 K) on an Avance III 500 MHz Bruker spectrometer equipped with a 5 mm TBI broadband probe or a 300 Ultrashield™ from Bruker (Billerica MA, USA). Data were processed with the software TopSpin. Samples were prepared typically at 1-5 mg/ml in deuterated solvents.

LC-MS

LC-MS analysis was performed using Exion LC system comprising an AC Pump, AC Autosampler, and AC Column oven. The initial mobile phase composition was ACN: 0.1% formic acid (60:40, v/v). All runs were performed using Phenomenex Luna®-C18 column (30 mm length, 4.6 mm internal diameter, 5 μ m particle size), which was maintained at 40 °C. The injection volume was 20 μ l, while the initial flow rate of the mobile phase was set at 400 ml/min. In the method development using an experimental design approach, five factors were selected as factors for potential significant effect on ionization efficiency: ion spray voltage (3000-5500 V), temperature of ion source (300-750 °C), curtain gas pressure (20-40 psi), nebulizer (Gas 1) gas pressure (20-60 psi), and auxiliary (Gas 2) gas pressure (40-80 psi). Design of experimental plans and data analysis in experimental design approach was performed with Design-Expert® 11.0.0 software (Stat-Ease Inc., USA) while data acquisition with Analyst® software (AB Sciex, Singapore).

Cell Culture

All cell lines used in this thesis are epithelial ductal breast carcinomas. The 4T1 cell line is TNBC line derived from the mouse mammary gland, while the MDA-MB-231 cell line is a human TNBC line. MDA-MB-213 is highly aggressive and metastasizes quickly. It is used as an animal model for stage IV human breast cancer.⁴⁹ The ZR-75-1 cell line is derived from a human malignant ascetic effusion, is triple positive for the ER, PR, and HER2, and xenografts forming after orthotopic implantation spontaneously metastasizes to lymph nodes. The human MDA-MB-453 cell line is ER-, PR- and Her2+ cell line⁵⁸.

In vitro Cytotoxicity Analysis

Cell lines were maintained in RPMI supplemented with 10% heat-inactivated FBS at 37 °C in a controlled atmosphere (air-CO₂ 95/5). Media was replaced every 48-72 h and underwent passaging when 80% cell confluence was reached. For cytotoxic assays, cells were seeded in a sterile 96-well microtiter plates at concentration ~6,250 cells/cm². Plates were incubated for 24 h and then solution of free drugs and conjugates were evaluated in determined concentration ranges. After 72h of treatment, cell viability was determined using Cell Titer 96 Aqueous non-radioactive cell proliferation assay according to manufacturer's guidelines. Optical density of wells was measured at 490 nm in a Wallac 1420 spectrophotometer. Cell viability was expressed as a percentage of the viability of untreated cells established as control.

Mouse strains

Eight-week-old female immunodeficient nonobese diabetic NOD/SCID (NOD.CB17-Prkdcscid/NCrHsd) mice used herein were purchased from Envigo Laboratories Inc. (Spain, EU). Four to eight animals have been used for each experimental time point.

SI-5.2. Synthesis Of Compounds

Synthesis of Poly-L-glutamate-Fasudil (PGA-FAS)

PGA100-OH (51 mg, 0.395 mmol) in 5 mL NaHCO₃(aq.) at pH 7 was added to an oven-dried two-necked flask at room temperature (RT) equipped with a stir bar. DMTMMCl (21.8 mg, 0.079 mmol, 0.2 eq. to glutamic acid units) was then added and the solution was allowed to stir for ten minutes. Then, fasudil (39.8mg, 0.0405 mmol, 0.1 eq. to glutamic acid units) was added and pH adjusted to 7-8 with NaHCO₃. Thin-layer chromatography (MeOH) confirmed the consumption of Fasudil. The solvent was then removed under vacuum and the reaction mixture was transferred into a dialysis membrane (Mw cut-off=3000 Da) and dialyzed against MilliQ water for 48h. The water was replaced every 8h. Finally, the resulting aqueous suspension was freeze-dried, and the white powder characterized. (Yield=87%).

¹H NMR (300 MHz, D₂O): δ 4.26 (s, 2H), 3.50 (d, *J* = 6.6 Hz, 1H), 2.65 (s, 1H), 2.23 (s, 4H), 1.92 (d, *J* = 27.8 Hz, 5H).

Synthesis of ethynyl (4-nitrophenyl) carbonate

Et₃N (0.8 ml, 5.8mmol) and 2-propyn-2-ol (134μl, 2.3mmol) at 0 °C under nitrogen was added to a solution of p-nitrophenyl chloroformate (502 mg, 2.49mmol) in THF. The mixture was stirred for 1 h, the solvent then removed under vacuum, and flash chromatography performed using 50% petroleum ether and ethyl acetate. The product was a yellow oil (298.3 mg, 1.35 mmol, 60% yield) and homogeneous (one spot) by TLC - R_f = 0.47 (EtOAc:Petroleum Ether 1:1).

¹H NMR (300 MHz, CDCl₃): δ 8.40 – 8.22 (m, 2H), 7.49 – 7.37 (m, 2H), 4.90 (d, *J* = 2.4 Hz, 1H), 2.64 (t, *J* = 2.4 Hz, 1H).

Synthesis of prop-2-yn-1-yl 4-(isoquinolin-5-ylsulfonyl)-1,4-diazepane-1-carboxylate

Et₃N (339 μl, 2.45 mmol) and fasudil (405.2 mg, 1.24 mmol) at room temperature was added to a solution of ethynyl (4-nitrophenyl) carbonate (298.3 mg, 1.35 mmol) in CH₂Cl₂ (10 ml). The residue was subjected to column chromatography on silica gel (ethyl acetate) to give a yellow viscous oil (338.6 mg, 73.5%).

¹H NMR (300 MHz, CDCl₃): δ 9.35 (s, 1H), 8.69 (d, J = 6.1 Hz, 1H), 8.38 (t, J = 6.1 Hz, 1H), 8.21 (d, J = 8.2 Hz, 1H), 7.68 (d, J = 8.0 Hz, 1H), 7.61 (s, 2H), 3.98 – 3.88 (m, 1H), 3.78 – 3.52 (m, 18H), 3.49 – 3.32 (m, 4H), 2.95 (s, 1H), 2.01 – 1.91 (m, 2H).

¹³C NMR (75 MHz, CDCl₃): δ 153.49 (d, J = 31.8 Hz), 145.18 (s), 133.48 (dd, J = 68.6, 29.6 Hz), 131.54 (s), 129.21 (s), 125.86 (s), 117.39 (s), 58.44 (s), 53.07 (s), 49.32 (dd, J = 57.7, 16.4 Hz), 45.99 (d, J = 25.7 Hz), 29.24 – 27.12 (m). MS

Synthesis of Azide-modified Poly-L-glutamate

DMTMMBF₄ (38.13 mg, 0.1162 mmol) at room temperature under nitrogen was added to a solution of PGA-OH (250 units) (50.9 mg, 0.394 mmol) in DMF (4 ml). The mixture was stirred for 10 minutes, then H₃N-(PEG)₂-N₃Tos (26.846 mg, 0.0775 mmol) was added. The mixture was stirred for 9 h, then the residue was concentrated under reduced pressure and precipitated over CHCl₃:Acetone (4:1) at 10°C. The solvent was then removed by centrifugation/decantation and the resulting polymer was dissolved in 5 mL NaHCO₃ 0.5 M to obtain the water-soluble salt form. It was then dialyzed (Mw cut-off=3000 Da) against MilliQ water for 24h. After lyophilization, compound was obtained as a white powder. Yield = 78%. Characterization shown in **Figure 5.4**.

Synthesis of Poly-L-glutamate Fasudil Conjugate through Carbamate Linker (PGA-O-FAS)

PGA-O-FAS was obtained via copper-catalyzed click-chemistry involving the alkine-fasudil derivative and the azide functionalized polyglutamate. In a two-neck round bottom flask fitted with a stirrer bar and a stopper, 0.53 mmol of azide-modified Poly-L-glutamate (sodium salt) was dissolved in MilliQ water. After that, the corresponding amount for the desired % of substitution of the prop-2-yn-1-yl 4-(isoquinolin-5-ylsulfonyl)-1,4-diazepane-1-carboxylate was added in dry DMF solution (0.08 mmol). Then, five eq. of sodium ascorbate in MilliQ water solution was added (Mw ¼ 198.11 g/mol) and the mixture was degassed by performing two freeze-pump-thaw cycles. One equivalent of CuSO₄ (Mw = 249.68 g/mol) was weighed under N₂ flow and added in MilliQ H₂O solution to the reaction mixture. The final complete mixture, containing a DMF–H₂O proportion of 4: 1, was degassed by performing another freeze-pump-thaw cycle and allowed to react at 40 °C in an oil bath protected from light for 48h. The reaction mixture was then precipitated by acidifying to -4 with 1 M HCl. The solid was freeze-dried and further converted into the salt form by the addition of 2 mL of 0.5 M NaHCO₃. Purification was achieved by size exclusion chromatography employing PD-10 columns. Yield = 65%. ¹H NMR Characterization shown in **Figure 6.4**.

Synthesis of 2-(pyridin-2-yl)disulfanyl ethanol (IC01)

2,2'-aldrithiol (3 g, 13.635 mmol) in 10 mL methanol purged with nitrogen was added to an oven-dried three-necked flask under nitrogen at room temperature equipped with a stir bar. 2-mercaptoethanol dropwise (318 µL, 4.545 mmol) was then added to this mixture and the solution was allowed to stir for two hours. The reaction was monitored by TLC - R_f=0.479 (95:5% DCM:EtOAc). The solution was concentrated under reduced pressure, and the residue was subjected to column chromatography on silica gel (DCM/ethyl acetate = 95/5) to give **IC01** as a slightly yellow liquid (600 mg, 72%).

¹H NMR (300 MHz, CDCl₃): δ 8.57 – 8.44 (m, 1H), 7.61 (ddd, J = 9.2, 6.0, 1.9 Hz, 1H), 7.41 (d, J = 8.1 Hz, 1H), 7.20 – 7.10 (m, 1H), 5.69 (t, J = 6.6 Hz, 1H), 3.82 (dd, J = 10.4, 5.8 Hz, 2H), 3.01 – 2.81 (m, 2H), 1.66 (s, 1H), 1.26 (s, 1H).

Synthesis of 4-nitrophenyl (2-(pyridin-2-yl)disulfanyl)ethyl Carbonate (IC02)

IC01 (600 mg, 3.2 mmol), p-nitrophenyl chloroform (711.3 mg, 3.528 mmol), and triethylamine (1060 μ L, 7.687 mmol) in anhydrous THF (30 mL) at 0°C was added to an oven-dried flask equipped with a stir bar under nitrogen, which provided a for the formation of a yellow precipitate. This was allowed to stir for one hour, then the solvent was evaporated under vacuum to generate a yellowish viscous liquid. thin-layer chromatography was performed using with 20% ethyl acetate and 80% methylene chloride.

The reaction was then quenched by the addition of 40 ml of 0.5M aqueous ammonium chloride solution. After extraction with ethyl acetate (3x60 ml), the combined organic layer was dried over anhydrous sodium sulfate and filtered. The filtrate was concentrated under vacuum, and the residue was subjected to column chromatography on silica gel (methanol/chloroform = 3/100) to give **IC02** as a colorless liquid (600 mg).

¹H NMR (300 MHz, CDCl₃): δ 8.56 – 8.48 (m, 1H), 8.35 – 8.25 (m, 2H), 7.74 – 7.61 (m, 2H), 7.44 – 7.34 (m, 2H), 7.19 – 7.10 (m, 1H), 4.59 (t, J = 6.4 Hz, 2H), 3.18 (t, J = 6.4 Hz, 2H).

Synthesis of the 2-(pyridin-2-yl)disulfanyl)ethyl 4-(isoquinolin-5-ylsulfonyl)-1,4-diazepane-1-carboxylate (IC03)

Et₃N (430 μ L, 3.10 mmol) and Fasudil-HCl (508 mg, 1.55 mmol) at room temperature was added to a solution of 4-nitrophenyl (2-(pyridin-2-yl)disulfanyl)ethyl carbonate (600 mg, 1.703 mmol) in CH₂Cl₂ (75 mL). The residue was subjected to column chromatography on silica gel (ethyl acetate (EtOAc)→EtOAc:Methanol 95:5) to give a yellow viscous oil (702 mg, 90%).

¹H NMR (300 MHz, CDCl₃): δ 9.37 (s, 1H), 8.72 (d, J = 6.2 Hz, 1H), 8.46 (t, J = 6.6 Hz, 2H), 8.26 – 8.10 (m, 3H), 7.84 – 7.54 (m, 3H), 7.18 – 7.08 (m, 1H), 6.96 – 6.85 (m, 2H), 5.32 (s, 1H), 4.35 (t, J = 6.2 Hz, 2H), 3.75 – 3.33 (m, 10H), 3.05 (t, J = 6.1 Hz, 2H), 2.02 (t, J = 11.7 Hz, 2H), 1.60 (s, 1H), 1.27 (s, 1H).

Synthesis of the 2-((2-aminoethyl)disulfanyl)ethyl 4-(isoquinolin-5-ylsulfonyl)-1,4-diazepane-1-carboxylate hydrochloric salt (IC04)

Cysteamine hydrochloride (46 mg, 0.4 mmol) was added to a solution of 2-(pyridin-2-yl)disulfanyl)ethyl 4-(isoquinolin-5-ylsulfonyl)-1,4-diazepane-1-carboxylate (200 mg, 0.4 mmol) in methanol (4 mL). The mixture allowed to stir for two hours at room temperature. The solvent was evaporated under vacuum and the residue was reprecipitated four times from methanol to diethyl ether (150 mg).

¹H NMR (300 MHz, DMSO-d₆): δ 9.49 (s, 1H), 8.69 (d, J = 6.2 Hz, 1H), 8.47 (dd, J = 7.6 Hz, 3.5 Hz, 1H), 8.32 (dd, J = 7.6 Hz, 3.5 Hz, 1H), 8.30 (d, J = 6.2 Hz, 1H), 8.26 (br.s, 3H), 7.84 (q, 1H), 4.18 (dt, 2H), 3.48 (br. s, 4H), 2.92-3.11 (m, 7H), 3.75 – 3.33 (m, 10H), 1.73 (m, 2H).

Synthesis of Poly-L-glutamate Fasudil conjugate through self-immolative disulfide linker (PGA-SS-FAS)

DMTMM BF₄ (107 mg, 0.1705 mmol) was added to a solution of polyglutamic acid (200 mg, 1.55 mmol) in DMF (20 mL). After 10 minutes, 2-((2-aminoethyl)disulfanyl)ethyl 4-(isoquinolin-5-ylsulfonyl)-1,4-diazepane-1-carboxylate hydrochloric salt (80 mg, 0.155 mmol) was added, and the pH of the solution adjusted to 8.0 with triethylamine. The solution was allowed to stir for 48 h at RT. The mixture was concentrated (around 50% of the volume), precipitated in diethyl ether, and then reprecipitated from DMF to ether. The precipitate was freeze-dried.

After freeze-drying, the conjugate was dissolved in 0.5 M aqueous sodium hydrocarbonate solution and dialyzed against water (membrane cut off 500-1000 Da) for two days and then the solution was freeze-dried. The conjugate was dissolved in water and purified with VivaSpin four times to remove residual low molecular weight impurities (235 mg, 84%). ^1H NMR Characterization is shown in **Figure 6.4**.

Synthesis of Poly-L-glutamate-dinaciclib (PGA-DIN) Conjugate through Direct Ester Coupling

Synthesis aimed for the conjugation of 5 % dinaciclib (molar relative to glutamate residues). PGA100-OH (100 mg, 0.775 mmol) in 10 mL of DMF was added to an oven-dried two-necked flask at room temperature equipped with a stir bar. Dinaciclib (0.085 mmol, 33.8 mg) and DMAP (0.0085 mmol, 1 mg) were added, and the mixture was cooled down to 0 °C. DIC (0.085 mmol, 10.7 mg) was added, and the mixture allowed to react for 24h. The mixture was precipitated into cold ether, filtered, dried, and suspended in water. NaHCO_3 was added and pH adjusted to 7-8. The mixture was transferred into a dialysis membrane (Mw cut-off=3000 Da) and dialyzed against MilliQ water for 48h and lyophilized.

Synthesis of the Fmoc-ethanolamine-Phosphate

Diphosphoryl chloride (0.15 mL, 1.1 mmol) was added to a stirred solution of Fmoc-ethanolamine (125mg, 0.44 mmol) in THF (0.9 mL) at -40 °C and the mixture was stirred for a further 40 min. The reaction was quenched with water, pH adjusted to 7 with NaHCO_3 , acidified with 1M HCl, and extracted with DCM. After 48 h, the solution was filtered off.

^1H NMR (300 MHz, CDCl_3): δ 7.90 (d, 2H), 7.68 (d, 2H), 7.30-7.44 (m, 5H), 4.29-4.20 (m, 3H), 3.75 (q, 2H), 3.20 (q, 2H).

Synthesis of Din-Phosphate

The synthesis was performed similarly to Fmoc-ethanolamine-Phosphate and the product was column purified (DCM:MeOH 90:10).

^1H NMR (300 MHz, MeOD): δ 8.51 (s, 1H), 8.20 (d, 1H), 7.79 (d, 1H), 7.62 (s, 1H), 7.51 (m, 1H), 5.53 (s, 1H), 4.56 (m, 1H), 4.34 (m, 1H), 3.83 (m, 1H), 2.83 (m, 1H), 2.56 (q, 2H), 1.91 (m, 2H), 1.8-1.36 (m, 8H), 1.20 (t, 3H).

^{31}P NMR (300 MHz, MeOD): δ 1.12 (s).

Synthesis of the Din-PP-(Fmoc-ethanolamine)

Triethylamine (0.05 mL, 0.36 mmol) and CDI (0.15 g, 0.9 mmol) was added to a stirred solution of Fmoc-ethanolamine-phosphate (0.10 g, 0.36 mmol) in DMF (2 mL). The resulting solution was stirred at RT for 30 minutes. Then, Din-phosphate (0.72 mmol) and ZnCl_2 (0.4 g, 2.75 mmol) were added and the mixture was allowed to stir at RT overnight. The reaction was diluted with 1 N HCl and extracted several times with ethyl acetate. The combined organic layers were concentrated and the compound was used for the next step without further purification.

^1H NMR (300 MHz, $\text{DMSO}-d_6$): δ 8.42 (s, 1H), 8.18 (d, 1H), 7.96 (d, 1H), 7.87 (d, 2H), 7.68 (m, 3H), 7.56-7.26 (m, 5H), 5.48 (s, 1H), 4.60 (m, 3H), 4.21 (m, 3H), 3.89-3.60 (m, 5H), 1.80-1.41 (m, 10H), 1.17 (t, 3H). ^{31}P NMR (300 MHz, MeOD) δ -11.4 (m)

Synthesis of the Din-PP-(ethanolamine)

The compound was deprotected by treatment with 20% piperidine in DMF (1 mL per 100 mg of the product) for 30 min. The product was then dried and washed with ether.

¹H NMR (300 MHz, DMSO-d₆): δ 8.32 (s, 1H), 8.09 (d, 1H), 7.95 (d, 1H), 7.67 (s, 1H), 7.50 (m, 1H), 7.41 (m, 1H), 5.52 (s, 1H), 4.56 (m, 2H), 3.84 (m, 2H), 3.92-3.59 (m, 5H), 1.79-1.40 (m, 10H), 1.16 (t, 3H). ³¹P NMR (300 MHz, DMSO-d₆) δ -11.2 (m)

Synthesis of the Poly-L-glutamate-dinaciclib (PGA-SS-DIN) Conjugate through biphosphate linker

To a solution of polyglutamic acid (120 mg, 0.93 mmol) in DMF (20 ml) was added DMTMM BF₄ (31 mg, 0.0931 mmol). After 10 minutes, Din-PP-(ethanolamine) (0.0621 mmol) was added, and pH of the solution was adjusted to 8.0 with triethylamine. The solution allowed to stir for 48 h at room temperature. The mixture was concentrated (around 50% of the volume), precipitated in diethyl ether, and reprecipitated from DMF to ether. The precipitate was freeze-dried.

After freeze-drying, the conjugate was dissolved in 0.5 M aqueous sodium hydrocarbonate solution and dialyzed against water (membrane cut off 500-1000 Da) for two days. The solution was freeze-dried. The conjugate was dissolved in water and purified with the Sephadex column to removed residual low molecular weight impurities.

Synthesis of the Din-SS-Pyr

DMAP (34.7 mg, 0.284 mmol) and dinaciclib (113 mg, 0.284 mmol) were added to a solution of 4-nitrophenyl (2-(pyridin-2-yl)disulfanyl)ethyl carbonate (100 mg, 0.284 mmol) in CH₂Cl₂ (15 ml) at RT. The residue was subjected to column chromatography on silica gel (DCM-MaOH 95:5) to give a yellow viscous oil (702 mg, 90%).

¹H NMR (300 MHz, CDCl₃): δ 8.41 (d, 1H), 8.30 (s, 1H), 8.09 (d, 1H), 7.67 (s, 1H), 8.37.6-7.55 (m, 2H), 7.46 (d, 1H), 7.25 (dd, 1H), 7.06 (m, 1H), 5.36 (s, 1H), 4.67-3.97 (m, 8H), 3.00 (t, 2H), 2.68 (m, 2H), 2.05(m, 1H), 1.91 (m, 1H), 1.81-1.44 (m, 7H), 1.21 (t, 3H).

Synthesis of the Din-SS-EDA-NH₃Cl

Cysteamine hydrochloride (0.1 mmol) was added to a solution of Din-SS-Pyr (0.1 mmol) in methanol (2 ml) and the mixture allowed to stir for two hours at RT. The solvent was evaporated under vacuum and the residue was reprecipitated four times from methanol to diethyl ether (150 mg).

¹H NMR (300 MHz, DMSO-d₆): δ 8.28 (s, 1H), 8.10 (m, 1H), 8.13-7.86 (m, 7H), 7.69 (s, 1H), 7.36 (d, 1H), 5.53 (s, 1H), 4.72 (m, 1H), 4.53 (d, 2H), 4.30-4.18 (m, 3H), 4.08-3.98 (m, 3H), 3.10 (m, 4H), 3.01-2.85 (m, 7H), 2.65 (dd, 1H), 2.06-1.8 (m, 4H), 1.59 (m, 4H), 1.18 (t, 3H).

Synthesis of Poly-L-glutamate Dinaciclib conjugate through self-immolative disulfide linker (PGA-SS-Din)

DMTMM BF₄ (31 mg, 0.0931 mmol) was added to a solution of PGA (120 mg, 0.93 mmol) in DMF (20 ml). After 10 minutes, Din-SS-EDA-NH₃Cl (38 mg, 0.0621 mmol) was added, and the pH of the solution was adjusted to 8.0 with triethylamine. The solution allowed to stir for 48 h at RT. The mixture was concentrated (around 50% of the volume), precipitated in diethyl ether, and reprecipitated from DMF to ether. The precipitate was then freeze-dried.

After freeze-drying, the conjugate was dissolved in 0.5 M aqueous sodium hydrocarbonate solution and dialyzed against water (membrane cut off 500-1000 Da) for two days. The solution was freeze-dried. The conjugate was dissolved in water and purified with VivaSpin four times to remove residual low molecular weight impurities.

5.7. References

- Price, P. and Sikora, K. *Treatment of cancer*. (CRC Press, 2014).
- Burrell, R. A., Mcgranahan, N., Bartek, J. and Swanton, C. *Nature*, **501**, 338–345 (2013).
- Podo, F. *et al. Mol. Oncol.*, **4**, 209–229 (2010).
- Crown, J., Shaughnessy, J. O. and Gullo, G. *Ann. Oncol.*, **23**, vi56–vi65 (2012).
- Dai, W. *et al. Adv. Drug Deliv. Rev.*, **115**, 23–45 (2017).
- Vogus, D. R., Krishnan, V. and Mitragotri, S. *Curr. Opin. Colloid Interface Sci.* **31**, 75–85 (2017).
- Ronson, A. *et al. Expert Opin. Orphan Drugs*, **5**, 369–374 (2017).
- Maeda, H. *Bioconjugate Chem.*, **21**, 797–802 (2010).
- Nino-Pariente, A., Nebot, V. J. and Vicent Maria, J. *Curr. Pharm. Des.*, **22**, 1274–1291 (2016).
- Canal, F., Sanchis, J. and Vicent Maria, J. *Curr. Opin. Biotechnol.*, **22**, 894–900 (2011).
- Duncan, R. and Vicent, M. J. *Adv. Drug Deliv. Rev.*, **65**, 60–70 (2013).
- Greco, F. and Vicent, M. J. *Adv. Drug Deliv. Rev.*, **61**, 1203–1213 (2009).
- Zagorodko, O., Arroyo-Crespo, J. J., Nebot, V. J. and Vicent, M. J. *Macromol. Biosci.*, **17**, 1600316 (2016).
- Barz, M. *Polym. Chem.*, **4**, 2989–2994 (2013).
- Vicent, M. J. *et al. Angew. Chem. Int. Ed.*, **44**, 4061–4066 (2005).
- Daladier, C. Polymer-drug conjugates as platforms for combination therapy in the treatment of hormone-dependent breast cancer. (Universitat de Valencia, 2013).
- Arroyo-Crespo, J. J. *et al. Adv. Funct. Mater.*, **28**, 1800931 (2018).
- Song, W. *et al. Acta Biomater.*, **10**, 1392–1402 (2014).
- Soni, K. S. *et al. J Control Release*, **264**, 276–287 (2018).
- Ramasamy, T. *et al. J. Acta Biomater.*, **48**, 131–143 (2017).
- Zhou, W. *et al. Front. Mol. Neurosci.*, **10**, 1–17 (2017).
- Song, H. *et al. Theranostics*, **9**, 2299–2314 (2019).
- Schaal, J. L. *et al. J. Control. Release*, **228**, 58–66 (2016).
- Vasey, P. A. *et al. Clin. Cancer Res.* **5**, 83–94 (1999).
- Johnston, S. R. D. and Dowsett, M. *Nat. Rev.*, **3**, 821–831 (2003).
- Strasser, K. and Goss, P. E. *J. Clin. Oncol.*, **19**, 881–894 (2016).
- Lunning, P. E. *Eur. J. Cancer*, **36**, S81–S91 (2000).
- Pietras, R. J. *Oncologist*, **11**, 704–717 (2006).
- Arroyo-Crespo, J. J. *et al. Biomaterials*, **186**, 8–21 (2018).
- Becker, A. *et al. Cancer Cell*, **30**, 836–848 (2017).
- Duro-Castano, A. *et al. Adv. Mater.*, **29**, 1702888 (2017).
- Vicent M.J. *et al. Patents* WO/2009/141826 and WO2017025298A1.
- Feng, Y., Lograsso, P. V., Defert, O. and Li, R. *J. Med. Chem.*, **59**, 2269–2300 (2015).
- Yamashita, K., Kotani, Y. and Nakajima, Y. *Brain Res.*, **1154**, 215–224 (2007).
- Gilkes, D. M. *et al. PNAS*, **111**, E384–E393 (2014).
- Liu, S., Goldstein, R. H., Scepansky, E. M. and Rosenblatt, M. *Cancer Res* **69**, 8742–8752 (2009).
- Guerra, F. S., Oliveira, R. G. De, Alberto, C. and Fraga, M. *Sci. Rep.*, **7**, 13723 (2017).
- Chen, W., Mao, K., Hua-Huy, T. and Bei, Y. *Oncol. Rep.*, **32**, 2795–2802 (2014).
- Ogata, S., Morishige, K. and Sawada, K. *Int. J. Gynecol. Cancer*, **19**, 1473–1480 (2009).
- Ying, H. *et al. Mol Cancer Ther*, **5**, 2158–2165 (2006).
- Vennin, C., Cox, T. R., Pajic, M. and Timpson, P. *Oncotarget*, **8**, 84635–84636 (2017).
- Tönges, L., Koch, J., Bähr, M. and Lingor, P. *Front. Mol. Neurosci.*, **4**, 39 (2011).
- Kurtoglu, Y. E., Mishra, M. K., Kannan, S. and Kannan, R. M. *Int. J. Pharm.*, **384**, 189–194 (2010).
- Ghosh, A. K. and Brindisi, M. *J. Med. Chem.*, **58**, 2895–2940 (2015).
- Zhang, Z. *Mar. Drugs*, **11**, 81–98 (2013).
- Yue, D. *et al. J. Mater. Chem. B Mater. Biol. Med.*, **2**, 7210–7221 (2014).

47. Brüning, A., Friese, K., Burges, A. and Mylonas, I. *Breast Cancer Res.*, **12**, R45 (2010).
48. Hsu, C., Chang, Z. and Lee, H. *BMC Cancer*, **15**, 943 (2015).
49. Arroyo-Crespo, J. J. *et al. Int. J. of Cancer*, **145**, 2267–2281 (2019).
50. Zhang, X. *et al. Cell Death Dis.*, **9**, 190 (2018).
51. Wang, J. *et al. Nat. Commun.*, **7**, 1–13 (2016).
52. Inhibitor, C. K. *et al. Clin. Breast Cancer*, **14**, 169–176 (2014).
53. Jo Chien, A. *et al. J. Clin. Oncol.*, **37**, 1072 (2019).
54. Gojo, I. *et al. Cancer Chemother Pharmacol*, **72**, 897–908 (2013).
55. Canduri, F., Filgueira, W. and Jr, D. A. *Curr. Comput. Aided Drug Des.*, **1**, 53–64 (2005).
56. Kern, J. C. *et al. JACS*, **138**, 1430–1445 (2016).
57. Cihalova, D. *et al. Biochem. Pharmacol.*, **356**, 354–365 (2015).
58. Michael, P. *Animal Models For The Study Of Human Disease*. (Elsevier, 2017).

Chapter 6

Supramolecular stabilization and crosslinking

6.1. Introduction

Both supramolecular and polymeric self-assembling systems suffer from low stability upon dilution. As soon as the system concentration decreases below CAC or CMC, micelles or other self-assembled structures rapidly disaggregate into their parent structural elements, thus diminishing the benefits of their 3D solution conformation (mainly size and shape) and significantly affecting their pharmacokinetics and final fate. There exist two principal particle stabilization strategies - covalent crosslinking and non-covalent stabilization that allows disassembly only under desired conditions (i.e., external or endogenous physiological triggers). A wide variety of crosslinking strategies have been already described and were discussed in **Chapter 1** (see references in **Chapter 1** [95]-[102]).

Non-covalent stabilization strategies have been less explored, including the application of hydrophobic molecules able to stabilize the whole structure by the formation of additional non-covalent bonds.^{1,2} While the majority of hydrophobic drugs are suitable stabilization agents, the most efficient, such as doxorubicin (Dox),³⁻⁵ paclitaxel (PTX)⁶ and camptothecin (CPT)⁷, are those molecules that can form clusters,

In this chapter, we will explore both approaches through the development of two different strategies for stPGA stabilization: (i) loading of **F3E10** with hydrophobic

drugs^{3-5,7} for the preparation of rod-shaped particles, and (ii) covalent crosslinking of stPGA with genipin⁸ for the preparation of spherical nanoparticles.

6.2. Hydrophobic Stabilization of Supramolecular Polymers

To stabilize the **F3E10** supramolecular nanoassemblies described in Chapter 2, we selected Dox, given its water-soluble and strongly hydrophobic nature. As a first step, we mixed doxorubicin hydrochloride (Dox.HCl) with a solution of **F3E10** and **F0E10** at pH 7.5 in a molar ratio of 10/1. We observed that the addition of Dox to solutions of **F0E10** resulted in immediate cloudiness with rapid precipitation in all cases. However, in solutions of **F3E10** the addition of Dox led to the immediate appearance of light cloudiness that rapidly completely disappeared (**Fig. 6.1**).

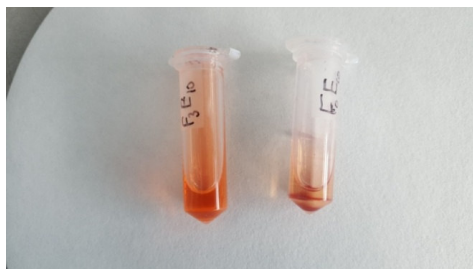


Figure 6.1. Image of 1 mM **F3E10** and **F0E10** complexes with Dox (10/1 mol/mol) in 120 mM NaCl pH 7.5 5 minutes after preparation.

As Dox is slightly cationic, it interacts with PGA chains through ionic interactions. In the case of **F0E10** complexes, the formation of precipitates occurs due to probable point-to-point Dox-induced aggregation, as the absence of phenylalanine significantly diminishes the hydrophobic content of the polymer and the competing π - π interactions present in **F3E10** are lost in **F0E10**.

Next, we prepared a series of **F3E10**/Dox complexes in a molar ratio from 50/1 to 5/1. Using TEM, we observed the presence of the mixture of unimers, flexible filaments, and small nanorods of 20-40 nm in length in solutions with low Dox concentrations. Upon an increase in Dox content, the length of the fibers increased to 50-120 nm for the 10/1 ratio. For 5/1 ratio **F3E10**/Dox, we observed the formation of long fibers from 100 nm to up to a micrometer. In cases, we observed a rod diameter of around 10 nm and particles remained well separated from each other and never formed aggregates or intertwined bundles (**Fig. 6.2**). As such, we selected a 10/1 ratio for stability studies. To determine the influence of pH on self-assembly, we prepared **F3E10**/Dox complexes (10/1 mol/mol) in a pH range of 5.5 to 8.5 (see **Fig. 6.3**). At low pH, we observed the formation of longer nanofibers, reaching 1 μ m in length as a consequence of a lower degree of glutamic residue ionization and lower chain repulsions. At pH 6.5-7.5, we observed similar nanorods of around 100 nm in length. At pH 8.5, we observed shorted rods (30-50 nm); however, it remains unclear if this occurs due to higher PGA chain repulsions or partial Dox degradation.

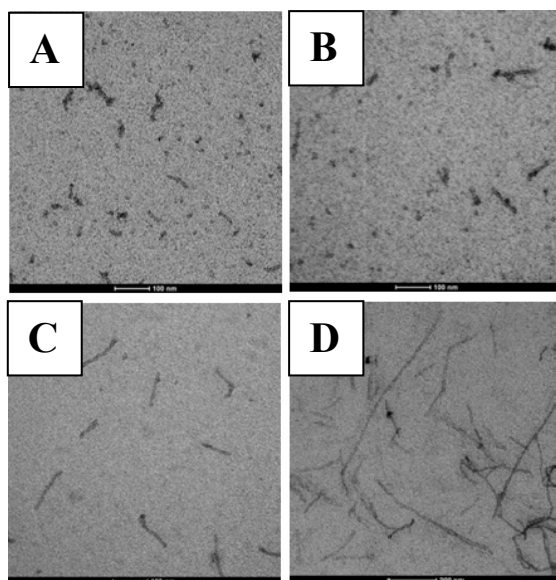


Figure 6.2. TEM images of 1 mM **F3E10**/Dox nanorods solution in water at pH 7.5 at molar ratio 50/1 (A), 25/1 (B), 10/1 (C) and 5/1 (D).

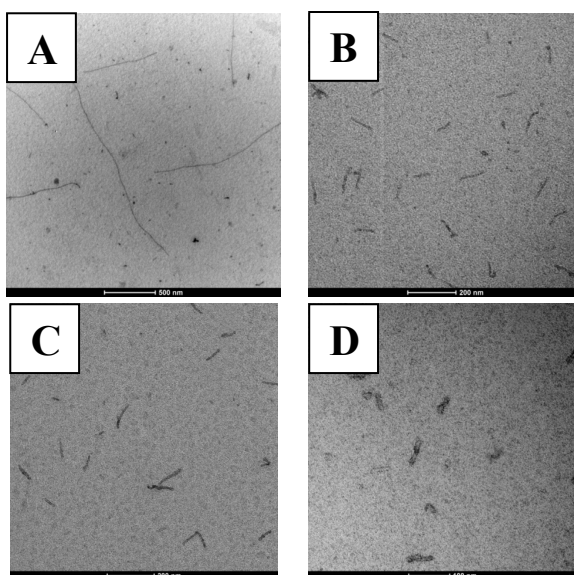


Figure 6.3. TEM image of **F3E10**/Dox complexes prepared at pH 5.5 (A), 6.5 (B), 7.4 (C), and 8.5 (D) (sample in 120 mM NaCl at 0.1 mM, uranyl acetate staining).

To understand the mechanism of self-assembly, we must first appreciate that Dox displays an extraordinarily diverse range interactions, including ionic complexes

with PGA chains, dimeric ionic complexes, dimers, and oligomers with itself; furthermore, Dox interacts with hydrophobic cores, as shown in **Fig. 6.4**.

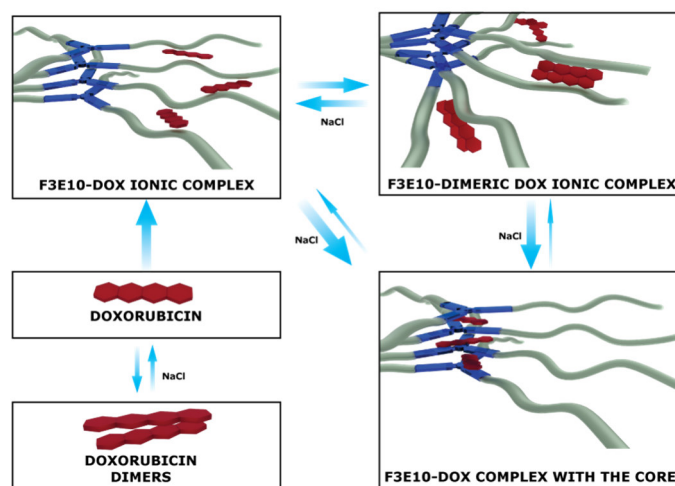


Figure 6.4. Schematic representation of the possible interactions of Dox with **F3E10**.

Based on the TEM studies of **F3E10**/Dox complexes, we discarded the possibility of self-assembly due to point-to-point interactions as we failed to observe any evidence of interparticle interactions. As such, we assume that Dox either intercalates in the core or diffuses deeper into the polymer chains. At pH 8.0 Dox forms nanorods by itself, which may further co-assemble with PGA forming rod-like particles⁹ that consist of an inner Dox core and outer PGA shells. To study this structure, we performed cryo-TEM microscopy for the obtained nanoassemblies; however, in our case, we observed an identical structure to that of the nanorods prior to Dox stabilization (**Fig.6.5A**). Image reconstruction demonstrated a helical structure suggesting that the particles represent supramolecular polymers stabilized by Dox rather than Dox nanorods stabilized by PGA (**Fig. 6.5B**).

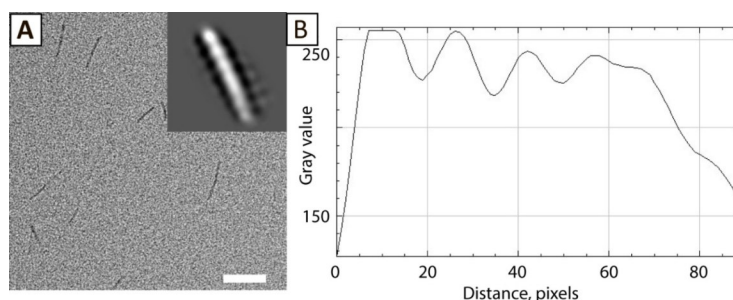


Figure 6.5. Cryo-TEM image of 1 mg/ml **F3E10**/Dox solution in 120 mM NaCl and particle reconstruction image (A) and corresponding plot profile (B). Scale bar 100 nm.

Regular TEM for the nanorods (**Fig. 6.6A**) demonstrated an identical morphology to the cryo-TEM results (**Fig. 6.4B**). Surprisingly, we did not observe flexible aggregates as in the case of **F3E10** without Dox. Even though the precise reason remains unclear, we hypothesize that the system equilibrium is strongly shifted towards nanorods, and the amount of non-aggregated molecules is rather small and they do not arise in the form of artifacts. We repeated the experiment several times and confirmed the suitability of uranyl acetate staining for the study of stabilized nanorods.

We additionally studied how particles respond to dilution below CAC values (for non-stabilized **F3E10**) in 120 mM NaCl solution using TEM (**Fig. 6.6A-C**). We prepared a 1 mM solution of **F3E10**/Dox in a molar ratio of 10/1 in 120 mM NaCl, diluted it to 0.014 mM, and studied both solutions immediately after preparation and after 48 hours. In all cases, we observed a similar nanorod size, even after 48 hours. The control experiment at 0.1 mM with non-stabilized **F3E10** demonstrated the absence of assembled particles (**Fig. 6.6D**).

The obtained particles remained stable during dialysis for five days, and we did not observe any significant Dox loss, as evidenced by UV-Vis spectroscopy (**Fig. 6.7**). We did not observe the loss of Dox and the polymer during dialysis with a 50 kDa cut-off membrane for 48 hours.

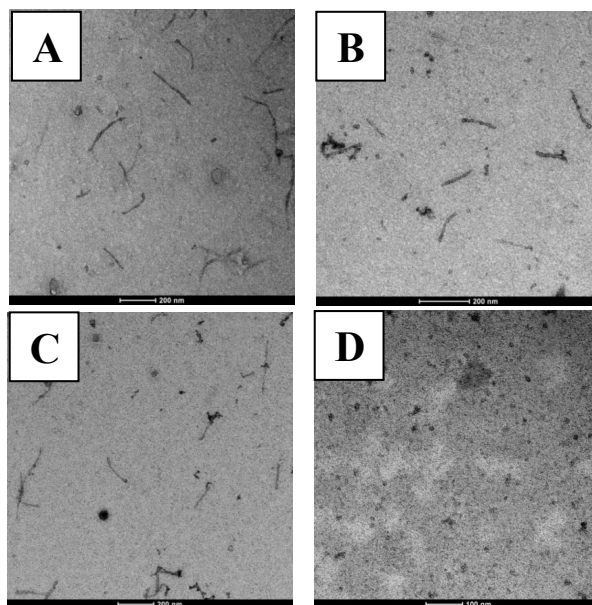


Figure 6.6. TEM images of 1 mM **F3E10**/Dox nanorods solution in 120 mM NaCl p at a ratio of 10/1, after preparation (A), 10x after dilution (B), and 48 h after dilution (C). TEM image of **F3E10** (sample in 120 mM NaCl at 0.1 mM, uranyl acetate staining as control (D).

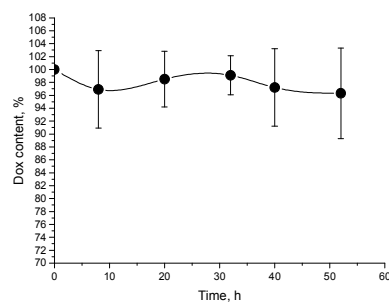


Figure 6.7. Particle stability measured by Dox content analysis in **F3E10**/Dox complexes during dialysis up to 60 h. Dox content is calculated by $100 \cdot c(\text{Dox})_t / c(\text{Dox})_0$ and represented as mean \pm SD (n=3).

We repeated this experiment several times to evaluate the reproducibility of the particles obtained. In all cases, we observed the formation of non-interacting nanorods with a length of 50-120 nm (**Fig.6.8**).

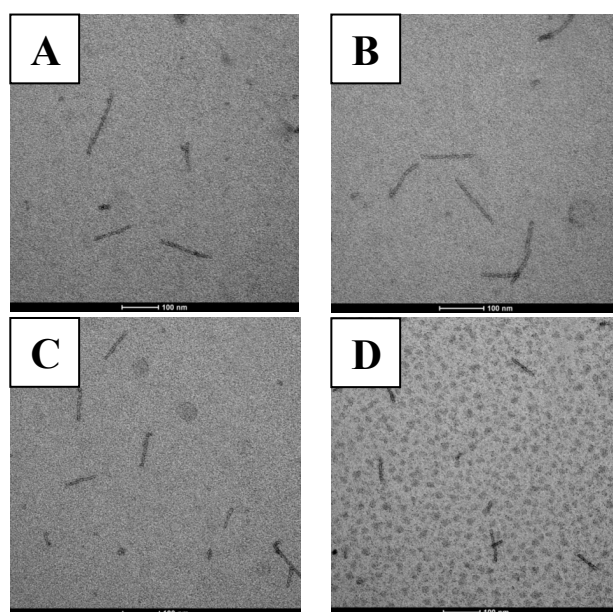


Figure 6.8. (A-D) TEM images of four different batches of **F3E10**/Dox to evaluate synthetic reproducibility (samples in 120 mM NaCl at 1 mM, uranyl acetate staining).

Next, we studied structural stabilization by other flat-water soluble hydrophobic molecules by performing a series of TEM experiments for solutions containing different amounts of Nile Red (NR), doxycycline (Dxc), and irinotecan (Iri). Excluding NR, we used all compounds as hydrochloride salts and added them to **F3E10** solutions at pH 7.4

and in similar molar ratios (5/1, 10/1, and 20/1). The addition of Iri to an **F3E10** solution at molar ratios of 10/1 and 5/1, we observed nanorods similar to those generated with Dox (**Fig. 6.9 A and B**) but more polydisperse in length, ranging from 30 to 200 nm. When we employed Dxc at a ratio of 5/1, 10/1, or 20/1, we only detected a few short nanorods of 50-70 nm in length (**Fig. 6.9 C and D**) independent of Dxc content. In all cases, we observed a significantly lower number of particles than for **F3E10/Dox** and **F3E10/Iri**. Finally, the application of Nile Red did not permit nanorod formation and the dye precipitated in a few days.

Overall, the data suggest that the nanorod stabilization mechanism observed with **F3E10** does not entirely relate to the hydrophobicity of the molecule, but instead to the planarity and particular supramolecular interactions in the core and/or with the PGA chains. While Dox, Dxc, and Iri are cationic, planar, and hydrophobic, they appear to display specific mechanisms of interaction with supramolecular polymers; this is pronounced in the case of Dox and Dxc as they possess relatively similar structures. Dox and Iri may be able to intercalate between BTA-oligophenylalanine molecules, in a similar manner to DNA; however, Dxc cannot intercalate due to the presence of bulky groups that inhibit structural stabilization. NR intercalates into the structures like DNA; however, it is not water-soluble at the studied concentration range and rapidly precipitates.

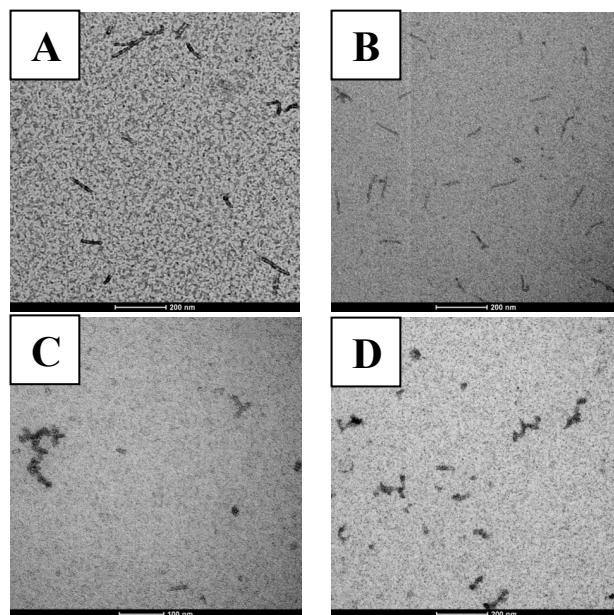


Figure 6.9. TEM images of **F3E10/Iri** and **F3E10/Dxc** complexes at amolar ration of 10/1 (A and C) and 5/1 (B and D) (samples in 120 mM NaCl at 1 mM, uranyl acetate staining).

Finally, we note that the preparation strategy followed is fundamental to the formation of stabilized nanorods. For example, following the addition of very

concentrated solutions of Dox to the **F3E10** polymer without vigorous stirring, the mixture resulted in very long rods of few mm long instead of defined nanorods; we also observed the generation of clots with coexisting uranyl-induced artifacts deriving from non-assembled unimers (**Fig.6.10**).

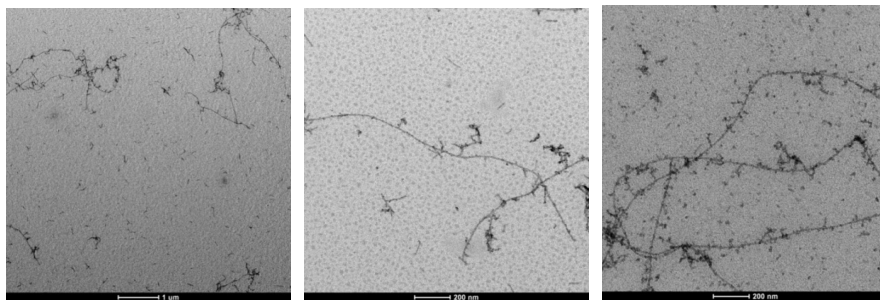


Figure 6.10. TEM images of **F3E10**/Dox particles obtained with non-optimal preparation strategy(samples in 120 mM NaCl at 0.1 mM, uranyl acetate staining).

The question remains as how Dox interacts with **F3Ex** particles. A previous study reported that the fluorescence of Dox significantly quenches upon DNA intercalation.¹⁰ Fluorescence spectroscopy represents a powerful tool for the study of Dox behavior in different systems, including self-quenching, non-covalent interactions, partial and complete intercalation. To answer this above-noted question, we selected four compounds with an increasing number of glutamic units - **F3Ex**, where $x = 0, 1, 10$ and a control compound **F0E10**.

The emission spectrum of **F3Cl** did not change following the increase in compound concentration (**Fig. 6.11**), while we observed a decrease in peaks in the range of 210-270 nm in the excitation spectrum. Therefore, we conclude that Dox does not intercalate into the structure of **F3Cl**, probably due to Coulomb repulsions between positively charged amines on both compounds.

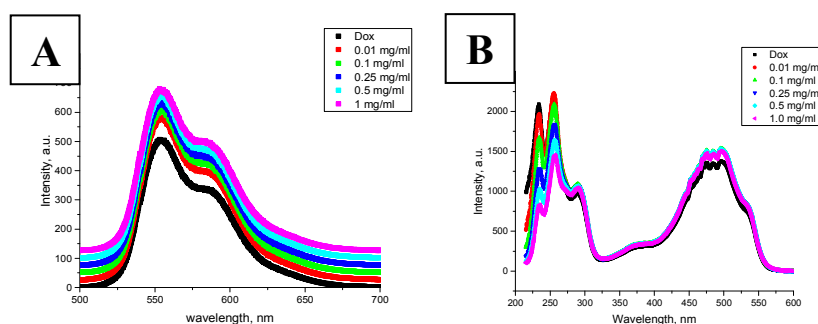


Figure 6.11. Fluorescent emission (A) and excitation (B) spectra of Dox in the presence of different concentrations of **F3** (ranging from 0.01 to 1 mg/ml in water pH 4.0).

We performed the study of compound **F3E1** in water and 120 mM NaCl at increasing concentrations of the compound (from 0.01 to 1.3 mg/ml) (**Fig. 6.12**). In water, the intensity of the peaks in the emission spectrum decreased until a concentration of 0.25 mg/ml and then started to increase, reaching almost the intensity value of free Dox in water. For the emission spectra of the salt solution, we observed a similar trend, albeit with a less pronounced drop in intensity. On the excitation spectra both in water and 120mM NaCl, we observed that peaks at 400-560 nm followed a similar trend; however, peaks at 210-270 nm decreased in intensity and shifted to a higher wavelength. The redshift of the peak at the range from 585 to 590 nm and the increase of intensity upon may occur due to possible dimerization and oligomerization of Dox molecules in solution. The addition of salt disrupts dimers of Dox; however, we failed to observe any disruption, and we conclude that Dox interacts with the aromatic groups of the **F3E1** core.

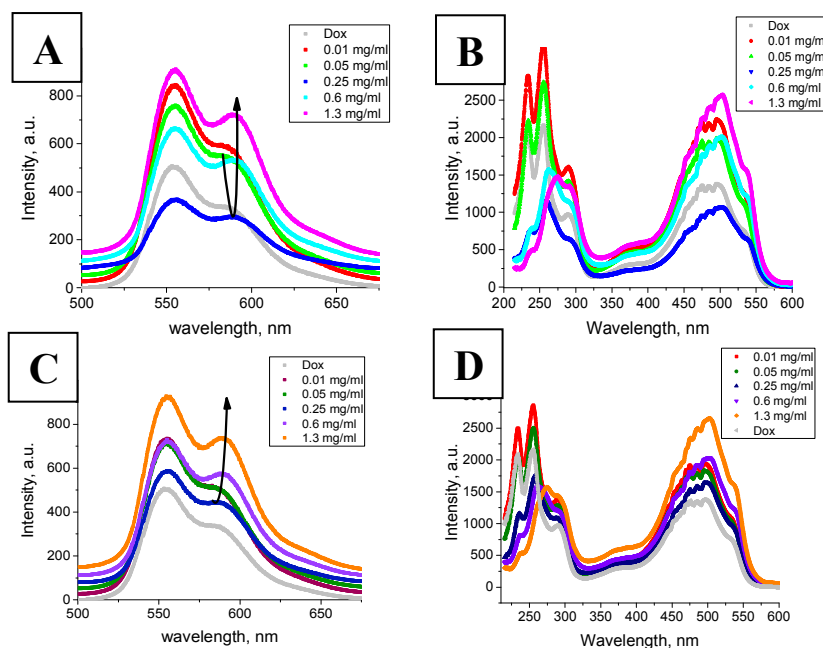


Figure 6.12. Fluorescent emission and excitation spectra of Dox in the presence of different concentration of **F3E1** (from 0.01 to 1.3 mg/ml) in water (A and B) and 120 mM NaCl (C and D) at pH 7.4.

For compound **F3E10** in 120mM NaCl, we observed similar behavior in the emission spectra – a decrease in intensity at low compound concentrations and an increase with a peak shift from 585 to 590 nm at higher concentrations (**Fig. 6.13**). In the excitation spectrum, we observed the complete disappearance of peaks at 234 and 255 nm and a slow shift of the peak from 290 nm to 299 nm. The position of some peaks from the multiplet at 400-560 nm also shifted.

Finally, for the control experiment for **F0E10** a stPGA with no hydrophobic core, we observed on similar changes in intensity as for **F3E10** in the emission spectrum, although this was less pronounced in the presence of salt (**Fig. 6.14A**). Nevertheless, we did not observe a peak shift at 585 nm. in the excitation spectra, peaks at 234 and 255 nm decreased in intensity, with a slower decrease in the presence of salt. We did not detect changes in peak positions at 400-560 nm (**Fig. 6.14B**).

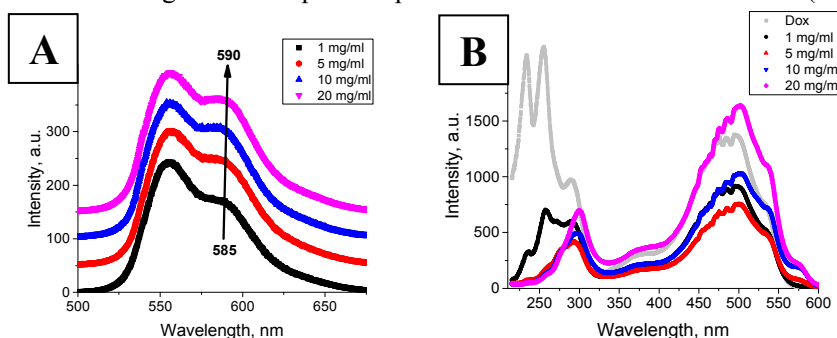


Figure 6.13. Fluorescent emission (normalized) (A) and excitation (B) spectra of Dox in the presence of different concentration of **F3E10** (from 0.01 to 20 mg/ml) in 120 mM NaCl at pH 7.5.

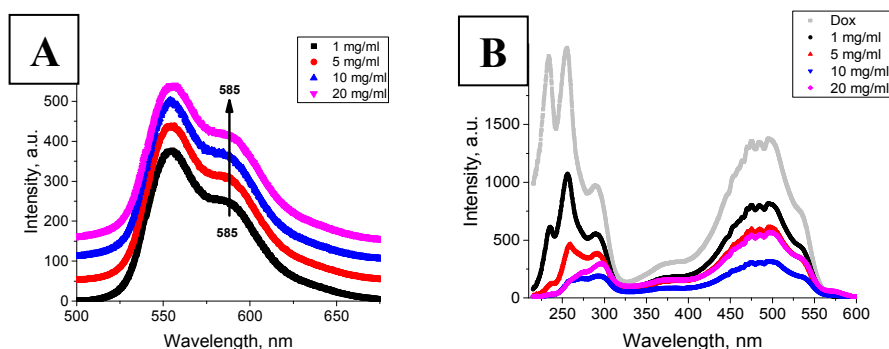


Figure 6.14. Fluorescent emission (A) and excitation (B) spectra of Dox in the presence of different concentration of **F0E10** (from 0.01 to 20 mg/ml) in 120 mM NaCl at pH 7.5.

Combining these data, we can draw certain conclusions regarding the mechanism of Dox interaction with **F3E10**. For stPGA without a hydrophobic core (**F0**), Dox interacts with PGA chains through ionic interactions, later forming dimers that provoke fluorescence quenching. Unimeric ionic pairs $\text{COO}^-:\text{Dox}^+$ are preferentially formed upon an increase in polymer concentration.^{11,12} The addition of salt disrupts dimer formation, leading to an increase in fluorescence intensity; however, we failed to observe a peak shift. For compounds with hydrophobic **F3** cores at concentrations below the CAC, the mechanism of interactions with Dox is identical to **F0E10**; however, at concentrations above the CAC, Dox interacts with the core and results in the redshift of several peaks on emission and excitation spectra. Considering that the expected

mechanism of self-assembly of **F3**-based compounds does not suppose the formation of a dense ordered structure of planar stacks, like in DNA, Dox cannot intercalate in the structure directly. Similar interactions have been reported for alternating (dA-dT)-(dA-dT) DNA duplexes (polyAT) with Dox.¹³ Unlike alternating (dC-dG)-(dC-dG) DNA duplexes (polyCG), Dox cannot intercalate into a polyAT structure, although they both interact with each other.¹³ Therefore, we conclude the formation of an association product with **F3** core, although we cannot unambiguously define the precise orientation of Dox in the core.

Due to the complexity of the interaction pattern of Dox with **F3E10** we cannot apply the Stern–Volmer relationship,¹⁴ as a switch in the mechanism of interactions (and not spectroscopic interference) cause apparent deviations from the relationship.

Finally, we studied drug release from **F3E10**/Dox (10/1 mol/mol) nanorods at pH 5.5, pH 7.4, and in the presence of cathepsin B (**Fig. 6.15**). At both pH 5.5 and pH 7.4, Dox release remained below 2% of total drug loading after 72 hours; however, we believe that this value corresponds to the free drug rather than as low release of Dox, as Dox levels remain almost constant. In the presence of cathepsin B, we observed significantly higher cumulative drug release, reaching 25 % after 72 h. These results confirm our hypothesis of Dox localization in the nanorod cores, as opposed to interacting with the PGA chains.

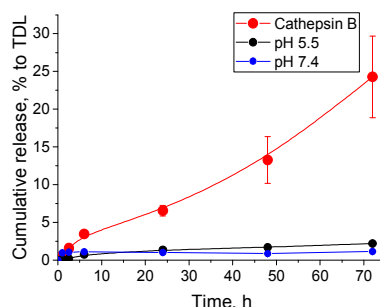


Figure 6.15. Time-dependent release of doxorubicin from **F3E10**/Dox (10:1) nanorods at pH 5.5, pH 7.4, and in the presence of cathepsin B.

As a confirmation fluorescence experiment, we employed a different polymer, **ABA-F3-C12-E20** that assembles into core-shell micelles (as described in **Chapter 4**, section 4.4). When we performed a TEM study of Dox interaction with **ABA-F3-C12-E20** we observed the formation of small, slightly elongated objects, with few short rods of less than 50 nm (**Fig. 6.16**). This confirms that the rods observed before do not arise from specific Dox aggregation, and suggests that the incorporation of Dox promotes a more ordered aggregation of the polymer.

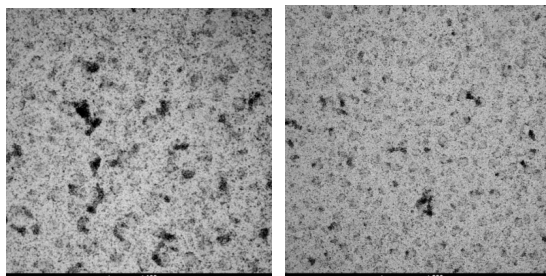


Figure 6.16. Representative TEM images of **ABA-F3C12-E20/Dox** complex at molar ratio 10/1 (samples in 120 mM NaCl at 1 mg/ml pH 7.4, uranyl acetate staining).

To corroborate our results, we performed SAXS studies of **F3E10** with Dox in 120 mM NaCl (**Fig. 6.17A**). For the samples at 10 mg/ml upon the addition of Dox, we observed an increase in intensity and higher slope of the curve (close to -1), which confirms the presence of rod-like particles. For the sample without Dox, we found a curve slope in medium q -range of -0.2, corresponding to an almost completely disassembled polymer solution.

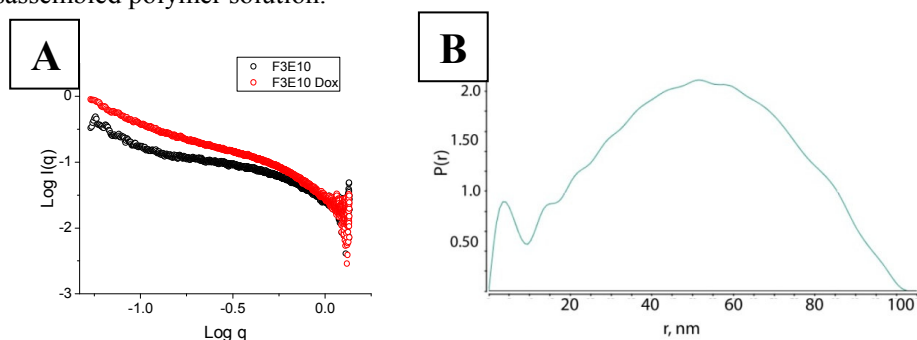


Figure 6.17. (A) SAXS profiles of **F3E10** and **F3E10/Dox** complex at molar ratio 10/1 (samples in 120 mM NaCl at 10 mg/ml, pH 7.4). (B) $P(r)$ functions of **F3E10/Dox** complex at molar ratio 10/1 (samples in 120 mM NaCl at 10 mg/ml, pH 7.4).

The $P(r)$ function of the **F3E10/Dox** complex possessed the usual appearance for short nanorods with an R_c around 2.6 nm and D_{max} of around 100 nm, correlating well with the TEM data (**Fig. 6.17B**).

6.3. Polyelectrolyte Crosslinking in Water

Despite the fact that the use of polyelectrolytes in the formation of nanosystem has been explored for at least 30 years,^{15,16} the crosslinking of polyelectrolytes in water remains a challenging task. Existing methods usually rely on crosslinking in organic solvents in conditions that provide for uncharged polymers¹⁷ or by using alternative techniques such as nanoprecipitation.¹⁸ Crosslinking in aqueous conditions was mainly employed for the preparation of gels and the synthesis of micrometer-size particles.

Herein, we attempted to develop a new method to obtain stable particles in aqueous conditions using our PGAs via chemical cross-linking strategies.

After several unsuccessful attempts with more straightforward crosslinking strategies, we decided to explore the use of genipin,⁸ which has been described as a useful approach to crosslink chitosan and proteins in water to obtain microparticles by a diamine crossreaction¹⁹ (**Fig. 6.18**). Genipin, a natural compound extracted from the fruit of *Gardenia jasminoides*,²¹ is well-known for its ability to interact with two amino groups with the formation of covalent non-biodegradable linkage (**Fig. 6.18**).⁸ To utilize this strategy in post-polymerization reactions, we modified 5-10 % (mol/mol) of the side-chains carboxylic acid groups in linear and stPGA with an ethylenediamine derivative through a two-step synthesis, as shown in **Fig. 6.19**.

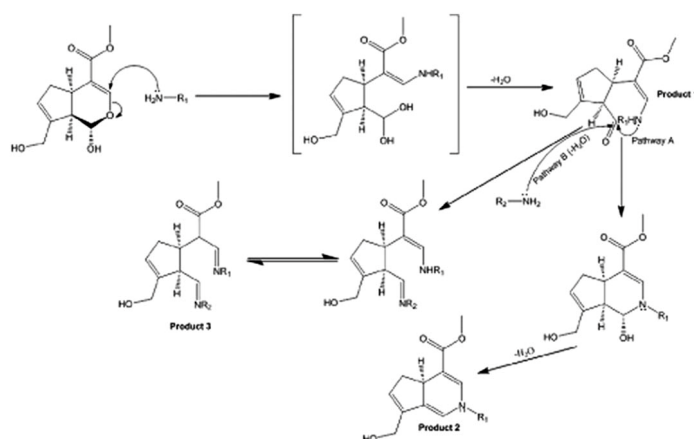


Figure 6.18. General scheme of a crosslinking reaction of two amine-containing molecules with genipin.²⁰

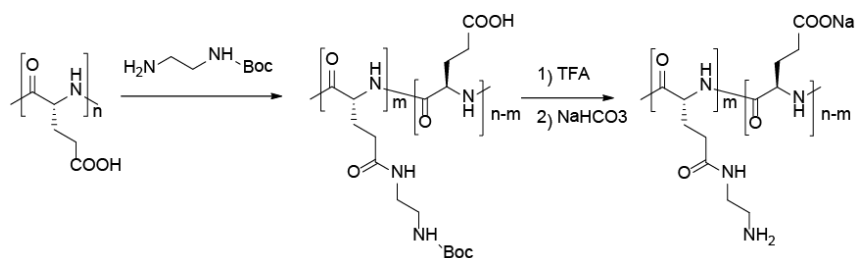


Figure 6.19. Synthetic scheme for the preparation of amine-functionalized PGA.

Initially, we prepared one conjugate of linear PGA and one conjugate of stPGA (**F0E50**) with 10% (mol/mol) of amino functionalization. We studied the crosslinking for three different concentrations (4, 10 and 20 mg/ml) and different amounts of crosslinker (25, 50, 75, and 100% mol) in water. After 48 h reaction at 37 °C, we dialyzed and lyophilized compounds, and observed that at high concentrations (20 mg/ml and

above) of polymer and 75-100 % crosslinking equivalents, we obtained dark-blue hydrogels that were insoluble in water. For lower concentrations of the polymer, we obtained solutions from light blue to dark blue in color. Color itself represents a helpful indicator that the reaction is proceeding. DLS analysis demonstrated that we obtained the best results for 10 mg/ml solutions with different concentrations of genipin. The best two samples displayed a main population of particles in a range of 3-7 nm for linear polymer and 3-30 nm for stPGA (Fig.6.20).

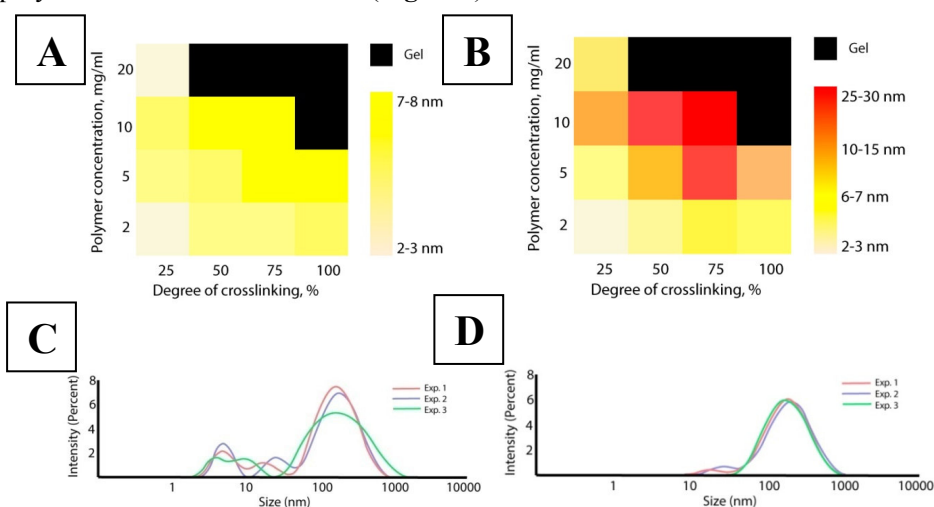


Figure 6.20. Particle size diagram for linear (A) and stPGA (B) in conditions of varied polymer concentration (from 2 to 20 mg/ml) and degree of crosslinking (from 25 to 100%). Representative DLS profiles of linear (C) and stPGA (D) crosslinked with genipin.

Based on the existing models of polyelectrolyte contraction,²² we hypothesized that if we performed the reaction in the presence of salt, the screening the interparticle repulsions would result in an increased particle size. We performed an experiment for two **F0E50**-EDA conjugates with 5% and 10% mol modification with 50% and 75% mol genipin (Gen) modification in NaCl (up to 360 mM) with a polymer concentration of 2, 5, and 10 mg/ml.

After plotting DLS data as size against salt concentration, we made some preliminary conclusions about the role of NaCl concentration in polymer crosslinking efficiency and resultant nanostructure formation (**Fig. 6.21**). At low concentration of the polymer (2 mg/ml) with 5% mol of amine loading and low Gen content, particle size did not strongly correlate with salt content, providing a low reaction efficiency. For polymers with 10 % mol of amines, the content of salt directly correlated with particle size, increasing up to around 20 nm in diameter. Finally, at high polymer concentration (10 mg/ml), we observed an increase in size, but again, a size decrease for the highest concentration of salt (20 mg/ml), probably related to chain collapse and the exposure of

amine groups on the polymer surface. Increase in the amount of genipin resulted in gel formation, therefore, we could not perform size measurements with 10 % mol **F0E50**-EDA modification at 10 mg/ml and 75 % mol Gen equivalents.

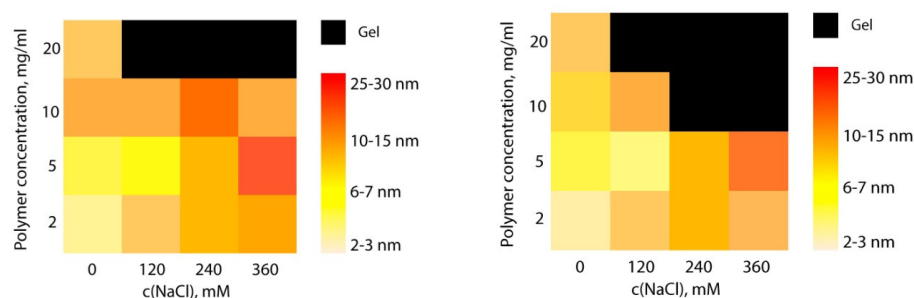


Figure 6.21. Particle size diagram, demonstrating dependence of particle diameter upon concentration of NaCl content at 50 % crosslinking equivalents at 5 %mol (left) and 10% mol (right) amine functionalization.

Finally, we evaluated phosphate buffer saline (PBS) with and without increasing concentrations of NaCl (up to 120 mM) as a solvent to screen interparticle interactions more efficiently and avoid chain collapse. We performed an experiment for two **F0E50** compounds with 5 and 10%mol amine functionalization, 50 and 75 % mol Gen equivalents in PBS (140 mM NaCl), and PBS with additional 120 mM NaCl (total 260 mM NaCl).

Analysis of DLS data demonstrated that the addition of extra salt, as well as a high concentration of the polymer, does not promote the attainment of large particle sizes (**Fig. 6.22**). The use of 75% (mol/mol) of crosslinker provided the best results and, therefore, we selected this for the preparation of a large batch of crosslinked particles.

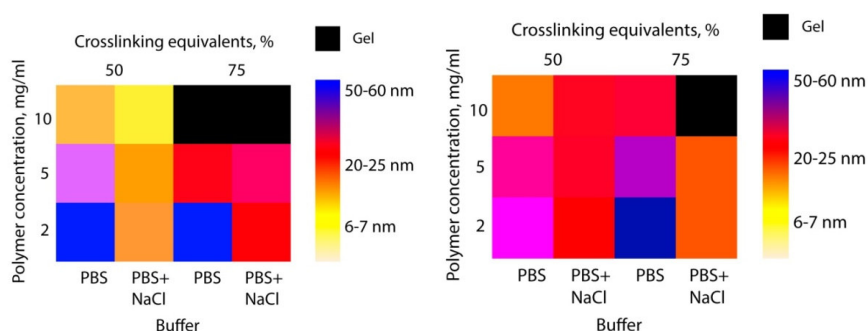


Figure 6.22. Particle size diagram, demonstrating dependence of particle diameter on buffer type (PBS; pH 7.4; PBS + NaCl: pH 7.4) and crosslinking equivalents for 5 % mol (left) and 10 % mol (right) amine-functionalized **F0E50**.

To avoid any additional crosslinking with unreacted or partially reacted genipin, we quenched the reaction with glycine, which was removed by dialysis. Firstly, we performed three separate experiments with chosen conditions (75 mol% of crosslinker, 2 mg/ml polymer concentration in PBS) and obtained the particles with the main particle population with an average size of 20-60 nm. Particle distribution by intensity was slightly different in one experiment in higher size particle, but considering that the size distribution is represented by intensity, this difference is not significant.

Using this optimized method, we prepared 100 mg of crosslinked star PGA particles and characterized them using DLS, TEM, SAXS, and AF4. DLS data demonstrated that particles possessed an average size by number of 20-30 nm (**Fig. 6.23**), thereby establishing that large batches maybe allow for a more controlled reaction with a narrower polydispersity index value.

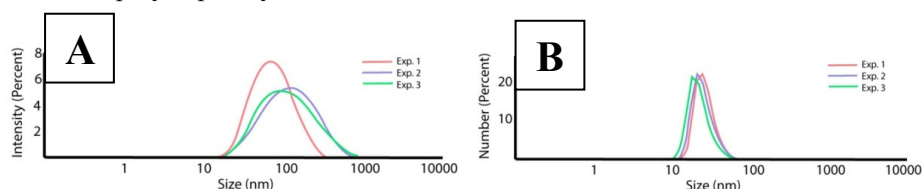


Figure 6.23. DLS profiles by intensity (A) and by number (B) of **F0E50** crosslinked according to optimized strategy (75 mol% of crosslinker, 2 mg/ml polymer concentration in PBS).

We performed TEM with negative staining to visualize particles, observing a generally uniform distribution of particles with a close to spherical shape and a size between 20 and 50 nm, which agrees well with DLS data (**Fig. 6.24**).

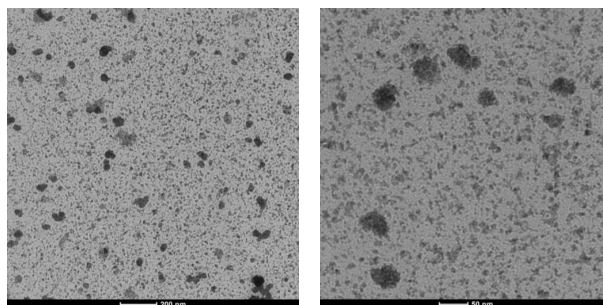


Figure 6.24. Representative TEM images of crosslinked **F0E50** nanoparticles (water, 1 mg/ml, stained with uranyl acetate).

We also performed SAXS studies on two different crosslinked stPGA to understand the role of glycine quenching. Comparing the SAXS profiles of the two samples, we observed almost identical curves at medium and high q -range; however, at a lower q -range, the non-quenched compound has a small uphill slope (**Fig. 6.25**). Uphill slope in the low q -range is the usual sign of aggregation in the sample that probably arises from additional crosslinking reaction within the particles upon concentration

processes by lyophilization or even in a dry state.

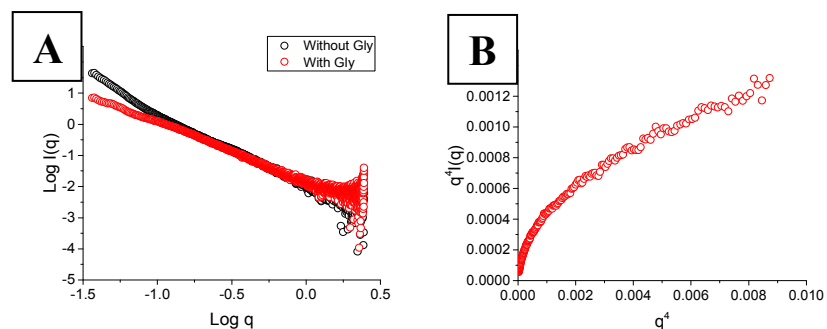


Figure 6.25. (A) SAXS profiles of crosslinked stPGA nanoparticles treated with and without glycine (10mg/ml in PBS) and corresponding Porod-Debye plot for stPGA nanoparticles treated with glycine (B).

We employed Porod asymptotics to determine R_g ,²³ as this method usually provides precise results. The obtained R_g value of 23.9 nm, correlating well with TEM; however, this value is slightly higher than that obtained by DLS.

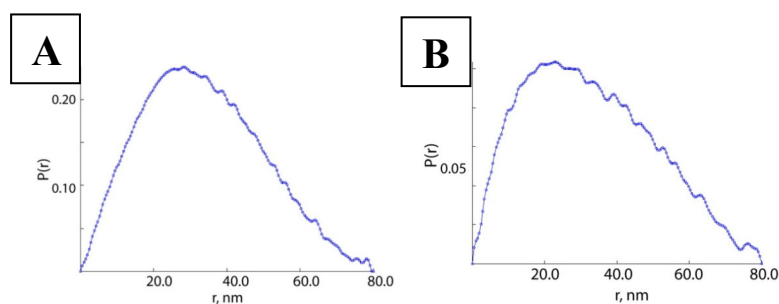


Figure 6.27. $P(r)$ functions of crosslinked **F0E50**-EDA nanostructures quenched (A) and non-quenched (B) with glycine.

The $P(r)$ functions obtained for both compounds were typical of a mixture of spherical particles with low polydispersity (**Fig. 6.27**).²⁴ While we found an average particle size for quenched samples of around 20 nm and non-quenched of around 25 nm, the polydispersity is higher for non-quenched samples. To note, we found a D_{max} value in both cases of around 80-85 nm, which agrees well with DLS and TEM data.

Finally, we performed AF4 studies for the **F0E50**-EDA sample quenched with glycine to ratify the obtained data (**Fig. 6.28**). The calculated particles radius obtained by AF4 ranged from 30 to 90 nm, which agrees with all previously described techniques.

We believe that expanding this crosslinking strategy to the preparation of crosslinked polypeptide-drug conjugates represents a promising approach, as this strategy requires very mild reaction conditions and due to the inherent orthogonality with

the majority of functional groups.

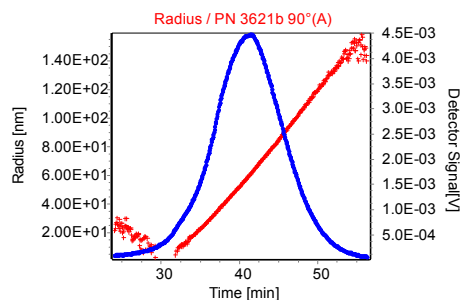


Figure 6.28. AFFF profile of crosslinked stPGA nanoparticles treated with glycine.

This crosslinking strategy can also be used for the rapid and straight forward preparation of polypeptide-based combination conjugates by simple physical mixing of two amine-functionalized single conjugates at a predetermined drug synergistic ratio followed by the addition of genipin. In particular, this crosslinking strategy will be a valuable method for synthesis of combination therapies where synergistic drug ratios require very different single drug concentrations; for example, synergistic ratios above 10:1 are hard to achieve on a single polymer main chain.

We attempted to implement this strategy with a therapeutically relevant nanoconjugate, we first tried to crosslink the previously prepared **F0E50**-SS-Fas conjugate obtained in **Chapter 5** (see **Section 5.2**; the size of the non-crosslinked conjugate of 4.2 nm). As the self-immolative carbamate linker exhibits high sensitivity to strong acids, bases, and reducing agents, we cannot apply monoprotected ethylenediamine with further deprotection. Instead, we conjugated ethylenediamine monohydrochloride using DMTMM coupling in water. The amine hydrochloride does not react under these conditions and can be easily transformed into an amine by a simple pH change. The residual amine can then be easily removed by dialysis.

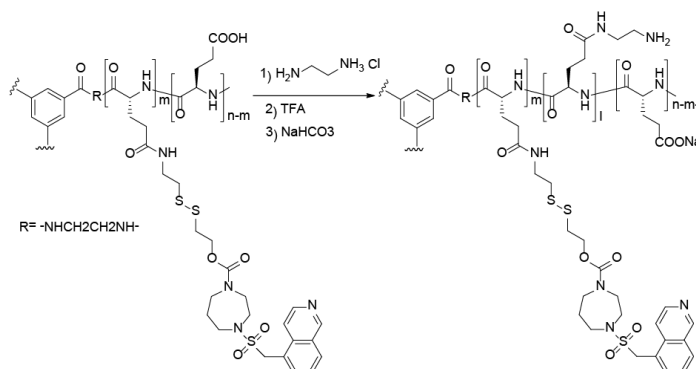


Figure 6.29. General synthetic scheme for amine-functionalized **F0E50**-SS-Fas.

After the reaction, we observed the appearance of a new peak at 3.01 ppm corresponding to one methylene group of ethylenediamine (**Fig. 6.30**).

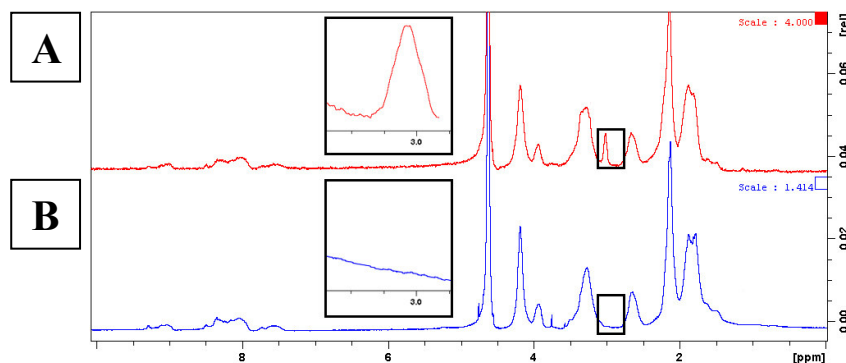


Figure 6.30. NMR spectra of stPGA-SS-Fas and after (A) modification with ethylenediamine monohydrochloride and before (B).

We failed to detect changes in fasudil-related peak area (2.66 ppm, 3.27 ppm, 3.94 ppm), confirming the stability of the linker under these conditions.

For crosslinking, we used an identical method to that described for non-modified polymer (75 mol% of crosslinker, 2 mg/ml polymer concentration in PBS). By means of TEM, we observed that the formed particles possess a diameter ranging from 15 to 30 nm (**Fig. 6.31**), a size range somewhat smaller than the obtained for the non-modified polymer, perhaps explained by the rather high degree of chain modification (reaching almost 20 %) that lead to altered polymer properties.

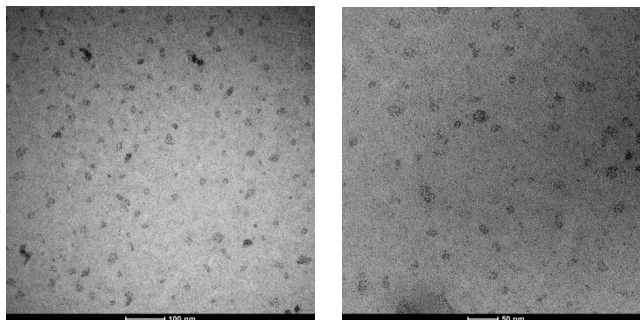


Figure 6.31. Representative TEM images of crosslinked **F0E50**-SS-Fas conjugates.

When we compared particle sizes between the methodologies employed, we observed a high correlation between different methods with the exception of DLS. While it remains unclear why DLS underestimates particle diameter for this particular system, it may relate to CONTIN algorithm issues used by the software.²⁵ As the double mathematical treatment of correlogram and intensity mean provide the number mean value, sufficient uncertainty arises to result in a lower hydrodynamic radius value.

Table 6.1. Summary of crosslinked particlesize values as obtained by different methodologies

| Properties/Compound | F0E50 | F0E50-SS-Fas |
|---------------------|-------|--------------|
| TEM (nm) | 30-50 | 15-30 |
| DLS(nm) | 25-30 | 12-20 |
| SAXS(nm) | 40-80 | - |
| AFFFF (nm) | 35-80 | - |

We are currently performing additional studies with polymers of varied chain functionalization to develop proper dependence of the particle size on the degree of modification and the nature of the drug.

6.4. Conclusion

In this chapter, we explored two different approaches in the search of particle stabilization - covalent crosslinking and non-covalent stabilization - that allow disassembly only under desired conditions to finally achieve our goal of rationally-designed nanoconjugates. We developed a method of nanorod stabilization with flat hydrophobic molecules such as Dox and Iri; obtained nanorods displayed a size range of 50-150 nm and a diameter of ~5 nm. Fluorescence spectroscopy and cryo-TEM confirmed that hydrophobic molecules interact with the cores of the polymers rather than with PGA or with itself. The particles displayed stability at pH 5.5-8.0. and we did not observe drug release. In the presence of cathepsin B, we observed delayed Dox release, thereby providing additional support to our hypothesis that Dox locates to the core of the particle and instead of interacting with the chains. We obtained nanorods with stability upon dilution for at least 48 hours and, therefore, represents prospective candidates for the preparation of new soft matter-based nanomedicines with non-spherical shapes.

In parallel, we also developed a method for crosslinking stPGAs with genipin. Crosslinking polyelectrolytes in aqueous solutions represents a highly complicated task due to strong interparticle repulsions. To counteract these problems, we functionalized PGA with amine groups and studied the role of polymer concentration, ionic strength, the content of crosslinker, and polymer architecture in crosslinking reaction efficiency. We determined that star polymers with 10% amine functionalization crosslinked with 75 mol% of genipin, at 2 mg/ml in PBS display the highest crosslinking efficiency. The developed method is simple and efficient in obtaining stable particles with a diameter of up to 60-70 nm. Additionally, we developed a method of mild amine-functionalization of PGA conjugates with acid-, base- and redox-sensitive linkers. Nevertheless, for the **F0E50-SS-Fas** conjugate crosslinked in similar conditions, we determined a much lower size (15-30 nm), thereby emphasizing the high importance of side-chain functionalization on reaction outcome.

We believe that this method represents a suitable approach for the quick and

efficient preparation of more complicated nanosystems, including combination therapies; however, we must first establish a connection between the chain modification and crosslinking for different drugs. Prior to any *in vitro* tests, we also propose that proteolytic degradation with cathepsin B should be studied extensively to correlate the degree of crosslinking and degradation efficiency.

6.5. Supplementary Information

SI-6.1. Materials

SI-6.2. Experimental Methods

SI-6.3. Synthesis of Stabilized Nanorods

SI-6.4. Genipin Crosslinking Procedure

SI-6.1. Materials

Linear PGA was provided by Polymer Therapeutics Solutions S.L. (Valencia, Spain). **F0E50** was prepared as described in **Chapter 2 (Section 2.5)**, and **F0E50-SS-Fas** was prepared as described in **Chapter 5 (Section 5.2.2)**.

SI-6.2. Experimental Methods

Asymmetric Flow Field-Flow Fractionation

Asymmetric Flow Field-Flow Fractionation (AF4) analysis was performed on a PN3212 AF4 fractionator (Postnova Analytics GmbH, Germany) equipped with MALS, RI, and UV-Vis detector under the following conditions:

Sample: C= 1 mg/ml in milliQ; Injection volume: 40 µl; Mobile Phase: 0.1M NaCl + 0.2 g/L Na₃N; Detector flow: 0.5 ml/min. **Focusing step:** Injection Flow 0.2 ml/min, Injection time 5 min, X-flow 2 ml/min, Focus flow 2.3 ml/min. **Elution step:** X-flow 2 ml/min for 5 min, then the X-flow was decreased linearly for 20 min from 2 ml/min to 0.22 ml/min, then with a power decay (exponent 0.8) the X-flow was decreased to 0.07 ml/min and stayed constant for 20 min; **Rinse step:** Detector flow 0.1 ml/min for 1 min.

Fluorescence Spectroscopy

Fluorescence spectroscopy measurements were performed on an FP-6500 spectrofluorimeter (JASCO, Easton, United States).

All fluorescent spectra were measured using a 1.0 cm quartz cuvette. Both excitation and emission slits were set at 5 nm, and the scan rate at 500 nm/min. Excitation spectra were measured with an emission wavelength of 634 nm. Emission spectra were measured with an excitation wavelength of 480 nm. To the solution of the compound was added Dox (1 µg), and the solution was equilibrated for 4 hours prior to measurements.

Pharmacokinetics of Doxorubicin Release. pH-dependent Release. 3 mg of **F3E10/Dox** (10:1) was dissolved in 1 ml of either 25 mM sodium acetate/ 1 mM EDTA buffer (pH 5.5) or PBS buffer (pH 7.4). Samples were incubated at 37 °C. At fixed time points, the mixture was transferred to Vivaspin

tubes with a membrane cut-off of 2 kDa and centrifuged at 3,200 rpm for 20 min. The permeate was collected, diluted six times, and Dox spectra collected with UV-Vis spectroscopy as described above.

Cathepsin-mediated Release. Cathepsin B mediated release was studied using an adapted method from Dubowchik et al.²⁶ Briefly, Cathepsin B (5U) in 60 μ L of 25 mM sodium acetate/1mM EDTA buffer (pH 5.5) was mixed with 120 μ L of 30 mM DTT/15mM EDTA and left to activate for 15 min at RT. 0.3 mL of 10 mg/mL **F3E10/Dox** (10:1) solution in PBS was mixed with 0.7 mL of 25 mM sodium acetate/1mM EDTA buffer (pH 5.5) at 37 °C. This solution was added to the cathepsin B solution, and the mixture was incubated at 37 °C. Samples were collected and analyzed as described for pH-dependent release.

SI-6.3. Synthesis of Stabilized Nanorods

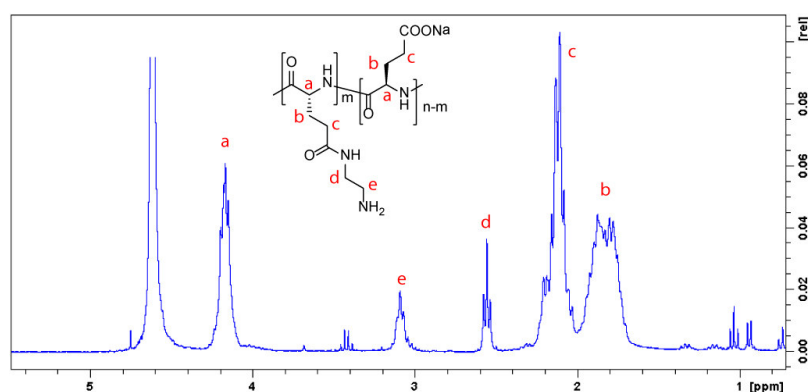
In a typical procedure, a 10 mg/ml solution of **F3E10** in 120 mM NaCl was added an aqueous solution of the corresponding compound at 10 mg/ml (Dox, irinotecan, or doxycycline) in a molar ratio PGA/drug of 5:1, 10:1 or 20:1. In the case of NR, the compound was added to acetone in a similar molar ratio. The solution was allowed to equilibrate for 4 hours at RT. The solution was dialyzed and lyophilized.

Synthesis of Amine Functionalized PGA

Synthesis of Amine-functionalized Linear and Star-PGA

In a typical procedure, PGA or stPGA (1.0 eq) was transferred to a round-bottom flask and dissolved in DMF to reach a final concentration of 10 mg/ml. DMTMM BF₄ (0.11 eq.) was added, followed by the addition of N-Boc-ethylenediamine (0.11 eq.). The pH of the solution was adjusted to 8.0 with DIEA and the mixture was allowed to react for 24 h at RT. The mixture was precipitated into cold diethyl ether, filtered, and then dried under vacuum. The obtained product was used without further purification.

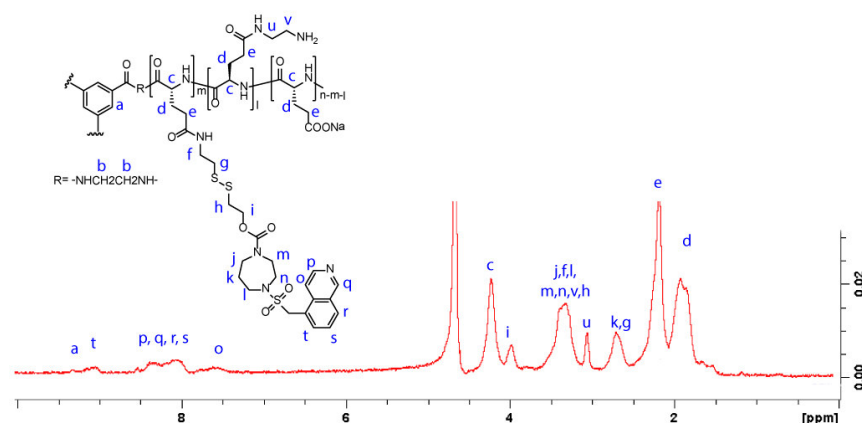
The product was then dissolved in TFA to reach a final concentration of 100 mg/ml. The mixture was stirred for 1 hour, precipitated in cold diethyl ether, filtered, and dried under vacuum. The obtained powder was dissolved in 0.5 M NaHCO₃ and dialyzed for 48 hours. Finally, the compound was lyophilized.



Synthesis of amine-functionalized **F0E50-SS-Fas**

In a typical procedure, **F0E50-SS-Fas** (1.0 eq) was transferred to a round-bottom flask and

dissolved in water to reach a final concentration of 10 mg/ml. DMTMM Cl (0.11 eq.) was added, followed by the addition of ethylenediamine monohydrochloride (0.11 eq.). Mixture allowed to react for 24 h at room temperature, and then the mixture was dialyzed for 72 hours and lyophilized.



SI-6.4. Genipin Crosslinking Procedure

In a typical procedure, 0.25-0.75 eq of genipin (recalculated per amino group amount) from a freshly prepared 10 mg/ml solution was added to a solution of stPGA modified with 5-10 % amine groups in PBS. The solution was allowed to react at 37 °C for 48 h. During this time, a blue to dark blue color of the solution developed. Solutions were dialyzed, treated with 10 eq. glycine, and dialyzed a second time. After lyophilization, compounds were isolated as blue to dark-blue solids.

6.6. References

- Hussein, Y. H. A. and Youssry, M. *Materials*, **11**, 688 (2018).
- Cabral, H. and Kataoka, K. *J. Control. Release*, **19**, 465–476 (2014).
- Liu, F. *et al. RSC Adv.*, **6**, 57552–57562 (2016).
- Yilmaz, Z. E., Vanslambrouck, S., Cajot, S., Thiry, J. *RSC Adv.*, **6**, 42081–42088 (2016).
- Tian, G., Sun, X., Bai, J. and Dong, J. *J. Mol. Med. Rep.*, **19**, 133–142 (2019).
- Zhang, X. and Zhang, Y. *Tumor Biol.*, **36**, 4949–4959 (2015).
- Zhaopei, G. *et al. Biomater. Sci.*, **5**, 2501–2510 (2017).
- Manickam, B., Sreedharan, R. and Elumalai, M. *Curr. Drug Deliv.*, **11**, 139–145 (2014).
- Yang, S. *et al. J. Mat. Chem. B*, **4**, 7283–7292 (2016).
- Hajian, R., Shams, N. and Mohagheghian, M. *J. Braz. Chem. Soc.*, **20**, 1399–1405 (2009).
- Tian, Y. *et al. J. Contr. Rel.*, **121**, 137–145 (2007).
- Kitaeva, M. V., Menger, F. M. and Yaroslavov, A. A. *Langmuir*, **20**, 6575–6579 (2004).
- Airolidi, M. *et al. Biochemistry*, **53**, 2197–2207 (2014).
- Green, N. J. B. and Pimblott, S. M. *J. Phys. Chem.*, **97**, 196–202 (1993).
- Mikhailov, A., Mtchedlishvily, B. and Morgunova, E. *Langmuir*, **10**, 4232–4236 (1994).
- Kabanov, A. *Pure Appl. Chem.*, **56**, 343–354 (1984).
- Polymer grafting and crosslinking. (Wiley, 2009).
- Janeth, C. *et al. Int. J. Pharm.*, **532**, 66–81 (2017).
- Song, F., Zhang, L., Yang, C. and Yan, L. *Int. J. Pharm.*, **373**, 41–47 (2009).

20. Tambe, N. *et al. J Biomed Mater Res B Appl Biomater*, **103**, 1188–1197 (2014).
21. Koo, H. *et al. Eur. J. of Pharmacology*, **495**, 201–208 (2004).
22. Van der Maarel, J. R. C., Groenewegen, W., Egelhaaf, S. U. and Lapp, A. *Langmuir*, **16**, 7510–7519 (2000).
23. Ciccariello, S. and Sobry, R. *J. Appl. Cryst.*, **32**, 892-901 (1999).
24. Arleth, L., Jensen, G. V. and Chakravarthy, S. *Nat Protoc.*, **9**, 1727–1739 (2017).
25. I.-G. Marino, rilt, Matlab central (2013).
26. Dubowchik, G. M. *et al. Bioconjugate Chem.*, **13**, 855–869 (2002).

Chapter 7

General discussion

Cancer represents one of the leading causes of death worldwide; in particular, about 12% of women will develop invasive breast cancer during their lifetime (according to U.S. Breast Cancer Statistics).¹ An ever-growing number of patients and the generally low efficacy of existing therapies, especially with regards to late-stage disease, strongly emphasize the acute clinical need for new and effective therapeutic approaches.^{2,3} Personalized nanomedicinal therapy represents one of the most promising approaches currently under development as it allows for the targeted delivery of active agents and takes into account the individual features of the patient.^{4,5} One of the major problems encountered in this area is the difficulty in creating a versatile technology that allows for the rapid preparation of nanotherapeutics with precisely controlled physicochemical properties.⁶

In the hope of overcoming such limitations, the work undertaken in this thesis has focused on the development of rationally designed nanosystems based on polyelectrolytes, polypeptide-based materials, and in particular star-shaped polyglutamates (PGAs)^{7,8} that display suitability for the rapid on-demand preparation of personalized nanomedicines. PGAs have already seen clinical application^{9,10} and represent a highly promising class of biomaterials for personalized approaches due to their biocompatibility, low immunogenicity, and structural versatility.⁸

Mimicking the wide structural diversity of biomolecules with synthetic polyelectrolytes remains a complicated task given the existence of multiple repulsive Coulomb interactions and a low degree of order that results in an almost exclusively spherical particle morphology in aqueous solutions containing physiological levels of salt.¹¹ Synthesis of stable polyelectrolyte nanoparticles in solution remains a significant issue due to their unique hydrodynamic properties and biodistribution profiles.⁸ Now, we introduce two new approaches for the preparation of polyelectrolyte-based nanomedicines, namely (i) supramolecular star-PGA assembly into one-dimensional (1D) nanorods and nanofibers in water and (ii) star-PGA crosslinking in aqueous solutions under mild conditions forming spherical nanomedicines.

Benzenetricarboxamide (BTA) is a well-established supramolecular motif widely employed in supramolecular polymerization in both aqueous and organic medium.^{12,13} Following the covalent attachment of various hydrophobic domains to BTA, the obtained molecules assemble into 1D fibers or rods due to the formation of a directional C3-symmetric network of non-covalent interactions; however, aqueous self-assembly requires additional shielding with neutral hydrophilic molecules.¹⁴ A plethora of BTA-based molecules have been studied; however, the vast majority of those reported were uncharged. While this facilitates self-assembly by minimizing charge repulsions, it also limits synthetic plasticity. Several studies have reported star-poly-amino acids with BTA-based cores;¹⁵ however, BTA played the role of a multifunctional core rather than a supramolecular motif in all cases.^{8,16} Charge screening with low molecular weight salts has been successfully applied for small BTA-based molecules bearing ionizable groups, achieving control for up to nine charges for Newkome dendron decorated molecules.¹⁷ We replaced Newkome dendrons with PGA chains to allow an increase in solubility and provide multiple functional groups for additional functionalization. After an exhaustive analysis of the available literature, we selected BTA derivatives of phenylalanine as a starting point for the preparation of supramolecular PGAs due to their strong tendency to assemble into 1D objects in aqueous solutions. We designed and prepared a small family of star-PGAs with BTA-based oligophenylalanine cores bearing 0 to 200 glutamic residues per arm. We extensively analyzed compounds with NMR, fluorimetry, SAXS, and TEM. Through the detailed analysis of self-assembly, we observed a smooth transition in particle morphology. Compounds with a lower amount of phenylalanine units in the core and longer PGA chains behaved as classical polyelectrolytes in solution and assembled into metastable spherical aggregates according to the ordinary-extraordinary transition mechanism described by Duro-Castaño et al.⁸

We observed that short oligo- and poly-glutamates with more hydrophobic cores assembled into fiber-like particles similar to supramolecular polymers. Furthermore, we discovered a reversed exponential dependence of compound CAC on the number of glutamic units per arm. When the PGA chain length becomes higher than 15-25 units, compounds lose the ability to self-assemble in aqueous solutions, independent of the conditions, and behave as normal polyelectrolytes (as depicted in **Fig. 7.1**).

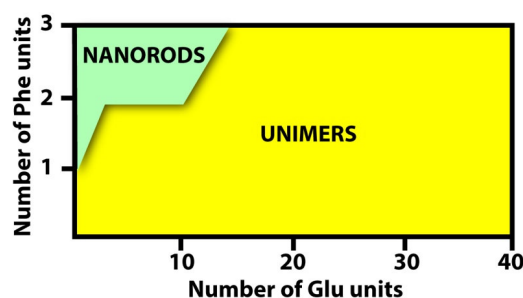


Figure 7.1. Diagram of existing morphologies in BTA-based star-oligo- and star-polyglutamates systems with general structure F_xE_y ($x = 1-3$, $y = 0-40$) in both water and 120 mM NaCl.

We selected **F3E10** as the most promising candidate for further studies, as it combines the properties of both supramolecular polymers and star-polyelectrolytes. Other **F3**-based star-polyelectrolytes demonstrated similar self-assembly behavior as observed for star-polyaspartate, star-polyornithine, and star-polylysine; however, the tendency to assemble increased with the increasing length of methylene chain of aminoacids (as explained in **Chapter 2**). Counterion variation demonstrated that large ions with deformable electronic layers (e.g., Cs) favored the disassembly of aggregates while small hard ions (e.g., Li, Na, and K) favored polymer aggregation. Quite unexpectedly, ammonium ions strongly favored self-assembly, and compound **F3E10-NH4** formed very long fibers, reaching tens of microns at a concentration lower than corresponding compounds with other counterions (Chapter 2).

Very interestingly, we also observed that **F3E10** nanorods formed adouble helix (by cryo-TEM and SAXS), an unreported occurrence for BTA-based systems. After an in-depth analysis by complementary physico-chemical techniques, we propose a hypothetical model of **F3E10** self-assembly that involves a shift of the molecule on both the X- and Y-axis in the XY plane with a twist of around 10° around the Z-axis.¹⁸ π - π stacking interactions are more energetically favorable in the case of offset stacking than sandwich stacking; in this way, the network of directional non-covalent interactions will not be disrupted. In the center of the molecule, BTA rings will be shifted one against the other, so that interactions will occur through amide- π stacking and/or π - π stacking. From cryo-TEM data, we estimated the number of molecules per full twist as 38 ± 5 units, which corresponds to a twist angle of 9.47 ± 1.43 degrees; however, the mechanism of fiber interaction remains unclear. The packing of negatively charged PGA chains in the center of the double-helical structure represents an unlikely scenario due to strong repulsions; furthermore, the distance between fiber centers (1.4 nm), as determined from cryo-TEM, is insufficient for the overlap of aromatic rings from two separate fibers. Therefore, we hypothesize that C3-symmetry deviation results in an exposed hydrophobic region in a single fiber that interacts with a similar region on another fiber, thereby prompting the

formation of a double helix. Despite everything described above, we underscore the requirement for further experiments to confirm the proposed model fully.

BTA-based supramolecular polymers, as well as polyelectrolyte rod-like or worm-like micelles, suffer from disassembly upon dilution that significantly limits their applicability in drug delivery. Micelles require crosslinking to achieve stabilization, and hydrophobic drugs, such as paclitaxel (PTX) or doxorubicin (Dox), have been used to non-covalently stabilize micelles.¹⁹ **F3E10-Na** nanorods display instability upon dilution, so, to promote the implementation of similar materials in the design of personalized nanomedicines, we developed a method of particle stabilization (or non-covalent crosslinking) with hydrophobic molecules such as Dox or irinotecan (Iri). Cryo-TEM analysis demonstrated that particles have an inner structure identical to non-stabilized particles; however, rod-like particles remain stable upon dilution for more than 48 hours. Furthermore, we failed to detect Dox loss upon dialysis of the particles using 1 kDa and 50 kDa cut-off dialysis filters. Careful control over construct preparation allowed the generation of nanorods with a length of 50-120 nm that displayed stability upon dilution for several days. Dox incorporation not only stabilizes nanorods but strongly pulls the equilibrium towards nanorod formation, thereby minimizing the presence of unimers or small oligomer species within the system.¹⁸

To understand the above-noted observation, we studied the interaction of Dox with a series of compounds bearing a different number of glutamic units per arm via fluorescence spectroscopy. While we observed Dox interaction with hydrophobic cores of the molecule rather than with the PGA chains, the precise mechanism of interaction remains still unclear. We did not observe spectroscopic signatures of Dox intercalation; however, the mode of interaction differs from a simple ionic interaction, in contrast with stPGA lacking hydrophobic cores (see **Chapter 6**). Of note, Dox does not interact with cationic supramolecular polymers such as **F3** due to strong charge repulsions.

Controlled drug release kinetics strongly determine the efficiency of a drug delivery system - in the case of loaded micelles and the absence of chemical conjugation, we have to consider that drug release might be complicated by strong drug-matrix interactions. While we found negligible Dox release from **F3E10/Dox** nanorods under acidic (pH 5.0) and slightly basic (pH 8.0) conditions, the presence of cathepsin B, a lysosomal serine protease capable of degrading PGAs,²⁰ prompted a delayed-release with a close to an exponential profile similar to that previously described for loaded micelles.²¹ Of particular interest, the specific release mechanism of this system requires the almost complete cleavage of PGA chains by cathepsin B for significant Dox release. We believe that the release kinetic profile observed with **F3E10/Dox** and its non-typical soft-matter shape represent hugely promising features for the development of a new family of nanodrug-delivery systems with higher control over physicochemical properties and pharmacokinetics.

As a next step, we attempted to optimize the **F3E10/Dox** system to obtain compounds with lower CAC values that form a stronger directional three-dimensional

(3D) network of hydrogen bonds that would increase system stability at higher dilutions without the need for crosslinking. Toward this aim, we prepared several families of BTA-based compounds with different core structures as a core variation, in addition to improving existing systems, can lead to compounds with new morphologies. Studies have demonstrated that shape and deformability can drive altered biodistribution and cell trafficking of designed nanomedicines;^{7,8,22,23} therefore, novel morphologies could improve drug(s) pharmacokinetics and pharmacodynamics and, therefore, enhance therapeutic value. Initially, we studied how the nature and order of amino acids in the core affect self-assembly (**Chapter 3**). We determined that amino acids in close proximity to the core play a pivotal role in determining self-assembly of the compound and interactions between fibers. When the hydrophobicity of a given amino acid decreases, fibers tend to interact more and form helices and ribbons, most probably due to the deviation of molecular shape away from planarity that occurs when more hydrophobic amino acids are present.

Interestingly, our studies also indicated that the length of the hydrophobic amino acid sequence significantly influences polymer self-assembly. BTA derivatives with both di- and tri-peptide derivatives and corresponding small star-PGAs assembled into 1D nanorods and nanofibers; however, when we studied tetrapeptide derivatives, we observed the formation of small core-shell micelles even at high polymer concentrations. Most probably, an increase in flexibility upon an increase in amino acid length leads to a more energetically favorable scenario for core-shell micelle formation (**Fig. 7.2**). Research on how particle morphology influences biodistribution, accumulation, cell penetration, and release kinetics remains scarce in the soft matter field as materials with different shapes usually possess diverse compositions even when they consist of similar structural elements. Circulation time and passive targeting due to enhanced permeability and retention (EPR) effect strongly depend on particle shape; as an example, studies have found that paclitaxel-based worm-like micelles display elevated circulation time and increased passive targeting activity when compared to PEG-polyethylene-based spherical micelles.^{24,25} Furthermore, soft particles with higher length-to-width ratio display higher bioavailability,²⁶ while small core-shell micelles exhibit lower systemic toxicity thanks to a more rapid renal clearance and are, therefore, more suitable for theranostics.²⁷

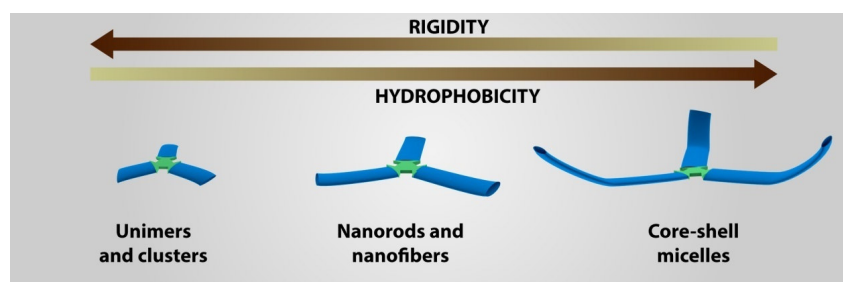


Figure 7.2. Dependence of core rigidity and hydrophobicity on the self-assembly morphology.

We next studied how various structural elements placed in-between the BTA core and aminoacid sequence influence self-assembly of BTA-based compounds and the corresponding polymers using **F2E10** star-shaped systems as a starting point. We observed that the insertion of *p*-aminobenzoate in-between the BTA core and a diphenylalanine sequence prompted the formation of short nanorods that interacted at higher concentrations to form mass fractals. Meanwhile, the insertion of *m*-aminoisophthalate resulted in the formation of disordered aggregates (**Chapter 4**). We believe that the difference in assembly derives from the greater steric complexity of *m,m*-aminoisophthalate derivatives that restrict the phenyl ring orientation within a single plane. For the corresponding polymers, we observed the formation of core-shell micelles most probably due to phase separation mechanism; however, when we prepared **ABA-F2** with 50 glutamic units per arm, we observed the formation of short rods of around 15 nm in length (**Chapter 4**).

Unexpectedly, the addition of hydrophobic aliphatic chains to the termini of **F2** resulted in the formation of two-dimensional (2D) objects with sharp edges. To the best of our knowledge, this morphology has never been described for BTA-based systems before, and the precise mechanism still remains unclear and deserves further investigation. The corresponding polymers self-assembled into very small objects below 10 nm, and we suggest an identical polymer self-assembly mechanism to the corresponding core. In the case of 2D rectangular ribbons, the corresponding polymers most probably failed to self-assemble due to a high spatial concentration of negative charges (**Chapter 4**).

Combining the data generated for all compounds prepared in this Thesis, we conclude that star-PGAs based on flexible hydrophobic cores do not generally assemble into 1D supramolecular aggregates and instead collapse into small core-shell micelles, with only sufficiently rigid cores trigger the formation of polyelectrolyte nanorods. Both morphologies may prove useful to the development of drug delivery systems with defined properties; the “beauty” of this finding is that with the same chemical tools, we can achieve drug delivery technologies with a very different pharmacokinetic/pharmacodynamic properties with the potential to cover the requirements derived from various patient profiles.

When we compiled all data regarding particle morphology and dependence on core hydrophobicity, we schematically depicted morphology diagrams, as shown in **Fig. 7.3**. For star-block-polyelectrolytes, and to some extent for anionic supramolecular polymers, the observed trends correspond to data currently in the literature;^{28,29} however, the diagram for supramolecular star-polyelectrolytes has never been reported until now. To the best of our knowledge, small star-block-polyelectrolytes that assemble into rod-like objects represents a new link between classical block-polyelectrolytes and charged supramolecular polymers.

The simple control of nanosystem shape (nanorods, nanofibers, and core-shell micelles) through subtle changes to structure represents a valuable tool that allows the

precise study of system biological behavior (e.g., biodistribution, circulation time, internalization pathway, etc.). The materials with multiple morphologies that we prepared may prove useful to applications beyond drug delivery, such as tissue engineering and theranostics. We also emphasize the versatility of star-PGA carriers, which, in addition to the previously demonstrated precise control of size and charge,⁸ can be shape-controlled to expand their applicability for the preparation of personalized medicines.

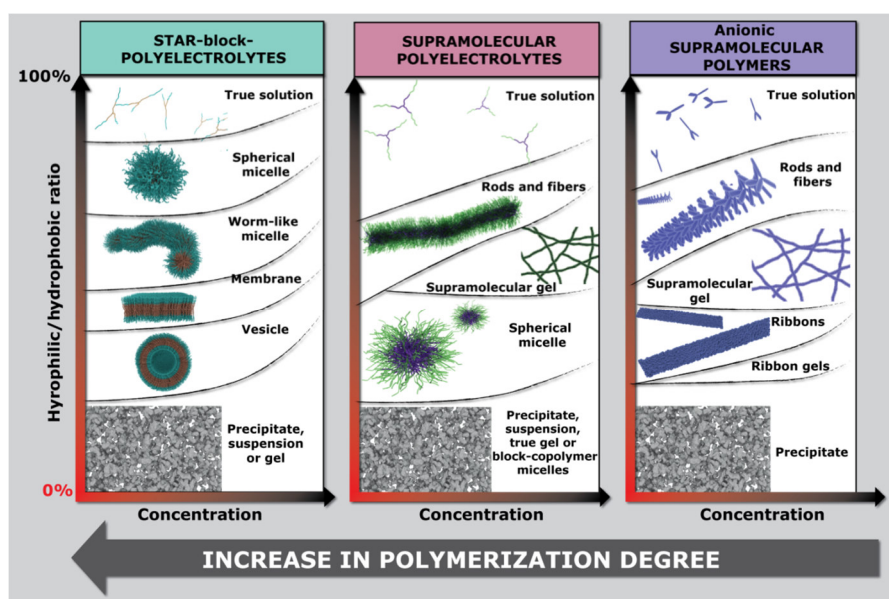


Figure 7.3. Schematic diagram of the self-assembly of previously described star-block copolymers and corresponding diagrams for supramolecular polymers and supramolecular polymers studied in this work.

After demonstrating the versatility offered by our PGAs, the final aim of this thesis was therapeutic validation with regards to their suitability as part of treatment approaches for aggressive breast cancer. Due to disease complexity, combination therapies have arisen as the most efficient treatment modality.³⁰ Polypeptide-based combination therapies include a physical mixture of a single polymer-drug conjugate with another polymer-drug conjugate or free drug(s), a strategy already in the clinics. However, the conjugation of several drugs to the same polymer chain using adequate drug-linker design permits the simultaneous release of both drugs at the same site of action at the desired ratio to allow for drug synergism.^{31–33} Other strategies include combinations of a given polymer-drug conjugate with other therapies, such as immunotherapy and radiotherapy.^{34,35}

The Polymer Therapeutics laboratory at the CIPF is a pioneer in the field of combination therapies using polymer therapeutics.^{15–17} We developed the first polymeric

combination conjugate for advanced hormone-dependent breast cancer; a conjugate of 2-(hydroxypropyl)methacrylamide-aminoglutethimide-doxorubicin (HPMA-AGM-Dox) that combines endocrine therapy (the AGM aromatase inhibitor) and chemotherapy (Dox), respectively.^{15–17} The development of this combination conjugate derives from the demonstrated activity of HPMA-Dox in chemoresistant breast cancer³⁶ and the observed synergism of aromatase inhibitors³⁷ with conventional chemotherapy.^{38–40} We further corroborated the utility of similar combination conjugates findings via the generation of a new family of biodegradable PGA-based combination conjugates that displayed improved clinical relevance.^{41,42}

To move a step beyond our previous studies, we aimed to develop another combination therapy based on star-PGAs crosslinked in aqueous solutions performed in two parts: (i) drug conjugation and linker design to control bioresponsiveness and adequate drug release kinetics profile (**Chapter 5**) and (ii) crosslinking of star-polymer and conjugate modeling to establish the basis for a successful combination therapy (**Chapter 6**).

In the framework of the European Research Council-funded project “MyNano,” our laboratory screened available chemotherapeutic drugs to determine possible synergism between different combinations suitable for the treatment of metastatic triple negative breast cancer (TNBC). One promising combination pair, when employed at the adequate ratio, was the Rho-associated protein kinase (ROCK) inhibitor fasudil⁴³ and the cyclin-dependent kinase inhibitor dinaciclib.^{44–46} We first generated single drug conjugates (PGA-Fas and PGA-Din) to optimize linking chemistry, and later developed these into a combination with optimized drug activity.

We prepared two families of conjugates with fasudil and dinaciclib with different responsive linking moieties, including enzyme-cleavable (amide and biphenyl, -PP-), pH- (ester, -O-), and redox-sensitive (self-immolative disulfide, -SS-) linkers. After their physicochemical characterization, we tested PGA-Fas and PGA-O-Fas in two breast cancer cell lines (MDA-MB-231 and 4T1) and PGA-SS-Fas on three breast cancer cell lines (MDA-MB-231, MDA-MB-453, and 4T1) to determine cell viability. PGA-Fas and PGA-O-Fas linked through ester or amide bond displayed very low to no activity that correlated with slow drug release. PGA-SS-Fas exhibited comparable or slightly lower toxicity than the free form of the drug; however, the IC₅₀ was more than five times lower than for the free drug in the MDA-MB-231 cell line. *In vivo* evaluations of our drug conjugates in a TNBC model⁴⁷ failed to demonstrate statistically significant decreases in metastasis progression, probably due to low cytotoxicity of the drug. After their physicochemical characterization, we tested PGA-O-Din, PGA-PP-Din, and PGA-SS-Din in the MDA-MB-231 and ZR-75-1 cell lines. We observed very low PGA-O-Din activity, at almost four orders of magnitude lower than the free drug. PGA-PP-Din and PGA-SS-Din also displayed 3–10 times less activity when compared to the free drug, with PGA-SS-Din displaying the highest activity among all Din conjugates.

Due to the high synergistic ratio required for the combination of fasudil and dinaciclib drugs (around 1:10000), it was impossible to prepare a single combination conjugate. However, we prepared a conjugate with the maximum achievable ratio (Fas:Din=10:1) and tested this combination conjugate in the MDA-MB-231 and ZR-75-1 cell lines. We did not observe synergism between the drugs, as the observed toxicity derived from the more active drug. To reach a higher ratio between the drugs, we developed a mild orthogonal crosslinking method for star-PGA and its conjugates (**Chapter 6**). A PGA modified with 5-10 % of amino groups can be non-reversibly crosslinked with natural compound genipin⁴⁸ in aqueous medium with precisely controlled salt composition. With this method, particles of 20-70 nm can be obtained as proven by DLS, SAXS, AF4, and TEM. When we tried to apply a similar approach to the PGA-SS-Fas conjugate at similar conditions, we observed the formation of smaller (10-25 nm) but homogeneous particles. We are currently attempting to determine how the degree of drug conjugation and the nature of the drug correlate with the final size of the crosslinked particles.

Overall, these findings depict the early development stages of a platform for the quick and efficient preparation of personalized therapies for TNBC with a high degree of control over the physicochemical properties and drug ratio.

Future Research

We envisage a number of possible research lines to follow the work described within the thesis, both at the applied and theoretical levels, some of which have been started in earnest.

- A more detailed study of the self-assembly mechanism of BTA-based molecules, including C3 symmetry deviation, to explain fiber interactions and twisting
- The development of nanosystems for the rapid preparation of combination therapies based on dinaciclib and fasudil conjugates through the evaluation of star-PGAs with self-immolative linkers and an exploration of their co-assembly and activity
- The development of a quick and easy platform for the rapid preparation of personalized nanomedicines with controlled physicochemical properties by establishing the dependence of the nature of the conjugated drug on the crosslinking efficiency and particle size, deformability, and density.
- The study of nanorod stability in plasma and their biodistribution, and a comparison with similar spherical particles, which will allow the validation of the application of non-covalently stabilized nanosystems *in vivo*.
- The development of materials for tissue engineering that mimic the extracellular matrix. A series of gelators (e.g., **F3G1**, **GFF**, or **LFF**) and polymers (e.g., **F3E10NH4**) prepared during the development of this Thesis assemble into long nanofibers and can be chemically modified to provide cell adhesion and differentiation. Further

modification with adhesion molecules and/or growth factors will allow the development of novel tissue engineering scaffolds with easily tunable properties.

References

1. www.breastcancer.org.
2. Siegel, R. L. and Miller, K. D. *CA Cancer J Clin*, **69**, 7–34 (2019).
3. Bray, F., Ferlay, J. and Soerjomataram, I. *CA Cancer J Clin*, **68**, 394–424 (2018).
4. Ren, J. *et al. P. Nano Lett.*, **19**, 4692–4701 (2019).
5. Lee, Y. and Lee, C. H. *Biotechnol. Adv.*, **36**, 335–343 (2018).
6. Zagorodko, O., Arroyo-Crespo, J. J., Nebot, V. J. and Vicent *Macromol. Biosci.*, **17**, 1600316.
7. Duro-Castano, A. *et al. Mol. Pharm.*, **12**, 3639–3649 (2015).
8. Duro-castano, A. *et al. Adv. Mater.*, **29**, 1702888 (2017).
9. Plummer, R. *et al. Br. J. Cancer*, **104**, 593–598 (2011).
10. Harburg, K., Hemer, L. and Freiburg, U. *Br. J. Cancer*, **98**, 1608–1613 (2008).
11. Chen, C., Wylie, R. A. L., Klinger, D. and Connal, L. A. *Chem. Mater.*, **29**, 1918–1945 (2017).
12. Matsumoto, N. M. *et al. JACS*, **140**, 13308–13316 (2018).
13. Cantekin, S., Greef, F. A. De and Palmans, A. R. A. *Chem. Soc. Rev.*, **41**, 6125–6137 (2012).
14. Krieg, E., Bastings, M. M. C., Besenius, P. and Rybtchinski, B. *Chem. Rev.*, **116**, 2414–2477 (2016).
15. Holm, R. *et al. Biomacromolecules*, **20**, 375–388 (2019).
16. Holm, R. *et al. Macromol Biosci.*, 1900152 (2019).
17. Ahlers, P. *et al. Macromol. Biosci.*, **17**, 1–7 (2017).
18. O. Zagorodko, V. J. Nebot, and M. J. Vicent *Pol. Chem.* Just accepted (2019).
19. Washington, K. E., Kularatne, R. N., Biewer, M. C. and Stefan, M. C. *ACS Biomater. Sci. Eng.*, **4**, 997–1004 (2018).
20. Wang, H., Wang, S. and Liu, Z. *Nanotechnology*, **28**, 055101 (2017).
21. Dheer, D., Nicolas, J. and Shankar, R. *Adv. Drug Deliv. Rev.*, **151–152**, 130–151 (2019).
22. Cabral, H. *et al. Nat. Nanotechnol.*, **6**, 815–823 (2011).
23. Kersey, F. R. *et al. Langmuir*, **28**, 8773–8781 (2012).
24. Wang, Y. *et al. Mol. Pharm.*, **11**, 3766–3771 (2014).
25. Geng, Y. A. N. *et al. Nat. Nanotechnol.*, **2**, 249–255 (2007).
26. Zhao, Y. *et al. Sci. Rep.* **7**, 1–11 (2017).
27. Smart, I. and Therapy, C. *Cancers*, **10**, 238 (2018).
28. Fahmi, A., Pietsch, T., Mendoza, C. and Cheval, N. *Mater. Today*, **12**, 44–50 (2009).
29. Borisov, O., Haataja, J. S., Ikkala, O., Mu, A. H. E. and Lo, T. I. *Nat. Commun.*, **7**, 12097 (2016).
30. Song, W. *et al. Acta Biomater.*, **10**, 1392–1402 (2014).
31. Al., K. S. S. *et al.* Tuning polypeptide-based micellar carrier for efficient combination therapy of ErbB2-positive breast cancer. *J Control Release*, **264**, 276–287 (2018).
32. Ramasamy, T. *et al. Acta Biomater.*, **48**, 131–143 (2017).
33. Zhou, W. *et al. Front. Mol. Neurosci.*, **10**, 1–17 (2017).
34. Song, H. *et al. Theranostics*, **9**, 2299–2314 (2019).
35. Schaal, J. L. *et al. J. Control. Release*, **228**, 58–66 (2016).
36. Conjugates, A. D. *et al. Clin. Cancer Res.*, **5**, 83–94 (1999).
37. Johnston, S. R. D., Dowsett, M. and Hospital, R. M. *Nat. Rev.*, **3**, 821–831 (2003).
38. Strasser, K. and Goss, P. E. *J. Clin. Oncol.*, **19**, 881–894 (2016).
39. Lunning, P. E. *Eur. J. Cancer*, **36**, S81–S91 (2000).
40. Pietras, R. J. *Oncologist*, **11**, 704–717 (2006).
41. Arroyo-Crespo, J. J. *et al. Adv. Funct. Mater.*, **28**, 1800931 (2018).

42. Arroyo-Crespo, J. J. *et al. Biomaterials*, **186**, 8–21 (2018).
43. Yamashita, K., Kotani, Y. and Nakajima, Y. *Brain Res.*, **1154**, 215–224 (2007).
44. Inhibitor, C. K. *et al. Clin. Breast Cancer*, **14**, 169–176 (2014).
45. Jo Chien, A. *et al. J. Clin. Oncol.*, **37**, 1072 (2019).
46. Gojo, I. *et al. Cancer Chemother Pharmacol* **72**, 897–908 (2013).
47. Arroyo-Crespo, J. J. *et al. Int. J. of Cancer*, **145**, 2267–2281 (2019).
48. Manickam, B., Sreedharan, R. and Elumalai, M. *Curr. Drug Deliv.*, **11**, 139–145 (2014).

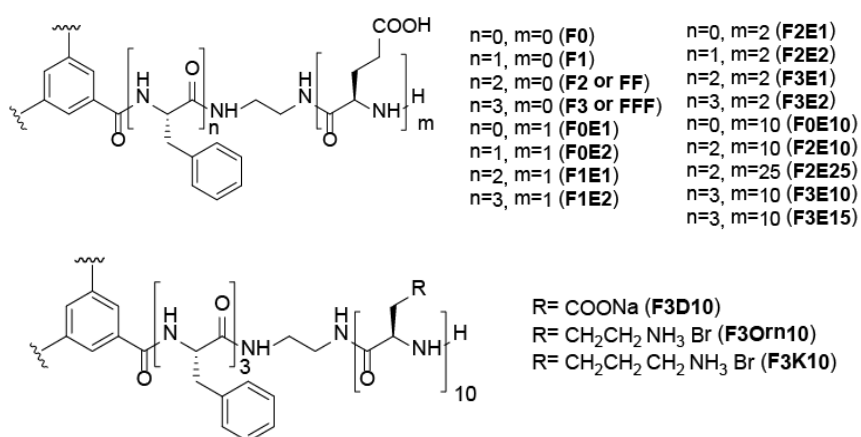
Annex

List of compounds studied in this thesis

Special note: Two compounds in this thesis with identical structure have different short names in different chapters. For example, F3 compound is also named FFF and (*L,L,L*)-FFF. F2 is also called FF and FF-C2. This is done in order to simplify the notation in general and to keep it coherent through the chapters and corresponding sections.

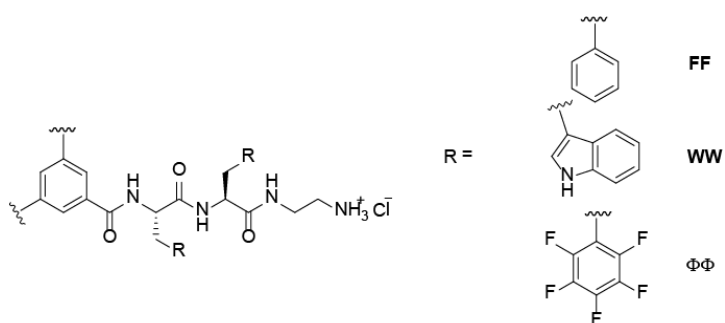
Chapter 2

Compounds with BTA-oligophenylalanine cores

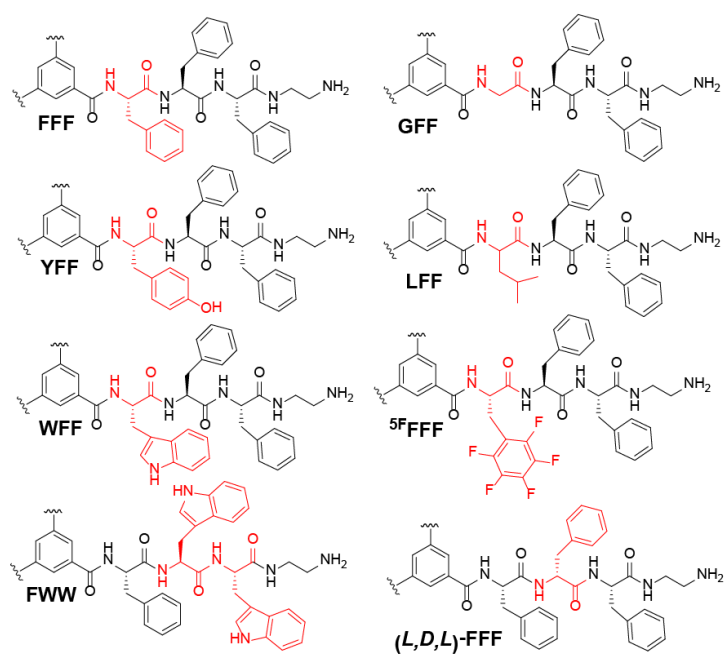


Chapter 3

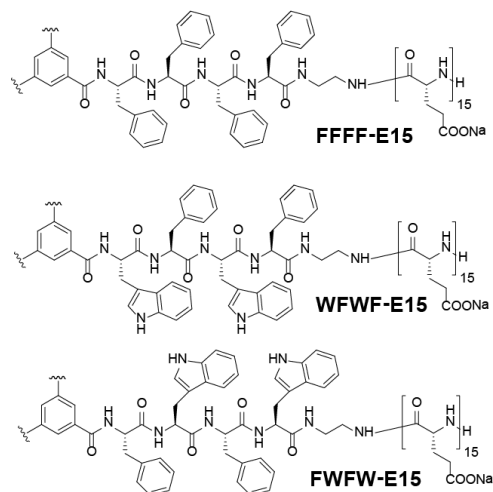
Compounds with BTA-dipeptide cores



Compounds with BTA-tripeptide cores

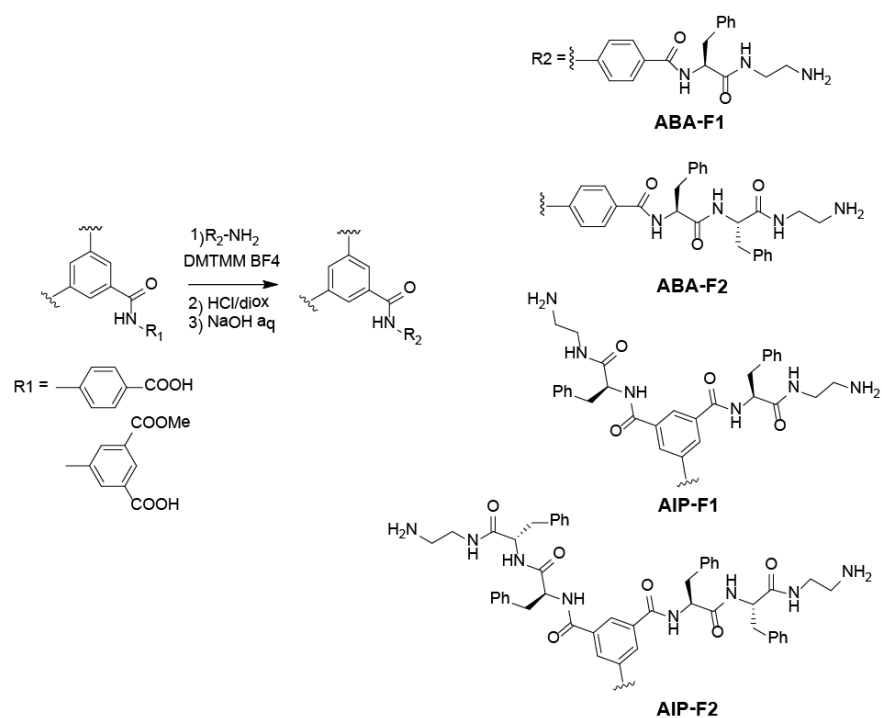


Compounds with BTA-tetrapeptide cores

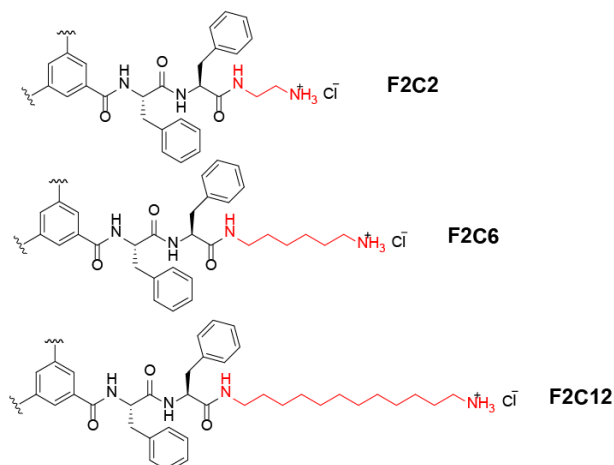


Chapter 4

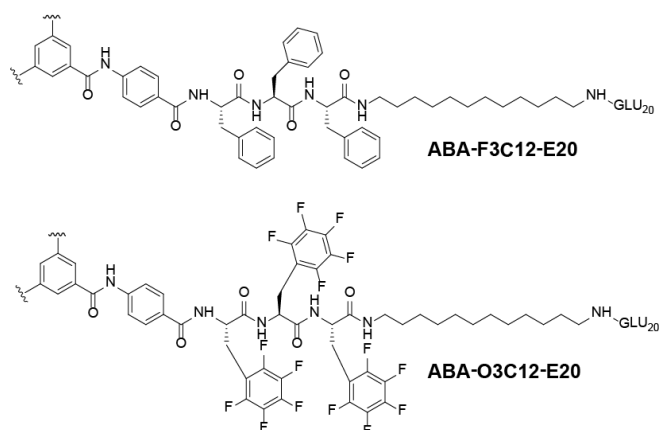
Compounds with aminobenzoate and aminoisophthalate insertions



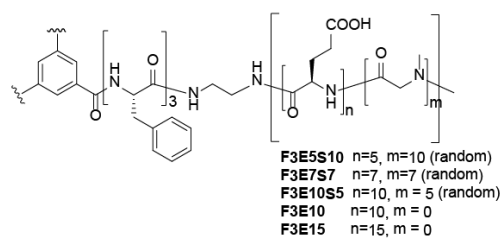
Compounds with varied length of terminal methylene chain



Compounds with varied composition

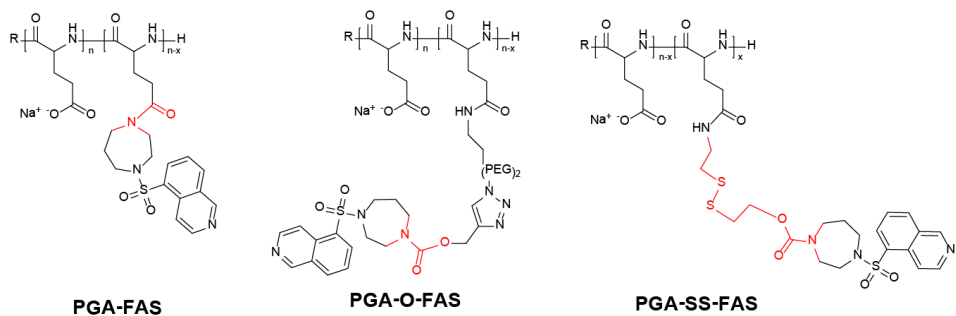


Compounds with varied charge density in the chain



Chapter 5

PGA-Fasudil conjugates with different linkers



PGA-Dinaciclib conjugates with different linkers

